2017

Elastocapillary Phenomena in Soft Elastic Solids

Aditi Chakrabarti
Lehigh University

Elastocapillary Phenomena
in Soft Elastic Solids

by

Aditi Chakrabarti

A Dissertation
Presented to the Graduate and Research Committee
of Lehigh University
in Candidacy for the Degree of
Doctor of Philosophy

in

Chemical Engineering

Lehigh University

May 2017

Certificate of Approval

Approved and recommended for acceptance as a dissertation in partial fulfillment of the requirements for the degree of Doctor of Philosophy.

_____

Date

_____

Accepted Date

_____

Professor Manoj K. Chaudhury
Department of Chemical and Biomolecular Engineering,
Lehigh University
Dissertation Advisor / Committee Chair

Other Committee Members:

_____

Professor Hugo S. Caram
Department of Chemical and Biomolecular Engineering,
Lehigh University

_____

Professor Mohamed S. El-Aasser
Department of Chemical and Biomolecular Engineering,
Lehigh University

_____

Professor Mayuresh V. Kothare
Department of Chemical and Biomolecular Engineering,
Lehigh University

_____

Professor Howard A. Stone
Department of Mechanical and Aerospace Engineering,
Princeton University

Acknowledgments

A doctoral degree is much more than just a scientific one for several reasons. For me, this journey has been transformational, both on scientific as well as personal levels. I will take this moment to express my gratitude to those without whom this journey would not have been possible.

I feel blessed to have had the opportunity to work with Professor Manoj K. Chaudhury as my Ph.D. advisor at Lehigh University for the past four and a half years. No amount of written acknowledgment can express the deep gratitude and admiration that I hold towards him for being a phenomenal mentor. His ideas, depth of knowledge and vastness of experience steered my doctoral research in a way that wouldn't have been possible without his constant inputs. From designing good experiments to writing papers, his patient guidance was instrumental in each step of my graduate education. Enthusiasm, rigor, discipline and dedication towards *Research* are some of his key qualities that have been inspirational in shaping me as a scientist. I would like to acknowledge his support in helping me participate in numerous conferences including a workshop on adhesion at ESPCI, Paris in 2014 and a research stay in Montpellier, France for several months during 2015-2016. Apart from the innumerable scientific discussions that we regularly had, I have been personally enriched by his views on diversified topics ranging from philosophy to poetry. On the whole, I will always treasure the experience of knowing and working with Professor Chaudhury during this period.

I would like to thank my Committee members: Professor Mayuresh V. Kothare, Professor Mohamed El-Aasser, Professor Hugo Caram and especially, Professor Howard A. Stone for taking out valuable time from their busy schedules to monitor my progress. Their encouragement, support, and discussions have been very helpful. It was really nice visiting Professor Stone's lab at Princeton University in August 2015 where I had stimulating discussions about our research and the role of viscosity in the motion of particles at the oil/gel interface.

I would also like to acknowledge several other Professors who mentored me during my doctoral voyage. Most importantly, many thanks to Professor Yves Pomeau and Professor Serge Mora, whose interest in our work early in 2013 marked the

beginning of an enriching collaboration leading to a joint publication, '*Elastobuoyant heavy spheres: A unique way to study nonlinear elasticity*' (*Physical Review X,* 2016). I am immensely grateful to Serge to have hosted me in his group (Physique et Mécanique des Milieux Divisés, LMGC) in University of Montpellier for seven months. I worked on the project 'Nonlinear Rayleigh-Taylor Instability in Soft Elastic Solids' in close collaboration with him, Professor Yves Pomeau and Professor Basile Audoly. My sincere gratitude to Yves for making several trips to Montpellier from Paris for our joint meetings that gave us very deep insights into the problem. I thank Serge for his patience and the daily discussions on the board about various aspects of the project and helping me whenever I got stuck with the calculations. It was a pleasure to work with Ty Phou, Jean-Marc Fromental, and Serge at Laboratoire Charles Coulomb (Montpellier) on experiments of hexagonal pattern formation in enormous gel slabs. Many thanks also to Basile for hosting me at École Polytechnique, Palaiseau in Paris for the several meetings on this project. This experience has supplemented and helped me tremendously in my scientific growth.

I had the opportunity to work closely with Professor L. Mahadevan along with Professor Chaudhury on the paper 'Elastic Cheerios Effect', where their molecular dynamics simulations on how particles interact on soft substrates together with our experiments made for an exciting publication. Thanks to Dr. Katharine Jensen and Professor Eric Dufresne for the generous opportunity to work with them on the project 'Wetting and phase separation in soft adhesion'. Many thanks to Dr. Thomas Salez and Professor Elie Raphaël for all the scientific discussions on our ongoing work on wetting of soft hydrogels.

I was fortunate to receive kind invitations to give talks on our research during the time as a graduate student. I would like to acknowledge Professor Marleen Kamperman from the Department of Physical Chemistry and Soft Matter, Wageningen University in Netherlands; Equipe Matière Molle from Laboratoire Charles Coulomb in Montpellier, France; Professor Animangsu Ghatak from Indian Institute of Technology, Kanpur and Professor L. Mahadevan from Harvard University to present our research to his group.

I am thankful to my fellow lab mates Dr. Jonathan Longley, Dr. Chih-Hsiu Lin and Dr. Partho Sarathi Gooh Pattader who helped me in coming up to speed with regards to the technical aspects during my initial months at Lehigh. Professor Susan

Table of Contents

Preface

Chapter 5: Surface Folding Induced Attraction and Motion of Particles in a Soft Elastic Gel: Cooperative Effects of Surface Tension, Elasticity and Gravity . . . 117

Chapter 6: Elasto-capillary interaction of particles on the surfaces of ultra-soft gels: a novel route to study self-assembly and soft lubrication 141

***

List of Figures

In Chapters

(a) Liquid droplet deposited on a soft substrate: the solid is deformed in the vicinity of the contact line (adapted from ref.). (b) Elastic sphere in contact with a solid surface, without any normal load: in the presence of surface forces (adhesion), the contact is not punctual but presents a disc shape of diameter a (adapted from ref.). Reprinted (along with caption) with permission from ref.

Examples of *Elastocapillary* phenomena. (a) Capillary origami induced by thin elastic sheets self-folding into organized shapes around a liquid drop that is gradually evaporating. Reprinted with permission. (b) Coalescence of wet hair due to negative pressure inside the capillary films in between the strands. Reprinted with permission[5]. (c) Durotaxis of liquid drops on a surface that has a periodic gradient in thickness. Liquid drops collect at the region where substrate thickness is maximum. Reprinted with permission. (d) Rayleigh Plateau instability in slender rods of agar gel. Reprinted with permission.

(a) Various kinds of instability patterns observed in thin and stiff elastic films in different geometries (b) Wavelength of instability from large variety of experiments (shown in the left panel) involving films of different shear modulus, $\mu = 0.25 - 2.0$ MPa and contactors of different rigidity all fall on a single master line. The symbol (■) indicates peeling instability (Ref., Fig. 3), (◆) indicates instabilities in a blister (Ref., Fig. 1) and (○,▲) indicate cavitation instability (Ref., Fig. 4a). Reprinted with permission.

with the radius of the ball. Although slight differences in the overall behavior is observed with gels prepared on the first day or after 24 hrs, each set of data could be fitted with an equation $h \sim R^2$.

(a - b) Examples of the height fluctuations of a $38\mu L$ gel sphere of two different moduli (55 Pa and 290 Pa) following a Gaussian probability distribution. Noise strength is 0.1 m^2/s^3.

Snapshots and schematics of the experiment. (**Top**) Side views of two transparent cells filled with a polyacrylamide gel with shear modulus 1160 Pa (a) and 13 Pa (b). Two identical steel beads (5 mm diameter) have been placed on the free air-gel interface. The vertical downshifts are respectively $\delta = 0.03\delta_0$ and $\delta = 320\delta_0$. (**Bottom**) Schematic representation of the deformation fields in the respective experiments.

Experimental evidence of reversibility of the gels. (a) A 10 mm diameter steel sphere immersed in 140 Pa gel, when slightly disturbed from its elastobuoyant position via an electromagnet, undergoes under-damped oscillations about its equilibrium depth δ_{eq}. (b) Depth of an elastobuoyant bead (2.8 mm diameter) in a 13 Pa gel plotted as a function of the strength of an external vertical magnetic force. The depth at zero-Force indicates the equilibrium-elastobuoyant position of the sphere. The data (red, blue and green) shown here are from three different experiments where the closed symbols indicate the loading cycles and the open symbols indicate the unloading cycles. (c) Depth of submersion δ of a 5 mm diameter steel sphere in a soft gel ($\mu \sim 13$ Pa) varying as a function of its temperature. The experiments in the cooling cycle were performed first following which the gel was heated systematically to obtain the data for the heating cycle.

slopes 1 and 2, *i.e.* values of the local exponent α_1 equal to 1 and 2. I_{10}^{*} is the value of the first invariant beyond which the local exponent is larger than 3/2.

(a) Snapshots of the experiment of loading a needle (diameter, D and grafted with ~ 5 nm layer of polydimethylsiloxane chains) inside the gel with a thin layer of silicone oil (AR20, Sigma Aldrich) on its surface. The oil above the gel reduces friction by lubricating the contact between the needle and the gel during indentation. The red dye demarcates the interface between the gel and silicone oil. After unloading the needle from the gel, the dyed interface retracted to its original position showing that there was no fracture in the gel. (b) For these experiments of loading a sharp needle (inset) inside the gel ($\mu = 478$ Pa), the non-dimensional force $P/\mu D^2$ varies almost as the square of the non-dimensional displacement δ/D. An uncertainty analysis yields the value of the power of δ/D as 1.99 $\pm$ 0.03. (c) When the same needle was indented in the gel while undergoing vertical vibrations, a fine fracture was induced by the indentation. The needle underwent square wave oscillations (amplitude of vibration ~ 0.64mm) along its axial direction that were generated by a waveform generator (Agilent, model 33120A), connected to a mechanical oscillator (Pasco Scientific, Model No: SF-9324) via an amplifier (Sherwood, Model No: RX-4105).

The fall of a small ceramic ball (3.2mm diameter) through a soft polyacrylamide hydrogel is captured with a high speed (500 frames per second) camera. The folding of the surface of the gel around the sphere (a), the pinch-off instability (b) and the formation of a thin line (c-d) connecting the ball and the surface of the gel are evident in these videographs. The surface of the gel relaxes slowly (d) with no sign of any fracture in the gel. The white scale bar here represents 1mm. (e-f) The schematic

illustrates the wrapping of the sphere by and the folding of the surface of the gel as the sphere penetrates the gel. Here, h_0 is the initial height of a single ball immersed in the gel.

Static Stokes experiment showing the depths of submersion of Silicon Nitride Ceramic balls of diameters 2.4mm, 3.2mm, 4mm, 4.8mm and 6.35mm respectively in a 3.1% PAM hydrogel. The white scale bar represents 5mm.

(a) The experimental data from the static immersion experiments are analyzed here by plotting the depth of submersion (h) against $mg/4\pi R$. Here, m denotes the effective mass of the spheres after correcting for buoyancy inside the gel, g is the gravitational acceleration and R is the radius of the sphere. The closed symbols represent the data obtained by performing the elastic Stokes experiment in the lower modulus (8 Pa) gel whereas the open symbols represent the previously reported data[28] obtained with a higher modulus (40 Pa) gel. (b) The data for the lower modulus (8 Pa) gel are re-scaled by dividing h with the capillary or Laplace length ($L_c = \sqrt{\gamma / \Delta \rho g}$) and plotting it against $\Delta \rho g R/\mu$. Here, $\Delta \rho$ is the difference between the density of the spheres and water, μ is the shear modulus of the gel (~8 Pa) and γ (~73mN/m) is its surface tension.[28] The data for the higher modulus (40 Pa) gel follows a linear relationship when h is rescaled with the radius and plotted with respect to $\Delta \rho g R/\mu$. Capillarity does not play a significant role in the higher modulus gel and hence the data does not exactly follow the behavior that is shown by the spheres in the lower modulus gel (8 Pa).

The video micrographs (upper panel) illustrate the long range attraction between two ceramic spheres (4.8 mm diameter) submerged inside a soft PAM hydrogel. The micrographs of the lower panel capture the events following the immersion of a glued dimer of similar balls inside the gel. The dimers orient (0s to 12s) as they descend inside the gel and approach each other. Finally (30s), they form a close packed structure. The white scale bar represents 5mm.

(a) The video micrographs show the attraction of two steel spheres of diameter 4mm in a chemically cross-linked gel. This experiment was performed after depositing ink on the surface of the gel with a fine needle. When a sphere is released into the gel, line formed from the folding of the surface of the gel above the ball is clearly highlighted by the intense color of the ink. Some ink is also observed around the line, which reveals that the gel in the intervening space is squeezed out as the spheres attract each other. The black scale bar represents 5mm. The sequence of events in the videographs is shown schematically in (b-c). Here, x denotes the distance between the balls, h is the height of submersion of the balls before contact and h_∞ is the height after contact.

(a) This graph reveals the long range nature of the attraction of two solid spheres inside the hydrogel. Here, D is the diameter of the sphere, h_∞ is the depth of the two spheres after they come in full contact, h_0 is the initial depth of the first submerged sphere and h is the average depth of the two spheres (see also the schematic of figure 5.1) that varies with the distance (x) of separation. The black curve was obtained from fitting the experimental data using Origin software, which has the following expression, $\bar{h} = 0.203 + 0.096\ln(\bar{x} + 0.104)$, where $\bar{h} = (h_\infty - h)/h_\infty$ and $\bar{x} = x/\sqrt{h_0 D}$ (b) The squared distance of separation varies linearly with time with correlation coefficients better than 98% . The symbols are same as in figure (a). $\bar{x}_0$ and $\bar{x}$ are the scaled distances of separation at times t=0 and t, respectively.

The video micrographs in (a) capture the motion of a steel ball (4 mm diameter) on a thickness graded gel, the surface of which is inclined by 14° from the horizontal plane. The gradient is constant and steepest at the central portion of the cell where both the horizontal (x) and the vertical (h) displacements of the ball increase linearly with time (c). The white scale bar represents 10mm. The micrographs in (b) capture the motion of a ceramic sphere (diameter 4.8mm) on a thickness graded gel that had ink marks. As the ball rolls down the gradient, the ink is pulled from the surface, rolls over the ball

and finally returns to the surface. The black scale bar represents 5mm. The schematic of the ball rolling down the graded gel is shown in (d).

These video-micrographs capture the events leading to the formation of a semi-circular ring caused by the attraction between the copper spheres (diameter ~2.4mm) and a pre-existing ceramic sphere (4.8mm diameter) inside the gel. The copper spheres were added sequentially in the gel. The white scale bar represents 5mm.

The micrographs in the upper panel show the growth of clusters on sequential addition of copper spheres (diameter 2mm) into the gel containing a ceramic sphere (diameter 3.2mm). The growing cluster eventually engulfs the ceramic sphere. When another ceramic sphere is added, it is attracted by the cluster as well. The copper spheres on their own exhibit a structure comprising of parallel columns. When the clusters are large enough (lower panel), they even attract and move towards each other. When the clusters coalesce, further re-organization of the spheres occurs that lead to a close packed state. In the online video, the abrupt stages of the re-organization of the spheres can be seen. These are reminiscent of elastic instabilities and/or plastic events. The black scale bar represents 5mm.

(a) Deformed surface profiles of water, and two representative gels are shown. In each case, a 2.4mm diameter PDMS grafted glass sphere was used to deform the surface. The white curves show the fitted Bessel function [$\xi(L) = \xi_0 K_0 (L/L_c^*)$] to match the deformed surface profiles. For clarity the fitted curves have been shifted from the deformed surface profiles along the direction of the red arrows. (b) The plot shows

how the elastocapillary decay length decreases with the shear modulus (μ) of the gel. The red open diamonds denote the experimental data and the solid black line is fitted according to $L_c^* = L_c \exp(-B\mu)$ with a value of B as 2.6×10^{-3} m^2/N. (c) This plot shows that the elasto-capillary decay length decreases with the elasto-capillary number ($\mu \xi_0 / \gamma$) for gels of shear modules ≤ 555 Pa. The datum for a gel of even a higher modulus (845Pa) deviates from the plot.

(a) Figure illustrating fine balances of the elastic, wetting and gravitational forces giving rise to different types of stabilities of glass spheres (3.2 mm diameter) released on the surface of a polyacrylamide hydrogel of modulus 10 Pa. An untreated (hydrophilic) glass sphere (right) immediately plunges into the gel and becomes neutrally buoyant afterwards. A hydrophobic glass (left) floats on the surface of the same gel. (b) This is an extension of the experiment in A, that shows when another hydrophobic particle is released in between the two, (c) it gets strongly attracted toward the hydrophilic particle, but moves on the gel's surface to minimize its distance of separation from the latter.

(a) A plan view of the interaction of two 3.2 mm hydrophobic glass spheres on the surface of a 10 Pa gel. A wire mesh lined with the base of the glass cell shows the field of deformation of the surface of the gel around the particles. (b) Attraction of the two 4 mm diameter hydrophobic glass spheres on the surface of a 10Pa gel in air (c) Attraction of the two 2.4 mm diameter hydrophobic glass spheres on the surface of a 10Pa gel in air (d) Attraction of the two 2.4 mm diameter hydrophobic glass spheres on the surface of a 10Pa gel in contact with heptane.

(a) Schematic showing elastocapillary attraction of two spheres of identical sizes at a distance L. h denotes the depth of submersion of the ball with respect to the initial undeformed level of the gel. The change of h as the spheres approach each other is denoted by Δh (see text and figure 6.4b) h_0 is the vertical distance of the three phase

contact line from the undeformed free surface of the gel when the spheres are far apart. (b) The change in the depth of separation Δh scaled with h_0 is plotted as a function of the non-dimensional distance of separation (L/L_c^*). Data from all the experiments cluster around the mean curve $\Delta h / h_0 = 1.5 K_o (L/L_c^*)$. The open circles [diameters: 2.4mm (red), 3.2mm (black) and 4mm (green)] denote the 10 Pa gel-Air data. The open squares [diameters: 3.2mm (purple) and 4mm (pink)] denote the 19 Pa gel-Air data. The blue open diamonds (diameter 2.4mm) denote the 10 Pa gel-Heptane data.

This plot shows that the squared distance of separation between two interacting particles decreases linearly with time. The blue open circles correspond to the 2.4mm diameter spheres at the gel- heptane interface. (Inset) The pink open squares correspond to the 2.4mm diameter spheres at the gel- air interface. The shear modulus of the gel in each case is 10 Pa.

A 3.2mm diameter hydrophobic glass sphere is attracted towards a 4mm size hydrophobic glass sphere. As the two spheres contact each other, the pair re-orients inside the tube adjoining the two (tubulation). Finally, the pair penetrates inside the gel and becomes stagnant to a point where it becomes elasto-buoyant.

A plan view of elastocapillary surface force mediated self-assembly of 2.4mm silanized glass spheres at the interface of a gel (10Pa) and n-heptane. As the spheres are randomly dispersed on the surface of the gel through heptane, they form random clusters, which then move towards each other forming one large cluster. A wire mesh lined with the base of the glass cell shows the field of deformation of the gel surface.

(A) Schematic of the method used to measure the shear modulus of a gel. The method involves the creation of a random magnetic field that interacts with the steel disk and vibrates the upper glass plate randomly with respect to the lower plate thus creating a

random shear deformation of the gel. (B)The resonance peak of the shear vibration of the gel was obtained from the power spectra of its random vibration with which the shear moduli were calculated using $2\pi\omega = \sqrt{\mu A / mH}$. (C) The shear moduli (μ) of different gels plotted as a function of the percentage of polyacrylamide (x) in them follows an empirical relationship $\mu = 2500\exp(-178/ x^{2.98})$.

(a) Two cylinders placed parallel to each other on a soft gel (μ=18 Pa) move towards each other and eventually coalesce. (b) If the distance between the cylinders is large enough, we also see elastically arrested configurations as well. (c) A similar self-organized pattern to (a) arises for this initial configuration after sufficient time. The time stamps in the second and third images in the panel in c) are relative to the panel's first image.

(a) A schematic illustrating the numerical model. (b) The deformed profile of the surface of a gel for a single cylinder. The red open circles show the experimental points and the black line are obtained from simulation. Both fit an exponential function $\xi_0(x) = \xi_o(0)\exp(-x/ L_c)$, with L_c = 7.23 (simulation) and 2.25 mm (experiment). (c) The settling depth of the cylinders $\xi_0(0) - \xi_o(\ell)$ scaled with their initial depth $h(0)$ is plotted as a function of the non-dimensional distance of separation ℓ / L_c where L_c is the effective decay length of elastic deformations. The open symbols represent the data obtained from three different experiments. The black line shows the results of the numerical simulations of the equations of motion (7.4-7.6) with parameter values R = 3, K = 2000, ρ = 0.35 with τ = 14.59. (Inset: Schematic of two cylinders approaching each other on the surface of a gel with appropriate notation used in the text) (d) The dynamics of attraction of two cylinders showing an exponential collapse (see text for

details). The open symbols represent the experimental data. The red line is obtained from simulations. The black line corresponds to a linear fit of the experimental data.

The space time dynamics of coalescence of five cylinders. The variable i represents the index of the cylinder and is used to eliminate the space between cylinders in contact. These simulations solve the equations of motion given in (7.4-7.6), with the parameter values $R = 3$, $K = 500$, $\rho = 0.25$, yielding $L_c = 10.03$. The dynamics qualitatively capture the experimental scenario shown in Figure 7.1, wherein the cylinders aggregate in pairs before slowing down and coalescing together.

Plan view of the folding and wrinkling instabilities at the end of a cylinder placed on an elastic film (3.3 μm thick) supported on a pool of a water-glycerol solution. The wire mesh lined with the base of the petri dish containing the sample shows the deformations in the film surface.

(a) The ink line (as shown by the arrow) follows the deformation of the surface of a 7.2 micron thick elastic film supported on the glycerol-water solution when a steel cylinder (diameter 1/8") is placed upon it. (b) The deformed profiles analysed from images of two different elastic films (1.8 μm and 12.1 μm) and the values of α^{-1} obtained from the analysis of the data using equation 8.8 are 2.7 mm and 5.9 mm respectively. (c) A typical snapshot of the intermediate profile between two steel cylinders on a 6.2 micron thick film. (d) Intermediate profile between two steel cylinders resting on a 5.7 micron film (having an initial separation distance of 17 mm) fitted with equation 8.3 to obtain the decay length (5.6 mm).

Comparison of contact angle*s* of water (top panel, a-d) and th*ose* of gel spheres (shear modulus = 61 Pa) (bottom panel, a'-d') on silicon wafers of varying work of adhesion. Each column (e.g. a-a') corresponds to silicon wafers of same surface energy, with (a-a') being completely hydrophilic. (b-d') are hydrophobized by exposure to vapors of dodecyltrichlorosilane. Scale bars indicate 1 mm.

The panel shows four different cases of wetting on completely hydrophilic silicon wafers. Water spreads completely as a thin film in (A). (B-D) As the shear modulus of the gel sphere increases, its contact angle increases with lesser deformation. The foot size also progressively decreases with increase in shear modulus.

(a) Observed contact angles θ^* of gel spheres of different shear moduli as a function of work of adhesion W between the gel and the silanized silicon wafers. The data sets for (μ= 61 Pa, 320 Pa and 789 Pa) indicate contact angles for gel spheres with similar radii (R~ 0.0019 mm) on surfaces with varying W. The data sets for (μ= 71 Pa, 93 Pa, 211 Pa and 520 Pa) indicate contact angles for constant W and varying as a function of the sphere radius R. The latter group is plotted separately in (b) to indicate the trend of the contact angle θ^* as a function of sphere radius R.

Plot of experimental data by using the model expressed in equation 9.7. The excess elastic tension $\left(1/1+\cos\theta^* - 1/1+\cos\theta\right)\sin\theta^*$ is plotted as a function of a dimensionless elasto-adhesive number, $\sqrt{\mu R/W}$. Here, θ^* indicates contact angle of gel and θ indicates contact angle of pure liquid formed on the same surface. In the X-axis, μ represents shear modulus of the gel, R is the radius of the gel sphere and W is the work of adhesion of the liquid/substrate.

Plot of experimental data for lip lengths (ℓ) as a function of the scaling obtained from the balance of surface and elastic shear energies in equation (9.9). **Inset**. An experimental snapshot to show how the lengths of lips were measured. The dotted circle is of diameter of the undeformed gel sphere (estimated from its weight). The horizontal line represents the reflection plane, *i.e,* at the substrate. The distance between a triple contact point of the gel sphere and the point of intersection of the dotted circle with the white horizontal line was noted as the lip.

Comparison of water (top panel, a-c) and the shape of the gel spheres (shear modulus 789 Pa) (bottom panel, a'-c') on silicon wafers with varying work of adhesion while completely immersed in a surrounding medium of heptane. Each column (e.g. a-a') corresponds to silicon wafers of same surface energy, with (a-a') being completely hydrophilic. (b-c') are hydrophobized by exposure to vapors of dodecyltrichlorosilane. A 'foot' has formed in the gel sphere in (a'). Scale bars represent 1 mm.

Figure illustrating fine balances of the elastic, wetting and gravitational forces giving rise to two different scenarios for same sized glass spheres (3.2 mm diameter) but with different surface energy in a polyacrylamide hydrogel of shear modulus 10 Pa. An untreated (hydrophilic) glass sphere (right) immediately plunges into the gel and becomes neutrally buoyant afterwards. A hydrophobic glass (left) floats on the surface of the same gel.

In Appendices

Appendix I: Rayleigh Taylor Instability in Soft Elastic Solids

Downward-facing initially at surfaces of two gel slabs fixed in a square container of lateral size 40 cm and height 2.5 cm. The free surfaces are pictured from below. (a) Specimen with a shear modulus equal to 45 Pa: the inverted surface remains at. (b) Specimen with a shear modulus equal to 37 Pa: a quasi-hexagonal pattern spontaneously appears as soon as the sample is turned upside down.

Mean amplitude (downward displacement) of the deformed gel surface as a function of the control parameter $\rho g h / \mu$.

A compliant layer of thickness $h = 1$ and shear modulus $\mu = 1$ is rigidly attached at its upper surface to an undeformable horizontal at substrate. The lower surface is free to deform. The system undergoes the downward volume force $\alpha = \rho g$ with ρ the density of the elastic material and g the gravity acceleration.

$z_{\text{interface}}(X, Y, 0)$ computed from Eq. I.34 with $\eta \beta = 1$, $k_c = 2\pi$, $\psi = 0$ (left) and $\psi = \pi$ (right). For $\psi = 0$, $z_{\text{interface}}(X, Y, 0)$ is maximum at the center of the hexagons, hence hollows at the center of the hexagons. For $\psi = \pi$, $z_{\text{interface}}(X, Y, 0)$ is minimum at the center of the hexagons, hence bumps at the center of the hexagons.

Amplitude β of the modes constituting the four branches arising from the LSK expansion at order 3, plotted as a function of the distance from the critical value of the control parameter. The unique stable branch is for $\beta = 0$ and $\alpha < \alpha_c$ (green solid line).

The other branches are unstable (red dashed lines). Left: for an elastic layer with $\gamma > 0$. Right: for an elastic layer with $\gamma < 0$.

Bifurcation diagram showing the amplitude of the modes as a function of the control parameter α, for $\gamma = 1.19$ (from Eq. I.30) and $(\kappa + \lambda) = 0.79$ in Eq. I.42. The stability of the branches are indicated in the plot.

(a) Formation of interfacial waves at the interface of a PDMS-grafted rigid hemisphere and a thin film of silicone elastomer supported on the surface of an incompressible liquid (1:1 mixture of water and glycerin by volume) due to sliding. When the hemispherical indenter (PDMS) is slid past the elastomeric film of thickness (7.5 µm), a single wrinkle develops, which propagates through the interface when the bending energy stored in it overcomes the adhesive energy. The sequences of the motion of the wrinkle are shown in (b). (c) A typical graph of the tangential force (F_T) experienced by the indenter as a function of time (Film thickness: 16µm and Stage velocity V_{stage}: 0.2 mm/s) that shows the signature of the periodic pulses of the Schallamach waves.

Graphs of the tangential force (F_T) experienced by the PDMS-grafted hemispherical glass slider (12.5 mm diameter) during each pulse of the interfacial instability as a function of the film thickness (left: 8 mm and right: 22 mm) on a pool of 1:1 aqueous glycerol. The stage velocity is 0.2 mm/s in each case. If a pulse gets pinned somehow, multiple waves may form as seen in the left case and then release altogether from the contact region.

Graphs of the tangential force (F_T) experienced by PDMS-grafted hemispherical glass sliders of different diameters (7.5 mm and 12.5 mm) during each pulse of the interfacial instability over an elastic film (thickness: 16μm) over a pool of 1:1 aqueous glycerol at stage velocity, V_{stage}=0.2 mm/s.

The maximum tangential force experienced by a PDMS-grafted hemispherical slider (diameter: 12.5 mm) as the stage velocity (V_{stage}) is varied. These experiments were performed with a 16 μm thick PDMS film over a pool of 1:1 aqueous glycerol (by volume).

Attraction or Repulsion of two gel spheres (shear modulus ~ 40 Pa) when placed on a thin gel film (40 Pa, 1 mm thick) (a) When two such gel spheres were placed close enough, they attracted and coalesced forming a curved ridge in between the two spheres. The coalesced gel spheres (a, final snapshot) maintain their original shape partially as opposed to that of liquid drops where they meet to form a single drop finally. (b) When the gel spheres were placed a little further away from each other, they were found to repel, thus moving apart.

Schematic of the experimental method to prepare perfectly spherical gel spheres in a density gradient, where the upper lighter liquid was octane (density 0.7 g/cc) and the lower heavier liquid was silicone oil (PDM-7040, density 1.07 g/cc). The gel drops were introduced in the density gradient as soon as the catalyst and initiator were mixed in the precursor solution and the drops were cured to form elastic gel spheres in the density gradient for 2h at room temperature before any experiments were performed.

Schematic of thermally induced durotaxis of rigid spheres on a soft hydrogel. The two opposite walls of a home-built glass container are attached with copper plate circulators (with temperature resistant double sided tapes). One of the circulator is connected with a hot temperature bath (T_{HOT} ~ 368 K) and the other one with a cold temperature bath (T_{COLD} ~ 268 K). The temperature gradient established in the gel (after 1h) leads to the gradient of elasticity (modulus decreasing in the direction of the arrow). The sphere moves towards the right as will be seen in experimental snapshots later. We used PDMS oil as the upper phase to prevent evaporation of the gel as well as maintain a thin lubricating layer between the PDMS grafted steel spheres and the gel.

A typical temperature profile generated in the gel across its length inside the glass container for four different experiments. The temperatures on the two extreme ends here denote those measured at the walls from the inner side of glass container with the gel. The temperatures of the two copper plate circulators (attached to the glass with temperature resistant tapes), read (left: T_{HOT} ~ 368 K) and (right: T_{COLD} ~ 268 K) respectively as measured from the outer exposed side.

Experimental snapshots of motion of steel spheres (PDMS grafted) along a temperature-induced elasticity gradient in the gel (shear modulus 294 Pa) with an upper layer of PDMS oil (DMS T-22, kinematic viscosity: 259.9 cSt). The temperature of the gel at the left wall was about 348 K and that at the right wall was about 278 K. (a) Motion of a 7mm diameter steel sphere on a horizontal surface along the gradient. (b) Motion of a 10mm diameter steel sphere on a horizontal surface along the gradient. (c) Motion of a 9mm diameter steel sphere uphill (0.6°). We observe formation of some bubbles in the gel after it has been heated that is not present when the gel is at room temperature or has been cooled.

(a) Experimental data showing the slopes of ($XT^2/\sqrt{t}$) for steel spheres of different radii and moving on a gel (shear modulus 294 Pa) through different PDMS oils DMS T-22 (η = 0.259 Pa s), DMS T-31 (η = 1.172 Pa s) and DMS V-35 (η = 4.744 Pa s). The dotted line shows a slope of $R^{7/2}$, which shows the experimental data does not follow the scaling for R as predicted by equation IV.4. (b) Rescaled slopes of ($XT^2/\sqrt{t}$) by multiplying with $\sqrt{\eta}$ (equation IV.4) show somewhat collapse of the experimental data.

Appendix V: Elastobuoyant Liquid Inclusion inside a Soft Gel

An elastobuoyant liquid inclusion inside a soft gel (μ = 14 Pa, density: 1000 kg/m^3). We used chloroform (density: 1450 kg/m^3) as the heavy liquid for this experiment. As soon as the chloroform was poured on the gel surface, due to its weight, a cavity was formed inside the gel substrate that was filled by the liquid. The stretched gel surfaces folded over the liquid forming a pendant shaped liquid inclusion. The entire experiment took about a few seconds and the picture was captured immediately. Even after several days, we didn't see any noticeable evaporation from the stored chloroform inside the gel pointing to the fact that the gel surfaces adhesively seal quite well above the liquid.

An elastobuoyant liquid filled cavity inside a soft gel (μ = 14 Pa, density: 1000 kg/m^3). We used silicone oil (density: 1050 kg/m^3) as the liquid phase for this experiment. As soon as the oil was poured on the gel surface, due to its weight, a cavity was formed inside the substrate storing the liquid inside it. However, we do not see the closure of the gel above. A layer of the oil is still maintained over the gel surface as shown in the figure.

Rayleigh Taylor instability in soft gels due to a heavier liquid phase at the top of the elastic gel (density: 1000 kg/m^3). (A) The liquid used here is a silicone oil (density: 1050 kg/m^3) and the shear modulus of the gel is 24 Pa. The gel interface was marked with a water-soluble red dye to help in visualizing the deformation of its surface. The snapshot on the right gives a side view of the same experiment. (B) The liquid used here is diiodomethane (density: 3320 kg/m^3) and the shear modulus of the gel is 52 Pa. Diiodomethane has been filled completely in the four lobes formed due to the gravity induced instability.

The center-to-center separation distance (ℓ) between two PDMS grafted glass beads (3.2 mm diameter) decreasing as a function of time as they attract on the surface of gel (shear modulus ~ 14.3 Pa) through a liquid medium and come into final contact. Each data set represents experiments with a different oil as the upper liquid medium on the gel as indicated in the legend.

∗∗∗

Abstract

Soft elastic solids play an important role in a wide range of applications such as in tissue scaffolds to grow artificial organs, in wearable contact lenses, as adhesives, in soft robotics and even as prototypical models to understand the mechanics of growth and morphology of organs. For a soft elastic material like hydrogel with its shear modulus in the range of tens of pascals, its surface tension also contributes to the mechanics of its deformation in addition to its elasticity. As opposed to a hard solid that is very difficult to deform, for the case of these soft solids, even a weak force like gravity can bring about significant deformation. Many of these aspects of the deformation and behavior of these *ultrasoft* materials are still not very well understood. Thus, the objectives of this dissertation were to understand the role of elastocapillarity (*i.e,* joint roles of solid surface tension and elasticity) and elastobuoyancy (*i.e,* joint roles of gravity and elasticity) that manifest in such solids.

In this dissertation, we studied the role elastocapillarity in adhesion-induced instability in thin elastic films bonded to rigid substrates and also in surface oscillation modes of soft gel spheres set to vibration; the elastobuoyancy effect; elasticity mediated interaction of particles in soft solids as well as on thin films supported over a pool of liquid. We also presented some new results on how soft spherical gels undergo restricted spreading on rigid substrates with varying surface energies.

In the first section, we studied how a thin confined layer of a soft elastic film loses adhesion from a rigid substrate by forming interfacial instabilities when a tensile stress is applied to it. We performed experiments to quantify the characteristic lengthscale of the patterns formed and found that they were significantly larger than the

1

wavelengths of purely elastic instabilities. A linear stability analysis of the elastic field equations by taking into account the role of surface tension showed that the amplification of the wavelength is due to the role of elastocapillarity where the surface tension, elasticity, and film thickness contribute jointly in a non-trivial way. In addition, we found experimentally as well as theoretically that the stress required to adhesively fracture these films is much larger than Griffith's fracture stress for stiffer elastic films, which is also due to the effect of elastocapillarity. We also studied the surface fluctuation of sessile hydrogel spheres subjected to mechanically-induced Gaussian white noise to understand the role of elastocapillarity in their oscillation modes. An important finding of this study is that they give a direct evidence that the surface tension of these elastic hydrogels is almost like that of water, which is the integral solvent in the swollen network of the polymeric gel.

In the subsequent section, we introduced the new phenomenon of *Elastobuoyancy*. When a rigid sphere is placed on the surface of an ultrasoft hydrogel, it plunges into the soft substrate to an equilibrium depth where the elastic strain energy of the surrounding medium balances its weight. We refer to this state of the sphere as *'Elastobuoyant'*. By performing systematic experiments where we varied the sphere size and the elasticity of the substrate, we obtained scaling laws of the depth as a function of the radii, elastic modulus and the spheres buoyant weight, which were also supported by asymptotic analyses of the same.

Following the section on elastobuoyancy, we reported a new set of principles to design self-assembly of particles by using the combined roles of surface tension, elasticity, and gravity in soft substrates. We used three different systems to study this elastic interaction macroscopically: (i) elastobuoyant assembly of particles suspended inside a soft elastic gel, (ii) elastocapillary assembly of particles floating on the surface

2

of soft gels analogous to capillary attraction of objects on the surface of liquids, and (iii) assembly of particles on the surface of thin elastic membranes supported over a viscous liquid.

In the second last chapter in this thesis, we presented some results on how soft elastic gel spheres spread on rigid substrates with different surface energies. Our observations indicate that their contact angles are slightly greater than those of equivalent liquid drops on similar substrates. The contact angles of these gel spheres increase as a function of elasticity and decrease when surface energy increases. We derived an expression for the excess elastic tension in the gel spheres at the crack tip by using an approach that is similar to estimating the viscous dissipation at the contact line during spreading of liquids. By using a general constitutive law where the elastic energy is not limited to the square of the strains, the singularity at the crack tip is artificially removed thereby forcing the gel to assume a liquid-like behavior. Our experimental results agreed reasonably well with the model.

In the last chapter, we summarized the doctoral research and presented suggestions for future investigations. There are several appendices in this thesis that have interesting observations from partially completed projects that need additional research and analysis in the future.

Chapter 1

Introduction

1.1 Motivation for the Current Research

Pierre-Gilles de Gennes (Nobel Laureate in Physics, 1991), the founding father of *Soft Matter*, said towards the end of his 1994 Dirac Memorial Lecture titled *'Soft Interfaces'*[1] –

"Long lectures like these tend to be over-optimistic, giving the impression that most physical questions are under control. The reality is different: soft interfaces are far from a happy end..."

Soft Matter is a broad class of Condensed Matter Physics that includes the studies of materials such as liquids, polymers, biological membranes, liquid crystals, gels, colloids, foams and granular materials. Our inspiration for the research presented in this thesis is oriented towards exploring one subset of this field, *i.e,* of soft elastic materials. Such soft solids are widely used in various applications such as in tissue implants during surgeries, in protective armor for warfare, as adhesives, in drug delivery, as scaffolds to grow artificial organs, and now as stretchable electronics too. These materials deform easily due to their low elastic modulus and their mechanics are governed by laws that are different from those applicable to their stiffer counterparts. Due to their lower elasticity, their surface stresses become important under certain geometric length scales and the coordination between the surface (*-capillary*) and the

elastic properties, *i.e.*, *elastocapillarity*, unfolds new physical phenomena in these solids.

In this dissertation, we studied elastocapillary phenomena in adhesion-induced instability in thin elastic films bonded to rigid substrates and surface oscillation modes of soft gel spheres set to vibration; the elastobuoyancy effect; elasticity mediated interaction of particles in soft solids as well as on thin films supported over a pool of liquid as well as how soft gels wet rigid substrates. Before going into each of these studies in detail, we discuss below the motivation behind studying the various physical aspects of these soft solids.

Based on our studies of how particles deform and move on soft solids may inspire one to design a new class of *soft fluidic devices*, in a spirit similar to *microfluidic devices* that are widely used nowadays. The advantage of having a device made with a softer gel like material would be to use its deformation properties to induce strain energy gradient to allow transport of particles. For the use of these solids in *soft robotics* and automation, it is important to know how the material behavior changes due to additional effects such as its surface tension or whether these undergo viscoelastic dissipation due to repetitive cycles of deformation and relaxation. Typically, our studies may inspire *Engineers* to design softer channels made of stretchable elastic gels for pipe flows where instead of introducing an external valve for flow restrictions, they could insert magnetic particles in an annular ring zone that could be closed or opened by applying only a magnetic field. Our results on the elastocapillary effect on enhancement of the critical stress required to fracture an interface between a soft film and a rigid substrate could help in the design of a more robust bonded interface just by using a softer adhesive. Additionally, as will be discussed later in the summary, we also propose designing a new kind of particle focusing mechanism, the *elasto-thermal trap*,

whereby using the temperature induced softening or rigidifying a polymeric elastic substrate, one can move around or focus a particle in a controlled fashion. Before moving into greater detail of the potential applications, we will begin by introducing briefly some background about the research in this dissertation. Owing to the great variety of topics that have been covered here, we will briefly discuss the common themes that underline the general direction and numerous results that culminated from this thesis, in the form of a review.

1.2 *Capillarity* and *Elasticity*: Role of Elastocapillarity

Capillarity refers to the role of surface tension, γ, in the case of liquids that is equal to its surface free energy. For solids, however, one has to be careful since these two quantities may not be the same due to an additional contribution generated by the surface strain. Shuttleworth[2] pointed out that the surface stress of solids is given by: $\Gamma \sim \gamma + d\gamma/d\varepsilon$, where γ is the surface free energy and $d\gamma/d\varepsilon$ is the stress generated by the strain applied, ε. Nevertheless, for amorphous materials like hydrogels or elastomers like polydimethylsiloxane (PDMS), it has been found that the surface stress of the solid is more or less equal to its surface free energy[3], and is often interchangeably referred to as the solid surface tension. The *elasticity* of solid materials is characterized by their shear modulus, μ. One can then define a material length scale by combining the capillarity and elasticity as γ/μ that is referred to as the elastocapillary length. If this length-scale is larger than the typical geometric length scale (ℓ) of the solid material in concern, $\gamma/\mu\ell \gg 1$, the surface tension effects become prominent. However, if it is much lower, such that $\gamma/\mu\ell \ll 1$, the surface tension does not play a

significant role. For example, if we consider a metal like steel, its shear modulus, $\mu \sim$ 80 GPa, and its surface tension, $\gamma \sim 1$ N/m, thus the elastocapillary length $\sim 1\times10^{-11}$ m, which is in the sub-atomic range. On the other hand, for a hydrogel such as crosslinked polyacrylamide gel with $\mu \sim 50$ Pa and $\gamma \sim 72$ mN/m, the elastocapillary length ~ 1.4 mm. We chose to work with these soft gels, such that by designing an experiment in which the geometric scale is much lower than the elastocapillary length, we could test the cooperative roles of capillarity and elasticity in action and use it to study various phenomena that will be introduced shortly.

The idea of elastocapillarity[4,5] is not absolutely new. On one hand, this effect may appear due to the capillarity of a liquid in contact with a soft solid, capable of deforming it. On the other hand, the solid itself may be soft enough such that its surface tension effects are strongly coupled to its elastic deformation. The former idea was first proposed by Lester[6] and Rusanov[7] in the context of a liquid drop wetting a solid surface. In the classical Young's equation[8], the contact angle θ, of a liquid drop on the substrate is determined from the balance of the horizontal components of surface tensions about the triple contact line, *i.e*, $\gamma_l \cos\theta = \gamma_s - \gamma_{sl}$, where, γ_l is the surface tension of the liquid, γ_s is the surface tension of the solid and γ_{sl} is the interfacial tension between the liquid and the solid substrate. However, for a soft solid, they[6,7] pointed out that the normal tension component at the triple contact line, $\gamma_l \sin\theta$, which is usually ignored, may pull upon the underlying substrate thus deforming it[9] (Figure 1.1 a). Elastocapillarity also manifests directly in the form of the radius (*a*) of the contact
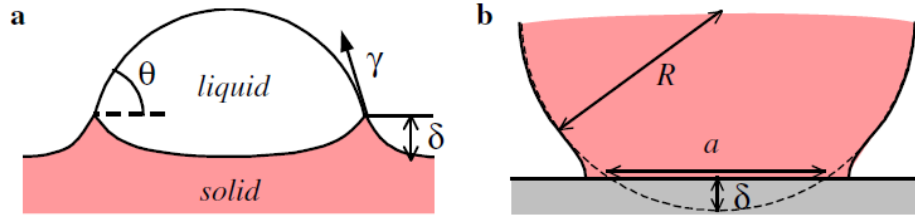
Figure 1.1: (a) Liquid droplet deposited on a soft substrate: the solid is deformed in the vicinity of the contact line (adapted from ref.[10]). (b) Elastic sphere in contact with a solid surface, without any normal load: in the presence of surface forces (adhesion), the contact is not punctual but presents a disc shape of diameter a (adapted from ref.[11]). Reprinted (along with caption) with permission from ref.[4]

deformation of rubber spheres with an effective radius R as $a^3/R^2 \sim \gamma/\mu$ [11] (Figure 1.1 b). This subject of deformation at the triple contact line has been of considerable interest to many who experimentally demonstrated that the surface at the triple line is uplifted[12,13] and Style *et. al*[14] showed that with a gradient of the substrate thickness, liquid droplets can be manipulated by durotaxis on this substrate (Figure 1.2 c). From common experience, we know that wet hair stick together as opposed to dry hair. Cohen and Mahadevan[15] pointed out the joint role of interfacial effects and elasticity where the capillary action of the liquid films in between the thin strands bring them together[16–19] (Figure 1.2 b). Due to this, one has to be careful while making micro-contact printing stamps[20] to avoid the coalescence of the fine elastic pillars[21]. In fact, a liquid drop in contact with two soft walls close enough to each other may lead to the spontaneous touchdown of the walls[22] that may pose a concern while designing microfluidic devices[23]. Thin elastomeric channels in these devices undergo bulging due to the stresses developed by the liquid on its walls[24]. The elastocapillary phenomenon is also well utilized to fold thin elastic sheets into various shapes in the form of capillary origami[25] (Figure 1.2 a) as well as in gravito-elastocapillary pipettes[26]. Mora *et. al*[27] showed that thin slender gel rods undergo Rayleigh-Plateau instability when surface

tension and elasticity effects compete to undulate the free surface under volume conservation, whereas they remain undeformed when they are too stiff (Figure 1.2 d). Surface tension effects also cause sharp features to blunt down[28,29].
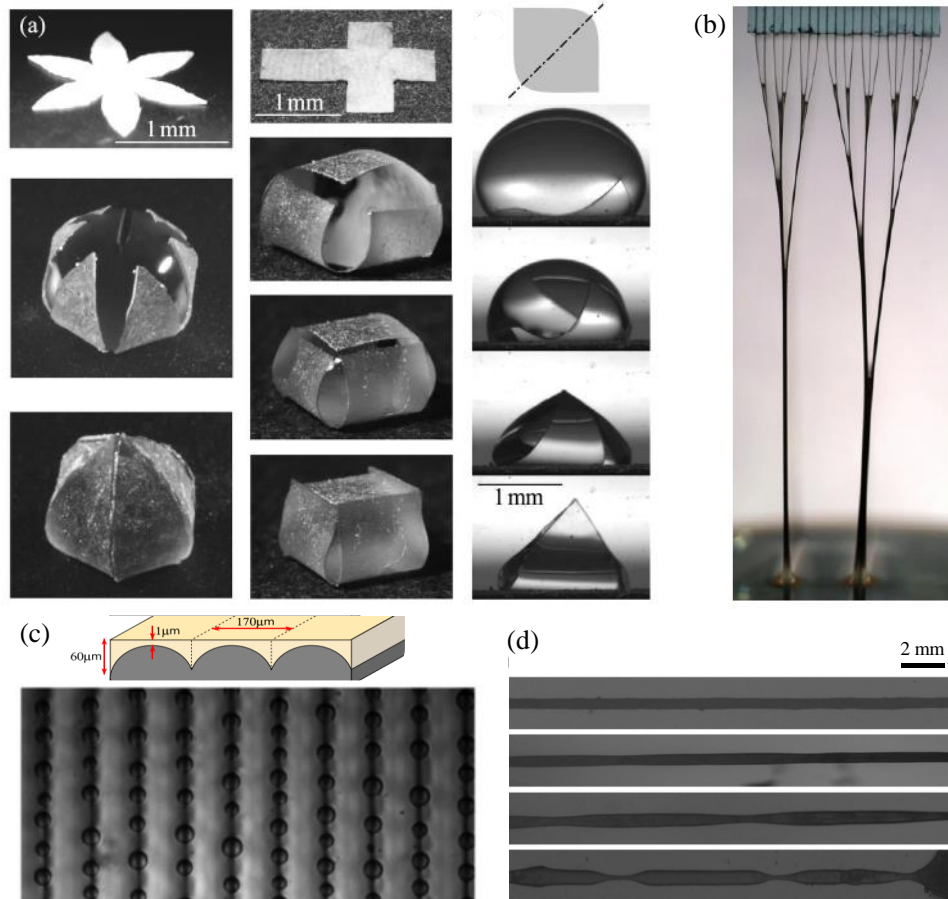
Figure 1.2: Examples of *Elastocapillary* phenomena. (a) Capillary origami induced by thin elastic sheets self-folding into organized shapes around a liquid drop that is gradually evaporating. Reprinted with permission[25]. (b) Coalescence of wet hair due to negative pressure inside the capillary films in between the strands. Reprinted with permission[16]. (c) Durotaxis of liquid drops on a surface that has a periodic gradient in thickness. Liquid drops collect at the region where substrate thickness is maximum. Reprinted with permission[14]. (d) Rayleigh-Plateau instability in slender rods of agar gel. Reprinted with permission[27].

While all the above studies demonstrate the role of *elastocapillarity* in various scenarios, we have found that it plays an important role in selecting the modes of patterns formed at the adhesive interface of a thin soft elastic film while debonding

from a rigid substrate[30,31]. It also manifests in the modes of vibration of a soft hydrogel sphere[32]. These are introduced in more details in the following parts.

1.2.1 *Elastocapillarity* in Adhesion induced Instability and Interfacial Fracture

Understanding how a thin confined elastic film fractures at its adhesive interface is central to its use in many practical applications. Usually, when a rigid substrate adhered to a thin rubber film is subjected to a tensile stress, the interface forms undulating instabilities partially detaching from the substrate. From the pioneering work[33–35] by our group *ca* 2000 in this field along with the studies performed by another group at University of Ulm[36], followed by many others, we have learnt that the entire surface or the line of contact of such an adhesively stressed elastic film roughens with a characteristic length scale, λ, that is simply proportional to the thickness of the film, H (Figure 1.3). Based on a scaling analysis that takes into account the various energies contributing to the interfacial roughening of the film by considering a sinusoidal mode of surface deflection (Figure 1.4), we find that the wavelength of instability would be of the following form[37], $\lambda \sim H\left(1+\gamma/\mu H\right)^{1/4}$. Inspecting this relation closely, one identifies the dimensionless parameter ($\gamma/\mu H$) that is a ratio of the elastocapillary length and the film thickness.
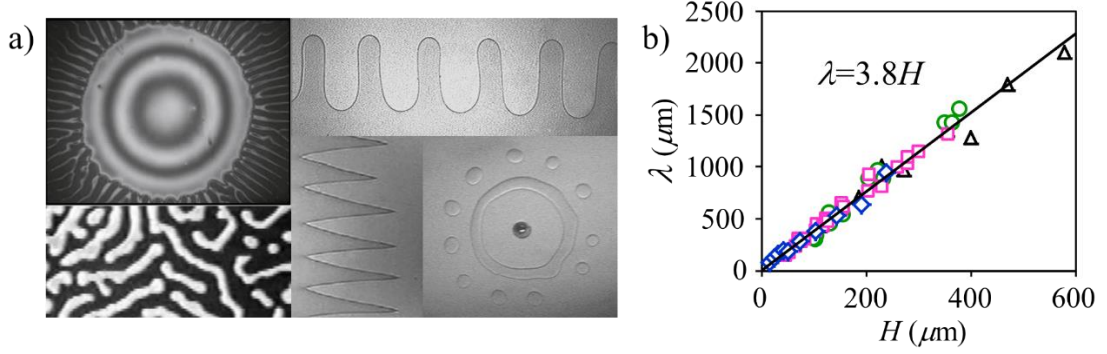
Figure 1.3: (a) Various kinds of instability patterns observed in thin and stiff elastic films in different geometries (b) Wavelength of instability from a large variety of experiments (shown in the left panel) involving films of different shear modulus, $\mu = 0.25 - 2.0$ MPa and contactors of different rigidity all fall on a single master line. The symbol (□) indicates peeling instability (Ref.[33], Fig. 3), (◆) indicates instabilities in a blister (Ref.[38], Fig. 1) and (○,△) indicate cavitation instability (Ref.[37], Fig. 4a). Reprinted with permission[35].

The previous studies were mainly concerned with the regime where elastic forces dominate ($\gamma/\mu H \ll 1$). For the case when surface tension forces are comparable or greater than elastic forces ($\gamma/\mu H \geq 1$), we would expect that $\lambda \sim H \, (\gamma/\mu H)^{1/4}$. Therefore, we performed experiments[30] to study the role of elastocapillarity in adhesion instability employing thin hydrogel films ($\mu \sim 40$ Pa and $\gamma \sim 72$ mN/m) sandwiched between two glass plates, and found that the wavelength of instability had a much stronger dependence on the thickness ($\lambda \sim 7H$), which contrasts the behavior in the case of purely elastic films ($\lambda \sim 3.8H$). A detailed theoretical analysis obtains the same scaling with a slight difference in the prefactors, which is discussed comprehensively in Chapter 2 in this thesis. Therefore, we establish the role of elastocapillarity in pattern formation during interfacial instability in thin confined films adhesively bonded to rigid substrates.
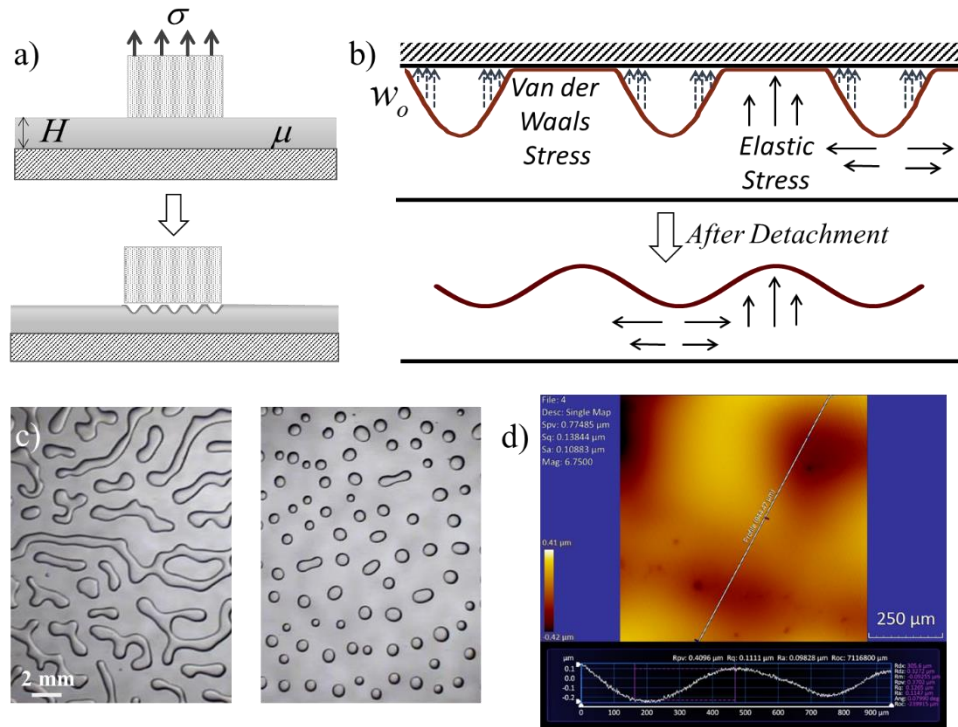
Figure 1.4: (a) A schematic of surface undulation when a rigid block is being pulled normal to the interface (b). When a glass plate is peeled from a thin ultra-low modulus hydrogel film, worm-like instability develops (c, left). However, when the plate is completely peeled from the gel and re-positioned on the same hydrogel film, bubble like instability is formed (c). (d) A profilometric image of the gel's surface soon after the plate was removed showing sinusoidal undulation. Reprinted with permission[35].

Another important aspect to consider in these studies of debonding thin elastic films is the critical stress (σ_c) at which the fracture takes place. In general, the thickness provides the relevant length scale underlying the well-known Griffith-Kendall criterion[39] of debonding of a rigid stud from a confined film. However, during the course of our study, we found that this stress is modified non-trivially by elastocapillarity for soft or very thin films. By performing experiments[30,35] of adhesive fracture of these films and measuring the critical stress, we confirmed the scaling derived from theoretical analyses of the same. This is also discussed in more detail towards the later part in Chapter 2.

12

1.2.2 *Elastocapillarity* in Oscillation modes of Spherical Hydrogels

Our next objective was to study what role elastocapillarity plays in the vibration modes of soft spherical hydrogels. For the case of liquid drops, there is a long history of studying the vibration modes of their surfaces. Rayleigh[40] predicted that the spherical harmonics of the capillary oscillations of an incompressible liquid drop with mass m, in the scaling form follows, $\omega_l \sim \sqrt{\gamma/m}$ or, $\omega \sim V^{-1/2}$, where V is its volume. For the case of solid spheres, previous experiments and intuitive scaling suggest that the frequency of vibration follows, $\omega \sim \sqrt{ER/m}$ or, $\omega \sim V^{-1/3}$. For soft hydrogels, we expect that elastocapillarity may play a role where the contributions of capillarity and elasticity may be coupled in a non-trivial way.

In order to test the role of elastocapillarity, our first goal was to see if the spheroidal modes of vibration could be detected for soft gel drops of different elastic moduli and how the resonance frequency varies with the volume of the sphere[32]. Secondly, we wanted to find out if the observed frequency could be expressed in terms of the surface tension and the shear modulus of the gel in a simple semi-empirical form. In order to achieve this objective, we developed a new method to produce soft gels (μ ~ 55 Pa to 290 Pa) of different radii, which are as spherical as possible. We then placed these gels on a hydrophobic substrate on which the gels subtend well-defined contact angles > 90°. The gels were vibrated vertically using a mechanically induced Gaussian random noise, the power spectra of which helped us identify the resonance frequencies (Figure 1.5). In chapter 3, we first describe the experimental method of preparing such spherical gels and the method used to identify their spheroidal modes. The principal resonant frequencies of the spheroidal modes of the gel drops were closest to the lowest
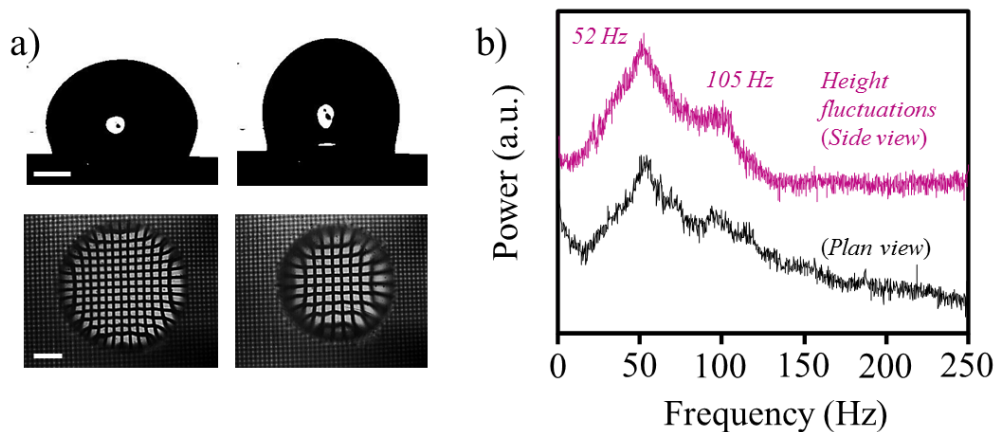
Figure 1.5: (a) Snapshots of a spherical hydrogel drop in contact with a hydrophobic substrate that is undergoing random vertical vibrations. The primary mode of oscillations where the gel stretches vertically and contracts is shown here taken with a high-speed camera (top: side view, bottom: plan view). Scale bars denote 1mm. (b) A comparison of the power spectrum obtained by analyzing the height fluctuations from the side view and the plan view. [32]

Rayleigh mode of vibration of a drop of pure water. Further, we observed that the resonance frequency varies inversely as the volume with an exponent close to 0.5 suggesting that they primarily correspond to the capillary (or a pseudo-capillary) mode of drop vibration. Followed by the experimental section, we present an analysis of how these modes can be collapsed about a single line with an appropriate scaling. As an offshoot from this study, we also discovered that the contact angles of the gel spheres with the solid substrate increase with the modulus of the gel. We believe that this method has the potential to measure directly the surface tension of soft elastic gels. The results from the studies on *elastocapillarity* in vibration modes of spherical hydrogels studies are presented in Chapter 3.

1.3 *Elasticity* and *Gravity*: Elastobuoyancy in Soft Elastic Solids

In a way similar to how capillarity and elasticity play their cooperative roles in the phenomena described above, the effect of gravity can also couple with elasticity in

these soft gels leading to interesting scenarios. As discovered by Mora *et. al*[41], when a thick layer of a soft solid attached to a rigid horizontal substrate such that its lower face is free, is subjected to its own weight, it undergoes nonlinear surface buckling forming exotic patterns. We studied a different scenario that is described as follows. When a rigid sphere is placed on the surface of an ultrasoft gel, it engulfs inside the compliant substrate and the stretched surfaces close above it[30,42]. The equilibrium depth of the sphere, δ, inside the gel, is determined by the balance of its weight and the elastic strain energy in the surrounding medium. We refer this state of the sphere as *'Elastobuoyant'*. We experimentally measured the elastobuoyant depths of steel spheres systematically by varying their sizes and in gels of different elastic moduli. By measuring the depth of submersion, δ, from the top surface of the gel to the bottom of the steel sphere -- we found that it scales with the size of the sphere (radius, R) in the large deformation limit as $\delta \sim R^{3/2}$. The depths scale as $\delta \sim R^2$ in the limit where the spheres only slightly deform the surface of the gels (Figure 1.6).
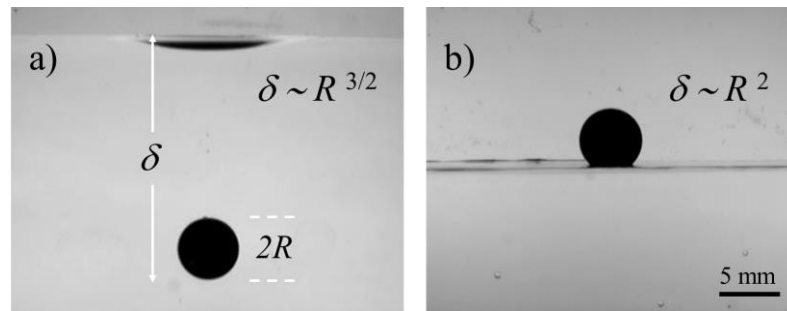
Figure 1.6: *Elastobuoyancy Phenomenon*[42] (a) A rigid steel sphere (radius, $R \sim 2.5$ mm) engulfs into a soft polyacrylamide gel (shear modulus, $\mu \sim 13$ Pa) and its equilibrium 'elastobuoyant' depth inside the gel is denoted by δ. The depth scales with the radius as $\delta \sim R^{3/2}$ in this regime. (b) The same sphere deforms a stiffer gel ($\mu \sim 1160$ Pa) only slightly. In this regime, the depth scales with the radius as $\delta \sim R^2$.

Elastobuoyancy being a fundamentally new observation, in addition to the observed experimental scaling, we developed an asymptotic analytical model to explain the same in the limit of gels undergoing large deformations.

Large deformations in soft elastic materials are ubiquitous—e.g. in polymeric gels, adhesives or biological tissues—yet systematic studies and methods to understand the mechanics of such huge strains are distinctly lacking. Small deformations of most elastic materials follow the well-known Hooke's law, in which the stress-strain relationship is linear. However, for the case of soft gels, the strain is no more linear with the applied stress. Although various semi-empirical constitutive laws exist to account for such large deformation behavior, a generalized approach to explain their behavior is lacking. Here, we investigate this complex problem using the elastobuoyancy experiment. We expect that our findings will be useful in cases where large deformations of a material are involved, such as in delicate surgeries in soft tissues. The details of this study are described in Chapter 4.

1.4 *Self-Assembly* **induced by cooperative roles of** *Elasticity, Capillarity, and Gravity*

'Self-Assembly' is a general term that is attributed to a wide range of phenomena starting from the organization of monolayers made up of various organic molecules to that of cells conglomerating to perform a specified function. In a spirit similar to Whitesides and Grzybowski[43], "Here, we limit the term to processes that involve pre-existing components (separate or distinct parts of a disordered structure) that are reversible." Different from the conventional approaches, we designed a completely new way to self-organize such individual components in elastic mediums by using

elastocapillary and *elastobuoyancy* field forces. We studied this effect in three different systems: (i) elastocapillary assembly of particles on the surface of soft gels analogous to capillary attraction of objects floating on the surface of liquids, (ii) elastobuoyant assembly of particles inside a soft elastic gel, and (iii) assembly of particles on the surface of thin elastic membranes, rigidly bound at the walls of a container, and supported over a viscous liquid. In the following subsections, we introduce each of these three self-assembly principles and the main results of these studies.

1.4.1 *Elastobuoyant* Assembly of Particles *inside* a Soft Elastic Medium

From Section 1.2, we learned that when a rigid heavy particle is placed on the surface of a soft elastic medium, it submerges itself to a depth, δ where its weight is balanced by the elastic strain energy of the surrounding gel. By virtue of a large elastocapillary length, the surface of the gel wraps around the particle and closes to create a line singularity joining the particle and the free surface of the gel[44]. A substantial amount of tensile strain is thus developed in the gel network parallel to the free surface that penetrates to a significant depth inside the gel. The field of this tensile strain is rather long range owing to a large gravito-elastic correlation length. Now, when a second particle is released into the same gel, within a separation distance of about δ or less, the strain energy field induced due to the inclusion of the objects, is strong enough to pull two submerged particles into contact (Figure 1.7). The particles move towards each other following an inverse distance law. When more monomers or dimers of the particles are released inside the gel, they orient rather freely inside the capsules they are in, and attract each other to form close-packed clusters. Eventually, these clusters themselves interact and coalesce. This is a new kind of self-assembly in which

the gravity, the capillarity, and the elasticity work together to create a long-range interaction. These studies are discussed in Chapter 5.
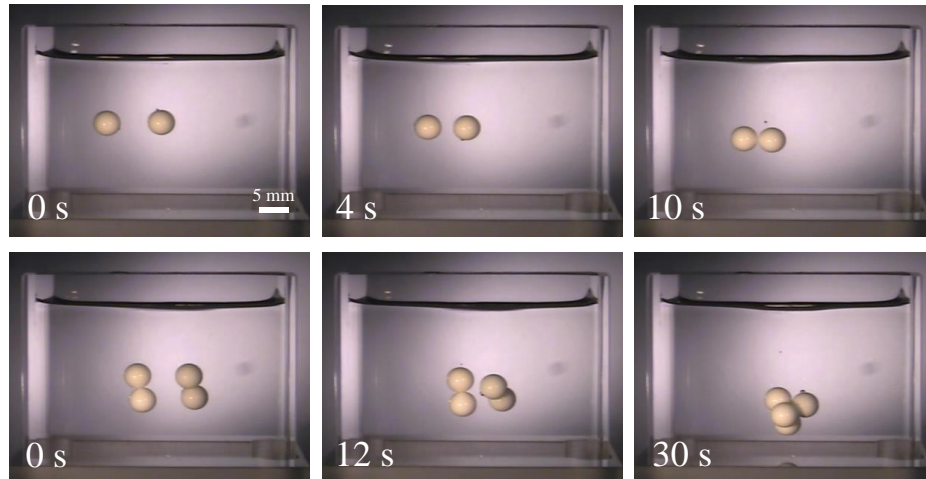
Figure 1.7: *Self-Assembly of ceramic beads inside a soft gel.* The video micrographs (upper panel) illustrate the long-range attraction between two ceramic spheres (4.8 mm diameter) submerged inside a soft PAM hydrogel ($\mu \sim 8$ Pa). The micrographs of the lower panel capture the events following the immersion of a glued dimer of similar balls inside the gel. The dimers orient (0s to 12s) as they descend inside the gel and approach each other. Finally (30s), they form a close-packed structure.[44]

1.4.2 *Elastocapillary* Assembly of Particles *on* a Soft Elastic Medium

It is well-known that a small particle can float at an air-liquid interface due to the capillary force acting along its contact line[45]. The combination of the gravitational and the surface energies can lead to an attractive or a repulsive interaction between particles depending upon their specific gravity relative to the liquid[46]. This observation dubbed the Cheerios effect[47] is the basis for capillarity-driven self-assembly. What we studied here is an elastic analog[48] of the Cheerios effect, *i.e.*, introducing an additional driving force, elasticity, along with surface tension and gravity.

We used a physically cross-linked polyacrylamide gel (shear modulus ~ 40 – 100 Pa) and deposited *mm*-sized hydrophobic glass particles on its surface. A small amount of elasticity of the medium balances the weight of the particles. The excess

energy of the surface of the deformed gel causes them to attract (Figure 1.8) as is the case with the generic capillary interactions of particles on a liquid surface. The variation of the gravitational potential energies of the particles resulting from their descents in the gel coupled with the superposition principle of Nicolson[45] allowed us to get a fair estimation of the distance dependent attractive energy of the particles.
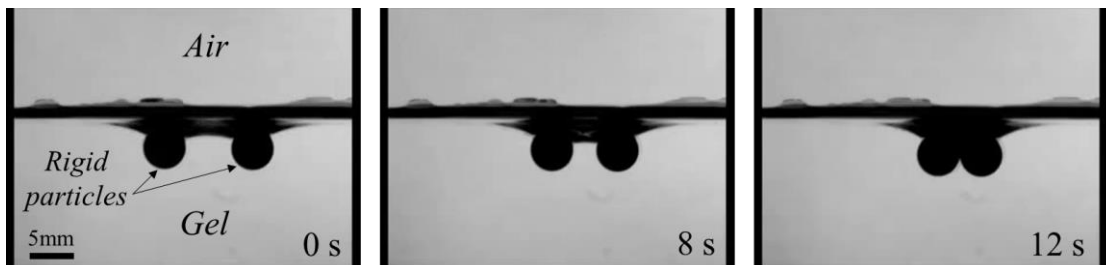
Figure 1.8: Two cylinders (aluminum, ¾'' long, 3/16 ''diameter, density 2.8 g/cc) placed parallel to each other on a soft gel (μ=18 Pa) move towards each other and eventually coalesce. Elastocapillary attraction of rigid cylinders on the surface of a soft gel.[48]

This energy follows a modified Bessel function of the second kind (zeroth order) with a characteristic elastocapillary decay length that decreases with the increase in the elasticity of the medium. An interesting finding of this study is that the particles on the gel move towards each other as if the system possesses a negative diffusivity that is inversely proportional to friction. In particular, this study points out that the range and the strength of the capillary interaction can be tuned in by appropriate choices of the elasticity of the support and the interfacial tension of the surrounding medium. This study illustrates how the capillary interaction of particles is modified by the elasticity of the medium, which is expected to have important implications in the surface force driven self-assembly of particles. The details of this work have been presented in Chapters 6 and 7.

1.4.3 Particle Assembly on a thin Elastic Film supported over a viscous Liquid

In chapter 8, we discuss the third system that we used to study interaction of particles was a thin elastic film supported over a pool of liquid.[49] We used aluminum cylinders for these studies that were grafted with polydimethylsiloxane chains to reduce its friction with the elastic films. When two such cylinders are placed on the film, the excess energy of the surface due to the curvature of the stretched film induces attraction of the particles until they finally meet. Even with reduced friction of the cylinders, we observed some hysteresis mainly due to the difference of the energies of the localized bond-forming at its front edge versus bond-breaking at its tail edge. This contribution of the adhesion hysteresis can be reduced considerably by introducing a thin hydrogel layer over the elastic film that enhances the range of attraction of the cylinders (as well as rigid spheres) in a dramatic way. We also observed the formation of morphological instabilities in the gel-film system that projected corrugated paths and led to directed motion of small spheres to form large aggregates along their defects.
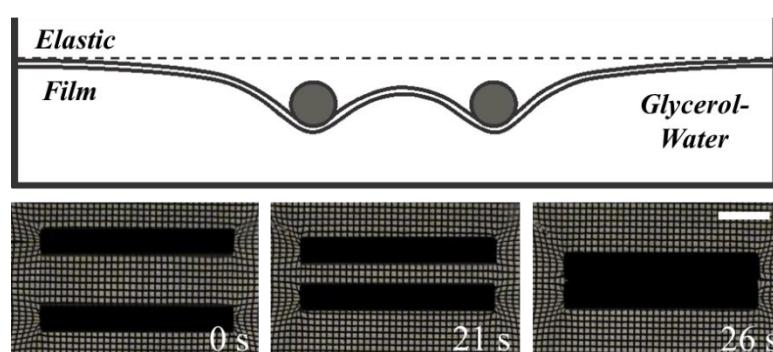
Figure 1.9: Schematic of two aluminum cylinders afloat on a thin PDMS elastic film supported over 50% aqueous glycerol. Below are experimental snapshots of the attraction of the cylinders due to the strain energy gradient in the elastic film (thickness of film = 9.2 μm). Scale bar represents 5mm.[49]

We estimated the free energy of this system comprising a single cylinder by using a minimal model including the stretching energy of the film and the gravitation energies due to the weight of the cylinder and the displacement of the liquid underneath the film. The profile is obtained from the minimization of the total free energy that yields an exponentially decaying deformation of the surface with a decay length, $\alpha^{-1} = \sqrt{T/\rho g}$, where T is the tension in the film, ρ is the density of the liquid and g is the acceleration due to gravity. For two cylinders, the intermediate profile is hyperbolic and the excess energy stored in the curved surface is released when they come together into contact. With the formal analysis, we found that the energetics of the attraction can be expressed as the variation of their gravitational potential energies as they descend into the liquid while being still supported on the film (Figure 1.9).

1.5 Wetting of Soft Hydrogels on Rigid Substrates

When a soft hydrogel sphere is placed on a hydrophilic rigid substrate, it spreads by forming a "foot"-like regime closer to the substrate, however, due to its opposing elastic forces, its spherical global shape is maintained away from the contact region. Conversely, for a similar hydrophilic substrate, an equivalent liquid drop will spread completely forming a thin film. In order to understand the phenomenon of soft wetting, we performed experiments using hydrogel spheres of different elastic moduli on hard substrates with varying surface energies. Here, we measured the contact angle of these soft spheres and found that they systematically increase as the elasticity of the gels increases. Furthermore, by modifying the wetting properties of the rigid substrates, we found that the contact angles of the gel spheres decreased as the work of adhesion increased. Additionally, we learned that the dimension of the "foot" follows a scaling

law derived from the balance of the adhesion and elastic strain energies in that region. In Chapter 9, we report a macroscopic picture of how soft spheres deform due to the adhesion forces thereby undergoing large deformation. We summarize by comparing our results of the wetting of soft hydrogel spheres with previous attempts to bridge the adhesive contact regime for rubbers with Young's contact regime for pure liquids using a global picture.

1.6 Dissertation Synopsis

As discussed above, this dissertation researches the role of elastocapillarity in soft solids as well as how gravity forces and elasticity are coupled in some situations involving these solids. We discuss the role of elastocapillarity in adhesion-induced instability in Chapter 2. This is followed by our work on the elastocapillary modes of vibration of soft hydrogel spheres that is presented in Chapter 3. Chapter 4 includes the work on elastobuoyancy phenomenon. Chapters 5-8 discuss the elasticity mediated in various systems such as inside and on the surface of soft hydrogels and on thin elastic films supported on a pool of liquid. Chapter 9 talks about the wetting of soft hydrogel spheres on rigid substrates. The thesis concludes with Chapter 10 that summarizes some essential themes and findings of our current research including suggestions for future work. There are several appendices in this dissertation that discuss some new observations, results and partially completed projects that were also done during this thesis and will be subjects of future investigations.

References

(1)   de Gennes, P. G.; Edwards, S. *Soft Interfaces: The 1994 Dirac Memorial Lecture*; Cambridge University Press, 2005.

(2)   Shuttleworth, R. The Surface Tension of Solids. *Proc. Phys. Soc. Sect. A* **1950**, *63* (5), 444–457.

(3)   Mondal, S.; Phukan, M.; Ghatak, A. Estimation of Solid–liquid Interfacial Tension Using Curved Surface of a Soft Solid. *Proc. Natl. Acad. Sci.* **2015**, *112* (41), 12563–12568.

(4)   Roman, B.; Bico, J. Elasto-Capillarity: Deforming an Elastic Structure with a Liquid Droplet. *J. Phys. Condens. Matter* **2010**, *22* (49), 493101.

(5)   Style, R. W.; Jagota, A.; Hui, C.-Y.; Dufresne, E. R. Elastocapillarity: Surface Tension and the Mechanics of Soft Solids. *Annu. Rev. Condens. Matter Phys.* **2017**, *8*, DOI: 10.1146/annurev-conmatphys-031016-025326.

(6)   Lester, G. R. Contact Angles of Liquids at Deformable Solid Surfaces. *J. Colloid Sci.* **1961**, *16*, 315–326.

(7)   Rusanov, A. I. Theory of the Wetting of Elastically Deformed Bodies. 1. Deformation with a Finite Contact-Angle. *Colloid J. USSR* **1975**, *37*, 614–622.

(8)   Young, T. An Essay on the Cohesion of Fluids. *Philos. Trans. R. Soc. London* **1805**, *95*, 65–87.

(9)   Shanahan, M. E. R.; de Gennes, P. G. Equilibrium of the Triple Line Solid/liquid/fluid of a Sessile Drop (Ed. Allen, K. W.), Elsevier Appl. Sci., London. *Adhesion* **1987**, *11*, 71–81.

(10)   Pericet-Cámara, R.; Best, A.; Butt, H. J.; Bonaccurso, E. Effect of Capillary Pressure and Surface Tension on the Deformation of Elastic Surfaces by Sessile

Liquid Microdrops: An Experimental Investigation. *Langmuir* **2008**, *24* (19), 10565–10568.

(11) Johnson, K. L.; Kendall, K.; Roberts, A. D. Surface Energy and the Contact of Elastic Solids. *Proc. R. Soc. A Math. Phys. Eng. Sci.* **1971**, *324* (1558), 301–313.

(12) Rimai, D. S.; Quesnel, D. J.; Bowen, R. C. Particle Adhesion to Highly Compliant Substrates: Anomalous Power-Law Dependence of the Contact Radius on Particle Radius. *Langmuir* **2001**, *17* (22), 6946–6952.

(13) Style, R. W.; Dufresne, E. R. Static Wetting on Deformable Substrates, from Liquids to Soft Solids. *Soft Matter* **2012**, *8*, 7177.

(14) Style, R. W.; Che, Y.; Park, S. J.; Weon, B. M.; Je, J. H.; Hyland, C.; German, G. K.; Power, M. P.; Wilen, L. a; Wettlaufer, J. S.; et al. Patterning Droplets with Durotaxis. *Proc. Natl. Acad. Sci. U. S. A.* **2013**, *110* (31), 12541–12544.

(15) Cohen, A. E.; Mahadevan, L. Kinks , Rings , and Rackets in Filamentous Structures. **2003**, *100* (21), 12141–12146.

(16) Bico, J.; Roman, B.; Moulin, L.; Boudaoud, A. Adhesion: Elastocapillary Coalescence in Wet Hair. *Nature* **2004**, *432* (7018), 690.

(17) Kim, H.-Y.; Mahadevan, L. Capillary Rise between Elastic Sheets. *J. Fluid Mech.* **2006**, *548* (1), 141.

(18) Duprat, C.; Protiere, S.; Beebe, A. Y.; Stone, H. A. Wetting of Flexible Fibre Arrays. *Nature* **2012**, *482* (7386), 510–513.

(19) Holmes, D. P.; Brun, P.-T.; Pandey, A.; Protière, S.; Lewis, J. A.; Baroud, C.; Jeronimidis, G.; Fratzl, P.; Burgert, I. Rising beyond Elastocapillarity. *Soft Matter* **2016**, *12* (22), 4886–4890.

(20) Hui, C. Y.; Jagota, A.; Lin, Y. Y.; Kramer, E. J. Constraints on Microcontact Printing Imposed by Stamp Deformation. *Langmuir* **2002**, *18* (5), 1394–1407.

(21)   Kang, S. H.; Pokroy, B.; Mahadevan, L.; Aizenberg, J. Control of Shape and Size of Nanopillar Assembly by Adhesion-Mediated Elastocapillary Interaction. *ACS Nano* **2010**, *4* (11), 6323–6331.

(22)   Wexler, J. S.; Heard, T. M.; Stone, H. A. Capillary Bridges between Soft Substrates. *Phys. Rev. Lett.* **2014**, *112*, 66102.

(23)   Whitesides, G. M. The Origins and the Future of Microfluidics. *Nature* **2006**, *442* (7101), 368–373.

(24)   Majumder, A.; Tiwari, A. K.; Korada, K.; Ghatak, A. Microchannel Induced Surface Bulging of a Soft Elastomeric Layer. *J. Adhes. Sci. Technol.* **2010**, *24* (15–16), 2681–2692.

(25)   Py, C.; Reverdy, P.; Doppler, L.; Bico, J.; Roman, B.; Baroud, C. N. Capillary Origami : Spontaneous Wrapping of a Droplet with an Elastic Sheet. *Phys. Rev. Lett.* **2007**, *98*, 156103.

(26)   Reis, P. M.; Hure, J.; Jung, S.; Bush, J. W. M.; Clanet, C. Grabbing Water. *Soft Matter* **2010**, *6* (22), 5705.

(27)   Mora, S.; Phou, T.; Fromental, J. M.; Pismen, L. M.; Pomeau, Y. Capillarity Driven Instability of a Soft Solid. *Phys. Rev. Lett.* **2010**, *105* (21), 1–4.

(28)   Jagota, A.; Paretkar, D.; Ghatak, A. Surface-Tension-Induced Flattening of a Nearly Plane Elastic Solid. *Phys. Rev. E* **2012**, *85* (5), 1–6.

(29)   Mora, S.; Pomeau, Y. Softening of Edges of Solids by Surface Tension. *J. Phys. Condens. Matter* **2015**, *27* (19), 194112.

(30)   Chakrabarti, A.; Chaudhury, M. K. Direct Measurement of the Surface Tension of a Soft Elastic Hydrogel: Exploration of Elastocapillary Instability in Adhesion. *Langmuir* **2013**, *29* (23), 6926–6935.

(31)   Gonuguntla, M.; Sharma, A.; Sarkar, J.; Subramanian, S. A.; Ghosh, M.; Shenoy,

V. Contact Instability in Adhesion and Debonding of Thin Elastic Films. *Phys. Rev. Lett.* **2006**, *97*, 18303.

(32) Chakrabarti, A.; Chaudhury, M. K. Vibrations of Sessile Drops of Soft Hydrogels. *Extrem. Mech. Lett.* **2014**, *1*, 47–53.

(33) Ghatak, A.; Chaudhury, M. K.; Shenoy, V.; Sharma, A. Meniscus Instability in a Thin Elastic Film. *Phys. Rev. Lett.* **2000**, *85*, 4329.

(34) Ghatak, A. Adhesion Induced Instability in Thin Elastic Film, Ph.D. Thesis, Lehigh University, Bethlehem, PA, 2003.

(35) Chaudhury, M. K.; Chakrabarti, A.; Ghatak, A. Adhesion-Induced Instabilities and Pattern Formation in Thin Films of Elastomers and Gels. *Eur. Phys. J. E* **2015**, *38* (7), 82.

(36) Mönch, W.; Herminghaus, S. Elastic Instability of Rubber Films between Solid Bodies. *EPL (Europhysics Lett.* **2001**, *53* (4), 525.

(37) Chung, J. Y.; Kim, K. H.; Chaudhury, M. K.; Sarkar, J.; Sharma, A. Confinement-Induced Instability and Adhesive Failure between Dissimilar Thin Elastic Films. *Eur. Phys. J. E* **2006**, *20* (1), 47–53.

(38) Longley, J. E.; Mahadevan, L.; Chaudhury, M. K. How a Blister Heals. *EPL (Europhysics Lett.* **2013**, *104* (4), 46002.

(39) Griffith, A. A. The Phenomena and Rupture in Flow of Solids. *Philos. Trans. R. Soc. London Ser. A* **1921**, *221*, 163–198.

(40) Rayleigh, Lord. On the Capillary Phenomena of Jets. In *Proc. R. Soc. London*; 1879; pp 71--97.

(41) Mora, S.; Phou, T.; Fromental, J.-M.; Pomeau, Y. Gravity Driven Instability in Elastic Solid Layers. *Phys. Rev. Lett.* **2014**, *113*, 178301.

(42) Chakrabarti, A.; Chaudhury, M. K.; Mora, S.; Pomeau, Y. Elastobuoyant Heavy

Spheres: A Unique Way to Study Nonlinear Elasticity. *Phys. Rev. X* **2016**, *6* (4), 41066.

(43)   Whitesides, G. M.; Grzybowski, B. Self-Assembly at All Scales. *Science (80-.).* **2002**, *295* (2002), 2418–2421.

(44)   Chakrabarti, A.; Chaudhury, M. K. Surface Folding-Induced Attraction and Motion of Particles in a Soft Elastic Gel: Cooperative Effects of Surface Tension, Elasticity, and Gravity. *Langmuir* **2013**, *29* (50), 15543–15550.

(45)   Nicolson, M. M. The Interaction between Floating Particles. *Proc. Cambridge Philos. Soc.* **1949**, *45*, 288–295.

(46)   Kralchevsky, P. a.; Nagayama, K. Capillary Interactions between Particles Bound to Interfaces, Liquid Films and Biomembranes. *Adv. Colloid Interface Sci.* **2000**, *85* (2), 145–192.

(47)   Vella, D.; Mahadevan, L. The "Cheerios Effect." *Am. J. Phys.* **2005**, *73* (9), 817.

(48)   Chakrabarti, A.; Ryan, L.; Chaudhury, M. K.; Mahadevan, L. Elastic Cheerios Effect: Self-Assembly of Cylinders on a Soft Solid. *EPL (Europhysics Lett.* **2015**, *112* (5), 54001.

(49)   Chakrabarti, A.; Chaudhury, M. K. Attraction of Mesoscale Objects on the Surface of a Thin Elastic Film Supported on a Liquid. *Langmuir* **2015**, *31* (6), 1911–1920.

Chapter 2

Direct Measurement of the Surface Tension of a Soft Elastic Hydrogel: Exploration of Elasto-Capillary Instability in Adhesion[a]

2.1. Introduction

The joint roles of the surface tension and the elastic forces have long been recognized in soft matter physics. Starting with the original proposal of Lester[1] that a soft solid can be deformed by the normal component of the surface tension of a liquid drop, the subject has continued to blossom[2-8] till date with the identification of a scale of the surface deformation in terms of the surface tension (γ) divided by the elasticity (μ). This so called elasto-capillary length (γ/μ) also appears in various other surface phenomena such as the wrapping of a liquid drop by a thin elastic film[9], coalescence of thin wet fibers[10,11], buckling of thin rods inside a liquid drop[12], cavitation in soft hydrogel[13,14], bulging[15] of a thin elastic channel due to capillary pressure, flattening[16] of a soft solid by surface tension, and Rayleigh instability[17] in a soft gel to name a few. Elasto-capillary effect has also been found to be important in the nucleation of creases[18] in soft solid and it manifests directly in the form of the radius (a) of the contact

---

deformation[19] of two spheres with an effective radius R as $a^3/R^2 \sim \gamma/\mu$, which can be used as a sensitive probe to study surfactant adsorption[20] related capillary effects as well.

The objective of this paper is to show that elasto-capillary instability can play an important role in the formation of self-generated cracks in soft confined films. Usually, when a rigid substrate adhered to a thin rubber film is subjected to a tensile stress, the interface ceases to be flat[21-27]. As was discovered independently at the Lehigh University[21] and at the University of Ulm[22], the entire surface or the line of contact of such an adhesively stressed film roughens with a characteristic length scale that is simply proportional to the thickness of the film (H). This happens when the elasto-capillary number ($\mu H/\gamma$) of the film is much larger than unity. On the other hand, if γ/μ is comparable to the film thickness, a material length scale emerges that moderates the interfacial roughness. A simple scaling analysis[26] suggests (see Appendix A) that the wavelength of the instability would be of the following form: $\lambda \sim H(1+\gamma/\mu H)^{1/4}$, according to which there are three distinct regimes of elastic instability. For a high modulus film ($\gamma/\mu << H$), the wavelength is proportional to thickness, i.e. $\lambda \sim H$. When γ/μ is slightly smaller than H, the instability wavelength depends on both the geometric and the material scales (γ/μ) almost additively: $\lambda \sim H + \gamma/4\mu$. On the other hand, when $\gamma/\mu >> H$, the elasto-capillary and the geometric scales are strongly coupled as $\lambda \sim (\gamma H^3/\mu)^{1/4}$. Gonuguntla et al[28] studied this regime using ultra-thin films of elastomeric PDMS, in which the patterns were frozen by UV ozone treatment and analyzed after the contactor was removed. They showed that the wavelength of instability deviates from the conventional $\lambda \sim 3H$ relationship. While

this was the first attempt to document the elasto-capillarity in adhesion induced pattern formation, there are certain concerns with the way these experiments were performed and interpreted. To begin with, since an UV-ozone treatment could modify the properties of the film to a substantial depth in a gradient fashion, it is not clear *a priori* whether the modulus of the ultra-thin film would be same as that of the untreated bulk elastomer. In addition, the surface tension of the ultra-thin elastomeric PDMS was assumed to be same as that in its liquid state, which cannot be guaranteed, either in the native state and, especially, when its surface is post-hardened. Most importantly, however, as the measurements were performed *ex-situ* after preserving the pattern and then removing the contactor, it is not at all clear whether the long wave features of the instability were the reminiscence of the surface tension induced flattening[16], in which the short wave features decay, or it was indeed due to the adhesion induced instability [28]. Whilst these criticisms do not take away the novelty and the elegance of these experiments[28], there is, nevertheless, a need to conduct definitive experiments and to carry out the related analysis on such types of instabilities in a system where the patterns can be observed *in situ* and where the solid surface tension and the elasticity of the deformable adhesive can be measured independently.

The purpose of this paper is to report such measurements performed with a physically cross-linked polyacrylamide hydrogel[29-31], the elastic modulus of which could easily be controlled and set to a rather low value. A further inspiration for such a study stems from the fact that these types of ultra-soft gels are increasingly used in various biomedical, cosmetic and adhesive technologies[32]. As the deformability is a major issue in these studies, the soft gels have become the testing grounds for various types of mechanical and rheological characterizations[33] over the years. In spite of considerable progress, however, characterizations of the ultra-soft gels can be quite

challenging in certain settings, especially when the elastic forces become comparable to capillarity. The interplay of these factors, nevertheless, makes these gels interesting candidates of study in an evolving branch of rheology where surface tension, elasticity and viscosity play their respective roles.

In order to observe the putative elasto-capillary instability and interpret it on a sound physical ground, we had to accomplish three different but related objectives. The main objective was to design an experiment with which the instability could be induced and measured *in situ* over a considerable range of film thickness. This objective was accomplished with a gel confined in a wedge shaped geometry, the thickness of which varied from about 0 micron to about 180 micron in a linear fashion. This idea of using a thickness gradient is philosophically similar to that of Stafford et al[34] in studying the effect of thickness of the top layer in wrinkling instability.

A linear stability analysis was performed to understand the long wavelength feature of the elasto-capillary instability, the execution of which, however, required values of the surface tension and the elasticity of the physically cross-linked hydrogel. Its surface tension was estimated from the spherical harmonic of the free surface of a hemispherical gel cap, whereas its elasticity was estimated from the natural shear resonance mode of a hydrogel slab after submitting each to a random mechanical vibration. In connection with measuring the elasticity of the gel, we also report a novel observation, in which a steel ball remains suspended in the gel by balancing its weight with the accumulated shear strain induced elastic force of the surrounding medium. This is the static or a self-braking version of the classical Stokes experiment that allowed estimation of the shear modulus of the gel both at small as well as at large deformations in the absence of dynamics. Once the surface tension and the elasticity

of the gel were measured, an elasto-capillary length could be estimated and compared with that obtained from the adhesion induced instability patterns.

The paper is organized as follows. After describing the experimental protocols, we discuss the methods to measure the elasticity and the surface tension of an ultra-soft hydrogel. These measurements established an elasto-capillary length of the hydrogel, which was then used to interpret the spatial wavelength of the adhesion induced interfacial instability. The paper is then concluded with a discussion on how elasto-capillarity could be an important factor in deciding the failure modes of the interface of an elastic film sandwiched between two rigid substrates.

2.2. Experimental Sections

2.2.1. Materials

The chemicals used for the preparation of the hydrogel were N-(hydroxymethyl)-acrylamide (48% solution in water, Sigma Aldrich®), potassium persulphate (99.99% trace metals basis, Sigma Aldrich®) and N,N,N',N'-Tetramethylethylenediamine (TEMED, ≥99.5%, purified by re-distillation, Sigma Aldrich®). Deionized water (DI water) was obtained from Thermo Scientific® Barnstead E-pure* unit. Glass slides of two different sizes (75 mm x 50 mm x 1 mm) and (75 mm x 25 mm x 1 mm) were obtained from Fisher Scientific (Fisherbrand® Microscopic slides). The glass cover slips were purchased from Corning (Corning Cover Glass, No. 1, 24 mm x 60 mm). Freshly opened Fisherbrand® Borosilicate Glass vials (27 mm diameter x 70 mm high) were already quite clean; but they were further washed thoroughly with DI (deionized) water and blow dried with ultra-high purity Nitrogen gas. The gel solutions were prepared in these vials. Steel balls (Bearing-

Quality E52100 Alloy Steel, Hardened Ball) of diameters ranging from 1 mm to 10 mm were purchased from McMaster-Carr®. These balls were sonicated in Acetone (General use HPLC-UV grade, Pharmco Aaper®) in a Fisher Scientific Ultrasonic Cleaner (Model no. FS5) for 10 minutes after which they were blow dried with pure Nitrogen gas. In some of the experiments, glass slides were reacted with a silane [dodecyltrichlorosilane (HC-12, Gelest Inc), hexadecyltrichlorosilane (HC-16, Gelest Inc.) or *1H,1H,2H,2H*-perfluorodecyltrichlorosilane (FC-10, Alfa Aesar)], the details of which were reported previously[35]. For some of the experiments, glass slides were modified with a thin (5 nm) film of polydimethylsiloxane (PDMS, Gelest DMS-T22) using a method reported in the literature[36].

2.2.2. Preparation of Gel

The physically cross-linked gel was prepared using a slight variation of the methods[29-31] reported in the literature in order to ensure that polymerization reaction could be carried out at room temperature in less than an hour. In a cleaned glass vial, N-(hydroxymethyl)-acrylamide and DI water were added to prepare a 3.5% (w/w) of the monomer in the solution, which was followed by degassing it with the bubbling of ultrapure nitrogen gas for 30 minutes while stirring it constantly with a magnetic stirrer. The polymerization reaction was initiated by first adding Potassium Persulphate (0.25 wt% basis) and then TEMED (0.3 wt% basis) to the above solution accompanied by constant stirring. The final solution was pipetted out of the vial and introduced in the respective setups soon after the TEMED was mixed. In all experiments, gelation reaction was carried out at room temperature for two hours, even though the reaction was complete within half an hour, which was ascertained from the fact that the modulus of the gel remains unchanged beyond this time.

2.2.3. Measurements of Elastic Moduli of the Gel

The shear modulus (μ) was determined from the resonant shear mode of vibration of a gel slab confined between two parallel glass slides. One of the glass slides (75 mm x 25 mm x 1 mm) was coated with a monolayer of HC-16, which was then was placed above an untreated clean glass slide (75 mm x 50 mm x 1 mm) by maintaining a uniform gap of 1 mm between the two slides by means of two 1 mm thick spacers. The spacers themselves were prepared from the microscope glass slides, the edges of which were lined with thin strips of Teflon tapes for easy removal from the gel once the gelation was complete. This assembly was set up inside a polystyrene petri dish (VWR[®], 150mm diameter, 15mm high) with stacks of deionized (DI) water soaked filter papers placed on the sides of the above assembly in order to create a humid environment (relative humidity of 99.9% at 23°C). The gel solution was inserted into the uniform gap between the slides by means of a sterile transfer pipette (7.7 mL, #202-1S, Thermo Scientific[®], Samco[*]). One hydrophobic (above) and another hydrophilic (below) glass slides allowed the liquid to fill the gap by capillarity, but prevented its spreading beyond the edges of the Teflon coated spacers. This setup was left undisturbed for the next two hours while the gel slab (57 mm x 25 mm x 1 mm) cured, following which the spacers were removed. The lower plate of the assembly was fixed carefully onto the aluminum stage connected to a mechanical oscillator (Pasco Scientific, Model No: SF-9324) that was subjected to either a lateral or a vertical vibration using a Gaussian white noise (strength of 0.005 to 0.12 m^2/s^3). The noise was generated by a waveform generator (Agilent, model 33120A) and passed through an amplifier (Sherwood, Model No: RX-4105) before reaching the oscillator. The entire experimental setup was placed on a vibration isolation table (Micro-g, TMC). The shear

and/or the vertical displacements of the upper glass slide were recorded with a high speed camera (Redlake Motion-Pro, Model no: 2000) operating at 1000 frames/s. The motion of the upper plate was later tracked using a MIDAS software (Midas2.0, Xcitex Inc., USA). The displacement fluctuations were fast Fourier transformed (FFT) using OriginLab® software to identify the resonant mode of vibration. The details of the basic methods can be found in previous publications[36,37].

2.2.4. Static Stokes' Experiment

In these experiments, the cleaned steel balls were gently dropped inside the glass vial containing the cured hydrogel. After submerging itself partially or fully inside the gel, the ball stood still inside the gel at a depth (h) , which was captured by a Video Microscope (Infinity®) equipped with a CCD camera (jAi®,Model no. CV-S3200) with the help of WinTV application (Hauppauge®, USA) on the computer. Care was taken to ensure that the steel balls were at the centers of the vials to minimize wall effects. The images were analyzed using ImageJ® for calculating the depth of the steel ball into the gel. The calibration factor of the variable focal length microscope was determined from the known diameter of a steel ball in every run. Even though there was a minor distortion of the shape of the ball in the horizontal direction when viewed through the cylindrical glass vials, there was no such distortion in the vertical direction. All calibrations and measurements were carried out in vertical direction only.

2.2.5. Direct Estimation of the Surface Tension of the Gel Using Vibration

The surface tension was estimated from the vibration modes of the free surface of the hemispherical caps of the hydrogel prepared on hydrophobic glass slides. Glass slides were cut into small pieces (10 mm x 8 mm) using a diamond scriber which were

then silanized by reacting them with the vapor of dodecyltrichlorosilane (HC-12). The pieces of these hydrophobic glass slides were fixed at the bases of small petri dishes (35 mm diameter x 10 mm high, Fisherbrand®) using a double sided Scotch® tape. After deposition of 2 to 40 μL size drops of the gel solution on these glass pieces (one drop per dish), the lids of the petri-dishes were closed. The filter papers placed on the sides of the petri-dishes were soaked with an aqueous solution of acrylamide monomer and TEMED with the same composition as the gel in order to suppress the evaporation of these ingredients from the gel drop itself.

The contact angle of the gel cap was ~90° on the silanized glass slide. The petri dishes were left undisturbed for 2 hours while the gel caps cured. After securely fixing the test substrate (the petridish with the samples inside it) on the aluminum stage of the mechanical oscillator, it was vibrated vertically with a Gaussian white noise (strength of 0.04 m^2/s^3). The height fluctuations of the gel caps were recorded with the high speed camera at 2000 frames/s which were subsequently analyzed with MIDAS 2.0. The fluctuations of the gel lenses were fast Fourier transformed (FFT) using OriginLab® software to identify the resonant mode of vibration.

2.2.6. Adhesion Instability Experiment

A hydrophobic glass slide (75 mm x 25 mm x 1 mm) was inclined above an untreated clean glass slide (75 mm x 50 mm x 1 mm) with the help of a spacer (Corning Cover glass) so that a linear thickness gradient was established (figure 4a) between the two. The spacer was 180 μm thick which gave rise to the gradient gel thickness ranging from 0 to 180 μm over a length of ~ 6.7 cm. This setup was assembled inside a polystyrene petri dish (VWR®, 150mm diameter x 15mm height) where stacks of DI water soaked filter paper were kept on either side of the assembly. As soon as the

mixing of the gel solution was complete, it was pipetted out with a sterile transfer pipette and introduced into the wedge formed between the two glass slides. The petri dish was immediately covered by its lid in order to maintain a water vapor rich environment inside.

After allowing the gel to crosslink for two hours, a razor blade was gently inserted in between the upper plate and the spacer till the instability patterns develop all throughout the contact of the gel and the upper plate. These experiments were carried out with the top glass plate coated with either a fluorocarbon silane (FC-10) or a thin (~ 5 nm) polydimethyl siloxane (PDMS) for its easy removal from the gelled film. The patterns were observed using a microscope (Infinity®) equipped with a CCD camera (MTI, CCD-72) and recorded to a computer, which were analyzed later using ImageJ® software. Thin longitudinal strips from the images, obtained at various thickness of the gel film, were taken and the numbers of darker bands cutting across this strip were counted. Wavelength of the instability (λ) at different thickness (H) was obtained by dividing the length of the strip by the number of these bands. We confirmed that this method of measuring λ is perfectly consistent with that obtained from the traditional method of Fast Fourier Transforming (FFT) an image provided that the pattern is isotropic and is comparable to the spacing between fingers when a fingering instability is induced by peeling a flexible cantilever from such a hydrogel film (see below). The method used here was quite convenient to analyze the slightly anisotropic spatial patterns resulting from the thickness gradient.

2.3. Results

2.3.1. Estimation of the Shear Modulus of the Gel
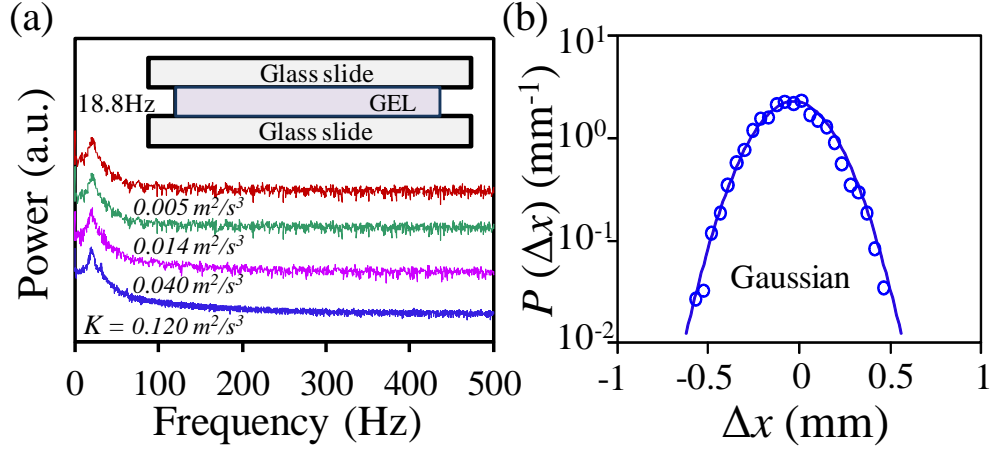
Figure 2.1: (a) The resonance mode of a thin slab of the physically cross-linked hydrogel was obtained by subjecting it to a random excitation parallel to the upper plate while the lower plate was held fixed on the stage of the oscillator. Several power spectra were added and averaged in order to reduce the background noise and improve the peak shape. (b) The probability distribution function of the displacement fluctuation is Gaussian (K=0.12 m²/s³) thus emphasizing the linear response of the system. The root mean square (RMS) displacement is 0.4 mm.

The shear elastic modulus of the gel was estimated in two different ways. The first method involved the transverse vibration of a thin slab of the gel of thickness H confined between two flat plates (figure 2.1a) with a random external noise. The fact that the gel is elastic is evident from the observation that it can support the weight of the upper plate (a glass slide) for an indefinite period of time. From the resonance peak (ω=18.8 Hz) of the gel that behaves like a shear spring, its shear modulus (μ) was estimated using the equation: $2\pi\omega = \sqrt{(\mu A / mH)}$, where m is the mass (4.62 g) of the top vibrating plate, and A is the area of contact between the gel slab and the glass plate. The shear modulus of the gel was found to vary between 42 Pa to 45 Pa. The probability

distribution of the shear displacement fluctuation is Gaussian (figure 2.1b), thus suggesting that the response of the gel is linear, which is reinforced by the fact that the resonance frequency of the gel is independent of the noise strength (figure 2.1a).

2.3.2. Self-braking Stokes Experiment
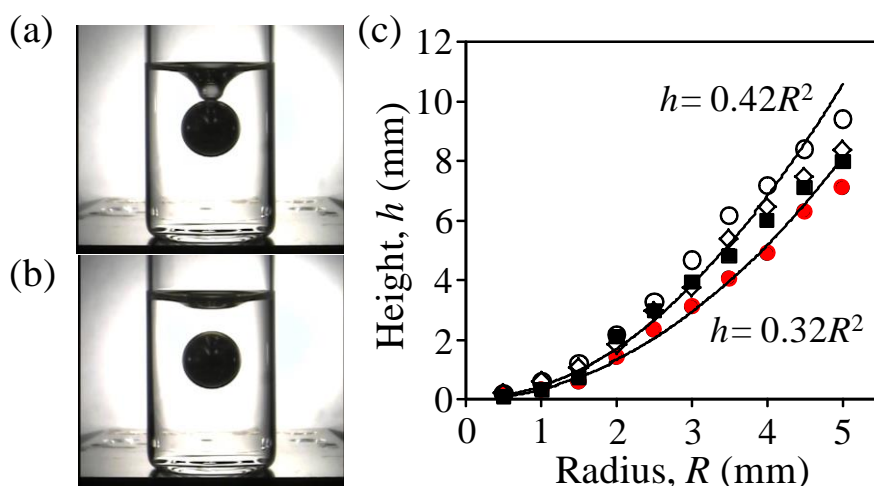
Figure 2.2: (a) A static version of the Stokes experiment, in which a steel ball (R = 5 mm) was released on the surface of a physically cross-linked hydrogel. The ball penetrates deep in the gel and becomes neutrally buoyant, at which stage the elastic shear force on the ball is balanced by the weight of the ball. In (a) the surface of the gel is in contact with the sphere, which can be released (b) by lowering its surface tension, e.g. by applying couple of drops of an aqueous surfactant solution (1.6 wt% of Brij 35).[b] (c) Experiments carried out with balls of different sizes show that the height of submersion increases with the radius of the ball. Although slight differences in the overall behavior is observed with gels prepared on the first day or after 24 hrs, each set of data could be fitted with an equation $h \sim R^2$.

The shear modulus obtained from the vibration experiment discussed as above

is adequate for the purpose of analyzing the pattern formation data. The above method

of measuring elasticity, however, involves substantial amount of sample preparation

---

[b] Below is a corrigendum for the stated observation in [Chakrabarti, A. and Chaudhury, M.K. Direct measurement of the surface tension of a soft elastic hydrogel: Exploration of elastocapillary instability in adhesion. *Langmuir* **2013**, *29*(23), pp.6926-6935]. When the surfactant drops are added, they merely fill the hollow created due to the stretching of the gel interface by the engulfment of the sphere. The surfaces do not close due to lowering of surface tension of the surfactant-gel interface.

time; furthermore, the experiments and analysis are somewhat time consuming. For repeated and routine analysis of the elasticity of the gel, we developed a simple technique in analogy to the classical Stokes experiment, in which a small steel ball is released over the surface of the gel. As shown in figure 2.2a, the ball submerges itself in the gel by a substantial depth following which the denser steel ball appears to become neutrally buoyant. When the vial is inverted, the ball easily comes out of the gel, which, upon reinsertion, returns to its original position. A larger ball sinks more deeply in the gel than a smaller one because of its greater weight. We also found that the depth to which the ball sinks in the gel is inversely proportional to the degree of gelation, i.e. modulus (Appendix B), the details of which will be published separately. When the experiment is conducted first with the larger ball and then with the smaller one, the latter would reach exactly the same position had the experiment been performed in the reverse order. When an external magnetic field is applied at the bottom of the glass vial, the ball sinks down further only to return to its original position upon the removal of the field. These observations suggested to us that these gels are quite elastic (we thank A. J. Crosby who shared with us some of his observations related to the elastic nature of similar soft hydrogels). When a sufficiently strong magnetic field is applied to the ball, fracture occurs inside the gel, which can then no longer support the weight of the steel ball; the latter simply passes through the gel with a uniform velocity. These results suggest that the gel is most generally not fractured, at least underneath the ball (figure 2.2a,b), when it stands suspended inside the gel without exhibiting any motion. Since the height of submersion (h) decreases with the increase of the shear modulus (μ) of the gel and increases with the radius (R) of the sphere, we expect that the shear force due to the accumulated strain would be $C\mu R h$ in analogy to the Stokes drag in a viscous

medium, in which the shear modulus and the height are exchanged with the viscosity and the velocity of the classical Stokes equation, respectively. Using the similarity of the structure of the elastic field (Navier) equation and the Navier-Stokes equation, one can estimate the value of C in the small deformation and linear elastic limit to be 4π so that the upward force experienced by the spherical ball is $4\pi\mu Rh$ (Appendix C). By balancing this force with that of downward gravity, we obtain an expression for the immersed height as: $h = \Delta\rho g R^2 /(3\mu)$, where $\Delta\rho$ is the excess density of the steel ball surrounded by the hydrogel and g is the gravitational acceleration. Here, we ignore the effect of the wall of the glass vial, which would be important when its inner diameter is comparable to the size of the ball. Figure 2.2c shows that the depth of submersion (h) indeed increases with the radius (R) of the sphere in a quadratic fashion. With the data obtained from different measurements, the shear modulus of the gel is estimated to be 58 ± 3 Pa at a confidence limit of 95% and by forcing the fitted line to pass through the origin. In order to get a better agreement between this value that (42-45 Pa) estimated from the resonance frequency of the gel (figure 2.1), the value of C has to close to 6π. We believe that this discrepancy is due to the fact that we used a simplified linear equation of elasticity in the small deformation limit. It would be more appropriate to employ an adequate constitutive relation between stress and strain for such a poro-elastic gel and the coupled effects of the normal stresses in order to account for any putative non-linear effects. Fortunately, at this stage, the discrepancy is not huge and can be taken care of with an empirical correction factor. The value of this simple method is that it allows rapid estimation of the shear modulus of the gel by precluding any dynamics, which can be easily adapted to measure not only the elasticity of a soft gel

but also the liquid to solid transition of the gel as gelation is carried out with different amounts of acrylamide.

2.3.3. Surface Tension of the Gel

The need to obtain a direct estimation of the surface tension of the gel is that the material points of its surface can stretch[16] during surface undulation and thus its surface tension may not necessarily be the same as that of liquid water. Direct measurement of the surface tension of a solid is, however, a well-known nuisance in surface physics as it is not usually possible to de-couple the surface from the bulk effects. Nevertheless, if the solid is very soft such as the case here and if the perturbation is small, it is possible to estimate its surface tension from the resonance vibration frequency of its free surface. A hemispherical cap of a liquid drop exhibits spherical harmonics with its fundamental frequency scaling with the volume (V) as $V^{-0.5}$ provided that the mode is carried out by capillarity[39-45]. For an elasticity driven mode[46], the frequency scales as $V^{-0.33}$.

Being inspired by such a clear and measurable distinction between the two types of modes, we subjected the hemispherical caps of the physically cross-linked gels to a random vertical vibration[45] and identified the resonance frequency from the power spectrum of its surface fluctuation.

These power spectra (figure 2.3) show that there is a fundamental vibration mode that varies with the volume of the drop as $\omega \sim V^{-0.55}$, which is similar to that of water in magnitude as well as in character [42-45], i.e. $\omega \sim V^{-0.5}$. The form $\omega \sim V^{-0.55}$ is clearly distinct from the eigen frequencies of the elastic modes[46] for which one expects $\omega \sim V^{-0.33}$. Since the contact angles of the hydrogel caps on the hydrophobic glass

(a)

(b)

(c)
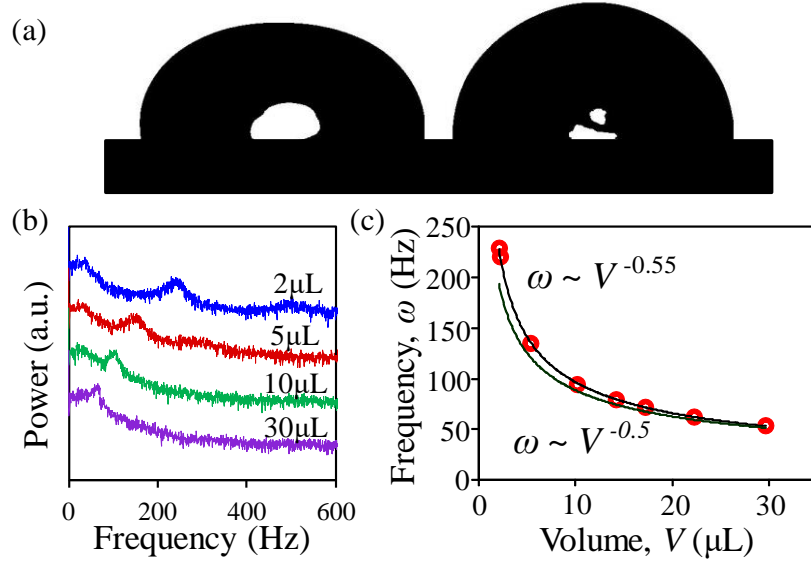
Figure 2.3: (a) The fundamental deformation mode of a *20 μL* hemispherical cap of the hydrogel as obtained from some random frames of the gel vibrating under a random noise. These two frames show the downward (left) and upward (right) deflecting deflections of the surface of the hemispherical gel (b) Power spectra of hemispherical caps of the hydrogel show the resonance modes that depend on the volume of the drop. Several power spectra were added and averaged in order to reduce the background noise and improve the peak shape. (c) The resonance frequency (ω) of the drop (red circles) varies with the volume of the gel following a $V^{-0.55}$ relationship, which is very close to that of water (lower solid line).

supports were 90°, we employ an equation given by Lyubimov et al.[44] according to which the fundamental resonance frequency (ω) of a hemispherical drop is:

$$\omega = \sqrt{\frac{\gamma \tilde{\omega}^2}{6\pi m}} \tag{2.1}$$

Where γ is the surface tension of the drop, m is the mass and $\tilde{\omega}$ is the root of the following equation:

$$\sum_{l=1}^{\infty} \frac{l(4l+1)}{\tilde{\omega}^2 - 4l(2l-1)(l+1)} \left(\frac{(2l-1)!!}{2^l l!} \right)^2 = 0 \tag{2.2}$$

Using the numerically evaluated value of $\tilde{\omega}$ (4.4268), the fundamental resonance frequency of a hemispherical cap of water of surface tension ~73 mN/m can be estimated from equation 2.1, which have been rigorously verified in previous

43

experimental studies[43,45]. Figure 2.3c shows that the experimental resonance frequencies of the gel are quite close to the values predicted from equation 2.1 for equivalent drops of water. These results encourage us to consider that the surface tension of the gel is very similar to that of pure water, i.e. γ (gel) ~ 73 mN/m.

With the above estimates of the elastic modulus and the surface tension of the hydrogel, its elasto-capillary length γ / μ is estimated to be 1.8 mm. Thus, as long as the thickness of the hydrogel film is comparable to or smaller than 1.8 mm, we expect to witness a pronounced elasto-capillarity effect in the interfacial instability. The pattern formation experiments performed with a graded hydrogel bear out this expectation as discussed below.

2.3.4. Elasto-capillary Instability

The adhesion instability experiment could be performed conveniently with a thickness gradient gel that was polymerized inside a wedge shaped geometry (Figure 4a). The lower slide of the wedge was an untreated glass slide, whereas the upper slide (flexural rigidity of $D = 8$ Nm) was silanized so that it could be easily peeled off the gel from its thicker side by inserting a razor blade underneath the slide resting on the spacer. With a very low wedge angle (0.15°) coupled with a material scale $(D/\mu)^{1/3}$ of deformation (0.6 m) being much larger than any geometric scale of the system, we expect that the entire hydrogel film would be hydrostatically stressed[47] when the upper plate is peeled. This expectation is consistent with the experimental observation that the instability pattern develops spontaneously all throughout the interfacial contact (figures 2.4b and 2.5a), with its characteristic wavelength decreasing in proportion to the thickness of the gel.
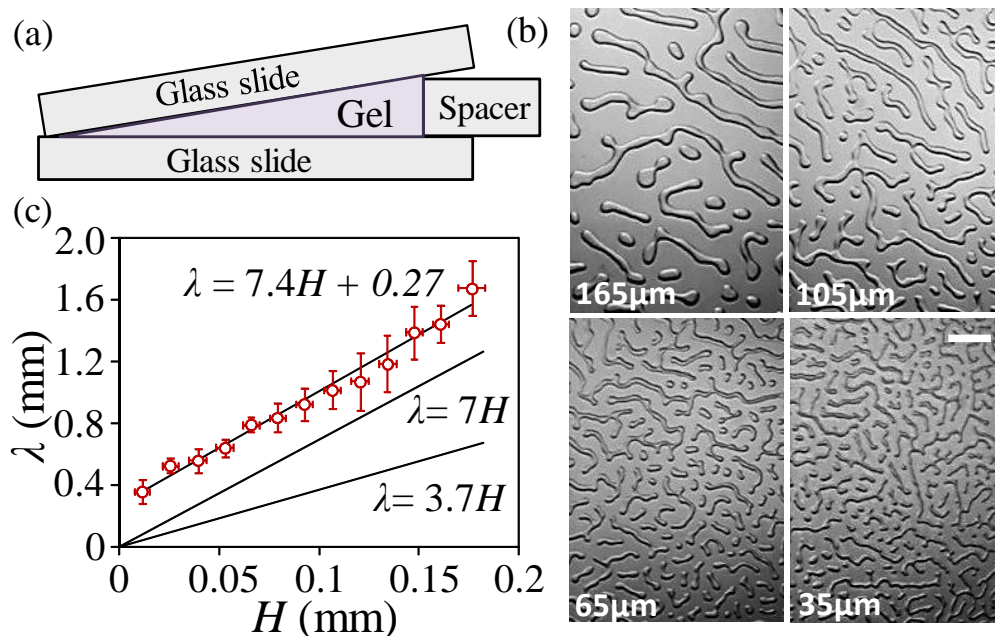
Figure 2.4: (a) A soft hydrogel is confined in the wedge formed by two glass slides. The lower slide is as-received, whereas the upper slide was made hydrophobic by reacting it with a fluorocarbon silane. (b) When the upper plate is slightly lifted from the thicker side of the gel, it detaches partially from the silanized glass thus forming the instability pattern. The white scale bar represents 2 mm. The thickness values are representative of the gel thickness at the center of the micrographs (c) The wavelength (red open circles) of the instability decreases with the thickness of the gel, with its value being much larger than the relationship expected of a purely elastic instability (the solid line, $\lambda=3.7H$).

While the gel cured in a wedge geometry simplifies the measurements performed over a significant range of thickness, we emphasize that a gel of uniform thickness also yields similar wavelength of instability as does the gradient gel. For example, while a gel film with an uniform thickness of 0.15 mm yields an instability pattern of $\lambda = 1.29(\pm0.06)$ mm, the section of the gradient gel of similar thickness yields a value λ as $1.39(\pm0.16)$ mm. This discrepancy is well within the error band of the measurement.
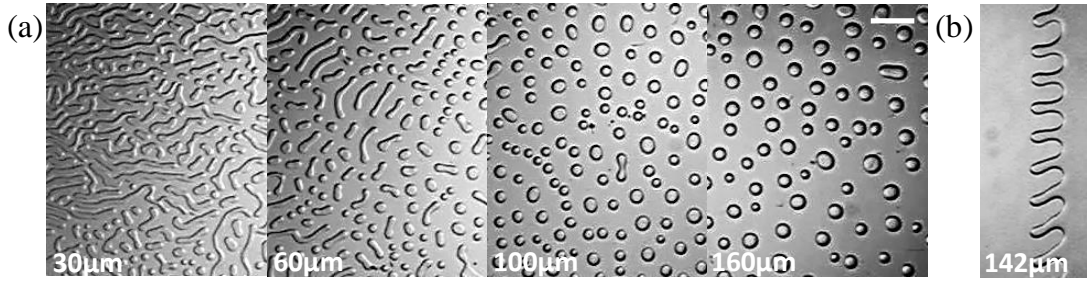
Figure 2.5: (a) This experiment is similar to that of figure 2.4, except that the upper glass plate was treated with a thin (5 nm) film of polydimethylsiloxane. The white scale bar represents 2 mm. The thickness values are representative of the gel thickness at the center of the micrographs (b) This panel shows the formation of fingering instability, observed at 142μm thickness, during the peeling of a soft PDMS cantilever (flexural rigidity 2x10^{-4} Nm) from a hydrogel film of varying thickness. The spacing of the fingers is also comparable to the spacing of the bubbles from a film of comparable thickness.

Even though the wavelengths of the instabilities observed with both the FC (fluorocarbon) and the PDMS (polydimethylsiloxane) coated glass slides are comparable, certain differences in their morphologies are evident in figures 2.4b and 2.5a. For example, while bubbles are observed with the PDMS coated slide peeling from the thicker part of the gel, interconnected stripes are observed with the FC coated slide. On neither of the two surfaces, the wavelength of the instability follows the standard λ=3.7H relationship as was observed previously[21,24-26] with the higher modulus (~ 1 MPa) elastomers. The line joining the data seems to intersect the ordinate axis at a finite value $(0.27 \pm 0.07\,\text{mm})$, which may tempt one to consider that this intercept is directly related to γ / μ . However, for such an interpretation to be valid, the shear modulus of the soft gel has to be about 240 Pa considering that the surface tension of the gel is similar to that of water. This value is considerably greater than that (*ca* 40 Pa) obtained from direct measurements of shear modulus as discussed above. Thus other explanations are sought, in which the effects of the finite compressibility of the film and the elasto-capillarity are explicitly considered.

2.4. Discussions

2.4.1. Interpretation of the Elasto-capillary Instability

In what follows, we carry out a linear stability analysis of the interface using a relationship between the vertical displacement $w(x)$ of an incompressible elastic layer and the surface normal stress $\sigma(x)$. This relationship between stress and displacement was originally developed by Kerr[48] and later used by Ru[49] to study pattern formation in thin elastic films. Ru[49] showed that such an analysis yields the same result as that of a more formal approach used by Shenoy and Sharma[23] in their studies of the adhesion induced elastic instability. Here we adopt the method of Ru[49], which is easy to use and amenable to the study of the effect of Poisson's ratio in a straightforward manner. While we follow here the lead of Ru[49], there is a technical difference between the method used here and that used by him as well by others[21-23]. In the previous analyses, it was assumed that a long range attractive force (such as a van der Waals force) triggers the instability as the contactor is brought in close vicinity to the soft film much like what was pointed out earlier by Attard and Parker[50]. In our experiment, the gel is already in contact with the substrate and the instability is caused by an external force in the post bonded state. As the long range van der Waals and other interactive forces act in the cohesive zones of detached regions, it is convenient to include the effect of these forces in the work of adhesion (W_a). The observed instability is due to the lowering of the potential energy of the system by an external load at the expense of the transverse and longitudinal shear deformations as well as surface undulation.

For a frictionless interface between the gel and the upper substrate, and with a perfect bonding between the film and the lower substrate, Kerr's equation[48,49] takes the following form:

$$w + A_1 H^2 D^2 w + A_2 H^4 D^4 w + A_3 H^6 D^6 w + A_4 H^8 D^8 w$$

$$= B_1 \frac{H}{E}\sigma + B_2 \frac{H^3}{E}D^2\sigma + B_3 \frac{H^5}{E}D^4\sigma + B_4 \frac{H^7}{E}D^6\sigma \qquad (2.3)$$

Where $w = w(x)$ is the normal displacement, $E = 2\mu(1+\nu)$ is the Young's modulus, ν is the Poisson's ratio, $\sigma = \sigma(x)$ is the normal stress, and D^n represents n^{th} derivative with respect to x. All the coefficients (A_i, B_i) are functions of the Poisson ratio (ν) as follows:

$$A_1 = -\frac{1}{1-\nu}, A_2 = \frac{(3-4\nu)}{12(1-\nu)^2}, A_3 = -\frac{(3-4\nu)}{90(1-\nu)^2}, A_4 = \frac{(3-4\nu)}{1260(1-\nu)^2},$$

$$B_1 = \frac{(1+\nu)(1-2\nu)}{1-\nu}, B_2 = -\frac{(1+\nu)(3-4\nu)}{3(1-\nu)}, B_3 = \frac{(1+\nu)(3-4\nu)}{15(1-\nu)},$$

$$B_4 = -\frac{2(1+\nu)(3-4\nu)}{315(1-\nu)} \qquad (2.4)$$

Equation 2.3 can be easily solved for a periodic undulation of the surface ($w = w_o \sin kx$) and the corresponding surface stress as $\sigma = \sigma_o + Mw_o \sin kx$, where M is the stiffness of the film that is determined upon the substitution of perturbed forms of w and σ in equation 2.3 (see also figure 2.6a). While a closed form relationship[49] can be given for M in terms of E, H and k, numerical analysis shows that MH/E follows a power law relationship with kH in the long wave limit (i.e. $kH \leq 1$). For an incompressible film we have an expression for M as follows:

$$M = \frac{E}{H}\left[\frac{1.74}{(kH)^{1.78}}\right] \qquad (2.5)$$

The sum of the surface (U_S) and the elastic (U_E) energies of the film can now be written down for a 2d deformation as follows:

$$U_S + U_E = \frac{\gamma L_1}{2}\left[\int_0^{L_2}\left(\frac{\partial w}{\partial x}\right)^2 dx\right] + L_1\int_0^{L_2}\int_0^{w_o}\sigma dw dx \qquad (2.6)$$

where L_1 and L_2 are the lateral dimensions of the film as shown in figure 2.6a. Using the periodic perturbations of the surface ($w_o\sin kx$) and stress ($\sigma_o + Mw_o\sin kx$) states, the energy per unit area can be expressed as:

$$\frac{U_S + U_E}{L_1 L_2} = \frac{w_o^2}{4}\left(\gamma k^2 + M\right) \qquad (2.7)$$

In order to carry out the energy analysis of the deformed film, we consider that a constant load is applied on the upper surface so that the system undergoes a net change in the potential energy per unit area as $-\sigma_o w_o$. There is also a decrease of the adhesion energy and a corresponding increase of the elastic and surface energies. Total change of energy per unit area can thus be expressed as

$$\overline{U} = (U_P + U_S + U_E + U_a)/A = -\sigma_o w_o + \frac{w_o^2}{4}\left(\gamma k^2 + M\right) - \phi W_a \qquad (2.8)$$

Where, ϕ is the fraction of the surface that is detached. At equilibrium, $\partial\overline{U}/\partial w_o = 0$; we thus obtain an expression for $\overline{U}$ in terms of the applied stress as:

$$\overline{U} = -\frac{\sigma_o^2}{\left(\gamma k^2 + M\right)} - \phi W_a \qquad (2.9)$$

The tendency of the system is to be maximally compliant via interfacial instability, so that the confined film can undergo maximum amount of vertical deflection under a given applied stress. $\overline{U}$ achieves its minimum value when $\gamma k^2 + M$ is minimal with respect to λ, which leads to an expression for the wavelength of the instability as:

49

$\lambda \approx 4.2H(\gamma / \mu H)^{0.27}$ for an incompressible film ($\nu = 0.5$). This result is consistent with

the prediction of our previous scaling analysis ($\lambda \sim H^{3/4}$) and is almost identical to the

result [$\lambda \approx 2\pi H(\gamma / 3\mu H)^{1/4}$] obtained by Gonuguntla et al[28] in which instability occurs

due to attractive forces during the pre-bonding process. This relationship can also be

written as $\lambda = 4.2H / ECa^{0.27}$ where $ECa = \mu H / \gamma$ is the elasto-capillary number that

contrasts the expression $\lambda = \pi H / Ca^{0.5}$ applicable for the classical Saffman-Taylor

instability[51,52] where Ca is the classical capillary number. The above relationship

clearly departs from the conventional $\lambda = 3.7H$ relationship observed [24-27] previously

with less compliant films. While we show below that the experimental results of pattern

formation are due to elasto-capillarity, it is tempting to inspect how far this result can

be explained by considering a small but finite dilation of the film that favors a long

wavelength instability on its own. Calculations with $\gamma = 0$ show that the Poisson's ratio

has to be in the range of 0.3 so that an instability pattern develops with its wavelength

somewhat comparable to experiments. However, the predicted relationship between

wavelength and thickness, i.e. $\lambda = 7H$, passes through the origin (0,0) that is markedly

different from the experimental observations (figure 4c).

A variation of the experiment summarized in figure 2.1 allows measurements

of the frequencies of the vibration of a thin gel slab confined between two parallel plates

in both the normal[c] ($\omega_\perp$) and shear ($\omega_=$) modes. The ratio of these two modes are

---

[c] We note that the value for the normal mode ($\omega_\perp$) reported here, i.e, 31.25 Hz is probably due to signal amplification during FFT analysis and not a true reflection of the normal mode. An experimentally measured value for the Poisson's ratio ($\nu = 0.457$) reported in[62] [Takigawa, T.; Morino, Y.; Urayama, K.; Masuda, T. Poisson's ratio of polyacrylamide (PAAm) gels. *Polymer Gels and Networks* **1996**, *4*(1), 1-5.] supports the analysis carried on further in the paper.

related to the Poisson's ratio as $(\omega_{\perp}/\omega_{=})^2 = 2(1+\nu)$. With the measured values of $\omega_{\perp}$

and $\omega_{=}$ as 31.25 Hz and 18.31 Hz respectively for a sample of dimensions (57 mm x 25

mm x 1 mm), ν is estimated to be about 0.46, which asserts that it is futile to try to

explain the experimentally observed long wavelength instability on the basis of a rather

low (0.3) Poisson's ratio. The issue of estimating the magnitude of the Poisson's effect

in a poro-elastic film by vibration is, however, somewhat complicated. When the gel

attempts to dilate, its Poisson's ratio should be close to that (~0.5) of water if no free

water is available to invade the network. On the other hand, during the compression

phase, as the network can deform by squeezing out some water, its apparent Poisson's

ratio can be smaller than 0.5.
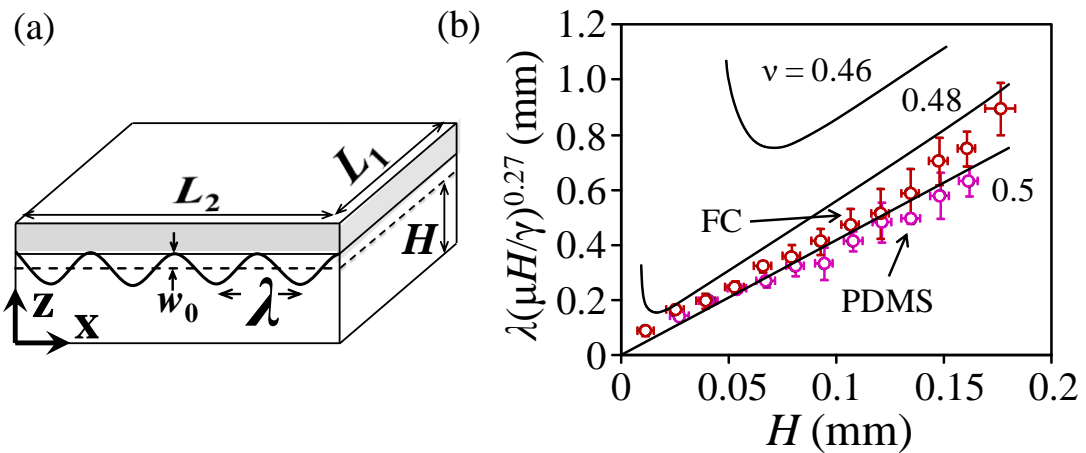
Figure 2.6: (a) Schematics of the geometry used to carry out the linear stability calculation. (b) Calculated values (lines) of the wavelengths are compared with experiments (filled symbols). The red circles represent the data obtained with the peeling of a fluorocarbon silane treated glass from the PAM hydrogel, whereas the pink circles represent the data obtained with a PDMS coated glass peeling from a PAM hydrogel. All the wavelengths are re-scaled by multiplying it with $(\mu H/\gamma)^{0.27}$ using the value of γ as 0.073 mN/m and μ as 40 Pa. The calculations are performed with three different Poisson's rations (0.5, 0.48 and 0.46) as indicated in the inset of the figure.

A gel, however, is always in hydrostatic tension when an external load is applied during

the pattern formation experiment. As no water is available to invade the gel, its

Poisson's ratio should be very close to that (~0.5) of water with the provision that the expansion of any small air bubbles trapped in the gel could lower its Poisson's ratio than that of water. Analysis of the pattern formation experiments, itself, would therefore be a better way of finding out what kind of Poisson's ratio manifests in the gel when it is under hydrostatic tension.

Now, considering that the hydrogel is incompressible, the values of the wavelength as obtained by minimizing $\gamma k^2 + M$ are plotted in figure 2.6b as a function of H after rescaling the wavelength as $\lambda(\mu H / \gamma)^{0.27}$. The data obtained with both the FC and PDMS coated glass slides cluster around this theoretical line corresponding to $\nu = 0.5$ with their intercepts on the ordinate axes being 0.016 ± 0.044 and 0.041 ± 0.032 respectively at a confidence limit of 95%. The significant error bands associated with the estimates of these intercepts prevent us from making definitive comments about the Poisson's dilation. Calculations also show that if the putative Poisson effect were present, it would have strongly influenced the wavelength of the interfacial patterns in the very thin film region. While the scaling $\lambda(\mu H / \gamma)^{0.27} \sim H$ would still be obeyed by the thicker films with a finite dilatation, the thinner films would exhibit such long wavelengths that the interface may not roughen at all below a critical thickness. The thickness of the film where this transition occurs is predicted to be inversely proportional to the Poisson's ratio, i.e. while this transition occurs at about $H = 10$ µm for $\nu = 0.48$, it occurs at about $H = 45$ µm for $\nu = 0.46$. Since the experimental instabilities are observed with H as low as 10 µm, we feel that the experimental data should be compared with the theoretical analysis performed with the Poisson's ratio being very close to 0.5.

We summarize by stating that we found convincing evidence of elasto-capillarity in adhesion induced pattern formation between a solid contactor and an ultra-soft gel film. The rescaled wavelength of instability varies fairly linearly with the film thickness, which is in good agreement with the theoretical analysis. Some differences in the morphological patterns of the instability are observed with the FC and the PDMS coated surfaces, which may arise due to some well-known differences[53] in hysteresis, adhesion, and friction of these surfaces. In other words, the slip boundary condition that is intrinsic in equation 2.3 may be different for the FC and PDMS surfaces.

2.4.2. Elasto-capillarity in Adhesive Fracture

Understanding the nature of elasto-capillary instability is also important in estimating the adhesive fracture stress (σ^*) of a flat ended rigid indenter from a thin confined film of thickness H. The subject has its origin in the classic work of Kendall[54], who laid down the foundation for such an analysis by proposing that the adhesive fracture stress of a very thin film undergoing volume dilation is $\sigma^* \sim \left(K_b W_a / H\right)^{0.5}$, where K_b is the bulk modulus and W_a is the work of adhesion. Later it was argued in the literature[25-27,55,56] that a thin film can bypass the above mode of interfacial separation in different ways, one being the elastic instability[25-27]. In such a case, Kendall's equation assumes a form: $\sigma^* \sim \left(\mu W_a / H\right)^{0.5}$ where the bulk modulus K_b is replaced by the shear modulus μ. This would be the case for a large elastocapillary number, i.e. $\mu H \gg \gamma$. However, when μH is comparable to or less than γ, certain non-trivial regimes may appear as follows.

In order to develop the premise for this discussion, we express k and M in terms of the wavelength of the instability λ so as to obtain the scaled total energy ($U = \overline{U}A$) of the system (eq. 9) as follows:

$$U \sim -\frac{F^2 \lambda^2}{\gamma A} - W_a A \qquad (2.10)$$

Where, F is the applied force, which is kept constant during the fracture process. With an expression for λ as $\lambda \sim (\gamma H^3 / \mu)^{1/4}$, the pull-off stress is given by the instability conditions: $\partial U / \partial A)_F = 0$ and $\partial^2 U / \partial A^2 < 0$, which lead to eq. 11.

$$\sigma^* \sim \left(\frac{\gamma W_a^2 \mu}{H^3}\right)^{\frac{1}{4}} \quad \text{or} \quad \sigma^* \sim \left(\frac{\gamma}{\mu H}\right)^{0.25} \left(\frac{W_a \mu}{H}\right)^{0.5} \qquad (2.11)$$

We thus have a situation where the adhesive stress depends more strongly on the thickness of a film than the usual case [$\sigma^* \sim (W_a \mu / H)^{0.5}$] of an elastic instability driven crack formation and the subsequent rupture of the contact. A non-trivial case may manifest with a very thin film, in which the surface tension no longer allows auto-roughening of the surface of a dilatable film (i.e. $\nu < 0.5$). The critical stress to fracture could then depend on the bulk modulus (K_b) as $\sigma^* \sim (W_a K_b / H)^{0.5}$, which is the classic equation proposed by Kendall[54] over forty years ago. Many practical soft adhesives however are viscoelastic[57] and thus additional improvisations would be needed. Further research needs to be carried out to verify these predictions with ultra-soft and/or ultra-thin elastic adhesives sandwiched between rigid places, which may be important in the construction of an appropriate phase diagram for thin film adhesion. These results may also be relevant in tribological settings involving soft materials for which there are suggestions[58] and ample evidences[59] of the roles played by the interfacial instabilities.
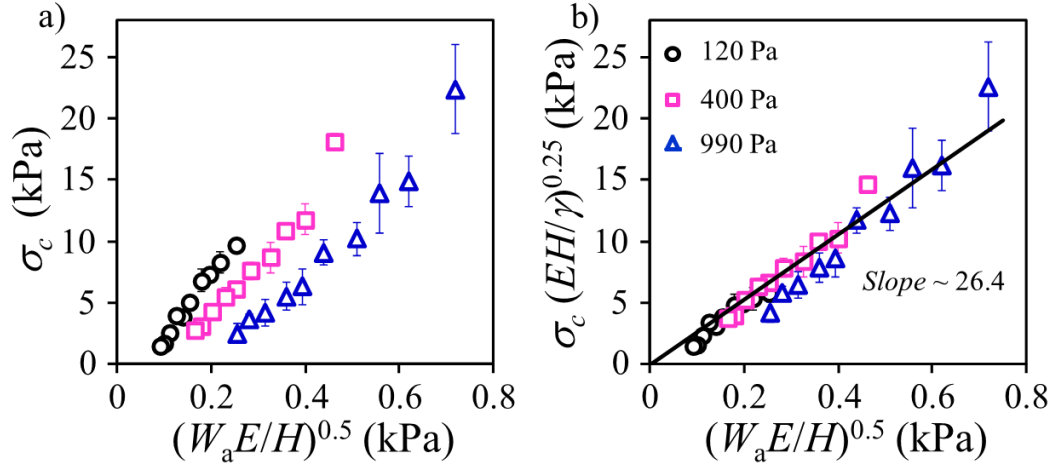
Figure 2.7: (a) The normal stress to debond a silanized circular rigid glass disc (12.8 mm diameter) from hydrogel films of different thickness and modulus are plotted against $(W_a E/H)^{0.5}$. (b) The data of figure A cluster around a single line when the stress is multiplied by $(EH/\gamma)^{0.25}$. These experiments were performed with Chih Hsiu Lin.

While the measured[60] pull-off stress of a rigid stud from the hydrogel films of different shear moduli and thicknesses show that the data conform to the scaling relationship shown in equation 2.11 (Figure 2.7), the slope of the plot $\sigma_c(EH/\gamma)^{0.25}$ versus $(W_a E/H)^{0.5}$ is substantially greater than unity. While we do not have a definite explanation for this result, we speculate on certain factors that might be considered in future for an amicable explanation of the discrepancy. One obvious consideration behind the high stress observed with a hydrogel gel is that there may be an underlying viscoelastic amplification of the Griffith's stress that has not been taken into account. However, as the hydrogel films, in our experiments, are very thin, it may not allow sufficient dissipation of energy for the viscoelastic amplification to be effective. In fact, by varying the pull-off speed over a factor of thousand led to an increase of the pull-off stress by only a factor of 2 to 3 with the soft hydrogel film, which is insufficient to explain the observed discrepancy.

Fracture, however, is fundamentally a non-equilibrium process that may not be described by the instability modes obtained from an energy minimization process. Here, the role of viscosity may just be to delay the decay of the non-principal modes. A more realistic situation would, however, be to develop a criterion that would impart an appropriate weightage to a specific mode, from which a reliable estimate of the fracture stress can be obtained.

2.5. Conclusions

The conclusions of this work are as follows:

1. Direct measurements of the surface tension and the elastic modulus led to the prediction of a rather large and macroscopically realizable elasto-capillary length in a soft elastic hydrogel.

2. Experimental and theoretical analysis corroborate that the long wave instability observed in a soft elastic film is the consequence of a large elasto-capillary length with some non-trivial effects arising from the Poisson's dilation.

3. It is further proposed that a long wavelength instability can affect the mode of fracture as well as the adhesive strength of a soft adhesive confined between two rigid substrates in non-trivial ways.

A. Scaling Analysis of Elasto-Capillary Instability

Here we show a scaling analysis[25,26] to obtain an expression for the spatial wavelength of the elasto-capillary instability. We begin by writing the sum of the elastic and surface energies (per unit area basis) in terms of the horizontal (u) and the vertical (w) displacements as follows:

$$\overline{U} \sim \mu H \left[\left(\frac{\partial u}{\partial z} \right) + \left(\frac{\partial w}{\partial x} \right) \right]^2 + \gamma \left(\frac{\partial w}{\partial x} \right)^2, \tag{2.12}$$

We wish to reduce equation 2.12 at the scaling level by choosing the characteristic length scales in the horizontal and vertical directions as the spatial wavelength (λ) and the thickness of the film (H) respectively. Now, taking the amplitude of the perturbation as w_o, we have $\partial u / \partial z \sim u / H$ and $\partial w / \partial x \sim w_o / \lambda$. The maximum horizontal displacement scales along the x direction can be obtained from the equation of continuity $(\partial u / \partial x + \partial w / \partial z = 0)$ or $u / \lambda \sim w_o / H$, which leads to $u \sim w_o \lambda / H$. Equation 2.12 can now be written at the scaling level as $\overline{U} \sim \mu H w_o^2 \left(\lambda / H^2 + 1 / \lambda \right)^2 + \gamma w_0^2 / \lambda^2$. Minimization of $\overline{U}$ with respect to λ yields the desired relation: $\lambda \sim H (1 + \gamma / \mu H)^{1/4}$.

References

(1)   Lester, G.R. Contact Angles of Liquids at Deformable Solid Surfaces. *J. of Colloid Sci.* **1961**, *16*, 315-326.

(2)   Rusanov, A. I. Theory of the Wetting of Elastically Deformed Bodies. 1. Deformation with a finite contact-angle. *Colloid J. USSR* **1975**, *37*, 614-622.

(3)   Shanahan, M. E. R.; de Gennes, P. G. Equilibrium of the triple line solid/liquid/fluid of a sessile drop. *Adhesion* **1987** (ed. Allen, K. W.), Elsevier Appl. Sci., London, *11*, 71–81.

(4)   Extrand, C. W.; Kumagai, Y. Contact Angles and Hysteresis on Soft Surfaces *J. Colloid Interface Sci.* **1996**, *184*, 191-200.

(5)   Jerison, E. R.; Xu, Y.; Wilen, L. A.; Dufresne, E. R. Deformation of an Elastic Substrate by a Three-Phase Contact Line. *Phys. Rev. Lett.* **2011**, *106*, 186103.

(6)   Style, R. W.; Che, Y.; Wettlaufer, J. S.; Wilen, L. A.; Dufresne, E. R. Universal Deformation of Soft Substrates Near a Contact Line and the Direct Measurement of Solid Surface Stresses. *Phys. Rev. Lett.* **2013**, *110*, 066103.

(7)   Yu, Y.-S. Substrate Elastic Deformation Due to Vertical Component of Liquid-Vapor Interfacial Tension. *Appl. Math. Mech.* -Engl. Ed. **2012**, *33*(9), 1095-1114.

(8)   Marchand, A.; Weijs, J.H.; Snoeijer, J.H.; Andreotti, B. Why is Surface Tension a Force Parallel to the Interface? *Am. J. Phys.* **2011**, *79*, 999-1008.

(9)   Roman, B.; Bico, J. Elasto-capillarity: deforming an elastic structure with a liquid droplet. *J. Phys.: Condens. Matter* **2010**, *22,* 493101.

(10)   Py, C.; Bastien, R.; Bico, J.; Roman, B.; and Boudaoud, A. 3D aggregation of wet fibers. *Europhys. Lett.* **2007**, *77(4)*, 44005.

(11)   Bico, J.; Roman, B.; Moulin, L.; Boudaoud, A. Elastocapillary Coalescence in Wet Hair. *Nature* **2004**, *432*, 690.

(12)   Cohen, A. E.; Mahadevan, L. Kinks, rings, and rackets in filamentous structures. *Proc. Natl. Acad. Sci. U.S.A.* **2003**, *100*, 12141-12146.

(13)   Zimberlin, J. A.; Sanabria-DeLong, N.; Tew, G. N.; Crosby, A. J. Cavitation Rheology for Soft Materials. *Soft Matter* **2007**, *3*, 763-767.

(14)   Zimberlin, J. A.; Crosby, A. J. Water Cavitation of Hydrogels. *J. Polym. Sci. B Polym. Phys.* **2010**, *48*, 1423-1427.

(15)   Majumder, A.; Tiwari, A. K.; Korada, K.; Ghatak, A. Microchannel induced surface bulging of soft elastomeric layer. *J. Adhes. Sci. Technol.* **2010**, *24*, 2681– 2692.

(16)   Jagota, A.; Paretkar, D.; Ghatak, A. Surface-tension-induced flattening of a nearly plane elastic solid. *Phys. Rev. E* **2012**, *85*, 051602.

(17) Mora, S.; Phou, T.; Fromental, J. M.; Pismen, L. M.; Pomeau, Y. Capillarity Driven Instability of a Soft Solid. *Phys. Rev. Lett.* **2010**,*105*, 214301.

(18) Chen, D.; Cai, S.; Suo, Z.; Hayward, R. C. Surface Energy as a Barrier to Creasing of Elastomer Films: An Elastic Analogy to Classical Nucleation. *Phys. Rev. Lett.* **2012**, *109*, 038001.

(19) Johnson, K.L.; Kendall, K.; Roberts, A. D. Surface Energy and the Contact of Elastic Solids. *Proc. R. Soc. London A.* **1971**, *324*, 301-313.

(20) Haidara, H.; Chaudhury, M. K.; Owen, M. J. A Direct Method of Studying Adsorption of a Surfactant at Solid-Liquid Interfaces. J. Phys. Chem. **1995**, *99*, 8681-8683.

(21) Ghatak, A.; Chaudhury, M. K.; Shenoy, V.; Sharma, A. Meniscus Instability in a Thin Elastic Film. *Phys. Rev. Lett.* **2000**, *85*, 4329-4332.

(22) Mönch, W.; Herminghaus, S. Elastic Instability of Rubber Films between Solid Bodies. *Europhys. Lett.* **2001**, *53*(4), 525-531.

(23) Shenoy, V.; Sharma, A. Pattern Formation in a Thin Solid Film with Interactions. *Phys. Rev. Lett.* **2001**, *89*, 119-122.

(24) Ghatak, A.; Chaudhury, M. K. Adhesion-Induced Instability Patterns in Thin Confined Elastic Film. *Langmuir* **2003**, *19*, 2621-2631.

(25) Chung, J.Y.; Chaudhury, M. K. Soft and Hard Adhesion. *J. Adhesion* **2005**, *81*, 1119-1145.

(26) Chung, J. Y.; Chaudhury, M. K. Roles of Discontinuities in Bio-Inspired Adhesive Pads. *J. R. Soc. Interface* **2005**, *2*, 55-61.

(27) Sarkar, J.; Shenoy, V.; Sharma, A. Spontaneous Surface Roughening induced by Surface Interactions between two Compressible Elastic Films. *Phys. Rev. E* **2003**, 67, 031607.

(28) Gonuguntla, M.; Sharma, A.; Sarkar, J.; Subramanian, S. A.; Ghosh, M.; Shenoy, V. Contact Instability in Adhesion and Debonding of Thin Elastic Films. *Phys. Rev. Lett.* **2006**, *97*, 018303.

(29) Hecht, A. M.; Duplessix, R.; Geissler, E. Structural Inhomogeneities in the Range 2.5-2500 Å in Polyacrylamide Gels. *Macromolecules* **1985**, *18*, 2167-2173.

(30) Davis, B. J. Disc Electrophoresis-II, *Ann. N.Y. Acad. Sci.*, **1964**, *121*, 404-427.

(31) Zhang, J.; Fang, Y.; Hou, J. Y.; Ren, H. J.; Jiang, R.; Roos, P.; Dovichi, N. J. Use of Non-Cross-Linked Polyacrylamide for Four-Color DNA Sequencing by Capillary Electrophoresis Separation of Fragments up to 640 Bases in Length in Two Hours. *Anal.Chem.***1995,** *67* (24), 4589-4593.

(32) Hoffman, A. S. Hydrogels for Biomedical Applications. *Adv. Drug Delivery Rev.* **2002**, *54* (1), 3-12.

(33) Larsen, T. H.; Schultz, K. M.; Furst, E. M. Hydrogel Microrheology near the Liquid-Solid Transition. *Korea-Aust. Rheol. J.* **2008**, *20*, 165-173.

(34) Stafford, C. M.; Roskov, K. E.; Epps, T. H.; Fasolka, M. J. Generating thickness gradients of thin polymer films via flow coating. *Rev. Sci. Instrum.* **2006,** *77*, 023908.

(35) Chaudhury, M. K.; Whitesides, G. M. Direct Measurement of Interfacial Interactions between Semispherical Lenses and Flat Sheets of Poly(dimethylsiloxane) and Their Chemical Derivatives. *Langmuir* **1991**, *7*, 1013-1025.

(36) Krumpfer, J. W.; McCarthy, T. J. Contact Angle Hysteresis: A Different View and a Trivial Recipe for Low Hysteresis Hydrophobic Surfaces. *Faraday Discuss.* **2010**, *146*, 103-111.

(37) Goohpattader, P. S.; Chaudhury, M. K. Diffusive Motion with Nonlinear Friction: Apparently Brownian. *J. Chem. Phys.* **2010**, *133*, 024702.

(38) Goohpattader, P. S.; Mettu, S.; Chaudhury, M. K. Stochastic Rolling of a Rigid Sphere in Weak Adhesive Contact with a Soft Substrate *Eur. Phys. J. E* **2011**, *34*, 120.

(39) Lamb, H. Hydrodynamics; Cambridge University Press: Cambridge, UK, **1932**.

(40) Chandrasekhar, S. The Oscillations of a Viscous Liquid Globe. *Proc. London Math. Soc.* **1959**, *9*, 141-149.

(41) Strani, M.; Sabetta, F. Free Vibrations of a Drop in Partial Contact with a Solid Support *J. Fluid Mech.* **1984**, *141*, 233-247.

(42) Noblin, X.; Buguin, A.; Brochard, F. Vibrations of Sessile Drops. *Eur. Phys. J. Special Topics* **2009**, *166*, 7-10.

(43) McGuiggan, P. M.; Daniel, A. G.; Wallace, J. S.; Cheng, S.; Prosperetti, A.; Robbins, M. O. Dynamics of a Disturbed Sessile Drop Measured by Atomic Force Microscopy. *Langmuir* **2011**, *27*, 11966- 11972.

(44) Lyubimov, D. V.; Lyubimova, T. P.; Shklyaev, S. V. Behavior of a Drop on an Oscillating Solid Plate *Phys. Fluids* **2006**, 18, 012101.

(45) Mettu, S.; Chaudhury, M. K. Vibration Spectroscopy of a Sessile Drop and Its Contact Line. *Langmuir* **2012**, *28*, 14100-14106.

(46) McDaniel, J. G.; Holt, R. G. Measurement of Aqueous Foam Rheology by Acoustic Levitation. *Phys. Rev. E* **2000**, *61*, 2204-2207.

(47) A complete solution to the problem would involve a method of calculating stress of a rigid beam on a soft foundation similar to that of Dillard (Dillard, D. A. Bending of plates on thin elastomeric foundations. *J. Appl. Mech.* **1989**, *56*, 382-386) with the provision of allowing the thickness of the foundation to vary continuously. Although such an analysis is reserved for future, the observation that the film exhibited instability patterns all throughout the contact area suggests that the entire film is hydrostatically stressed.

(48) *Kerr*, *A. D.* On the Formal Development of Elastic Foundation Models. *Ingenieur-Archiv.* **1984,** *54*, 455- 464.

(49) Ru, C. Q. Surface Wrinkling of two Mutually Attracting Elastic Thin Films due to van der Waals Forces. *J. Appl. Phys.* **2001**, *90* (12), 6098-6104.

(50) Attard, P; Parker, J.L. Deformation and adhesion of elastic bodies in contact. *Phys. Rev. A* **1992**, *46*, 7959-7971.

(51) Saffman, P. G.; Taylor, G. The Penetration of a Fluid into a Porous Medium or Hele-Shaw cell containing a more Viscous Liquid. *Proc. R. Soc. London A.* **1958**, *245*, 312-329.

(52) Brown (Brown, H. R. Rayleigh-Taylor Instability in a Finite Thickness Layer of a Viscous Fluid. *Phys. Fluids A*, **1989**, *1*, 895-896) provided a general equation for the surface tension driven interfacial instability: $\lambda \sim (\gamma / \dot{\sigma})^{0.5}$, where $\dot{\sigma}$ is the gradient of the applied stress. This form is suitable for studying the auto-roughening of hydrostatically stressed viscous films.

(53) Newby, B.-M. Z.; Chaudhury, M. K.; Brown, H. R. Macroscopic Evidence of the Effect of Interfacial Slippage on Adhesion. *Science* **1995**, *269*, 1407-1409.

(54) Kendall, K. The Adhesion and Surface Energy of Elastic Solids. *J. Phys. D: Appl. Phys*. **1971,** *4*, 1186-1195.

(55) Yang, F.; Li, J. C. M. Adhesion of a Rigid Punch to an Incompressible Elastic Film. *Langmuir*, **2001**, *17* (21), 6524-6529.

(56) Mowery, C. L.; Crosby, A. J.; Ahn, D.; Shull, K. R. Adhesion of Thermally Reversible Gels to Solid Surfaces. *Langmuir*, **1997**, *13* (23), 6101-6107.

(57) Nase, J.; Lindner, A.; Creton, C. Pattern Formation during Deformation of a Confined Viscoelastic Layer: From a Viscous Liquid to a Soft Elastic Solid. *Phys. Rev. Lett.*, **2008**, *101* (7), 074503.

(58) Persson, B. N. J. Elastic instabilities at a sliding interface. *Phys. Rev. B*, **2001**, *63*, 104101.

(59) Chaudhury, M. K.; Kim, K. H. Shear-induced adhesive failure of a rigid slab in contact with a thin confined film. *Eur. Phys. J. E.*, **2007**, *23*, 175-183.

(60) Chaudhury, M. K., Chakrabarti, A. and Ghatak, A. Adhesion-induced instabilities and pattern formation in thin films of elastomers and gels. *Eur. Phys. J. E*. **2015**, 38(7), 1-26.

Chapter 3

Vibrations of Sessile Drops of Soft Hydrogels[a]

3.1. Introduction.

In recent years, estimation of the surface tension and the elasticity of soft gels has become the subject of considerable interests[1,2]. Starting with the pioneering study of Harden, Pleiner and Pincus (HPP)[3], several studies have focused on identifying the capillary and the elastic modes of vibration of either a half space or a thin film of the gel in terms of the various wave vectors that its free surface displays[4-7]. There is also a long history of studying the vibration modes of the surface of spherical liquid drops[8-17]. These studies start with the original prediction of Rayleigh[8,9], which shows that the spherical harmonics of the capillary oscillations of an incompressible liquid drop surrounded by a rarified medium, are given as follows:

$$\omega_l = \sqrt{l(l-1)(l+2)\frac{\gamma}{\rho R^3}} \qquad (3.1)$$

Where, ω_l is the resonant frequency, l (=2,3,4…) is the eigen-mode of the oscillation, R is its undeformed radius; γ and ρ are its surface tension and density respectively. For the case of a sessile drop, several authors have modified Rayleigh's equation with appropriate slip and no-slip boundary conditions at the three phase contact line[10-14].

Nevertheless, the basic scaling relation $\omega_l \sim R^{-3/2}$ has been found to be preserved in all the subsequent modifications of Rayleigh's equation.

One advantage of studying the spherical harmonics of a sessile liquid or gel drop is that the wave number of the surface vibration is uniquely determined by its perimeter. In that spirit, we recently studied[2] the surface vibration of a soft (shear modulus, 40 Pa) hemispherical gel preformed on a flat substrate and found that the variation of its resonance mode as a function of its volume is very similar to that of pure hemispherical drop of water[15]. Based on these previous results, here we venture to investigate how these modes depend on the elasticity of the gel with a wide variation of its mass.

The frequency of vibration of the soft gel sphere depends upon its inertia and the restoring force it experiences due to the change in the energy of adhesion resulting from the motion of contact line (dE_{adh}), and that due to the change in surface (dE_s) and the elastic (dE_e) energies:

$$dE \sim dE_{adh} + dE_s + dE_e \qquad (3.2)$$

dE_{adh} is negligible if the three phase contact line is sufficiently pinned, which happens to be the case with the experiments to be presented below. Let the initial free surface area of the gel sphere in contact with the substrate (contact angle θ) be $S_0 = R^2 f(\theta)$. For a small perturbation of the surface area ΔS corresponding to a displacement of the center of mass of the drop as δy, $dE_s \approx \gamma \Delta S = \gamma \psi_1(\theta)(\delta y)^2$. Variation of this energy with respect to δy yields a restoring force $F_s \sim \gamma \psi_1(\theta)\delta y$ and a corresponding spring constant: $k_s = \gamma \psi_1(\theta)$. The restoring force due to elastic deformation is (dimensionally) expected to be of the Hertzian form: $F_e \sim \mu \sqrt{R}(\delta y)^{3/2}$ with $\delta y = R g(\theta)$. With appropriate substitution, the elastic spring constant is:

$k_e = \mu R \psi_2(\theta)$. The total restoring force is obtained by adding the contributions due to surface and elastic deformations as their corresponding energies are additive. Thus, by assuming that the system is conservative, the frequency of vibration of density ρ and volume V is expected to follow the scaling relationship:

$$\omega \sim \left(\frac{\gamma \psi_1(\theta) + \mu R \psi_2(\theta)}{\rho V} \right)^{1/2} \tag{3.3}$$

A more exact equation of the elasto-capillary vibration frequency of a hemispherical drop can be derived by solving the equation of (irrotational) motion of the drop in a spherical co-ordinate in conjunction with a stress jump boundary condition comprising of the capillary and elastic contributions. This treatment would allow us to obtain the various spherical harmonic modes. For the purpose of the current study, where we focus on the spheroidal (l=2) mode, this detailed analysis is not required, which, essentially, produces the same result as that captured in equation 3.3. We, however, reserve this analysis for a detailed publication in future, where we would investigate the higher vibration modes (i.e. $l >$2). We point out here that an equation similar to equation 3.3 has been observed by various authors[1,3-6] for the case of a half space in terms of a surface wavenumber k. For example, Choi[4,5] et al derived an equation for the elasto-capillary wave velocity in a gel as $V = [(\gamma k + 4\mu)/\rho]^{0.5}$, which yields a similar scaling relation for frequency as shown in equation 3.3, when the surface wavenumber is replaced by $1/R$. In our problem, as stated above, the wave number is pinned by the perimeter of the drop. There are two extreme limits to equation 3.3. With a elasto-capillary number $\mu R / \gamma <<$1, only the capillary mode should prevail, in which case, the frequency of vibration would vary inversely as the square root of the volume of the drop. On the other hand with $\mu R / \gamma >>$ 1, the frequency of vibration would vary

66

inversely as the cubic root of the volume. Both types of scaling have indeed been reported for the cases of pure liquid drops[15] as well for solid spheres of high elastic modulus[18]. In the intermediate range a pseudo-capillary mode with an effective surface tension $\gamma + C\mu R$ (C is a numerical constant) should be in effect; however the frequency of vibration would depend on volume with an exponent lying between of -1/3 and -1/2.

The scaling relation as captured in equation 3.3, however, is valid for a conservative system. In the case with a real gel, we also have to consider the effect of surface and bulk viscous effects. One obvious consequence of viscosity is that the surface and the elastic modes may not be in phase; i.e. they may not necessarily coalesce as suggested by the simple scaling relation (3.3).

At this juncture, we should point out a couple of other reasons why a simple relation of the type shown in equation 3.3 may not be valid with a real gel. The surface tension term that appears in equation 3.3 could actually be the surface stress[19] given as $\gamma + d\gamma/d\varepsilon$, ε being the surface strain. Surface rheology may have a frequency spectrum that is different from that of the bulk deformation. Thus, not only can the surface tension of a vibrating gel be different from the thermodynamic surface excess free energy, but there may also be other non-trivial reasons for a possible phase difference between surface and bulk modes of vibration. Furthermore, both the rheological spectra could also be non-linear in frequency that may not be captured with a simple Maxwell-like viscoelastic model.

In view of the above mentioned complexities, our objectives of this study are quite modest. First, we intend to find out if the spheroidal modes of vibration could be detected for soft gel drops of different elastic moduli and how the resonance frequency

67

varies with the volume of the sphere. Secondly, we wish to find out if the observed frequency could be expressed in terms of the surface tension and the shear modulus of the gel in a simple semi-empirical form.

In order to achieve this objective, we developed a new method to produce gels of different radii, which are as spherical as possible. We then placed these gels on a hydrophobic substrate on which the gels subtend well-defined contact angles > 90°. The gels were then vibrated vertically using a mechanically induced Gaussian random noise, the power spectra of which helped us identify the resonance frequency corresponding to the l=2 mode. In the subsequent sections, we first describe the experimental method of preparing such spherical gels and the method used to identify their spheroidal modes. Followed by the experimental section, we analyze how these modes depend on the volume and shear modulus (55 Pa to 290 Pa) of the gel and show how the data can be collapsed about a single line with an appropriate scaling.

3.2. Materials and Methods

3.2.1. Measurement of Elastic Moduli of Gels

Before performing the vibration experiments with the spherical drops of the gel, we needed to estimate their shear moduli independently. The shear moduli of the different gels were determined by vibrating a thin slab of a gel in the shear mode in a confined geometry, the details of which are explained in our previous publications[2,20]. Here, we briefly describe the main idea behind such a measurement. A schematic of the experimental setup is shown in Figure 3.1a (More details can be found in Ref. 20). A thin slab of gel was cured in between two clean glass plates (Fisherbrand, top: 25mm x 75mm, 1mm; lower: 50mm x 75mm, 1mm) separated by uniform spacers. Once the gel

was cured, a steel disk was fixed to the upper glass plate of the sample. The lower plate of the sample was fixed atop a platform mounted on a vibration isolation table (Micro-g, TMC). A strong magnet was fixed at the edge of an aluminum stage, which in turn was connected to a mechanical oscillator (Pasco Scientific, Model no. SF-9324). Random white noise was generated using a waveform generator (Agilent, model 33120A) that was transferred to the mechanical oscillator and thus generating a random magnetic field. When the magnet was brought close enough to the gel sample, the thin gel slab vibrated randomly in a shear mode due to the random vibration of the steel disk attached to the upper plate. A high speed movie (Redlake Motion Pro, model no 2000, at 1000frames/s) capturing the random motion of the gel slab and its subsequent analysis in a motion tracking software (Midas 2.0, Xcitex Inc., USA) yielded the displacement fluctuations. The resonant peaks (Figure 3.1b) of the shear vibrations were identified from the power spectra of these fluctuations by averaging data taken from ten videos each had a duration of 4s. The shear modulus was estimated by using the formula $\mu = 4\pi^2 \omega^2 mH/A$, where ω is the resonant frequency, m is the mass of the glass plate and the steel disk, H is the thickness of the gel slab and A is the lateral cross-sectional area of the gel slab.
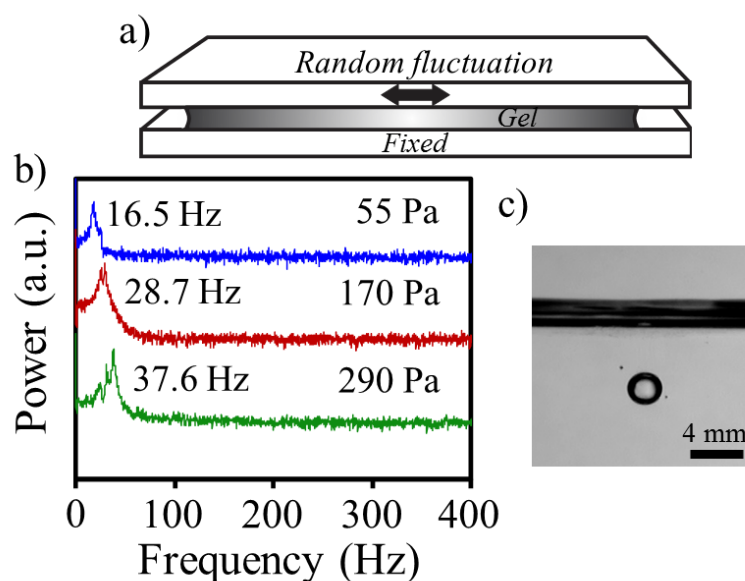
Figure 3.1: (a) Schematic of a thin gel slab (1 mm thick) sandwiched between two parallel glass plates undergoing shear vibration. (b) The resonant peaks of the shear vibration of gel as obtained from the power spectra of their random vibration (RMS fluctuation 0.03 mm). Powers are in logarithmic scale. (c) An example of a spherical gel drop of shear modulus 55 Pa; this is a snapshot of a video that was captured while the sphere sank slowly through mineral oil in a quartz cell.

3.2.2. Preparation of Gel Spheres

Highly spherical gel spheres (Figure 3.1c) were made by curing polyacrylamide gel solution drops of different volumes by suspending them in a liquid density gradient. Three different gels (55 Pa, 170 Pa and 290 Pa) were used for the study, the details for the preparation of which are described elsewhere[2,20]. The density gradient was formed in small beakers with a liquid heavier than the gel solution (PDM-7040, Gelest Inc., density 1.07 g/cc) at the bottom and a lighter liquid (n-octane, 97% pure, Acros organics, density 0.7 g/cc) on the top. After all the ingredients of the gel were mixed, different volumes of the gel solution were released gently over the top surface of the octane in the container housing the density gradient. The drops of gel solution become neutrally buoyant at the diffusing interface of the two liquids forming the density gradient. These suspended gel drops cure to form highly spherical gel drops (Figure

70

3.1c) that were subsequently washed in fresh n-heptane (Fisher Chemicals) repeatedly and dried moderately in air. The volume of gel spheres thus formed ranged from $2\mu L$ to $100\mu L$ as determined from their weights.

3.2.3.   Vibration Studies of Gel Spheres

A rectangular polystyrene cuvette was used to house each gel sphere for the vibration studies (Figure 3.2a). A small glass piece (8 mm x 8 mm, 1mm), was hydrophobized using the usual method of reacting with dodecyltrichlorosilane (Gelest Inc.) by vapor deposition technique and was fixed on one of the walls inside the polystyrene cuvette. As soon as the gel sphere was placed on the hydrophobic glass piece, the open end was sealed firmly with parafilm to avoid drying of the gel during the time the studies were carried out. Filter paper soaked with deionized water stacked inside the cuvette maintained its relative humidity to about 99.9%. The cuvette housing the sample was then fixed onto an aluminum stage that was set to vertical vibration with random white noise by the mechanical oscillator and waveform generator as described in section 2.1. The surface fluctuations of the gel drops (i.e. the height of the drop) were video recorded with a high speed camera at 1000 frames/s that were subsequently fast Fourier transformed using Origin software to yield their power spectra (Figure 3.2b). The resonant frequency for the spheroidal mode was identified from the power spectrum for each gel sphere. As we reported earlier[15], the probability distribution function of the accelerations of the stage was Gaussian that was white up to a practical bandwidth of 5 kHz. With these random accelerations (γ), the strength of the noise was estimated as, $K = \langle \gamma^2(t) \rangle \tau_c$, where $\gamma(t)$ is the value (m/s^2) of the noise pulse and τ_c is its duration (40 μs). A constant noise strength (0.1 m^2/s^3) was used to perform all the vibration studies

although we noted that the primary peak position for each spheroidal vibration mode is independent of the noise strength (Figure 3.2b). Although an effective temperature can be obtained by multiplying K with the mass of the object and its characteristic relaxation time, we refrained from doing so in this work. Here we present directly the root mean square value of the surface fluctuation to distinguish the states of the system.

The vibration modes of the gel sphere can also be obtained from their plan views. In this method, a wire mesh (opening 0.0046", wire dia 0.0026", Mc Master Carr)[21] was firmly attached to the base of the polystyrene cuvette. When viewed from above, the lateral contraction and stretching of the drop can be easily discerned from the change of the shape of the wire mesh. Fast Fourier transform of the fluctuation of the grid
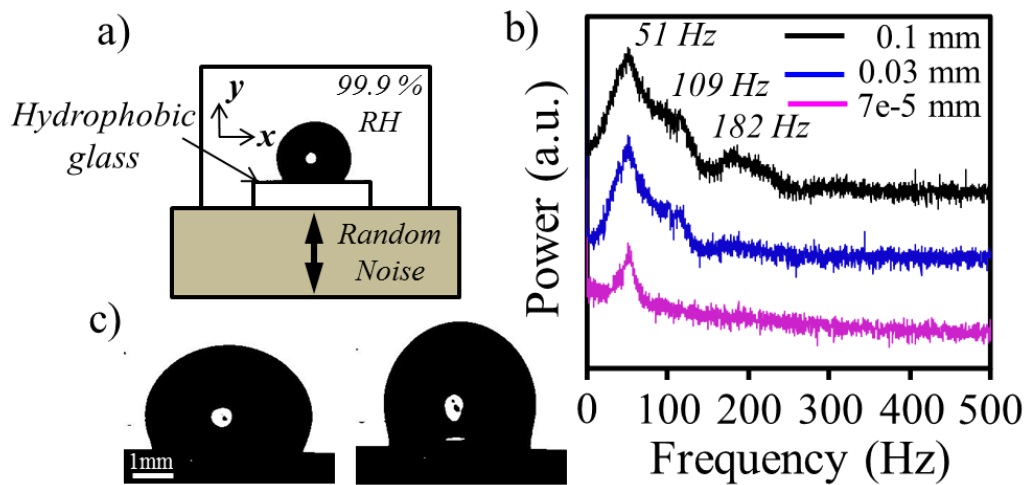
Figure 3.2: (a) Schematic of the experimental setup for studying the height fluctuation of the gel drops placed on a hydrophobic substrate after subjecting it to a random white noise. (b) The power spectra for a $38\,\mu L$ gel sphere (55 Pa) at different noise strengths, each has its resonant mode corresponding to $l=2$ at 51 Hz, their RMS fluctuation being marked in legend. (c) Two randomly selected snapshots of vibration of a $47\,\mu L$ (55 Pa) gel sphere from a high speed movie of it undergoing random fluctuation. This corresponds to a spheroidal mode of $l=2$.

obtained from the diagonal distance of two selected points allowed identification of the resonant modes (Figure 3.3), which were, essentially, same as those obtained from the

height fluctuation of the drop. In both cases, the $l=3$ and $l=4$ modes were undiscernible from the visible inspections of the random frames of the drop fluctuations, while the $l=2$ mode was very prominent. However, the presence of these higher modes was weakly evident in the FFT spectra of both the height and lateral fluctuations of the drop. For all the results presented below for detailed analysis, we use the vibration modes obtained from the height fluctuations of the drops.

3.3. Experimental Results and Discussion

The power spectrum of the height fluctuation of a gel drop ($\mu= 55$ Pa) is shown in figure 3.4, where it is compared with those of a drop of water and two different mixtures of
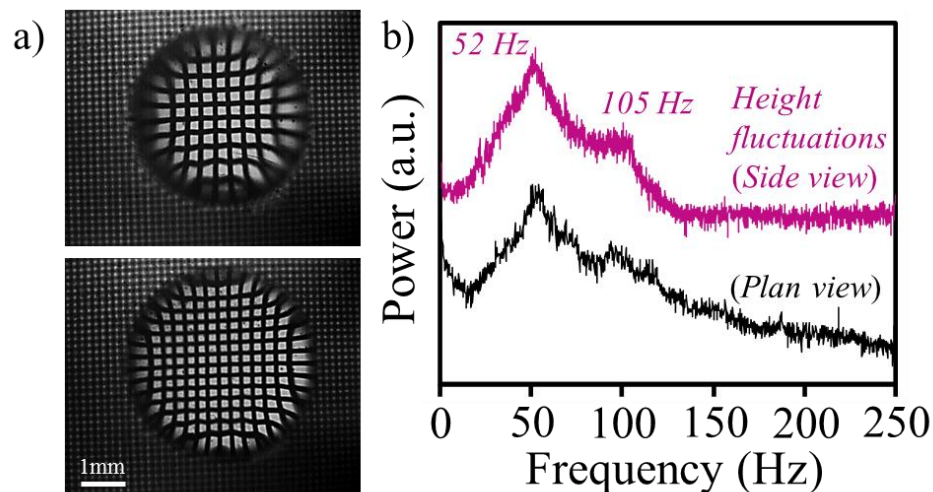
Figure 3.3: (a) Two randomly selected snapshots of the lateral vibration of a $35\,\mu$L (45 Pa) gel sphere from a high speed movie of it undergoing random fluctuation. (b) Similarity of the power spectra for a 53 μL gel sphere (45 Pa) as obtained from height and lateral fluctuations at a noise strength of 0.014 m^2/s^3.

water and glycerol, both of which have comparable surface tension and density but largely different in viscosity. From the experiments performed with the liquid drops, it is evident that the lowest mode ($l=2$) is relatively unaffected by viscosity, but the higher

modes are progressively damped with increasing viscosity. The frequency dependent damping of modes is known for a long time[9,15,16,22].

For example, Behroozi[22] proposed that this damping increases with the capillary driven eigen-frequency (ω_l) in proportion to $\left(\eta^3\omega_l/\gamma^2\rho\right)^{1/2}$. The three modes ($\omega$ = 51, 109 and 182 Hz) observed with the gel (Figure 3.2b) are close to those of water and the mixtures of water and glycerine that correspond to l=2, 3 and 4 and respectively. It is quite clear that the higher modes of the gel are rather damped by viscous relaxation, while the lowest mode (l=2) is quite pronounced. The remarkable similarity of the power spectra of height fluctuation of the PAM gel and that of water-glycerol (20:80) mixture indicates that the viscosity of the gel is, perhaps, in the range of 47 Pa.S. In this study, we focus on the resonance frequency of the spheroidal mode (l=2) of each gel drop (Figure 3.5a) as a function of its volume and shear modulus.
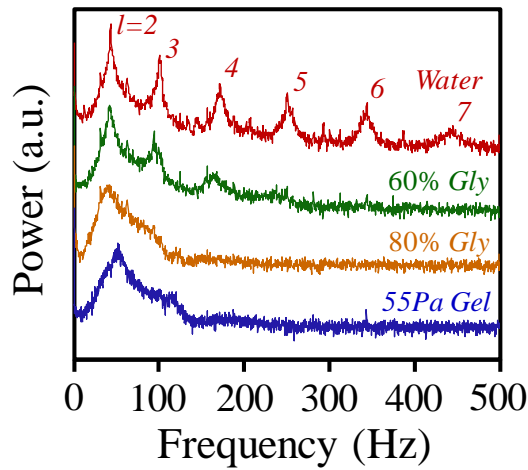
Figure 3.4: Power spectra of the height fluctuations of a 38 μL drop of pure water, 60% glycerine in water, 80% glycerine in water and polyacrylamide gel (shear modulus 55 Pa) [The power spectrum for the gel sphere plotted here is same as that shown in blue in Figure 3.2b]. The noise strength at which the stage was vibrated is 0.014 m^2/s^3.

For gels of modulus spanning by a factor of six, the resonance frequencies vary inversely with volume with an exponent close to 0.5 (figure 3.5), which are not too different from the previously published values of pure hemispherical water drops[15]. The frequencies for these gels of different moduli (Figure 3.5a) do not diverge significantly with the increase of the size of the gel sphere nor do they converge at small drop sizes. The log-log plots of these frequencies (ω) as a function of V obtained for gels of different shear moduli (55 Pa- 290 Pa) are nearly parallel to each other as shown in figure 3.5B.

These observations contrast Equation 3.3, which suggests that the resolution of the frequencies should increase with the drop volume as modulus increases and they would approach each other at small volume as the elastocapillary number decreases. In order to appreciate the discrepancy, consider a 290 Pa gel sphere of radius 1 mm. Here, the elasticity (μR) term is four times larger than surface tension (γ) with the discrepancy increasing with the size of the drop. Thus ω must decrease with volume with an exponent of V close to 1/3, not 1/2 as observed experimentally. We feel that the origin of this discrepancy is that equation 3.1 applies for hemispherical drops, which should not apply to large drops that flatten somewhat due to gravity. The exact solution of the problem starting from the elastic field equations is quite complex and require numerical methods.

Here we provide a heuristic equation that preserves the form of equation 3.1 at small radius, deviate from it for larger drops. We start with a flat slab of gel of thickness h that is vibrated perpendicular to the free surface that generates surface waves of frequency ω, and wavenumber k. Our starting point is to define a spring constant of the
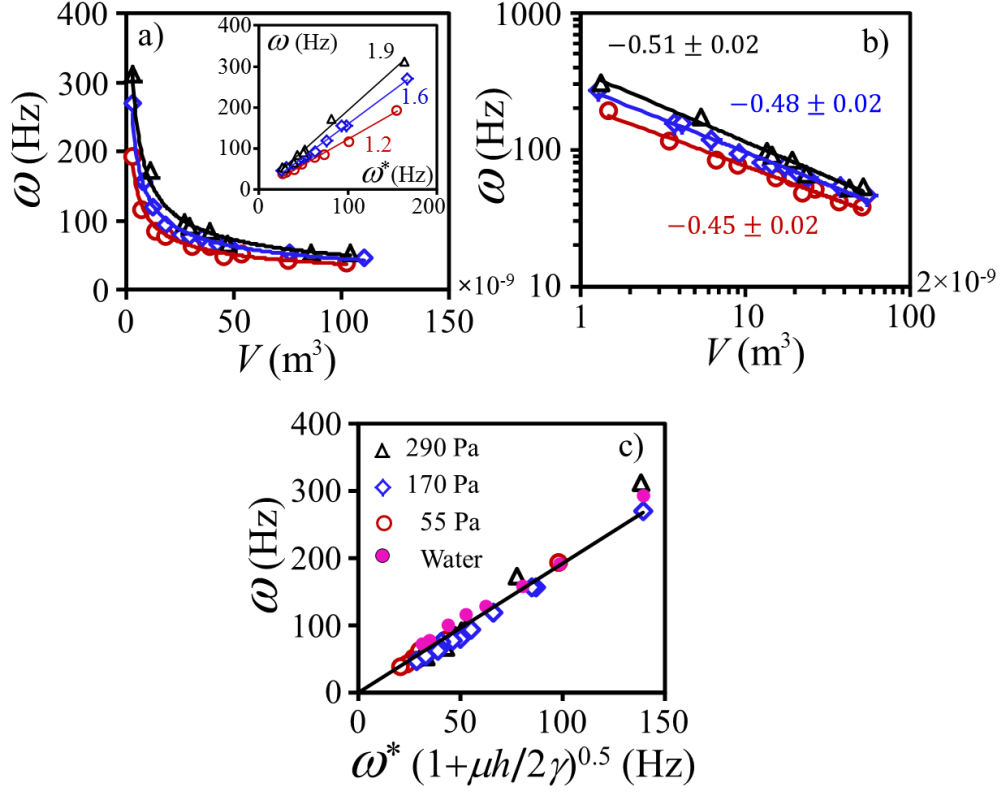
Figure 3.5: (a) Experimentally observed resonant frequencies for the spheroidal mode (*l*=2) of vibration of gel drops of different shear moduli plotted as a function of their volume. The inset shows the plots of ω versus $\sqrt{\gamma/m}$ for the three gels. (b) All the resonance frequencies are plotted as a function of the volume of the gel spheres in a log-log scale (c) The values of ω are plotted as a function of frequency $\omega^* = \sqrt{\gamma/\rho P^2 h}$ multiplied by a scale factor: $\sqrt{1+\mu h/2\gamma}$. The linear fit has a slope ~ 1.92 ± 0.04 with a regression coefficient of 0.96. This shows how the values of the resonant frequencies of equivalent water drops fall on the same line.

slab as $\gamma + \mu h$ so that its vibration frequency is expressed in terms of wavenumber k as:

$$\omega^2 \sim \left(\frac{\gamma + \mu h}{\rho h k^{-2}}\right) \qquad (3.4)$$

We now convert equation 3.4 for the case of a sphere, somewhat like what Noblin *et al*[12] did in converting an equation of vibration of a flat liquid film to that of a

hemispherical drop, by defining k to be the inverse of the perimeter (P) of the drop and thickness h to be equal to $\sqrt{V/P}$. We thus re-write equation 3.4 as:

$$\omega \sim \left(\frac{\gamma}{\rho P^2 h}\right)^{0.5} \sqrt{1 + c\mu h/\gamma} \quad \text{or} \quad \omega \sim \omega^* \sqrt{1 + c\mu h/\gamma} \tag{3.5}$$

Where c is a numerical constant to be evaluated experimentally. It is easy to show that equation 3.5 reduces to the same form as equation 3.3 for the case of hemispherical drops, for which the perimeter is proportional to the radius, but it deviates from equation 3.3 as the drop becomes flatter.

It is found that that the contact angle of the gel drop increases with its modulus: (θ =100° for 55 Pa, 115° for 170 Pa and 125° for 290 Pa). Furthermore, as stated above, the drops are not spherical for large drops. However, in order to apply equation 3.5 to our problem, we need only to know the volume of the drop (V) and its maximum arc length (P) in the rest state. The first one is estimated directly by measuring the weight of the deposited drop and the latter is estimated from the side profile of the drop using the ImageJ software.

Experimentally measured frequencies of the three gels with different volumes collapse (Figure 3.5c) nicely about a single line when they are plotted against the fundamental capillary frequency scale $(\gamma / \rho P^2 h)^{0.5}$ (estimated using the surface tension of water, 72 mN/m) shifted by $\sqrt{1 + \mu h/2\gamma}$, i.e.

$$\omega \sim \omega^* \sqrt{1 + \mu h/2\gamma} \tag{3.6}$$

Some additional remarks are in order here. Firstly, we note that the resonant mode corresponding to l=2 is rather insensitive to the strength of the noise (Figure 3.2b). This coupled with the observation that the random displacement of the surface is Gaussian

(Figure 3.6) suggest that these gels behave more or less linearly as was also observed previously with pure water drops[15].
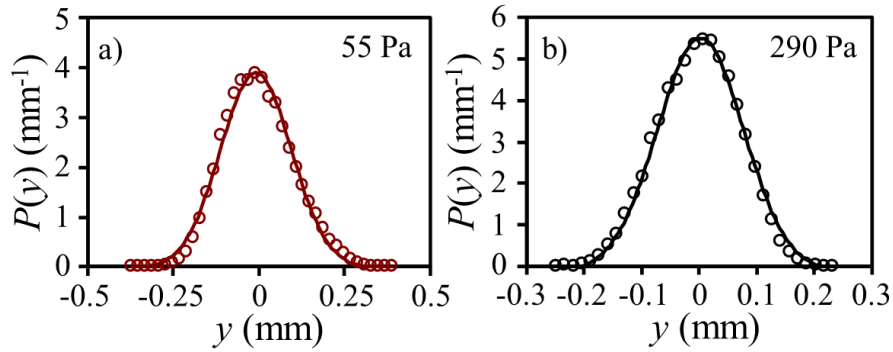
Figure 3.6: (a-b) Examples of the height fluctuations of a $38\mu L$ gel sphere of two different moduli (55 Pa and 290 Pa) following a Gaussian probability distribution. Noise strength is 0.1 m^2/s^3.

A detailed analysis of the vibration modes of the gel along the line of HPP, but in polar spherical coordinate, is critical to make further inroads to the problem. The statistical mechanical aspect of the current problem is similar as well as different from that studied by HPP in that these authors consider the roles of thermal fluctuations in which the autocorrelation of random stress is related to temperature and viscosity via usual fluctuation dissipation relation. In our problem both the thermal and an externally imposed random mechanical noises are in effect, in which the autocorrelation of random stress would depend on both thermodynamic temperature as well as the strength of the mechanical noise manifesting in terms of an "effective temperature". The Gaussian nature of the displacement fluctuations suggest that the viscous term enters in the problem linearly, which should simplify the analysis. The problem is challenging, but it also provides opportunities for new physics to be discovered as the externally imposed noise and internal friction are de-coupled, and thus the role of friction could be studied independently of noise, which is not the case with thermal systems. These

studies, when carried out in conjunction with the analysis of the vibration of a half space should also enhance the scope of these studies.

3.4. Summarizing Comments

What we presented here is a report of a preliminary experimental study, in which the spheroidal (l=2) mode of vibration of a sessile soft gel drop is studied as a function of its volume and elasticity. The resonance mode varies with volume as is the case with a liquid drop governed by capillarity, but its effective surface tension is weakly dependent on the modulus as expected of a pseudo-capillary mode. The important finding of this work is that all the resonance frequencies could be collapsed about a line obtained from a plot of ω vs $\omega^* \sqrt{1 + \mu h/2\gamma}$ using γ to be the surface tension of water (72 mN/m) and the measured elastic moduli of the gels. We have not taken into account the detailed viscoelastic properties of the gels, although the sharpness of the shear deformation peaks (figure 3.1) suggest that viscous damping in these gels is probably not very large for the lowest frequency mode. The low viscous damping in these films were also evident in another measurement[23] in which a silanized glass disc was pulled off a gel film (150 to 200 μm thick) bonded to a rigid substrate at different velocities. Adhesive separation occurred at the disk/gel interface. For gels of moduli ranging from 40 to 330 Pa, the adhesive pull-off stress varied only a factor of three within three decades pull-off velocity (1 $\mu m/s$ to 1000 $\mu m/s$). Since adhesion tests are very sensitive to viscous dissipation in a soft adhesive, the lack of significant dependence of adhesive fracture stress on speed suggests that these gels are behave mainly elastically at low frequencies. On the other hand, we also observe that the higher frequency modes are effectively damped. Therefore, detailed rheological measurements are necessary for making

further progress in the interpretation of the results obtained with the higher modes, which is a subject of our future study. In this regard, the beautiful technique developed by Pottier *et. al* [24,25], which allows measurement of surface rheological properties of a soft object from the thermal fluctuation spectrum will be ideally suited for further understanding the roles of elasto-capillarity and (possible) viscous damping of the eigen-modes of the spherical drops as reported here. Nevertheless, the simplicity of the equation $\omega \sim \omega^* \sqrt{1 + \mu h/2\gamma}$ that successfully collapsed the frequencies of the gel spheres on one master curve motivates us to consider that this method of vibration using a stochastic noise can indeed be used to measure directly the surface tension of gels. We hope that this preliminary study will motivate further experimental and theoretical studies of the vibration of spherical gels. Presently, we have investigated only the spheroidal mode of vibration corresponding to $l=2$ for the gel spheres. We expect that more in-depth insights into the gel vibration problem can be gained by studying its higher modes, which are activated with increasing noise strengths. These detailed studies are reserved for future.

References

(1)   Yoshitake, Y.; Mitani, S.; Sakai, K.; Takagi, K. Surface tension and elasticity of gel studied with laser-induced surface-deformation spectroscopy, *Phys. Rev. E* **2008**, *78*, 041405.

(2)   Chakrabarti, A.; Chaudhury, M.K. Direct measurement of the surface tension of a soft elastic hydrogel: Exploration of elastocapillary instability in adhesion, *Langmuir* **2013** *29*, 6926-6935.

(3)   Harden, J.L.; Pleiner, H.; Pincus, P.A. Hydrodynamic surface modes on concentrated polymer solutions and gels, *J. Chem. Phys.* **1991**, *94* , 5208–5221.

(4)   Onodera, Y.; Choi, P-K. Surface-wave modes on soft gels, *J. Acoust. Soc. Am.* **1998**, *104*, 3358-3363.

(5)   Choi, P-K.; Jyounouti, E.; Yuuki, K.; Onodera, Y. Experimental observation of pseudocapillary and Rayleigh modes on soft gels, *J. Acoust. Soc. Am.* **1999**, *106*, 1591-1593.

(6)   Monroy, F.; Langevin, D. Direct experimental observation of the crossover from capillary to elastic surface waves on soft gels, *Phys. Rev. Lett.* **1998**, *81*, 3167-3170.

(7)   Kumaran, V. Surface modes on a polymer gel of finite thickness, *J. Chem. Phys.* **1993**, *98*, 3429-3438.

(8)   L. Rayleigh, On the capillary phenomena of jets, *Proc. Royal Soc. London* **1879**, *29*, 71-97.

(9)   Lamb, H. Hydrodynamics, Cambridge University Press, Cambridge, UK, 1932.

(10) Strani, M.; Sabetta, F. Free vibrations of a drop in partial contact with a solid support, *J. Fluid Mech.* **1984**, *141*, 233-247.

(11) Lyubimov, D.V.; Lyubimova, T.P.; Shklyaev, S.V. Behavior of a drop on an oscillating solid plate, *Phys. Fluids* **2006**, *18*, 012101.

(12) Noblin, X.; Buguin, A.; Brochard, F. Vibrated sessile drops: Transition between pinned and mobile contact line oscillations, *Eur. Phys. J. E* **2004**, *14*, 395−404.

(13) Dong, L.; Chaudhury, A.; Chaudhury, M.K. Lateral vibration of a water drop and its motion on a vibrating surface*, Eur. Phys. J. E* **2006**, *21*, 231-242.

(14) Celestini, F.; Kofman, R. Vibration of submillimeter-size supported droplets, *Phys. Rev. E* 2006, *73*, 041602.

(15) Mettu, S.; Chaudhury, M.K. Vibration spectroscopy of a sessile drop and its contact line, *Langmuir* **2012**, *28*, 14100-14106.

(16) Sharp, J.S. Resonant properties of sessile droplets; contact angle dependence of the resonant frequency and width in glycerol/water mixtures, *Soft Matter* **2012**, *8*, 399-407.

(17) Basaran, O.A.; DePaoli, D.W. Nonlinear oscillations of pendant drops, *Phys. Fluids* **1994**, *6*, 2923−2943.

(18) Ma, R.; Schliesser, A.; Del'Haye, P.; Dabirian, A.; Anetsberger, G.; Kippenberg, T.J. Radiation-pressure-driven vibrational modes in ultrahigh-Q silica microspheres, Optics lett. **2007**, *32*, 2200-2202.

(19) Shuttleworth, R. The surface tension of solids, *Proc. Phys. Soc. Sec. A* **1950**, *63*, 444-457.

(20) Chakrabarti, A.; Chaudhury, M.K. Elastocapillary Interaction of Particles on the Surfaces of Ultrasoft Gels: A Novel Route To Study Self-Assembly and Soft Lubrication, *Langmuir* **2014**, *30*, 4684-4693.

(21) Chang, C.-T.; Bostwick, J.B.; Steen, P.H.; Daniel, S. Substrate constraint modifies the Rayleigh spectrum of vibrating sessile drops, *Phys. Rev. E* **2013**, *88*, 023015.

(22) Behroozi, X.F.; Smith, J.; Even, W. Effect of viscosity on dispersion of capillary–gravity waves, *Wave Motion* **2011**, *48*, 176-183.

(23) Chaudhury, M.K., Chakrabarti, A. and Ghatak, A., Adhesion-induced instabilities and pattern formation in thin films of elastomers and gels. *Eur. Phys. J. E* **2015**, *38*(7), 1-26.

(24) Pottier, B.; Ducouret, G.; Fretigny, C.; Lequeux, F.; Talini, L. High bandwidth linear viscoelastic properties of complex fluids from the measurement of their free surface fluctuations, *Soft Matter* **2011**, *7*, 7843–7850.

(25) Pottier, B.; Raudsepp, A.; Fretigny, C.; Lequeux, F.; Palierne, J.-F.; Talini, L. High frequency linear rheology of complex fluids measured from their surface thermal fluctuations, *J. Rheol.* **2013**, *57*, 441-455.

Chapter 4

Elasto-buoyant heavy spheres: a unique way to study non-linear elasticity[a]

4.1 Introduction

Singularities are pervasive in various problems of linear continuum mechanics. In wetting, stress diverges at a moving contact line;[1,2] it diverges at the tip of a crack or even at a sharp point indenting a plane.[3] Understanding how such singularities can be tempered has often given rise to new physics invariably prompting us, on many occasions, to investigate a material phenomenon at a molecular dimension and then herald a way to bridge the near field with the far field behavior in a rather non-trivial manner. Nature, however, performs the difficult task herself and leaves her signature in a way that is independent of the constitutive property of a material, yet it belongs to a class of universality. What we report here is such a universality that is discovered in the large deformation behavior of ultra-soft gels. Soft solids undergoing huge deformations exhibit various fascinating and puzzling mechanical behaviors.[4-15] Our experimental protocol to study extra-large elastic deformations is remarkably simple, in that a heavy bead of stainless steel is gently deposited on the horizontal flat surface of a gel. The compliant gel is deformed by the load exerted by the heavy bead. It reaches a stable (elasto-buoyant) equilibrium position when the elastic force exerted by the surrounding

gel balances its weight,[14] within few tenths of a second. This experiment can be viewed as an elastic analog of the falling ball viscometry, in which the bead reaches a terminal sedimentation velocity resulting from the balance of the bead's weight and the viscous drag force.[16] In the limit of Hookean elasticity, an analogy with the Stokes equation (by replacing shear viscosity with shear modulus and velocity with depth of submersion, δ)[17] suggests that $\delta \sim a^2$, a being the sphere radius. While for the higher elastic moduli gels (Fig.4.1-a), such a relationship is more or less valid, for the softer ones, when the bead is totally engulfed by the gel and the deformations are very large (Fig.4.1-b), it is observed that the depth scales with the bead's radius raised to an exponent of 3/2. This is a non-trivial result that cannot be explained by the usual neo-Hookean model, i.e, by considering a quadratic elastic energy density with respect to finite strains. According to this model, the displacement would be infinite! When the same problem is analyzed using an original analysis presented in this paper, it is found, remarkably, that the exponent of the radius of the bead is just at the juncture of what would be required for the field variables to avoid divergence. What is quite remarkable about this analysis is that no detailed non-linear behavior of elastic solids[18–22] needs to be speculated. The scaling laws are universal that being independent of the particular constitutive law of the elastic material. Other examples of the absence of a crucial parameter in some important physical relation is the case of Newton's drag force at large Reynolds number: the drag is proportional to the square of the velocity but is independent of the viscosity, even though viscosity is crucial for dissipating energy. Similarly, in our system, the stress-strain relation at large strains is crucial for determining the field of deformation but, if the material is stiff enough at large strains, the details of this strong non-linear limit of the elastic response disappear in the scaling law for delta as a function of the physical parameters. This unique correspondence between a mathematical prediction and the experimental results, thereby unfolding new physics of highly non-linear deformations, is the subject of this paper.
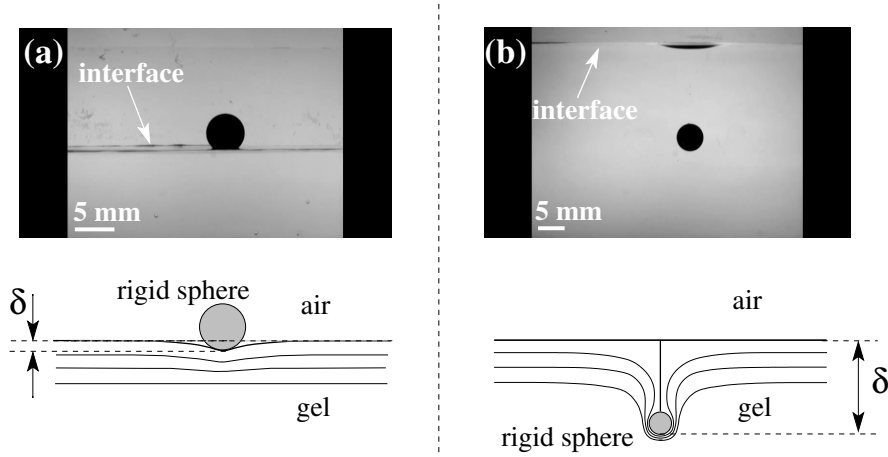
Figure 4.1: Snapshots and schematics of the experiment. (**Top**) Side views of two transparent cells filled with a polyacrylamide gel with shear modulus 1160 Pa (a) and 13 Pa (b). Two identical steel beads (5 mm diameter) have been placed on the free air-gel interface. The vertical downshifts are respectively $\delta = 0.03\ \delta_0$ and $\delta = 320\ \delta_0$. (**Bottom**) Schematic representation of the deformation fields in the respective experiments.

4.2   Experimental evidence of elasto-buoyancy

Cross-linked polyacrylamide gels were used in the experiments reported below. The gel solutions were prepared according to the recipe published previously[14,23] and cured in home-built glass containers (70 mm x 50 mm x 40 mm). The inner walls of the containers were grafted with a thin layer ($\sim$5 nm) of polydimethyl siloxane chains so that the gel solution contacted the walls at 90° to ensure that the surface of the cured gel was flat. All the experiments were performed after two hours of gelation. For the estimation of the shear modulus of the gel, a linear elastic model is used in order to ensure consistency of quantification for all the gels. The shear modulus was determined from the resonant mode of vibration of a gel slab confined between two parallel glass slides.[23] Steel spheres (density 7.8 g/cc, diameters 1 - 10 mm) were gently placed one by one on the gel surface and its side-view image was captured by a camera. Dissipative processes within the gel dampen any oscillations, and the spheres sank until they became stagnant in the polyacrylamide gel, the whole process taking only fractions of a second. The depth of submersion, δ, was measured from the upper surface of the

gel till the base of sphere, that denoting the net downward displacement due to the inclusion of the spherical particle by the surface (Fig.4.1). The cells are large enough to avoid any finite boundary effects, from the side walls as well as the bottom. The measurement of depth for each sphere was made in the central region of the container. After each measurement, the sphere was gently removed from the gel using a magnet, held slightly away from the free surface. We waited for a few minutes between each measurement that ensured there was no memory of the position of the previous sphere inside the gel.

If the bead is too small and the gel is stiff,[7,24] the surface bends slightly under the weight of the bead and $\delta \ll a$ (Fig.4.1-a). By increasing the bead radius or decreasing the elastic modulus, the particle submerges itself to a considerable depth inside the gel. The surface of the gel wraps around the particle and closes to create a line singularity connecting the particle to the free surface of the gel (Fig.4.1-b). Strings of tiny air bubbles appear in this thin channel, which soon coalesce and escape through it while the channel further closes due to the auto-wetting forces of the gel's surface. If the surface of the gel is premarked with ink spots, it is easy to visualize that the surface of the gel becomes appreciably stretched while the sphere sinks through the gel while being still connected to the free surface via a thin channel. These basic experiments were reported in a previous article,[14] but without a detailed analysis. Here we report a detailed set of experiments, in which the shear modulus of the gel was varied from 13 Pa to about 3000 Pa.

Prior to subjecting these experimental results to a comparison with a theoretical analysis, we needed to verify how meaningful it is to consider only the effect of elasticity by ignoring the surface tension of the gel in predicting the depth of submersion of the bead and how reversible the deformation of the gel is within the experimental timescale, *i.e,* a few seconds. First question is partly philosophical that rests upon the distinction between surface free energy γ and surface tension. The latter differs from the former by surface stress $d\gamma/de$, e being the surface strain. As the major constituent

of these amorphous gels is water, we expect that the surface stress is negligible. In fact, several recent studies that measured surface tensions of various amorphous soft polymers strongly suggest that their surface tensions are practically same as their surface free energies.[25] Thus, we needed to figure out only if the surface free energies of the gels play any role. This could be more or less resolved by comparing them with the equivalent spring constant of the sample. The latter can be obtained by slightly raising the height of the bead by an electromagnet and releasing it so that the bead undergoes an under-damped oscillation and reaches the neutral position. For three gels, in which the beads were completely submerged, the equivalent spring constants were estimated from the frequency of oscillation to be 0.2 N/m, 5.6 N/m and 13 N/m, which increase systematically with their shear moduli (13 Pa, 140 Pa and 360 Pa). Fig.4.2-a shows a typical profile of such an oscillation. Comparing these spring constants with the surface tension (0.07 N/m) of water, we conclude that the contribution of surface tension can be safely neglected for all the gels used in this study except, perhaps, for the lowest modulus gel for which the spring constant is three times that of the gel's surface tension. However, when a bead is completely submerged in the gel, any variation of the height of the sphere does not alter the area and the excess energy of the free surface of the gel. We thus believe that the surface tension spring does not play a significant role in determining the depth of submersion of the sphere as long as it is completely engulfed by the gel. Further support to this viewpoint, *i.e.* the dominant role of elasticity over surface tension was gathered from the experiments described below that also exemplified the reversibility of the deformations.

With respect to the second question, it is important for us to emphasize what type of reversibility of the gel is pertinent to the current studies, as a system loaded externally can deform with an appreciable dissipation of energy due to viscous or plastic flow. Fracture can also occur in the material if the load is large enough, or contrarily, it could get locked into a different state via internal rearrangement of bonds. The material would, therefore, not return to its original state when the load is removed. We performed

certain experiments, as discussed below, which ensured that none of the above types of irreversibility is a concern within the timescale relevant for the elasto-buoyancy experiments. The first experiment was performed by studying the variation of the depth of a steel bead (2.8 mm diameter) inside a soft gel ($\mu = 13$ Pa) by imposing an additional vertical magnetic force to the sphere. The depth of the bead was noted as a function of the increasing force in the loading cycle and similarly for the decreasing force in the unloading cycle (Fig. 4.2-b). These experiments were performed over a timescale of a few minutes. After repeating the experiments a few times, the sphere went back to its initial elastobuoyant position, showing no significant hysteresis (See Appendix A for a movie and more details). This kind of reversibility was also checked with a slightly stiffer gel ($\mu = 101$ Pa) and a larger bead (10 mm diameter) (Appendix B). The above observations lead us to conclude that the deformation of the gel generated by a bead is predominantly reversible and controlled by elastic forces. This is the case even when the gel undergoes large deformations, and, as will be shown below, when it is loaded with a sharp pointed needle.

The second experiment was performed by studying the sensitivity of the elasto-buoyancy phenomenon to temperature as by increasing the system temperature, the elastic modulus of a polyacrylamide gel increases and on cooling, such gels become softer with a corresponding decrease of the modulus. The depth of submersion of a bead inside the softest gel ($\mu \sim 13$ Pa) was studied by varying its stiffness in a temperature-controlled oven by covering its surface with a thin layer of Paraffin oil to prevent the gel from drying out. The temperature of the gel was monitored by placing a thermometer inside an identical sample of gel in a similar sized container, placed inside the oven. After the gel was heated to 70 ^{o}C, a 5 mm diameter steel sphere was released into it through the layer of paraffin oil. The depth of the sphere was measured at this temperature while it was in the oven. As the gel was gradually cooled, the sphere sank deeper inside it. A waiting time of an hour before the measurement of the depth of the sphere at each temperature allowed the gel to equilibrate reasonably well. After the gel was

cooled to about 5 °C, it was heated again that decreased the depth of the embedded steel sphere (Heating Cycle, Fig.4.2-c). The depth of submersion of the sphere plotted as a function of the temperature for both the cooling and the heating cycles (Fig.4.2-c) shows that there is a little hysteresis in this system, in that the difference in the depths of the sphere for a given temperature is within 5%. Taken together, we conclude that the gels are thermo-mechanically stable and the deformations of the gel generated by a bead are predominantly reversible and controlled by elastic forces.
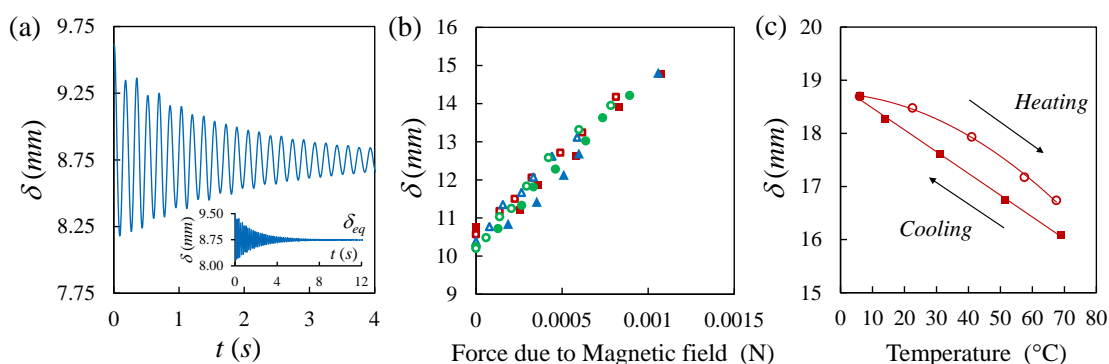
Figure 4.2: Experimental evidence of reversibility of the gels. **(a)** A 10 mm diameter steel sphere immersed in 140 Pa gel, when slightly disturbed from its elastobuoyant position via an electromagnet, undergoes under-damped oscillations about its equilibrium depth δ_{eq}. **(b)** Depth of an elastobuoyant bead (2.8 mm diameter) in a 13 Pa gel plotted as a function of the strength of an external vertical magnetic force. The depth at zero-Force indicates the equilibrium-elastobuoyant position of the sphere. The data (red, blue and green) shown here are from three different experiments where the closed symbols indicate the loading cycles and the open symbols indicate the unloading cycles. **(c)** Depth of submersion δ of a 5 mm diameter steel sphere in a soft gel ($\mu \sim 13$ Pa) varying as a function of its temperature. The experiments in the cooling cycle were performed first following which the gel was heated systematically to obtain the data for the heating cycle.

The penetration depth, δ, is plotted versus the radius a of the steel spheres in log-scales in upper inset of Fig.4.3, for ten different gels (μ : 13 Pa - 2930 Pa) and different radii. The upper white region of this inset shows the data points for beads that were completely below the surface of the gel. The non-dimensionnalisation of the depths

90

as well as the radii of each bead in each gel by the intrinsic lengthscale δ_0 defined as $\delta_0 = \frac{\mu}{\Delta\rho g}$ (Fig.4.3), where μ is the shear modulus of the gel, $\Delta\rho$ is the apparent density of the buoyant spheres, and g is the gravitational acceleration, shows that all the data cluster around a mean master curve with two distinctive asymptotic limits. The value of $\Delta\rho$ varied between $(\rho_{steel} - \rho_{gel})$ for the fully engulfed beads to $(\simeq \rho_{steel})$ for the beads that were almost on the surface of the stiffer gels. Thus, for each sphere-gel system, $\Delta\rho$ was precisely evaluated from experimental images on the basis of the volume of bead engulfed by the gel, analogous to the Archimedes principle of buoyancy for floatation on a liquid.[26] The normalized data can be divided more or less into two regimes: one with the non-dimensional radii $a/\delta_0 < 1$ and other one with $a/\delta_0 > 1$ with an intermediate transition regime. A fit of the non-dimensional depths as a function of the non-dimensional radii for the regime $a/\delta_0 < 1$ with the power law function $(\delta/\delta_0) = k(a/\delta_0)^\alpha$ with adjustable parameters, α and k, yields $\alpha = 1.96 \pm 0.06$ and $k = 1.09 \pm 0.1$. The error bars are obtained from a 95% confidence limit analysis. We conclude that for $a/\delta_0 < 1$, the depths as a function of the radii follows $\delta \sim a^2$ within the error limits. On careful examination of the experimental points corresponding to large deformations, i.e. $a > \delta_0$, we find that the data corresponding to the two softest gels (μ : 13 Pa and 25 Pa) are shifted from the rest of the data due to their multiplicative factor (k) being significantly larger than the rest of the data for the other gels. This indicates that the lengthscale δ_0, which is defined with the elastic linear properties of the sample, is therefore not sufficient to describe the whole data accurately, and non linear effects have to be taken into account. We conclude that all the data in this regime ($a/\delta_0 > 1$) cannot be investigated together. It is more appropriate to investigate the data for each gel composition separately *i.e,* for a given non-linear material stress-strain relationship. By fitting the data for the two softest gels (μ : 13 Pa and 25 Pa) where all the beads are completely engulfed, with the power law function, we find that $\alpha_{13\ Pa} = 1.42 \pm 0.05$ (see lower inset of Fig.4.3), $k_{13\ Pa} = 2.52 \pm 0.3$ and $\alpha_{25\ Pa} = 1.52 \pm 0.09$, $k_{25\ Pa} = 1.63 \pm 0.3$. The exponents for the fits for the gels ($a/\delta_0 \sim 1$) in the intermediate

regime lie between $\alpha \sim 1.5$ and $\alpha \sim 2$. Thus, from the experimental observations, we infer that in the limit of a significantly greater than δ_0, the general trend is close to $\delta \sim a^p$, where p is in the range of 1.4-1.5, within the error limits. Thus, we conclude that the power law observed ($\delta \sim a^2$) in the gels of higher shear moduli is closer to the regime already studied before what one would expect with an analogy with the elastic Stokes equation in the Hookean limit. What is astounding is the observation of an exponent close to 1.5 ($\delta \sim a^{1.5}$) in the case of the gels where the beads are entirely below the surface of the gel, *i.e,* $\delta > 2a$. The small uncertainty of the exponent (less than 6 %) clearly indicates a different regime, as compared to the higher modulus gels. Note that an exponent close to 1.5 for a is also fully supported by the experimental scaling law that we found from indentation tests of the gels, performed with sharp needles as shown in section 4.4.

In order to interpret these novel observations in the ultra-soft gels, we develop a new model to tackle such extra-large deformations in the following part of the paper.

4.3   Asymptotic analytic model for large elastic deformations

From the outset, a motivating picture of the problem can be gleaned from the comparison of the potential energy of the bead in the gravitational field and the energy of the elastic deformation of the gel.   In the limit of small deformations, the elastic deformation energy is given by the elastic modulus times the volume integral of the square of the strain. The strain is displacement (δ) divided by range of this displacement (radius of bead, a). Therefore, the elastic energy is $\sim \mu a^3 \left(\delta/a \right)^2 \sim \mu \delta^2 a$, which is to be compared with the gravitational potential energy $\Delta \rho g a^3 \delta$. This leads to the scaling: $\delta \sim a^2$. However, the experimentally observed scaling $\delta \sim a^{3/2}$ implies that the elastic energy in extremely large deformation must scale as δ^3. The detailed analysis based on a model, presented in this paper for the first time, shows that the above scaling is
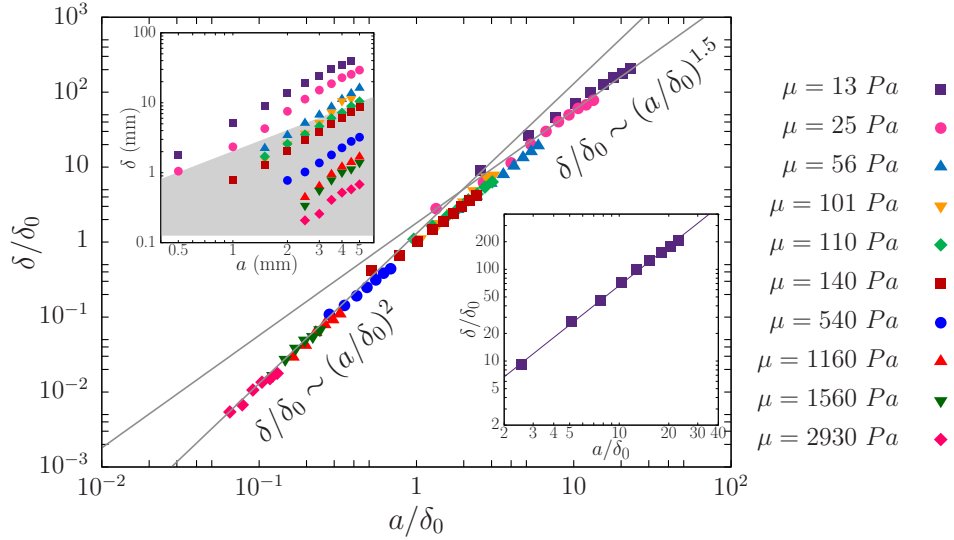
Figure 4.3: Dimensionless depth of spheres (δ/δ_0) plotted as a function of its dimensionless radius a/δ_0, for various shear moduli of the gels from $\mu = 13$ Pa to 2930 Pa. The grey lines indicate power law curves ($\delta/\delta_0 \sim (a/\delta_0)^\alpha$) with $\alpha = 2$ and $\alpha = 1.5$ for the two asymptotic limits for the normalized data. (Upper Inset). Depths (δ) versus radii (a) for all the spheres. The plot area is divided into two domains; the boundary indicating $\delta = 2a$. The data points above the boundary indicates that the spheres were entirely below the gel's surface. (Lower Inset). Best fit ($\delta/\delta_0 = k(a/\delta_0)^\alpha$) for the softest gel (13 Pa) highlighted (see text).

non-trivial. Moreover, the scaling result that follows is independent of the constitutive laws of an elastic material.

4.3.1 Gravity energy of engulfed spheres

Consider deformations that preserve the volume, as is the case with the elastic gels used in the experiments. Since the bead is supposed to be totally engulfed with $\delta \gg a$, the surface of the deformed gel is fairly flat and horizontal. A supplementary (virtual) downshift δ' produces an opposite rise of the same volume of gel. Therefore the gravitational energy variation of the system consisting of the sphere plus the gel is $\frac{4}{3}\pi a^3 \Delta\rho g \delta'$. We conclude that the gravitational energy shift is $\mathcal{E}_{gr} \simeq \frac{4}{3}\pi a^3 \Delta\rho g \delta$ in the limit we are considering.

4.3.2 Outline of calculating the elastic energy in the limit $\delta \gg a$

The axis of symmetry being the vertical axis, the two coordinates changed by the deformation are the radius in the horizontal plane, r, and the vertical coordinate, z. The deformation maps the undisturbed state with coordinates (r, z) to a disturbed state $(R(r, z), Z(r, z))$, or, in radial coordinates from coordinates $(\tilde{r}; \theta)$ to $(R(\tilde{r}, \theta); Z(\tilde{r}, \theta))$ with $\tilde{r}$ radius and θ polar angle of the $(r; z)$ plane (see Fig.4.4-d). The elastic energy
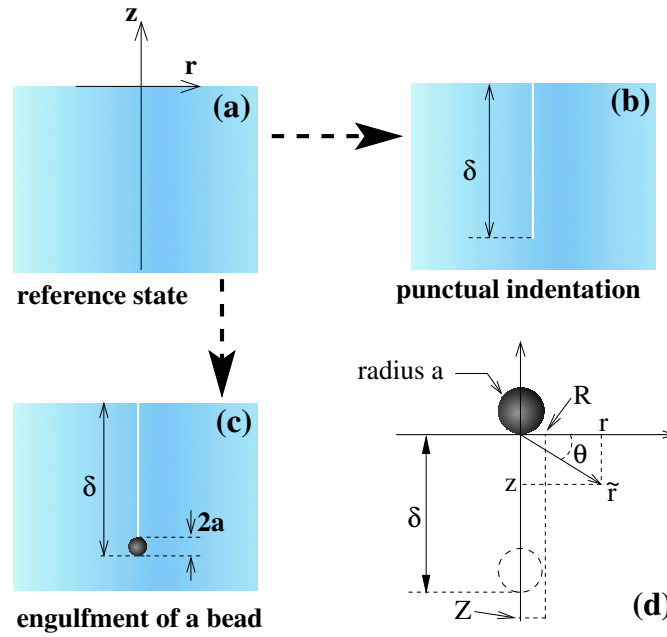
Figure 4.4: Sketches corresponding to the steps of the calculation of the elastic energy. **(a)** Reference state (no deformation); **(b)** A point-load is applied at the free surface. The displacement at the application point is δ. **(c)** A sphere of radius a indents the free surface over the distance δ. **(d)** Mapping from the reference state (solid lines, with the bead at the surface) to the deformed state. A point of the gel in the rest state is located with coordinates (r, z). $\tilde{r}$ is the distance from the initial contact point of the bead. In the deformed state, the point that was at (r, z) is located at $R(r, z), Z(r, z)$.

is a function of the strain tensor (also called *right Cauchy-Green deformation tensor*), which gives the square of local change in distances due to deformation: $C = F^T F$, F being the deformation gradient tensor.[27] In the absence of any preferred direction, the elastic energy density W of an incompressible solid may depend only on two scalars (invariant under global rotation) that can be made out of the strain tensor: the trace

(I_1) and the sum of the square of its components (I_2). In cylindrical coordinates with an azimuthal invariance, these invariants read $I_1 = R_{,r}^2 + \frac{R^2}{r^2} + R_{,z}^2 + Z_{,r}^2 + Z_{,z}^2$ and $I_2 = (R_{,r}^2 + Z_{,r}^2)^2 + (R_{,z}^2 + Z_{,z}^2)^2 + 2(R_{,r}R_{,z} + Z_{,z}Z_{,r})^2 + \frac{R^4}{r^4}$, where indices preceded by a comma denote partial derivatives. For the neo-Hookean model, which is commonly used to describe soft gels, the strain energy density is $W = \frac{\mu}{2}I_1$. However, beyond a certain deformation, the neo-Hookean model cannot be a fair representation of rubber-like materials whose elasticity originates from unfolding of polymer chains: once these chains reach their full extension, the energy cost for a supplementary unfolding diverges so that a further deformation is accompanied by a diverging additional elastic energy, in contrast with the ideal neo-Hookean law (see Fig. 4.6). In what follows, we do not restrict ourselves to the neo-Hookean case.

The deformation field of the gel can be described with two characteristic lengths, the downshift of the sphere δ, and the radius of the sphere a. Here, we are dealing with the limit of large downshifts, that is δ far larger than a. Below we demonstrate that in this asymptotic case, the elastic energy of the system does not depend on a in the limit $a \ll \delta$. As a first step we consider a normal point-load applied on the free elastic surface at $(r, z) = (0, 0)$ (Fig 4.4-(b)) and we find a scaling law for the elastic energy per unit volume at a given distance $\tilde{r}$ from the loading point. The condition for the elastic energy to be convergent is established. Then as a second step we consider a hard sphere with a finite radius, producing a displacement δ at the contact point $(r, z) = (0, 0)$ equal to the displacement at $(r, z) = (0, 0)$ induced by the previously considered point-like load. We demonstrate that for $\delta \gg a$, the elastic energy associated with the displacement field generated by the sphere or the point-like load are equal: These are independent of a and proportional to δ^3.

4.3.3 Elastic energy for a point-like load

Since we are interested in the case $a \ll \delta$, we first deal with the limit of a point-like

force acting vertically on the free horizontal surface of an elastic solid, and we find scaling laws for the strain by assuming first a particular form for the strain density elastic energy.

Incompressibility of the elastic medium is imposed by writing that the determinant $\mathcal{D}$ of the first derivatives of $\mathbf{R}(x, y, z)$ is equal to one. For axisymmetric deformations, $\mathcal{D} = \frac{R}{r}\left(R_{,r}Z_{,z} - R_{,z}Z_{,r}\right)$. The total energy of the system {gel + sphere} reads :

$$\mathcal{E} = \frac{4}{3}\pi\Delta\rho a^3 g Z(0,0) + 2\pi \int_{-\infty}^{0} \mathrm{d}z \int_{0}^{\infty} \mathrm{d}r\,(W - q\mathcal{D})\,r, \qquad (4.1)$$

where the Lagrange multiplier $q(r, z)$ imposes the incompressibility condition $\mathcal{D} = 1$.[28]

For the point-like heavy sphere we first consider (see Fig. 4.4-(b)), the weight the bead can be reduced to a point force located at $(r, z) = (0, 0)$. Eq. 4.1 simplifies into:

$$\mathcal{E} = \frac{16\pi^2}{3}\Delta\rho a^3 g \int_{-\infty}^{0} \mathrm{d}z \int_{0}^{\infty} r Z(\mathbf{r})\delta^3(\mathbf{r})\mathrm{d}r + 2\pi \int_{-\infty}^{0} \mathrm{d}z \int_{0}^{\infty} \mathrm{d}r\,(W - q\mathcal{D})\,r, \quad (4.2)$$

where $\delta^3(r, z)$ is the 3D Dirac distribution.

The Euler-Lagrange conditions of minimization of the energy (Eq. 4.2) read:[5]

$$\left(\frac{\partial\,(W - q\mathcal{D})\,r}{\partial R_{,r}}\right)_{,r} + \left(\frac{\partial\,(W - q\mathcal{D})\,r}{\partial R_{,z}}\right)_{,z} = \frac{\partial\,(W - q\mathcal{D})\,r}{\partial R} \qquad (4.3)$$

$$\left(\frac{\partial\,(W - q\mathcal{D})\,r}{\partial Z_{,r}}\right)_{,r} + \left(\frac{\partial\,(W - q\mathcal{D})\,r}{\partial Z_{,z}}\right)_{,z} = \frac{8\pi r\Delta\rho g a^3}{3}\delta^3(\mathbf{r}) \qquad (4.4)$$

Let δ be the displacement of the gel at $(r; z) = (0; 0)$. δ is the unique relevant length for the displacement field. For points located at a distance to the load $\tilde{r}$ much smaller than δ, δ is no more relevant at these short length-scales. Therefore no length-scales are expected to occur in the scaling laws and one assumes a power law of $\tilde{r}$ for the displacements for $\tilde{r} \ll \delta$: $Z = \delta + \tilde{r}^\beta f_1(\theta)$ and $R = \tilde{r}^\gamma f_2(\theta)$. Since the gel is vertically stretched and horizontally squeezed in the vicinity of the bead one assumes that $\gamma > \beta$.

This hypothesis will be checked afterwards (see Eq. 4.16 below).

The constraint of conservation of volume reads (for $\tilde{r} \ll \delta$):

$$\mathcal{D} = 1 \Rightarrow \overset{\sim\tilde{r}^{\gamma-1}}{\overbrace{\frac{R}{r}}} (\overset{\sim\tilde{r}^{\gamma-1}}{\overbrace{R_{,r}}} \overset{\sim\tilde{r}^{\beta-1}}{\overbrace{Z_{,z}}} - \overset{\sim\tilde{r}^{\gamma-1}}{\overbrace{R_{,z}}} \overset{\sim\tilde{r}^{\beta-1}}{\overbrace{Z_{,r}}}) = 1 \Rightarrow \gamma = \frac{3-\beta}{2}. \tag{4.5}$$

The condition that $\gamma > \beta$ with Eq. 4.5 yields $\beta < 1$.

We assume first that the strain energy density function W is proportional to $I_1^{\alpha_1} I_2^{\alpha_2}$ (the exponents α_1 and α_2 are constant) in the range of strains undergone by the elastic solid in the vicinity of the application point, *i.e.* for $\tilde{r}$ far smaller than δ. This choice for W is crucial to obtain the scaling law, but it has no effect on the final results, as argued in section 4.3.5: it does not limit the general nature of the theory.

The scaling laws for the first and the second invariants of the Cauchy deformation tensor are:

$$I_1 = Tr(C) = \overset{\sim\tilde{r}^{1-\beta}}{\overbrace{R_{,r}^2}} + \overset{\sim\tilde{r}^{1-\beta}}{\overbrace{\frac{R^2}{r^2}}} + \overset{\sim\tilde{r}^{1-\beta}}{\overbrace{R_{,z}^2}} + \overset{\sim\tilde{r}^{2\beta-2}}{\overbrace{Z_{,r}^2}} + \overset{\sim\tilde{r}^{2\beta-2}}{\overbrace{Z_{,z}^2}} \sim \tilde{r}^{2\beta-2}, \tag{4.6}$$

$$\begin{aligned} I_2 = Tr(C^2) &= (R_{,r}^2 + Z_{,r}^2)^2 + (R_{,z}^2 + Z_{,z}^2)^2 + 2(R_{,r}R_{,z} + Z_{,z}Z_{,r})^2 \\ &+ \frac{R^4}{r^4} \sim \tilde{r}^{4\beta-4}. \end{aligned} \tag{4.7}$$

These scaling laws for I_1 and I_2 are used to obtain the scaling laws for the various terms

of the Cauchy-Poisson equations (Eqs. 4.3 and 4.4). We first deal with Eq. 4.3:

$$
\begin{aligned}
\frac{\partial \left(W - q\mathcal{D}\right) r}{\partial R_{,r}} &= r\frac{\partial W}{\partial I_1}\frac{\partial I_1}{\partial R_{,r}} + r\frac{\partial W}{\partial I_2}\frac{\partial I_2}{\partial R_{,r}} - qr\frac{\partial \mathcal{D}}{\partial R_{,r}} \\
&= \underbrace{2r\frac{\partial W}{\partial I_1}R_{,r}}_{\sim \tilde{r}^{\frac{3-\beta}{2}+2(\alpha_1+2\alpha_2-1)(\beta-1)}} \\
&+ \underbrace{4r\frac{\partial W}{\partial I_2}\left(R_{,r}(R_{,r}^2 + Z_{,r}^2) + R_{,z}(R_{,r}R_{,z} + Z_{,z}Z_{,r})\right)}_{\sim \tilde{r}^{\frac{3-\beta}{2}+2(\alpha_1+2\alpha_2-1)(\beta-1)}} - q\,\underbrace{RZ_{,z}}_{\sim \tilde{r}^{\frac{\beta+1}{2}}}.
\end{aligned}
$$

$$(4.8)$$

In the same way one finds:

$$
\frac{\partial \left(W - q\mathcal{D}\right) r}{\partial R_{,z}} \sim \tilde{r}^{\frac{3-\beta}{2}+2(\alpha_1+2\alpha_2-1)(\beta-1)}, \tag{4.9}
$$

$$
\frac{\partial \left(W - q\mathcal{D}\right) r}{\partial R} \sim \tilde{r}^{\frac{\beta-1}{2}}. \tag{4.10}
$$

From Eq. 4.3 and Eqs. 4.8, 4.9 and 4.10 one obtains $\tilde{r}^{\frac{1-\beta}{2}+2(\alpha_1+2\alpha_2-1)(\beta-1)} \sim q\tilde{r}^{\frac{\beta-1}{2}}$, and the scaling law for the Lagrange multiplier:

$$
q \sim \tilde{r}^{(\beta-1)(2\alpha_1+4\alpha_2-3)}. \tag{4.11}
$$

The last Cauchy-Poisson equation (Eq. 4.4) is now used to get an expression of β as a function of α_1 and α_2. It writes:

$$
\frac{1}{r}\left(r\frac{\partial \left(W - q\mathcal{D}\right)}{\partial Z_{,r}}\right)_{,r} + \left(\frac{\partial \left(W - q\mathcal{D}\right)}{\partial Z_{,z}}\right)_{,z} = \frac{8\pi\Delta\rho g a^3}{3}\delta^3(\mathbf{r}). \tag{4.12}
$$

Denoting as $\sigma_{zr} = \frac{\partial(W-q\mathcal{D})}{\partial Z_{,r}}$ and $\sigma_{zz} = \frac{\partial(W-q\mathcal{D})}{\partial Z_{,z}}$, the two quantities present on the left-hand side of Eq.4.12, one finds that this left-hand side is the divergence (expressed in cylindrical coordinates) of the z-components of the stress tensor σ.[27]

We first calculate the scaling laws for σ_{zr} and σ_{zz} using Eqs. 4.5, 4.6, 4.11:

$$\sigma_{zr} = \frac{\partial (W - q\mathcal{D})}{\partial Z_{,r}} \quad = \quad \frac{\partial W}{\partial I_1}\frac{\partial I_1}{\partial Z_{,r}} + \frac{\partial W}{\partial I_2}\frac{\partial I_2}{\partial Z_{,r}} - q\frac{\partial \mathcal{D}}{\partial Z_{,r}} \tag{4.13}$$

$$= \quad \underbrace{2\frac{\partial W}{\partial I_1}Z_{,r}}_{\sim \tilde{r}^{(\beta-1)(2\alpha_1+4\alpha_2-1)}} \quad +\underbrace{q\frac{R}{r}R_{,z}}_{\sim \tilde{r}^{1-\beta}}. \tag{4.14}$$

The second term of the right-hand side of Eq. 4.14 scales as $\tilde{r}^{(\beta-1)(2\alpha_1+4\alpha_2-3)}\tilde{r}^{1-\beta}$. It is negligible when $\tilde{r}$ tends to zero when compared to the first term of Eq. 4.14 provided that the exponent of the second term is larger than the exponent of the first one, *i.e.*:

$$(\beta - 1)(2\alpha_1 + 4\alpha_2 - 3) + 1 - \beta > (\beta - 1)(2\alpha_1 + 4\alpha_2 - 1), \tag{4.15}$$

which is formally equivalent to $\beta < 1$. Since it is assumed from the beginning that $\beta < 1$, we conclude that $\sigma_{zr} \sim \tilde{r}^{(\beta-1)(2\alpha_1+4\alpha_2-1)}$ and in the same way, $\sigma_{zz} \sim \tilde{r}^{(\beta-1)(2\alpha_1+4\alpha_2-1)}$: σ_{zr} and σ_{zz} follow the same power law when $\tilde{r}$ tends to zero. The right-hand side of Eq. 4.12 being a delta-like charge density, we conclude from Gauss's theorem that the scaling law for σ_{zr} and σ_{zz} is also $\sigma_{zr} \sim \sigma_{zz} \sim \frac{1}{r^2}$. Therefore, $\tilde{r}^{(\beta-1)(2\alpha_1+4\alpha_2-1)} \sim \tilde{r}^{-2}$, and:

$$\beta = \frac{2\alpha_1 + 4\alpha_2 - 3}{2\alpha_1 + 4\alpha_2 - 1}. \tag{4.16}$$

β is an increasing function of $(\alpha_1 + 2\alpha_2)$. It is negative for $\alpha_1 + 2\alpha_2 < 3/2$, and it is always smaller than 1. The displacement at the application point is finite if the exponents are positive, *i.e.* if $\alpha_1 + 2\alpha_2 > 3/2$. Otherwise the material cannot withstand a point-load. In the following we assume that $\alpha_1 + 2\alpha_2 > 3/2$, an ansatz that will be legitimized later.

Since δ is the unique length-scale of the deformation, the coordinates in the deformed configuration can be written as: $R = \delta f_0 \left(\frac{r}{\delta}\right)$ and $Z = \delta g_0 \left(\frac{r}{\delta}\right)$, where f_0 and g_0 are two numerical functions depending only on the constitutive law of the elastic

medium. The invariants I_1 and I_2, and thus the elastic energy density are dimensionless functions depending only on $\mathbf{r}/\delta$. The elastic energy due to the deformation induced by the point load is

$$\mathcal{E}_{el\ 0} = \iiint_{z>0} W_0 \mathrm{d}^3\mathbf{r}, \tag{4.17}$$

where W_0 is the elastic energy density evaluated at $(\tilde{r}, z)$ for the deformation field resulting from the normal point force:

$$W_0(\tilde{r}, z) = W\left(I_1\left(\frac{\mathbf{r}}{\delta}\right), I_2\left(\frac{\mathbf{r}}{\delta}\right)\right). \tag{4.18}$$

Note that W is assumed to scale as $I_1^{\alpha_1} I_2^{\alpha_2}$ just for the strains encountered at $\tilde{r} \ll \delta$. We therefore put a generic expression for the elastic energy density in eq. 4.18 in order to take into account for the contributions of the strain in the whole material.

The convergence of the integral in Eq.4.17 is ensured since the work done by the applied force is finite for $\alpha_1 + 2\alpha_2 > \frac{3}{2}$. On the contrary, the integral in Eq. 4.17 diverges for $\alpha_1 + 2\alpha_2 < \frac{3}{2}$.

The shear modulus μ being defined from $W(I_1, I_2)$ as:[27]

$$\mu = 2\left(\frac{\partial W}{\partial I_1}(0,0) + \frac{\partial W}{\partial I_2}(0,0)\right), \tag{4.19}$$

one introduces $\mathcal{W}_0$, the dimensionless elastic energy density, as $\mathcal{W}_0 = W_0/\mu$. It depends on the "shape" of the non-linearities of the strain energy density function, and is independent of the shear modulus μ. Furthermore, as $\mathcal{W}_0$ is a function of $\mathbf{r}/\delta$ only, Eq. 4.17 yields, for $\alpha_1 + 2\alpha_2 > \frac{3}{2}$:

$$\mathcal{E}_{el\ 0} = \mu\delta^3 c_0, \tag{4.20}$$

where c_0 is a dimensionless parameter which depends on the non-linear "shape" of the

constitutive equation of the elastic material, but depends neither on δ nor on μ:

$$c_0 = \iiint_{z>0} \mathcal{W}_0 \left(\frac{\mathbf{r}}{\delta}\right) d^3 \left(\frac{\mathbf{r}}{\delta}\right).$$

(4.21)

We stress that Eq. 4.20 is valid only for $\alpha_1 + 2\alpha_2 > \frac{3}{2}$ (so that c_0 is defined).

4.3.4 Elastic energy for a finite sphere

In this section, it is demonstrated that the elastic energy associated to a normal point-like force is equal to the elastic energy corresponding to a finite sphere of radius a, provided that *(i)* the downshifts (δ) are identical in both cases, and *(ii)* the strain energy density function follows the condition for the convergence of the integral in Eq.4.17, a condition which is automatically fulfilled by any real elastic material. We will therefore conclude that Eq. 4.20 gives the elastic energy of an engulfed sphere of any radius a, provided that $a \ll \delta$.

We consider a heavy bead of radius a, and denote δ its vertical downshift, which is supposed to be far larger than a (Fig. 4.4-(c)).

- The unique relevant length-scale for $\tilde{r} \gg a$ being δ, the displacement field reduces in this range of $\tilde{r}$ to the displacement field for a point-load with the same penetration depth δ: $Z = \delta g_0 \left(\frac{\mathbf{r}}{\delta}\right)$, where g_0 has been defined in section 4.3.3.

- The power law for $Z - \delta$ with the exponent given by Eq. 4.16 applies in the intermediate range $a \ll \tilde{r} \ll \delta$. Combining it with the previous expression of Z (valid for $\tilde{r} \gg a$) yields:

$$Z - \delta \sim \delta \left(\frac{\tilde{r}}{\delta}\right)^{\beta} = \delta \left(\frac{a}{\delta}\right)^{\beta} \left(\frac{\tilde{r}}{a}\right)^{\beta}.$$

(4.22)

- Close to the bead ($\tilde{r} \ll \delta$) the unique relevant length-scale is a. $Z - \delta$ can be

expressed as

$$Z - \delta = K g_1 \left(\frac{\mathbf{r}}{a} \right), \tag{4.23}$$

where g_1 is a numerical function and the constant K (with the dimension of a length) depends on a and also on the far field deformation, *i.e.* on δ. Comparing Eq. 4.22 with the general expressions for Z in the range $\tilde{r} \ll \delta$, one obtains $K = \delta \left(\frac{a}{\delta} \right)^\beta$.

A similar expression for R can be obtained with the exponent $(3 - \beta)/2$, leading to negligible contributions for the elastic energy.

For $\tilde{r} \ll \delta$, the first invariant I_1 scales as $Z_{,z}^2$ and $Z_{,r}^2$, and the second invariant I_2 scales as $Z_{,z}^4$ and $Z_{,r}^4$. The (dimensionless) strain energy density function $\mathcal{W} \sim I_1^{\alpha_1} I_2^{\alpha_2}$ can thus be written for $\tilde{r} \ll \delta$ (using Eq. 4.23 with the expression of K) as $\mathcal{W} \sim \left(\frac{a}{\delta} \right)^{\beta-3} g_2(\frac{\mathbf{r}}{a})$. In the range $\tilde{r} \gg a$, $\mathcal{W} \simeq \mathcal{W}_0$, $\mathcal{W}_0$ being the dimensionless elastic energy density of the point-load problem (Fig. 4.5).

Moreover, in the range $\tilde{r} \ll \delta$, one finds from the scaling laws of section 4.3.3: $\mathcal{W}_0 \sim \left(\frac{r}{\delta} \right)^{\beta-3} \sim \left(\frac{r}{a} \right) \left(\frac{a}{\delta} \right)^{\beta-3}$.

One concludes that, for any $\tilde{r}$, $\mathcal{W} - \mathcal{W}_0 \sim \left(\frac{a}{\delta} \right)^{\beta-3} g_3(\frac{\mathbf{r}}{a})$, with g_3 a numerical function (depending neither on δ nor on a) whose limit as its argument approaches ∞ equals 0. Thus, we obtain:

$$\iiint_{z>0} (\mathcal{W} - \mathcal{W}_0) \, \mathrm{d}^3 \mathbf{r} = \left(\frac{a}{\delta} \right)^{\beta-3} a^3 \iiint_{z>0} g_3 \left(\frac{\mathbf{r}}{a} \right) \mathrm{d}^3 \left(\frac{\mathbf{r}}{a} \right) \sim \delta^3 \left(\frac{a}{\delta} \right)^\beta. \tag{4.24}$$

Since one assumes again that $\alpha_1 + 2\alpha_2 > \frac{3}{2}$, $\beta > 0$ and the difference of the elastic energy with the bead of radius a, $\mathcal{E}_{el}$, to the elastic energy with the point-load, $\mathcal{E}_{el\,0}$, is negligible with respect to δ^3 (since $(a/\delta)^\beta \ll 1$). One concludes from Eq. 4.20 that the elastic energy $\mathcal{E}_{el}$ is proportional to δ^3.

Note that if $\alpha_1 + 2\alpha_2$ were smaller than $3/2$ the near-field part of the elastic energy
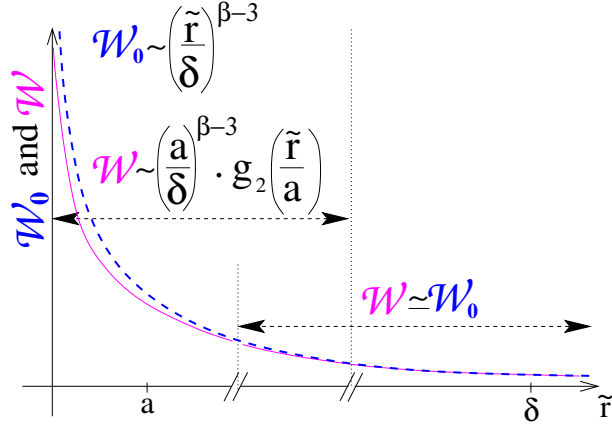
Figure 4.5: Sketch of the (dimensionless) energy density profiles $\mathcal{W}_0$ (e.g. dotted line) and $\mathcal{W}$ (e.g. solid line) as a function of the distance $\tilde{r}$ to the initial contact point. The dashed horizontal double arrows highlight two domains, corresponding to (i) $\tilde{r} \gg a$ where the (dimensionless) elastic energy densities $\mathcal{W}$ and $\mathcal{W}_0$ are similar, and (ii) $\tilde{r} \ll \delta$ where they are different.

would not be negligible anymore compared to the far field contribution.

4.3.5 The strain energy density function

In sections 4.3.3 and 4.3.4 the strain energy density function has been assumed to scale as $I_1^{\alpha_1} I_2^{\alpha_2}$ for the strains encountered at $\tilde{r} \ll \delta$. It has been then demonstrated that the elastic energy corresponding to the downshift of a sphere of finite radius a over the distance δ is proportional to δ^3 in the limit $\delta \gg a$ if $\alpha_1 + 2\alpha_2 > 3/2$. In this section, we explain why this choice for the strain energy density function does not limit the generality of the theory, and therefore why the theory can be applied for any real elastic material.

It is worth considering the case of an elastic material for which the strain energy density function increases softer than $I_1^{\alpha_1} I_2^{\alpha_2}$ with $\alpha_1 + 2\alpha_2 = 3/2$. For $\tilde{r} \ll \delta$ we demonstrated that $Z - \delta = \delta \left(\frac{a}{\delta}\right)^\beta g_1 \left(\frac{r}{a}\right)$ and then $Z_{,z} \sim \left(\frac{\delta}{a}\right)^{1-\beta}$, showing that the strain is arbitrarily large in the limit $\delta \gg a$, if $\beta < 1$, *i.e.* if $\alpha_1 + 2\alpha_2 < 3/2$. However, due to the finite maximum stretch of the polymer chains constituting the material, the maximum stretching of any real elastic rubber-like material is bounded.

To this maximum stretching corresponds a divergence of the strain energy function. This divergence results in a steeper and steeper increase of $\mathcal{W}$ with I_1, I_2, or both, which is associated with increasing values of the exponents α_1 and/or α_2.[27]

In order to illustrate this last point, let us consider a particular strain energy density function, for instance the Gent hyper-elastic model.[21,29] The strain energy density function of this model has a singularity when the first invariant I_1 reaches a limiting value. It is plotted in Fig. 4.6: deviations from the initial neo-Hookean behaviour ($\alpha_1 = 1$ and $\alpha_2 = 0$) yield an increasingly stiffer and stiffer strain energy density function. At any value I_{10} of I_1 one can define the *local* exponent $\alpha_{10} = \frac{I_1}{\mathcal{W}} \frac{\mathrm{d}\mathcal{W}}{\mathrm{d}I_1}$ so that at the vicinity of I_{10} the strain energy density function is $\mathcal{W} \sim I_1^{\alpha_{10}}$, locally. Beyond a certain finite value I_{10}^* of I_{10} the exponent is larger that $3/2$, ensuring that for any I_1 larger than I_{10}^* the condition $\alpha_1 + 2\alpha_2 > 3/2$ is fulfilled. Note that values of I_1 larger than I_{10}^* are automatically reached, otherwise the strain would diverge around $\tilde{r} \sim 0$, leading to arbitrarily high values of I_1 (as explained above).

What is illustrated using the example of the Gent model is general, and can be applied to any elastic constitutive law involving I_1 and I_2 of a real elastic material: starting from low to moderate strains for which the neo-Hookean model is expected to apply far from the bead, energy density functions stiffer than $I_1^{\alpha_1} I_2^{\alpha_2}$ with $\alpha_1 + 2\alpha_2 > \frac{3}{2}$ are necessarily encountered next to the bead for any real elastic material.

A material for which the failure limit is reached before the strain energy density is stiffer than $I_1^{\alpha_1} I_2^{\alpha_2}$ with $\alpha_1 + 2\alpha_2 > 3/2$ would not be able to sustain the heavy sphere, and thus would be drilled by the sphere. These cases can be definitively excluded for the experiments we are dealing with since no fracture, plasticity nor creep have been observed during these experiments.

One concludes that for any elastic material, the elastic energy of the gel is given by Eq. 4.20 within the limit $\delta \gg a$.
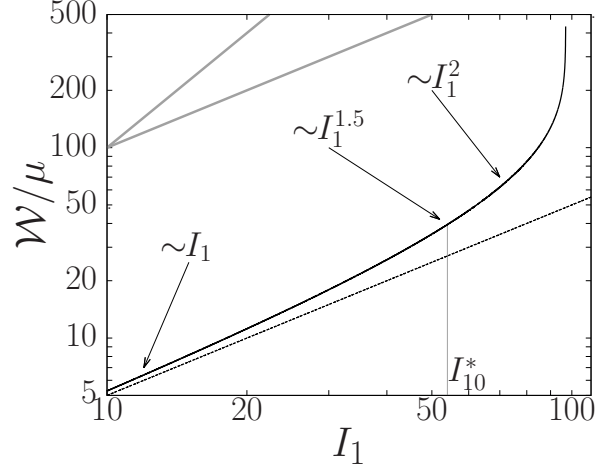
Figure 4.6: Strain energy density function given by the incompressible Gent material model $W = -\frac{1}{2}\mu J_m \log\left(1 - \frac{I_1-3}{J_m}\right)$[21] with $J_m = 97$, plotted in log-log scales (black solid line). $J_m + 3$ is the limiting value of the first invariant I_1. The strain energy density function for the neo-Hookean material is plotted with dashed line. The two gray straight lines indicate slopes 1 and 2, *i.e.* values of the local exponent α_1 equal to 1 and 2. I_{10}^* is the value of the first invariant beyond which the local exponent is larger than $3/2$.

4.3.6 Equilibrium condition

For an engulfed bead of radius a deposited on the initially flat surface of an elastic solid of shear modulus μ with a density contrast $\Delta\rho$, the gravity energy $\mathcal{E}_{gr}$ and the elastic energy $\mathcal{E}_{el}$ have been derived separately for any arbitrary downshift δ (assuming $\delta \gg a$) respectively in sections 4.3.1 and 4.3.4: $\mathcal{E}_{gr} \simeq \frac{4}{3}\pi a^3 \Delta\rho g \delta$ and $\mathcal{E}_{el} \simeq \mathcal{E}_{el\,0} = c_0 \mu \delta^3$. c_0 is a dimensionless parameter depending neither on δ, μ and a. Upon a change of the substrate (*e.g.* a change in the gel composition) the shear modulus μ will certainly change. c_0 will also change if W/μ changes. In the limit of the small deformations, $W/\mu \sim \frac{1}{2}I_1$ for any isotropic and incompressible elastic material. The possible change in c_0 therefore comes from the specific elastic behaviour of the substrate at finite deformations.

The total energy, $\mathcal{E}_{el} + \mathcal{E}_{gr}$, is minimum in the equilibrium state. The δ-derivatives of $\mathcal{E}_{gr}$ and $\mathcal{E}_{el}$ are therefore equal giving the scaling law valid for $\delta \gg a$, for a given

elastic material:

$$\frac{\delta}{\delta_0} = \sqrt{\frac{4\pi}{9c_0}} \cdot \left(\frac{a}{\delta_0}\right)^{3/2}, \tag{4.25}$$

with $\delta_0 = \frac{\mu}{\Delta\rho g}$. The crucial point is the non-dependence of c_0 with respect to a. c_0 depends only on the non-linear elastic properties of the elastic solid, and therefore, for a given elastic material, the downshift of the bead, δ, is expected from theory to be proportional to the radius of the bead to the power $\frac{3}{2}$ times the square root of $\Delta\rho g$.

Note that the beads has been assumed to be spherical although this is not a crucial point in this theory: if it is compact with all typical lengths of the same order a the previous scaling arguments apply.

4.4 Discussion and conclusion

The theoretical analysis presented above provides an understanding of the experimentally observed scaling law. It arises from a specific property of the system: the elastic energy does not depend on the radius of the sphere.

The scaling behaviour found for the downshift of spheres with different radii and/or different densities is general and the specific property of the elastic material has an effect only on the coefficient c_0 in this law (Eq. 4.25). These predictions are in quantitative agreement with the observations: an experimental scaling law for the depth is a function of the radius raised to an exponent close to $3/2$, and the prefactor is not only related to the linear elastic properties (μ), but also to the non-linear features of the elastic material. These non-linear features being *a priori* distinct from one gel to another one, explains why plotting δ/δ_0 as function of a/δ_0 for different gel compositions yields slightly different curves for the extremely soft gels but more or less a master curve for the stiffer gels. Thus, the prefactor in the scaling law depends not only on the shear modulus of the solid, but also on the elastic behaviour at large deformations. This provides a way to assess some characteristics such as strain stiffening properties of elastic materials under large strains.

The range of applications of the derived scaling goes far beyond the description of the elasto-buoyancy phenomenon. For instance, we show here that these soft gels can sustain much larger deformations than those induced by the elastobuoyant spheres when a sharp-pointed needle is indented into the gel, through a layer of silicone oil to minimize friction, without fracturing the gel (Fig. 4.7-a). The fact that no fracture occurs in the gel is evident with a dyed interface that returns to its original state following the removal of the needle from inside the gel. In this case, the indentation force (P) varies as the square of the displacement (δ) (Fig. 4.7-b), a scaling that was reported previously with studies involving large deformations of soft solids[15] but not with a sharply pointed load. In this current study, we also paid special attention to removal of lateral solid-like friction, which can contribute to the indentation load through complex coupling between the normal stress difference and the shear strain in a non-linear solid.[30] The scaling for the energy for the case of large deformations can be directly checked from these observations: $P \sim \partial \mathcal{E}_{el} / \partial \delta \sim \delta^2$, *i.e*, $\mathcal{E}_{el} \sim \delta^3$. This scaling for the force is in unison with the exponent 3/2 for the penetration depth of an elastobuoyant sphere in the limit of the large deformations. It is here observed within a wider range of strains, an indication that the scaling law of elastobuoyant spheres in these gels is valid for larger and heavier beads, and/or with even softer gels. Furthermore, this testifies that our analysis is general and goes beyond the phenomenon of elastobuoyancy.

While on one hand such materials could be potentially used for various applications where one would need to make use of large deformations, on the other hand, one could also ask the question, how one could induce fracture[15,31] in such systems that are otherwise capable of handling such huge strains without failure. The gels we use in the experiments are stiff in a sense because they are made of polymers which cannot stretch beyond a given limit; there arises the question of the initiation of fracture in such systems. In the scenario where a sharp slender body has deformed the gel hugely, such that the elastic energy is distributed over a large volume ($\sim \delta^3$) as explained by the theory, there is not enough energy available locally to initiate fracture. This ap-

plies regardless of the shape of the body provided that its characteristic lengths are far smaller than the static penetration depth δ. Nevertheless, when the same sharp-pointed object undergoes vertical vibrations while penetrating the gel, through the silicone oil to minimize lateral friction that could potentially lead to irregular fracture, it induces a sharp cut in an irreversible way (Fig. 4.7-c) much easily. This is so even when the lateral friction induced interfacial jamming between the gel and the needle is eliminated. We hypothesize that this sharp cut is facilitated by the local rheological stiffening of the gel that is made possible by not allowing sufficient time for it to relax from a high frequency-high modulus state to a relaxed one. Such vibration assisted puncturing of soft materials were demonstrated with marked precision as early as almost fifty years ago, even with a single cell;[32] however the detailed mechanics of such kinds of fracture are not well-known. Puncturing of such soft gels assisted with vibration thus provides a good model system to study such an important phenomenon that has immense practical applications including precision surgery on soft tissues in humans. The analysis presented in this paper provides the motivation required for developing such a model, in which the local fields are manipulated by the frequency response of the gel, while an overarching large deformation field surrounds the locality.

In this paper, we have shown that the depth of a bead scaling as exponent $3/2$ for the radius is independent of the strain-stress relation provided that the increase in the elastic energy density (W) with the strain is stiff enough. The generality of the scaling and the observations are supported by indentation experiments using a sharp pointed needle that follows a similar trend for large deformations as that observed in the elastobuoyancy phenomenon. Generic behaviors for elastic materials undergoing large and complex deformations can therefore be identified, going beyond scaling arguments that is blind to the crucial effect of strain stiffening. This work sheds new lights on the mechanics of extremely large elastic deformations that are crucial in various emerging techniques that even encompass an important procedure such as the computer-assisted surgery involving human organs,[33–35] which are indeed non-linear materials and un-
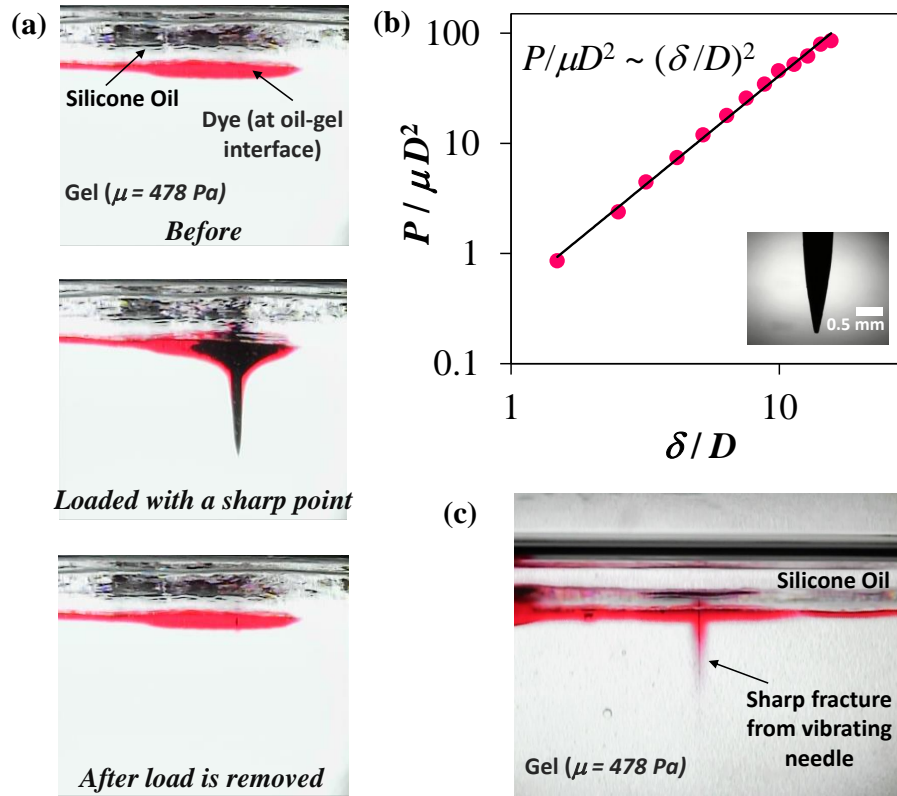
Figure 4.7: **(a)** Snapshots of the experiment of loading a needle (diameter, D and grafted with ~ 5 nm layer of polydimethylsiloxane chains) inside the gel with a thin layer of silicone oil (AR20, Sigma Aldrich) on its surface. The oil above the gel reduces friction by lubricating the contact between the needle and the gel during indentation. The red dye demarcates the interface between the gel and silicone oil. After unloading the needle from the gel, the dyed interface retracted to its original position showing that there was no fracture in the gel. **(b)** For these experiments of loading a sharp needle (inset) inside the gel($\mu = 478$ Pa), the non-dimensional force $P/\mu D^2$ varies almost as the square of the non-dimensional displacement δ/D. An uncertainty analysis yields the value of the power of δ/D as 1.99 ± 0.03. **(c)** When the same needle was indented in the gel while undergoing vertical vibrations, a fine fracture was induced by the indentation. The needle underwent square wave oscillations (amplitude of vibration ~ 0.64mm) along its axial direction that were generated by a waveform generator (Agilent, model 33120A), connected to a mechanical oscillator (Pasco Scientific, Model No: SF-9324) via an amplifier (Sherwood, Model No: RX-4105).

dergo large deformations. In all these important fields, an ideal neo-Hookean model is used that, according to our current work, is not a suitable choice for such studies. The danger is that one may miss the divergences of the solution that is inherent in the ideal neo-Hookean model because the full solution is not used. The work presented here pro-

vides a redress to the possible pitfalls that one may embark upon in studying extreme deformations of non-linear materials, thereby also offering possible benchmarks for numerical simulations and even opportunities to formulate new simulations methods.

A   Reversibility with an External Magnetic Field

In order to test the reversibility of the deformation in the gels, we experimentally studied the variation of the depth of a steel bead inside a soft gel by imposing an additional vertical magnetic force to the sphere. The gel container was placed above a frame that was in turn kept on a weighing balance. A magnet, attached to a micromanipulator, was positioned inside the frame, under the container of gel. A layer of silicone oil above the gel prevented evaporation of water from its surface. A steel bead (2.8 mm diameter) was dropped inside the gel ($\mu = 13$ Pa) and its elastobuoyant position was noted, when the magnet was far away from the bottom of the container such that the magnetic force was zero. After axially aligning the magnet with the bead, we slowly brought the magnet closer to the bottom of the container such that the bead was attracted to it and went deeper inside the gel. Subsequently, the magnet was brought further away that allowed the bead to return to its original position. Note that the oil helps to lubricate the contact between the gel surfaces folding over the sphere during these experiments. The depth of the bead was noted as a function of the increasing force in the loading cycle and similarly for the decreasing force in the unloading cycle (Fig. 2-b, Manuscript). After repeating the experiments a few times, we found that the sphere went back to its initial elastobuoyant position, showing no significant hysteresis, in that the difference of the depths before and after the magnetic loading is within 2 %. Fig. A.1 below pictorially depicts the phenomenon of reversibility due to an external magnetic field. We performed the same experiments using a slightly stiffer gel ($\mu = 101$ Pa) where we studied the variation of the depth of a 10 mm diameter bead that too showed no signifi-

cant hysteresis (Fig. A.2).

| Before | Magnetic field turned ON | Magnetic field turned OFF |
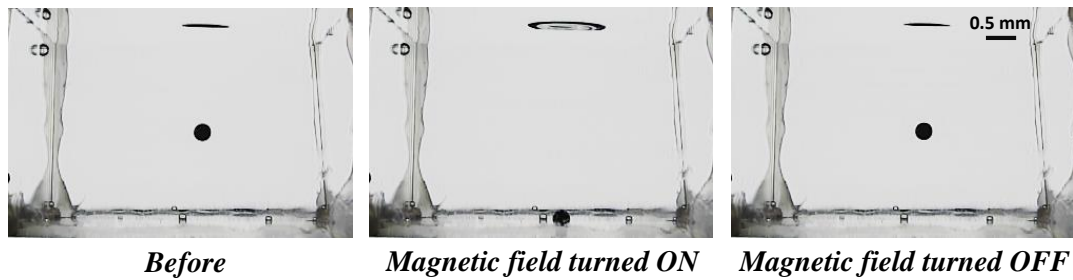
Figure A.1: Experimental images of a steel bead (2.8 mm diameter) engulfed by a soft polyacrylamide gel ($\mu \sim 8$ Pa). The first snapshot shows its initial equilibrium position. Note that the gel surface has wrapped around the bead and closed till the uppermost part in the gel. When the magnetic field of the electromagnet (placed underneath the container) is slowly increased, the bead goes down and touches the bottom of the container. When the field is slowly reduced to zero, it almost returns to its initial elastobuoyant position.
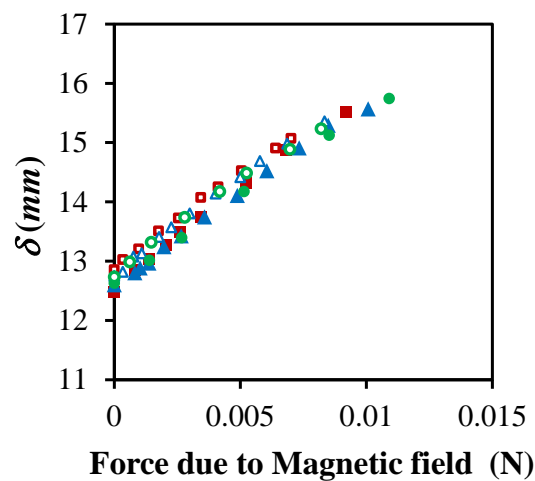
Figure A.2: Depth of an elastobuoyant steel bead (10 mm diameter) in a gel ($\mu = 101$ Pa) plotted as a function of the strength of an external magnetic field. The depth at zero-Force indicates the equilibrium-elastobuoyant position of the sphere. The data (red, blue and green) shown here are from three different experiments where the closed symbols indicate the loading cycles and the open symbols indicate the unloading cycles. This experiment was performed over a timescale of a few minutes.

B   Movie: Reversibility in the softest gel

The movie (https://journals.aps.org/prx/abstract/10.1103/PhysRevX.6.041066) shows a steel bead (2.8 mm diameter) engulfed by a soft gel ($\mu = 13$ Pa) at its initial elastobuoyant position. A layer of silicone oil at the top of the gel helped prevents evaporation of water from its surface. When the steel bead was dropped in the gel through the layer of oil, a small amount of oil was trapped just above the sphere. Note that the gel surface doesn't close completely due to the reduced interfacial tension at the oil-gel interface as opposed to the elastobuoyancy experiments with gel-air interface (Fig. A.1). This, however, does not alter the elastobuoyant position of the same bead in a similar gel as the equilibrium height is determined from the balance between the elasticity and gravity fields.

When the magnetic field underneath the container of gel is applied and increased slowly, the bead is attracted to the magnet and slowly engulfs deeper into the gel. After the bead touches the bottom of the container, the magnetic field strength is slowly reduced to zero that allows the bead to return to its initial equilibrium position. The experiment is repeated thrice here and no significant hysteresis is observed.

References

(1) De Gennes, P. G. Wetting: Statics and Dynamics. *Reviews of Modern Physics* **1985**, *57*, 827–863.

(2) Pomeau, Y. Recent progress in the moving contact line problem: a review. *Comptes Rendus Mécanique* **2002**, *330*, 207 – 222.

(3) Johnson, K. L. *Contact Mechanics*; Cambridge University Press, 1985; Cambridge Books Online.

(4) Kim, J.; Yoon, J.; Hayward, R. C. Dynamic display of biomolecular patterns through an elastic creasing instability of stimuli-responsive hydrogels. *Nature Mater.* **2010**, *9*, 159.

(5) Mora, S.; Phou, T.; Fromental, J. M.; Pismen, L. M.; Pomeau, Y. Capillarity Driven Instability of a Soft Solid. *Phys. Rev. Lett.* **2010**, *105*, 214301.

(6) Mora, S.; Abkarian, M.; Tabuteau, H.; Pomeau, Y. Surface Instability of Soft Solids under strain. *Soft Matter* **2011**, *7*, 10612–10619.

(7) Style, R.; Hyland, C.; Boltyanskiy, R.; Wettlaufer, J.; Dufresne, E. Surface tension and contact with soft elastic solids. *Nature Communications* **2013**, *4*, 2728.

(8) Saintyves, B.; Dauchot, O.; Bouchaud, E. Bulk Elastic Fingering Instability in Hele-Shaw Cells. *Phys. Rev. Lett.* **2013**, *111*, 047801.

(9) Mora, S.; Maurini, C.; Phou, T.; Fromental, J. M.; Audoly, B.; Pomeau, Y. Solid drops: Large capillary deformations of immersed elastic rods. *Phys. Rev. Lett.* **2013**, *111*, 114301.

(10) Jagota, A.; Paretkar, D.; Ghatak, A. Surface-tension-induced flattening of a nearly plane elastic solid. *Physical Review E* **2012**, *85*, 051602.

(11) Chaudhury, M. K.; Chakrabarti, A.; Ghatak, A. Adhesion-induced instabilities and pattern formation in thin films of elastomers and gels. *The European Physical Journal E* **2015**, *38*, 1–26.

(12) Tallinen, T.; Chung, J. Y.; Biggins, J. S.; Mahadevan, L. Gyrification from constrained cortical expansion. *Proceedings of the National Academy of Sciences* **2014**, *111*, 12667–12672.

(13) Zhao, X.; Suo, Z. Theory of Dielectric Elastomers Capable of Giant Deformation of Actuation. *Phys. Rev. Lett.* **2010**, *104*, 178302.

(14) Chakrabarti, A.; Chaudhury, M. K. Direct Measurement of the Surface Tension of a Soft Elastic Hydrogel: Exploration of Elasto-Capillary Instability in Adhesion. *Langmuir* **2013**, *29*, 6926–6935.

(15) Fakhouri, S.; Hutchens, S.; Crosby, A. Puncture mechanics of soft solids. *Soft Matter* **2015**, *11*, 4723–4730.

(16) Stokes, G. G. On the theories of the internal friction of fluids in motion and of the equilibrium and motion of elastic solids. *Trans. Camb. Phil. Soc.* **1845**, *8*, 287–347.

(17) Rayleigh, L. *Theory of Sound*; Dover, 1922; Vol. II.

(18) Rivlin, R. S. Large elastic deformations of isotropic materials. IV. Further developments of the general theory. *Phi. Trans. Royal Soc. London Series A* **1948**, *241*, 379–397.

(19) Ogden, R. W. Large Deformation Isotropic Elasticity On the Correlation of Theory and Experiment for Incompressible Rubberlike Solids. *Proceedings of the Royal Society of London. Series A* **1972**, *326*, 565584.

(20) Yeoh, O. H. Some forms of the strain energy function for rubber. *Rubber Chemistry and technology* **1993**, *66*, 754–771.

(21) Gent, A. A new constitutive relation for rubber. *Rubber Chemistry Tech.* **1996**, *69*, 59–61.

(22) Mangan, R.; Destrade, M.; Saccomandi, G. Strain energy function for isotropic non-linear elastic incompressible solids with linear finite strain response in shear and torsion. *Extreme Mechanics Letters* **2016**,

(23) Chakrabarti, A.; Chaudhury, M. K. Elastocapillary Interaction of Particles on the

Surfaces of Ultrasoft Gels: A Novel Route To Study Self-Assembly and Soft Lubrication. *Langmuir* **2014**, *30*, 4684–4693.

(24) Rimai, D.; Quesnel, D.; Busnaina, A. The adhesion of dry particles in the nanometer to micrometer-size range. *Colloids and Surfaces A: Physicochemical and Engineering Aspects* **2000**, *165*, 3 – 10.

(25) Mondal, S.; Phukan, M.; Ghatak, A. Estimation of solid liquid interfacial tension using curved surface of a soft solid. *Proceedings of the National Academy of Sciences* **2015**, *112*, 12563–12568.

(26) Vella, D. Floating versus sinking. *Annual Review of Fluid Mechanics* **2015**, *47*, 115–135.

(27) Ogden, R. *Non-Linear Elastic Deformations*; Ellis Horwood Limited: Chichester, 1984.

(28) Fox, C., Ed. *An Introduction to the Calculus of Variations*; Dover: New-York, 1987.

(29) Gent, A. Elastic instabilities in rubber. *International Journal of Non-Linear Mechanics* **2005**, *40*, 165–175.

(30) Chaudhury, M. K. Viewpoint: A Cut Above the Rest. *Physics* **2012**, *5*, 139.

(31) Das, S.; Ghatak, A. Puncturing of soft gels with multi-tip needles. *Journal of materials science* **2011**, *46*, 2895–2904.

(32) Chowdhury, T. K.; Snell, F. M. A microelectrode study of electrical potentials in frog skin and toad bladder. *Biochimica et Biophysica Acta (BBA)-Biophysics including Photosynthesis* **1965**, *94*, 461–471.

(33) Cotin, S.; Delingette, H.; Ayache, N. Real-time elastic deformations of soft tissues for surgery simulation. *IEE trans. on Visualization and Computer Graphics* **1999**, *5*, 62–73.

(34) Liu, A.; Tendick, F.; Cleary, K.; Kaufmann, C. A survey of surgical simulation: Applications, technology, and education. *Presence-Teleoperators and Virtual Environments* **2004**, *12*, 599–614.

(35) Taylor, Z. A.; Cheng, M.; Ourselin, S. High-speed Nonlinear finite element analysis for surgical simulation using graphics processing units. *IEEE Transactions on Medical Imaging* **2008**, *27*, 650–663.

Chapter 5

Surface Folding Induced Attraction and Motion of Particles in a Soft Elastic Gel: Cooperative Effects of Surface Tension, Elasticity and Gravity[a]

5.1. Introduction

Interaction between particles mediated by the mechanical distortion of the surrounding medium has been the subject of considerable interests in physical[1,2], metallurgical[3] and biological[4-6] literatures. When atoms and solid particles are inserted in the bulk of a solid matrix[3,7], its elastic energy is increased that usually gives rise to a distance dependence repulsive force. Such forces are thought to play important roles in the dispersion of defects in an elastic medium. While elastic interactions of particles prevail in anisotropic fluids such as nematic liquid crystals[2], there are also examples[4-6] with proteins and other integral components of a cell exhibiting attractive as well as repulsive interactions via membrane mediated elastic forces. Interaction mediated by capillary and gravity forces[8-12] has also been the subject of considerable interests in the past and the present. In such cases, a large length scale emerges from the competition between gravity and capillarity that rules the range of interaction between particles dispersed on

a liquid surface when the Bond number of the system is comparable to or greater than unity. Co-operative effects of surface tension and elasticity give rise to a plethora of other interesting phenomena[13-28]. However, to the best of our knowledge there has not been any report till this date regarding the co-operative roles of gravity, capillarity and elasticity in any type of attractive or repulsive interactions between particles. What we report here is a novel observation related to the long range interaction between rigid particles in a soft elastic gel, in which the surface of the gel folds to form singular line defects connecting the particles and the outer surface of the gel. These line singularities create a tensile strain field parallel to the surface that extends deep inside the gel and leads to some fascinating long range attractive interactions between the suspended particles. When a particle is suspended in such a gel that has a gradient of thickness, it is found to move from the thicker to the thinner part of the gel due to the gradient of elastic strain energy.

5.2. Experimental Section

5.2.1. Materials

The spheres used for this study include two types of ceramic balls (fracture-resistant silicon nitride with density $3.25 g/cm^3$ and non-porous high alumina ceramic with density $3.9 g/cm^3$), copper balls (Alloy 102, 99.95% pure copper, density $8.94 g/cm^3$) and steel balls (bearing-quality E52100 alloy steel, hardened ball, density $7.8 g/cm^3$) that were purchased from McMaster-Carr. The diameters of the spheres used in the study range from 2mm to 6.4mm. The spheres were sonicated in acetone (General use HPLC-UV grade, Pharmco Aaper) in a Fisher Scientific Ultrasonic Cleaner (Model no. FS5) for 10 minutes after which they were blow dried with ultra-pure nitrogen gas.

In some experiments, dimers were formed by joining two spheres with super glue (Scotch). The materials used in the preparation of the gel are N-(hydroxymethyl)-acrylamide (48% solution in water, Sigma Aldrich), potassium persulphate (99.99% trace metals basis, Sigma Aldrich), and N,N,N′,N′- tetramethylethylenediamine (TEMED, ≥99.5%, purified by redistillation, Sigma Aldrich). For most of the experiments a quartz cell (45mm x 30mm, 45mm high, Rame Hart p/n 100-07-50) was used to study the interaction between the spheres. Borosilicate Glass vials (27 mm diameter × 70 mm high) were purchased from Fisherbrand for use in the static Stokes experiment. These were cleaned with deionized (DI) water and blow-dried with nitrogen gas before use. All experiments were performed after placing the test cells on a 3d manipulated stage that was situated atop a vibration isolation table (Micro-g, TMC).

5.2.2. Preparation of Gel

A 3.1% (by weight of acrylamide monomer) physically cross-linked hydrogel was used for the present study. We provide below the salient features of the method used to prepare the gel based on what was described in our recent publication[28]. In a clean glass jar, N-(hydroxymethyl)-acrylamide (3.1 wt% basis) was added to DI water obtained from a Thermo Scientific Barnstead E-pure unit. This solution was stirred for 30 minutes with pure nitrogen gas bubble purging through it. This step was followed by the addition of 0.25% potassium persulphate and further stirring the solution for 20 minutes. The gelation begins within few minutes after the addition and stirring of the last ingredient, 0.3% TEMED, to the mixture. The gel solution was poured into the quartz cell and the glass vials immediately after all the ingredients were mixed to prepare the gel. The quartz cell was covered with Parafilm and the vials were tightly

secured with their caps to avoid evaporation of water. The gelation was complete in 2 hours at room temperature. While the gels prepared as above were used for most of the experiments, in a couple of experiments (see figures 5.5 and 5.7) small amount (0.01 %) of N,N'- Methylene bisacrylamide (99%, Sigma Aldrich) was used as the crosslinking agent (see below) to increase its modulus slightly.

5.2.3 Elastic Stokes Experiment

This experiment was performed by gently placing either the ceramic, copper or steel spheres on the surface of the polyacrylamide (PAM) hydrogel cured in the vials, one at a time (Figure 5.2). The sphere immersed itself inside the gel and stood still at a depth of h, which was measured from the surface of the gel in the vial to the sphere's center. Care was taken to ensure that the spheres were at the centers of the vials in order to avoid putative wall effects. Even though some distortion of the shape of the spherical ball occurred when it was viewed through the sides of the cylindrical vial, no distortion of the image occurred in the vertical direction, which is what was needed for the measurement of h. The details of how the images were captured and processed are described in a later section. An experiment in which an alumina ceramic ball (3.2mm diameter) was released on the surface of the hydrogel prepared inside a rectangular quartz cell was captured by a high speed camera (Redlake Motion-Pro, Model no: 2000) at the rate of 500 frames per second. Snapshots from the high speed movie (Figure 5.1, A-D) gave an insight into the mechanism by which the gel surface wraps around the sphere, and relaxes with time.

5.2.4 Interaction of Spheres inside the Gel

A copper (2 mm or 2.4 mm) or an alumina ceramic (3.2 mm or 4.8 mm) sphere was released gently on the surface of the gel with the help of a prong holder (McMaster-Carr). The second sphere of same diameter as the first one was then released inside the gel in the same plane, perpendicular to the direction of the camera, within approximately 0.5- 1.0 cm away from the other sphere. The attraction and the descent of each pair of spheres in the gel were recorded with a CCD camera connected to a microscope for further analysis. In one experiment involving 4.8 mm alumina ceramic spheres, a dimer made of two glued balls (4.8 mm each) was released a distance of about 1 cm away from another dimer formed by the attractive contact of two other spheres in the same gel. The attraction of these dimers was also captured with a CCD camera. In the experiments illustrating the interactions of the clusters, the balls were released into the gel in such a way that two clusters grew by the self-assembly process not very far from each other. The interactions of the spheres, the growth of the clusters, their movements and attractions were all recorded with a CCD camera connected to a microscope as discussed below.

5.2.5 Thickness Graded Gel

A 3% chemically cross-linked PAM gel containing 0.01% (w/w basis) N,N'-Methylene bisacrylamide was used for the preparation of the thickness graded gel. The as-prepared gel solution was immediately poured into the Quartz cell that was then tightly secured with parafilm. In order to obtain a thickness gradient of the gel in the cell, it was inclined by elevating one end to a height of ~8mm. The gel was allowed to cure in the tilted cell for about 2 h after which the cell was brought back to its initial horizontal position. The gel surface was concave and flatter on both the edges due to the gel material sagging

down from the edges, however there was a large length (~20mm; total length of the cell being 45mm) over which the gradient of thickness was more or less constant. The cell was placed on a 3d manipulated stage. A steel or a ceramic sphere was released on the thicker part of the gel. The video of the motion of the sphere down the gradient was captured using a CCD camera equipped with a variable focal length microscope.

5.2.6 Videography and Analysis

The interactions of the spheres were captured using a Video Microscope (Infinity) that was equipped with a CCD camera (jAi, Model no. CV−S3200) and connected to a computer using the WinTV application (Hauppauge, USA). The images for the Static Stokes experiment were also captured with the same video micrographic setup. The recorded videos were decomposed into image sequence in VirtualDub and the images were analyzed to measure the depth of submersion and the distance of separation between the spheres using a tracking algorithm, SpotTracker, in ImageJ. The calibration factor of the variable focal length microscope was obtained from the known diameter of the spheres in all the images.

5.3. Results and Discussion

5.3.1 Penetration of a single particle through the gel's surface

A millimeter size spherical object made of either ceramic, copper, or any metal submerges itself to a considerable depth[28] inside a soft hydrogel, the modulus of which is in the range of few Pascals. Even though the modulus of the gel is so low, its mesh size $[(k_BT/\mu)^{1/3} \sim 100$ nm$]$ is still vanishingly small as compared to the size (~ mm) of the sedimenting object. The deformed network can exert sufficient elastic force to

balance the weight of the sphere thus making it neutrally buoyant after it descends by a decent distance inside the gel. While the elastic field is symmetric around each sphere in the classic problems of elastic inclusions, the stress and the strain fields here are asymmetric, e.g. the elastic stress beneath the sphere is higher than that above the sphere[28].
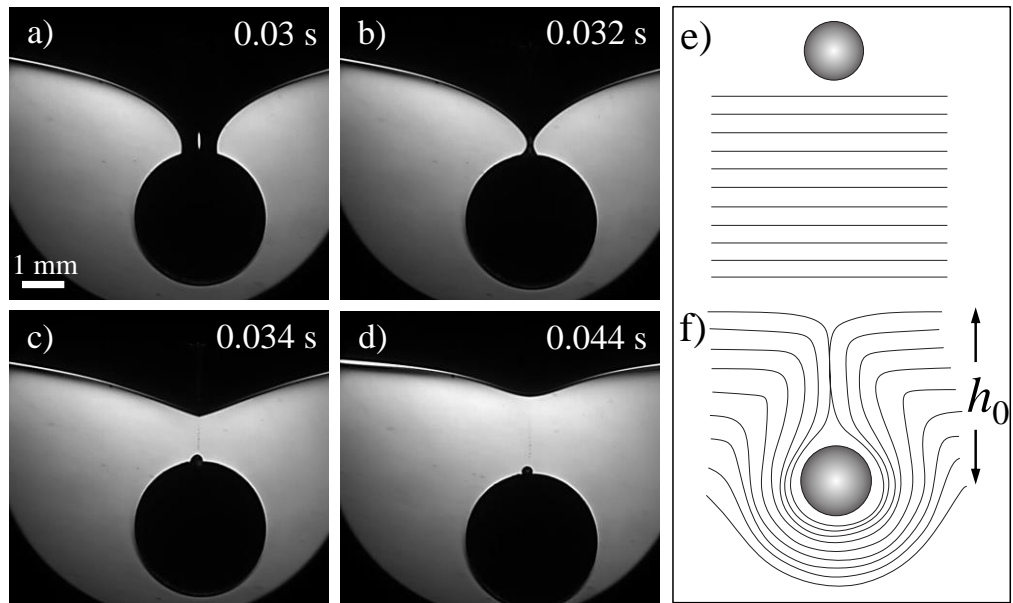
Figure 5.1: The fall of a small ceramic ball (3.2mm diameter) through a soft polyacrylamide hydrogel is captured with a high speed (500 frames per second) camera. The folding of the surface of the gel around the sphere (a), the pinch-off instability (b) and the formation of a thin line (c-d) connecting the ball and the surface of the gel are evident in these videographs. The surface of the gel relaxes slowly (d) with no sign of any fracture in the gel. The white scale bar here represents 1mm. (e-f) The schematic illustrates the wrapping of the sphere by and the folding of the surface of the gel as the sphere penetrates the gel. Here, h_0 is the initial height of a single ball immersed in the gel.

Figure 5.1 (A to D) depicts the case of a single ceramic ball released on the surface of a soft hydrogel, which sediments down to its equilibrium position within about 2 seconds. These high speed video micrographs do not provide any evidence of fracture in the gel. Instead the free surface of the gel wraps around the ball and folds into line contact above it. The contact region necks down so that a small bubble remains attached

to the zenith of the sphere, while strings of very tiny air bubbles appear in the thin channel above it. These tiny air bubbles soon coalesce and escape through the narrow channel, which further closes due to auto-wetting forces of the gel's surface. This phenomenon has certain resemblance to the pinch-off instability[29,30] of a dripping liquid drop. However, unlike the snap-off of the liquid drop[29,30] by its weight, the spherical ball here does not detach from the thin channel that connects it to the free surface of the gel as the elastic force supports the weight of the ball[28]. A substantial stress concentration is expected to develop around the thin line joining the sphere and the free surface; thereby the region of the gel above the sphere remains in a state of tensile stress parallel to the surface (Figure 5.1F), the magnitude of which depends on the shear modulus, the radius of the sphere and how far the ball descends inside the gel. If the surface of the gel is pre-marked with ink spots, it is easy to visualize that the surface of the gel gets appreciably stretched while the sphere sinks through the gel. It is also possible to release ink inside the gel in the form of thin vertical lines with the help of a fine needle, which bend towards the sphere in a dramatic way when the sphere is released inside the gel[31]. The role of self-adhesion of the free surface of the gel above the sphere is crucial in keeping the folded surface intact against the tensile elastic field. It is surprising that the soft gel beneath the ball does not fracture, which we feel is a manifestation of two effects: blunting[32,33] of the crack brought about by the spherical geometry of the suspended object and the Lake-Thomas effect[34], in which the tearing energy of a rubber increases with the compliance of a network up to a certain extent. Intentional fracture can, however, be induced by the imposition of a stronger external field aided by thermal fluctuation, which we reserve for a detailed future study. In the absence of any disruptive external field, the sphere can be entirely supported by the elastic force, in which the depth of penetration increases with the mass (m) of the ball.
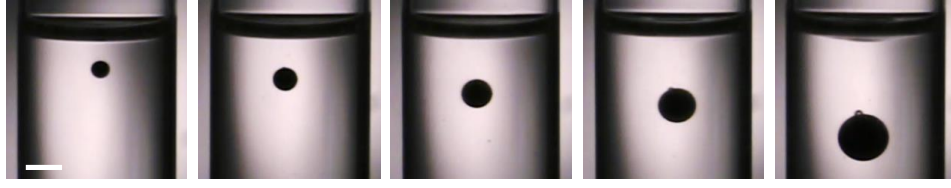
Figure 5.2. Static Stokes experiment showing the depths of submersion of Silicon Nitride Ceramic balls of diameters 2.4mm, 3.2mm, 4mm, 4.8mm and 6.35mm respectively in a 3.1% PAM hydrogel. The white scale bar represents 5mm.
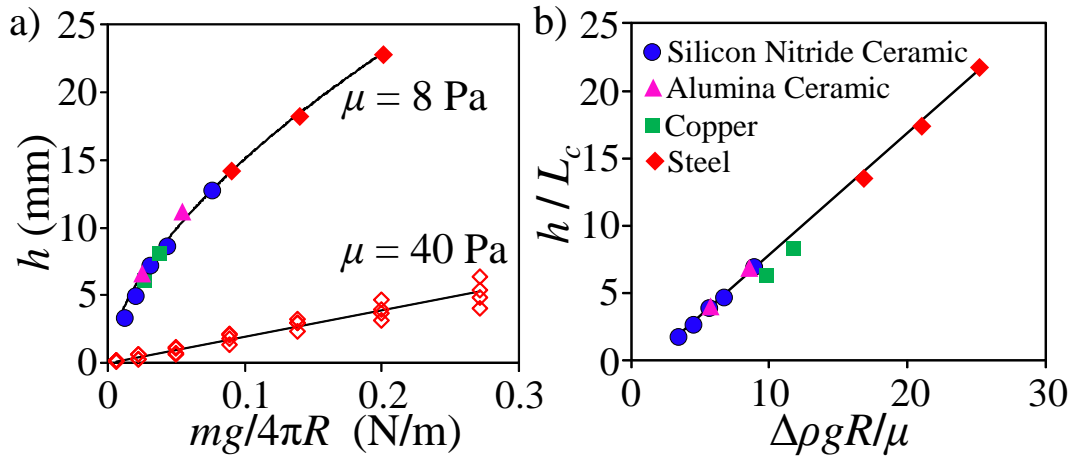
Figure 5.3: (a) The experimental data from the static immersion experiments are analyzed here by plotting the depth of submersion (h) against $mg/4\pi R$. Here, m denotes the effective mass of the spheres after correcting for buoyancy inside the gel, g is the gravitational acceleration and R is the radius of the sphere. The closed symbols represent the data obtained by performing the elastic Stokes experiment in the lower modulus (8 Pa) gel whereas the open symbols represent the previously reported data[28] obtained with a higher modulus (40 Pa) gel. (b) The data for the lower modulus (8 Pa) gel are re-scaled by dividing h with the capillary or Laplace length ($L_c = \sqrt{\gamma/\Delta\rho g}$) and plotting it against $\Delta\rho gR/\mu$. Here, $\Delta\rho$ is the difference between the density of the spheres and water, μ is the shear modulus of the gel (~8 Pa) and γ (~73mN/m) is its surface tension.[28] The data for the higher modulus (40 Pa) gel follows a linear relationship when h is rescaled with the radius and plotted with respect to $\Delta\rho gR/\mu$. Capillarity does not play a significant role in the higher modulus gel and hence the data does not exactly follow the behavior that is shown by the spheres in the lower modulus gel (8 Pa).

The relationship between the depth of penetration (h) and the weight (mg) of the ball in the gel of shear modulus μ should be linear for small deformation, i.e. $h = mg/4\pi\mu R$ or, $h \sim R^2$ as was observed by us previously[28] with a higher modulus hydrogel that too

underwent a large deformation although not as much as the current gel. This surprising observation suggested that a linear elastic modulus pleasingly scales out of the mechanics of the deformation of a system that is intrinsically neo-Hookean. However, this relation is non-linear for the lower modulus gel used in the current study. Although a power law equation (h (m)=0.06($mg/4\pi R$)$^{0.6}$, mg is in Newtons) describes the data well, the equation is dimensionally incomplete. Close observation revealed a clear difference in the deformation in these two gels as the balls were released upon them. While for the higher modulus gel, the ball penetrates to a considerable distance inside the gel, its surface wraps around the ball incompletely, whereas the lower modulus gel completely wraps the ball and folds above it. The low value of the shear modulus (8 Pa), coupled with the work of cohesion (2γ) of the gel as 144 mN/m give rise to an elasto-adhesive length ($2\gamma/\mu$) of about 20 mm, from which it is inferred that the surface tension driven auto-wetting can support a substantially long line connecting the sphere and the free surface of the gel. For the lower modulus gel, excellent linear collapse of all the data can be obtained if h divided by the Capillary length ($\gamma/\Delta\rho g$)$^{0.5}$ is plotted against $\Delta\rho gR/\mu$. This linear variation of $h/(\gamma/\Delta\rho g)^{1/2}$ with $\Delta\rho gR/\mu$ suggests that h follows the geometric mean of two length scales: the elastocapillary length (γ/μ) and the elastic Stokes length $\Delta\rho gR^{2}/\mu$. Thus, the surface tension seems to play some role in the depth of the submersion of the ball in the lower modulus gel, which is not surprising considering the large elastocapillary length of the system.

5.3.2 Long Range Attraction between Spheres Suspended in the Gel

Upon the release of a second ball at a moderate distance away from the first one, similar sequences of the above events lead to the development of tensile stress parallel to the

126

free surface that too penetrates to a considerable distance inside the gel. However, as the tensile stress in between the two spheres can relax (figures 5.5 B-C), a net attraction ensues between the spheres (figure 5.4). As they approach each other, both the spheres
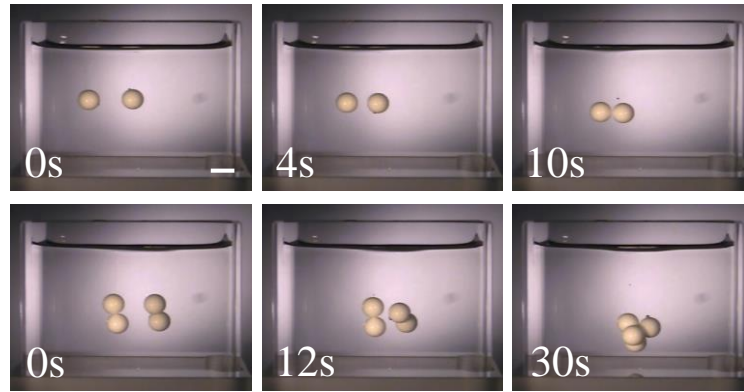
Figure 5.4: The video micrographs (upper panel) illustrate the long range attraction between two ceramic spheres (4.8 mm diameter) submerged inside a soft PAM hydrogel. The micrographs of the lower panel capture the events following the immersion of a glued dimer of similar balls inside the gel. The dimers orient (0s to 12s) as they descend inside the gel and approach each other. Finally (30s), they form a close packed structure. The white scale bar represents 5mm.

sink down further in the gel till they reach a final equilibrium position. This observation clearly illustrates that the elastic energy corresponding to the strain parallel to the surface of the gel is being released with the concomitant decrease in the gravitational potential energy (with some increase of the elastic energy due to the deformation of the gel perpendicular to its surface). The process is by no means entirely passive as evidenced by the slow clockwise and the corresponding counter-clockwise rotations of the two spheres that suggests a relative motion between gel and the spheres, i.e. material is being squeezed out of the space between the spheres.

The sequences involving the attraction and the squeeze out of the gel through the space between two spheres can be observed if ink sports are introduced on the surface of the gel before releasing the balls over it. When the balls descend through the gel, the line

arising from the folding of the gel's surface above each sphere gets intensely colored

as this is where the ink concentrates, which is surrounded by the region with lighter

coloration by the ink. The diffusion of the ink in the gel is relatively slow, so that the
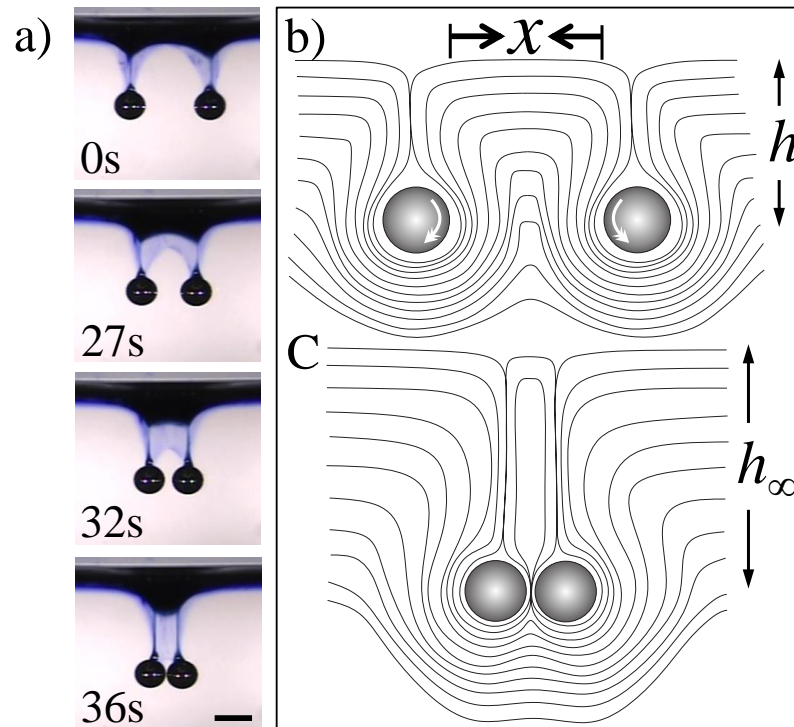
Figure 5.5: (a) The video micrographs show the attraction of two steel spheres of diameter 4mm in a chemically cross-linked gel. This experiment was performed after depositing ink on the surface of the gel with a fine needle. When a sphere is released into the gel, line formed from the folding of the surface of the gel above the ball is clearly highlighted by the intense color of the ink. Some ink is also observed around the line, which reveals that the gel in the intervening space is squeezed out as the spheres attract each other. The black scale bar represents 5mm. The sequence of events in the videographs is shown schematically in (b-c). Here, x denotes the distance between the balls, h is the height of submersion of the balls before contact and h_∞ is the height after contact.

squeeze out of the gel can be clearly observed, in that the inked gel gradually fills up

the space between the lines of contact as the unmarked gel escapes (see also the

schematic of figure 5.5) that region. The change in the total energy (elastic+potential)

of the system has to be proportional to $-mg\Delta h$ in such a process. This can be shown by

writing the elastic and the potential energies of a sphere as $E = \int_{0}^{h} f_{el}dh' - mgh$, where

f_{el} is the force on the sphere due to elastic deformation. Setting $\partial E/\partial h=0$ leads to the

equilibrium condition $mg=f_{el}$. For an elastic deformation, $f_{el}=Ch'^{n}$ (n>1). Substitution

of this expression in the above integral leads to the result: $E = -nmgh/(n+1)$. As the

spheres descend, x decreases and E becomes more negative.
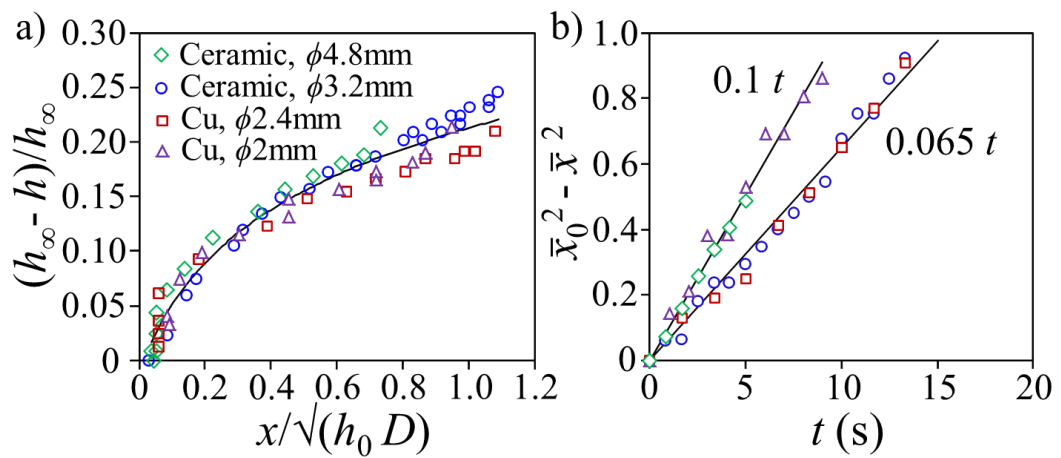
Figure 5.6: (a) This graph reveals the long range nature of the attraction of two solid spheres inside the hydrogel. Here, D is the diameter of the sphere, h_∞ is the depth of the two spheres after they come in full contact, h_0 is the initial depth of the first submerged sphere and h is the average depth of the two spheres (see also the schematic of figure 5.1) that varies with the distance (x) of separation. The black curve was obtained from fitting the experimental data using Origin software, which has the following expression, $\overline{h} = 0.203 + 0.096\ln(\overline{x} + 0.104)$, where $\overline{h} = (h_\infty - h)/h_\infty$ and $\overline{x} = x/\sqrt{h_0 D}$ (b) The squared distance of separation varies linearly with time with correlation coefficients better than 98% . The symbols are same as in figure (a). $\overline{x}_0$ and $\overline{x}$ are the scaled distances of separation at times t=0 and t, respectively.

We should be able to extract a first order estimate of how attractive force varies with

the distance of separation of two spheres from the variation of $-mg\Delta h$ as a function of

the distance of separation. In order to make such an analysis, we measured h as a

function of x for two identical spheres but with materials having different radii and

129

densities. The videos of the experiments involving the attraction of the spheres were decomposed into images in VirtualDub followed by the analysis of those images to obtain the distance of separation between the spheres using the SpotTracker plugin[35] in ImageJ. Although the data obtained from each experiment could be analyzed independently to obtain the distance dependent law of attractive force, it is more convenient to process the data in terms of non-dimensional variables. In that spirit, the depth of the submersion of the ball was divided by the maximum descent of the adhered spheres [$\bar{h} = (h_\infty - h)/h_\infty$], and the distance of separation (x) was normalized by dividing it with $\sqrt{Dh_0}$, where D is the diameter of the sphere and h_o is the initial depth of descent of the first sphere. For a linear elastic system the scale $\sqrt{Dh_0}$ has the same meaning[36] as $\sqrt{mg/\mu}$. An equivalent length can also be extracted for a non-linear elastic gel as well. The experimental data plotted as above cluster around a single curve and can be fitted with a logarithmic function, i.e. $U(\bar{x}) \sim -\ln(\bar{x} + c)$, which is an asymptotic form of a more realistic modified Bessel function ($K_0(\bar{x} + c)$) of the second kind so that $U(\bar{x})$ saturates at large separation distances. The spheres do not interact significantly at large distances, e.g. $x > 1.5$ cm. Here c is a small curve fitting constant that prevents the divergence of the interaction energy at $\bar{x} = 0$. In real situation, the cut-off can be provided by a short range repulsive force between the spheres. The force of attraction obtained from the derivative of $U(\bar{x})$ therefore follows $F(\bar{x}) \sim 1/(\bar{x} + c)$ in conformity with the observation that the interaction is rather long range. This inverse distance law ($F(\bar{x}) \sim 1/\bar{x}$) in conjunction with a linear kinematic friction law ($F_{drag} \sim d\bar{x}/dt$) suggest that the square of the distance of separation would decrease linearly with time, which is also observed experimentally (figure 5.6B).

5.3.3 Motion of a Sphere in a Thickness Graded Gel

The above discussions suggest that two identical spheres approach each other inside a gel following an inverse square law, and with a friction that is linear with the approach velocity. The kinematics should be contributed by such factors as the bulk dissipation in the gel as it folds and relaxes, the relative sliding of the hydrogel surfaces within the contact region, and the relative motion of the sphere inside the capsule it is in.
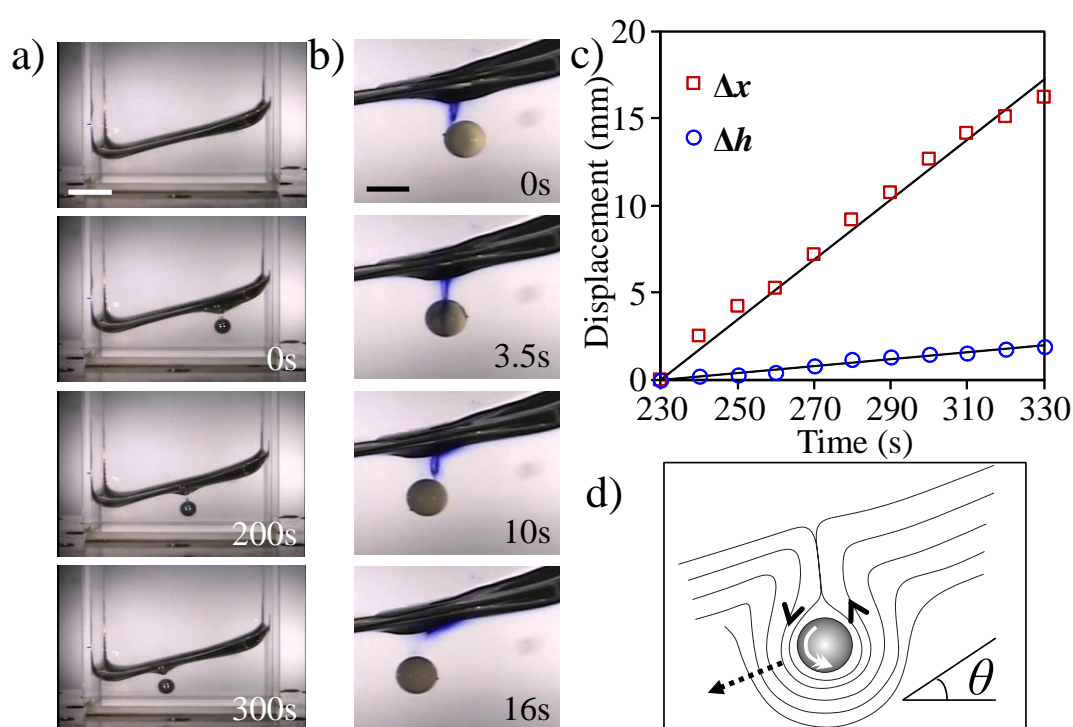
Figure 5.7: The video micrographs in (a) capture the motion of a steel ball (4 mm diameter) on a thickness graded gel, the surface of which is inclined by 14° from the horizontal plane. The gradient is constant and steepest at the central portion of the cell where both the horizontal (x) and the vertical (h) displacements of the ball increase linearly with time (c). The white scale bar represents 10mm. The micrographs in (b) capture the motion of a ceramic sphere (diameter 4.8mm) on a thickness graded gel that had ink marks. As the ball rolls down the gradient, the ink is pulled from the surface, rolls over the ball and finally returns to the surface. The black scale bar represents 5mm. The schematic of the ball rolling down the graded gel is shown in (d).

Motion due to the gradient of elastic strain energy has been observed previously by Hore *et al.*[37] in which the differential swelling of an elastomeric rod created the force

needed to propel it uphill even carrying a load that is larger than the cylinder itself. Style *et al.*[38] used a thickness graded silicone elastomer to study the phenomenon of durotaxis, in which the gradient of elastic strain energy induces a liquid drop to move on its surface. We show here that motion of an object can also be induced by the gradient of the strain energy resulting from the continuous folding and relaxation of the surface of a thickness graded gel. As a sphere submerges inside such an asymmetric gel, it experiences a gradient of strain energy and thus moves from the thicker towards the thinner part of the gel. If ink dots are introduced on the surface of the gel, it can be seen to be drawn inside the gel as the sphere moves and returns to the gel's surface when the sphere passes by it. Within the observation window, where the gel has a constant gradient of thickness, both the descent and the translation of the sphere in the gel increase linearly with time. Since the driving force is equal to the frictional drag force at steady state, we anticipate that $\xi(dx/dt) \sim mg(dh/dx)$, or $\xi \sim mg\dot{h}/\dot{x}^2$, where the dot indicates a derivative with respect to time. Using the data shown in figure 5.7c we estimate the value of ξ to be 1.7 Ns/m. A comparable value of ξ is also needed to explain the dynamics of attraction of two spheres as summarized in figure 5.6B. The fact that the solvent viscosity induced friction coefficient ($\sim 8\pi\eta R$) is orders of magnitude smaller than the above values suggest[39] that the viscous friction related to the rotation of sphere inside the capsule is not the limiting factor in these experiments. The process is most certainly related to the deformation and the relaxation within the volume of the gel that is much larger than that of the sphere.

5.3.4 Interactions between Dimers and Clusters

The long range interaction coupled with the fact that an object can freely rotate inside the capsule created by the surrounding gel lead to several interesting scenarios prevailing in complex geometries. For example, if a dimer made of two glued balls is released inside the gel that already had the dimer formed by the contact of first two spheres, they recognize each other via long range interactions and sample the most stable energetic state by orienting their axes well before coming into an intimate contact. The interaction between small and large spheres is equally interesting in that the smaller spheres of one kind (e.g. copper) released on the surface of the gel gets pulled into contact by a pre-existing sphere of another kind (e.g. a ceramic ball) of a larger diameter. The process continues with the sequential release of small spheres that lead to the formation of interesting patterns some of which are shown in figures 5.8 and 5.9.
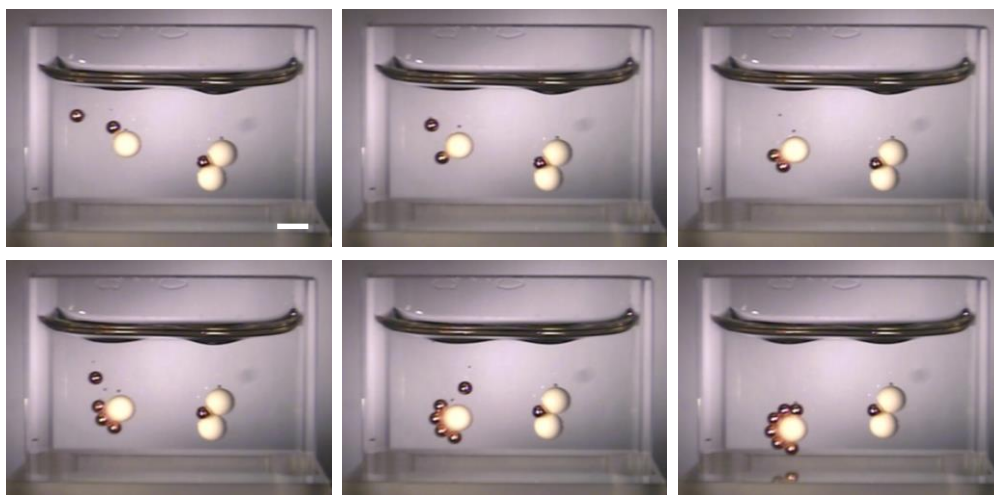
Figure 5.8. These video-micrographs capture the events leading to the formation of a semi-circular ring caused by the attraction between the copper spheres (diameter ~2.4mm) and a pre-existing ceramic sphere (4.8mm diameter) inside the gel. The copper spheres were added sequentially in the gel. The white scale bar represents 5mm.
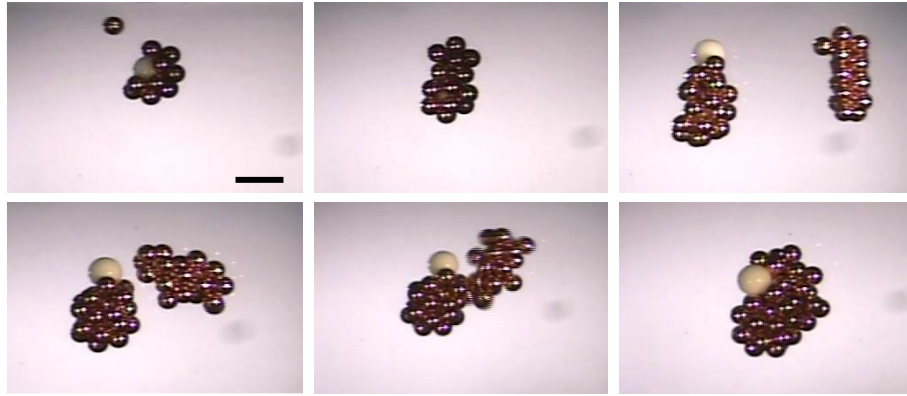
Figure 5.9: The micrographs in the upper panel show the growth of clusters on sequential addition of copper spheres (diameter 2mm) into the gel containing a ceramic sphere (diameter 3.2mm). The growing cluster eventually engulfs the ceramic sphere. When another ceramic sphere is added, it is attracted by the cluster as well. The copper spheres on their own exhibit a structure comprising of parallel columns. When the clusters are large enough (lower panel), they even attract and move towards each other. When the clusters coalesce, further re-organization of the spheres occurs that lead to a close packed state. In the online video, the abrupt stages of the re-organization of the spheres can be seen. These are reminiscent of elastic instabilities and/or plastic events. The black scale bar represents 5mm.

5.4. Conclusions and Outlook

Motions of biological cells[40], liquid drops[38] and defects[41] due to the gradient of elastic strain energy are now known in various settings. The phenomenon reported here is considerably different from these other effects due to the long range nature of the interaction, which manifests macroscopically and which takes advantage of all three forces: elastic, surface tension and gravity in a co-operative way. What we discovered here is essentially the formation of singular line defects that interact via a long range elastic field and even move towards each other thereby giving rise to a viable interaction between suspended objects. Analyses of the interactions of two spheres suggest that the attractive force follows an inverse distance law.

This work illustrates that by intercepting various material scales contributed by the elasticity, capillarity and gravity it is possible to tune in a new type of interaction

134

that would, otherwise, not exist without the co-operative effects of its parts. Although the length scale (millimeter) explored in the current study has its own place in the repertoire of self-assembling systems[42], this philosophy of self-assembly with a tunable interaction may be extended to microscopic size objects with even softer gels and by replacing gravity with an electrical or a magnetic force, or, perhaps, even subjecting the gel to a pre-determined mechanical deformation.

Finally, we feel that a detailed study involving a non-linear field theory is critically needed for further expositions of the types of interactions reported here. This is, however, not a simple proposition as some of the deformations encountered here may go beyond the scope of the existing large strain neo-Hookean models. Hopefully, new theoretical and experimental works will be inspired by the current report. Based on various observations described here, we are, however, hopeful that some simple scaling models might even emerge from rigorous treatments.

References

(1)   Lau, K. H.; Kohn, W. Elastic interaction of two atoms adsorbed on a solid surface. *Surf. Sci.* **1977**, *65*, 607-618.

(2)   Poulin, P.; Stark, H.; Lubensky, T. C.; Weitz, D. A. Novel colloidal interactions in anisotropic fluids. *Science* **1997**, *275*, 1770-1773.

(3)   Ardell, A. J.; Nicholson, R. B. On the modulated structure of aged Ni-Al alloys: with an Appendix On the elastic interaction between inclusions by J. D Eshelby. *Acta Metall.* **1966**, *14*, 1295-1309.

(4)   Dan, N.; Pincus, P.; Safran, S. A. Membrane-induced interactions between inclusions. *Langmuir* **1993**, *9*, 2768-2771.

(5)   Schwarz, U. S.; Safran, S. A. Elastic Interactions of Cells. *Phys. Rev. Lett.* **2002,** *88*, 048102.

(6)   Bruinsma, R.; Pincus, P. Protein aggregation in membranes. *Curr. Opin. Solid State Mater. Sci.* **1996**, *1*, 401-406.

(7)   Goodier, J. N. Concentration of Stress around spherical and cylindrical inclusions and flaws. *J. Appl. Mech.* **1933**, *1*, 39-44.

(8)   Nicolson, M. M. The interaction between floating particles. *Proc. Cambridge Philos. Soc.* **1949**, *45*, 288-295.

(9)   Chan, D. Y. C.; Henry Jr., J. D.; White, L. R. The interaction of colloidal particles collected at fluid interfaces. *J. Colloid Interface Sci.* **1981**, *79*, 410-418.

(10)   Bowden, N.; Terfort, A.; Carbeck, J.; Whitesides, G. M. Self-Assembly of Mesoscale Objects into Ordered Two-Dimensional Arrays. *Science* **1997**, *276*, 233-235.

(11)   Vella, D.; Mahadevan, L. The "Cheerios effect". *Am. J. Phys.* **2005**, *73*, 817−825.

(12)   Botto, L.; Lewandowski, E. P.; Cavallaro, M.; Stebe, K. J. Capillary interactions between anisotropic particles. *Soft Matter* **2012**, *8*, 9957-9971.

(13)   Shanahan, M. E. R.; de Gennes, P. G. Equilibrium of the triple line solid/liquid/fluid of a sessile drop. *Adhesion* **1987** (ed. Allen, K. W.), Elsevier Appl. Sci., London, *11*, 71–81.

(14)   Extrand, C. W.; Kumagai, Y. Contact Angles and Hysteresis on Soft Surfaces *J. Colloid Interface Sci.* **1996**, *184*, 191-200.

(15)   Marchand, A.; Das, S.; Snoeijer, JH.; Andreotti, B. Capillary pressure and contact line force on a soft solid. *Phys. Rev. Lett.* **2012**, *108*, 094301.

(16) Py, C.; Bastien, R.; Bico, J.; Roman, B.; and Boudaoud, A. 3D aggregation of wet fibers. *Europhys. Lett.* **2007**, *77*, 44005.

(17) Cohen, A. E.; Mahadevan, L. Kinks, rings, and rackets in filamentous structures. *Proc. Natl. Acad. Sci.* **2003**, *100*, 12141-12146.

(18) Zimberlin, J. A.; Sanabria-DeLong, N.; Tew, G. N.; Crosby, A. J. Cavitation Rheology for Soft Materials. *Soft Matter* **2007**, *3*, 763-767.

(19) Style, R. W.; Che, Y.; Wettlaufer, J. S.; Wilen, L. A.; Dufresne, E. R. Universal Deformation of Soft Substrates Near a Contact Line and the Direct Measurement of Solid Surface Stresses. *Phys. Rev. Lett.* **2013**, *110*, 066103.

(20) Roman, B.; Bico, J. Elasto-capillarity: deforming an elastic structure with a liquid droplet. *J. Phys.: Condens. Matter* **2010**, *22*, 493101.

(21) Chen, D.; Cai, S.; Suo, Z.; Hayward, R. C. Surface Energy as a Barrier to Creasing of Elastomer Films: An Elastic Analogy to Classical Nucleation. *Phys. Rev. Lett.* **2012**, *109*, 038001.

(22) Majumder, A.; Tiwari, A. K.; Korada, K.; Ghatak, A. Microchannel induced surface bulging of soft elastomeric layer. *J. Adhes. Sci. Technol.* **2010**, *24*, 2681-2692.

(23) Jagota, A.; Paretkar, D.; Ghatak, A. Surface-tension-induced flattening of a nearly plane elastic solid. *Phys. Rev. E* **2012**, *85*, 051602.

(24) Mora, S.; Phou, T.; Fromental, J. M.; Pismen, L. M.; Pomeau, Y. Capillarity Driven Instability of a Soft Solid. *Phys. Rev. Lett.* **2010**, *105*, 214301.

(25) Gonuguntla, M.; Sharma, A.; Sarkar, J.; Subramanian, S. A.; Ghosh, M.; Shenoy, V. Contact Instability in Adhesion and Debonding of Thin Elastic Films. *Phys. Rev. Lett.* **2006**, *97*, 018303.

(26) Huang, J.; Juszkiewicz, M.; De Jeu, W. H.; Cerda, E.; Emrick, T.; Menon, N.; Russell, T. P. Capillary wrinkling of floating thin polymer films. *Science* **2007**, *317*, 650-653.

(27) Nadermann, N.; Hui, C. Y.; Jagota, A. Solid surface tension measured by a liquid drop under a solid film. *Proc. Natl. Acad. Sci.* **2013**, *110*(26), pp.10541-10545.

(28) Chakrabarti, A.; Chaudhury, M. K. Direct Measurement of the Surface Tension of a Soft Elastic Hydrogel: Exploration of Elastocapillary Instability in Adhesion. *Langmuir* **2013**, *29*, 6926-6935.

(29) Edgerton, H. E.; Hauser, E. A.; Tucker, W. B. Studies in Drop Formation as Revealed by the High-speed Motion Camera. *J. Phys. Chem.* **1937**, *41*, 1017-1028.

(30) Cohen, I.; Brenner, M. P.; Eggers, J.; Nagel, S. R. Two fluid drop snap-off problem: Experiments and theory. *Phys. Rev. Lett.* **1999**, *83*, 1147-1150.

(31) These are, however, delicate experiments as the gel gets punctured by the needle, which can be a source of certain artifacts if quantitative analysis is attempted.

(32) Hui, C. Y.; Jagota, A.; Bennison, S. J.; Londono, J. D. Crack blunting and the strength of soft elastic solids. *Proc. R. Soc. London Ser. A* **2003**, *459*, 1489-1516.

(33) Lake, G. J.; Yeoh, O. H. Effect of crack tip sharpness on the strength of vulcanized rubbers. *J. Polym. Sci. A* **1987**, *25*, 1157-1190.

(34) Lake, G. J.; Thomas, A. G. The strength of highly elastic materials. *Proc. R. Soc. London Ser. A* **1967**, *300*, 108-119.

(35) Sage, D.; Neumann, F. R.; Hediger, F.; Gasser, S. M.; Unser, M. Automatic tracking of individual fluorescence particles: application to the study of chromosome dynamics. *IEEE Trans. Image Process*. **2005**, *14*, 1372-1383.

(36) The geometry independent material length scale in this problem could be $\mu/\Delta\rho g$, which, however, yields a fraction of a millimeter. The range of the elastic interaction in our system is in the range of a centimeter. Hence other length scales should be sought. Since the hydrostatic pressure around the sphere falls of as $(R/r)^2$, we could choose the diameter of the sphere to normalize the distance. Empirically, we have also the choice to pick the initial depth of submersion h_0 as the normalizing length scale as the strain field would depend on it. Although reasonable collapse of data was obtained when either of these scales was used, a better collapse of data was obtained when we used a geometric mean of the two: $\sqrt{Dh_0}$. It turns out that this length scale is comparable to the range of long range attraction and is identical to $\sqrt{mg/\mu}$. This situation is remotely comparable to what emerges when a flexible cantilever of bending stiffness $\mathcal{D}$ is peeled from a soft adhesive, in which the material scale of deformation $(\mathcal{D}/\mu)^{1/3}$ is inversely proportional to the shear modulus of the adhesive.

(37) Hore, D.; Majumder, A.; Mondal, S.; Roy, A.; Ghatak, A. How to make a cylinder roll uphill. *Soft Matter* **2012**, *8*, 5038-5042.

(38) Style, R. W.; Che, Y.; Park, S. J.; Weon, B. M.; Je, J. H.; Hyland, C.; German, G. K.; Rooks, M.; Wilen, L. A.; Wettlaufer, J. S.; Dufresne, E. R. Patterning droplets with durotaxis. *Proc. Natl. Acad. Sci.* **2013**, *110*(31), pp.12541-12544.

(39) Lamb, H. *Hydrodynamics*; Dover Publications: New York, 1945.

(40) Lo, C. M.; Wang, H. B.; Dembo, M.; Wang, Y. L. Cell movement is guided by the rigidity of the substrate. *Biophys. J.* **2000**, *79*, 144-152.

(41)   Chaudhury, M. K.; Kim, K. H. Shear-Induced Adhesive Failure of a Rigid Slab in Contact with a Thin Confined Film. *Eur. Phys. J. E: Soft Matter Biol. Phys.* **2007**, *23*, 175-183.

(42)   Whitesides, G. M.; Grzybowski, B. Self-Assembly at All Scales. *Science* **2005**, *295*, 2418-2421.

Chapter 6

Elasto-capillary interaction of particles on the surfaces of ultra-soft gels: a novel route to study self-assembly and soft lubrication[a]

6.1. Introduction

Capillary forces prevailing at the surfaces of liquids are exploited in various fields[1-27], a well-known example of which is the self-assembly of small particles into well-defined two dimensional structures[7-27]. Based on the studies spanning over several decades, the mechanisms underlying such interactions can be broadly classified into two major categories. If the bond number ($\Delta \rho g R^2 / \gamma$), $\Delta \rho$ being the buoyant density of the particle, γ is the surface tension of the liquid, g is the acceleration due to gravity and R is particle's radius) of a particle is significant, it can deform the surface of a liquid. In that case, the effective weight of a particle may be balanced by the capillary force of the deformed liquid surface if the particle is suitably hydrophobic. In delineating such interactions, Nicolson[7] showed that a superposition principle can be used by virtue of which the field energy is expressed in terms of the force that balances the effective weight of a single particle and the profile of the liquid surface that is deformed by the other proximous particle. The net result is that the energy of interaction follows[9-11] a

modified Bessel function of second kind (zeroth order), the argument of which is the ratio of the distance of separation between the two particles and the capillary length of the liquid L_c ($= \sqrt{\gamma / \rho g}$), ρ being the density of the liquid. The Capillary length is an important material length scale in this problem that defines the range over which interaction prevails. Following the lead of Nicolson, several authors[9-11] derived detailed analytical expressions for the attraction between particles of spherical as well as cylindrical geometries on a liquid surface, which resolved some previous incomplete observations and analysis of Gifford and Scriven[8].

If the Bond numbers are very small, the particles can still interact[12,13,19] with each other on a liquid surface if the three phase contact line is uneven either due to chemical heterogeneity, rugosity or other anisotropies. In both cases of low and large particle bond numbers, however, the driving force is derived from the excess energy of the liquid surface intervening the particles. Kralchevsky and Nagayama[13] provided a detailed synopsis of the existing theories of capillary attractions and extended them to the interactions between particles embedded in thin films supported on a solid support. Significant progress has also been made in recent years that is based on the ideas of field theory[28] within the formalism of the Hilbert-Einstein action in a pseudo-Riemannian geometry. There are also various discussions in the literature[20-25] involving capillary interactions in conjunction with hydrodynamic and electrostatic forces leading to the self-assembly of colloidal particles.

Another class of interaction between particles arises due to the elastic forces of the surrounding medium, be it a thin membrane[29-31], an elastic string[32,33], a liquid crystal[34-37] or via an Eshelby type inclusions[38] in an elastic medium. In all these cases, the energetics of elastic distortion provides the necessary force for interaction.

142

Interactions in liquid crystals are of recent interests, where a plethora of studies[35-37] following the lead of Poulin et al[34] shows that the distortion of the director fields in a liquid crystal around the dispersed particles give rise to a short range repulsion but a long range attraction. The orientational elastic energy dependent interaction in a liquid crystal also give rise to an interesting phenomenon as levitation[35,36] of nanoparticles above the ground surface. Elastic interactions in conjunction with defects in liquid crystals[37] have also been used to assemble particles in a pre-determined fashion. Combined effects of elasticity and capillarity have been observed in many two part systems, one of which provides the capillarity and the other elasticity[39-44]. However, to the best of our knowledge the literature is essentially devoid of the studies of interactions in a single medium that display both the above properties.

We recently reported[45,46] some experimental results related to the attraction of two spheres as they plunge deeply into a very soft hydrogel. Here as a sphere penetrates the gel, the neck of contact thins rapidly and forms a line singularity owing to the combined effects of a hoop stress and the adhesion forces thereby ensuring that the gel completely folds and self-adheres over the particle. The excess energy of the deformed surface coupled with the accumulated elastic strain energy is released as the particles approach each other, thus guaranteeing a net attraction[46] between the particles. This emergent[47] attractive force between the particles follows an inverse linear distance law that is long range and induces 3d assembly of small particles inside the gel. In this paper, we study the interactions of small particles that do not deeply plunge inside the gel; rather they float on its surface. This is a simpler system to consider for further exposition of the roles played by the elastocapillarity in the attraction of particles, which is also advantageous in studying the 2d self-assembly processes in a systematic way.

There are several motivating factors for such studies. In recent years[39-46,48-51], the roles played by elasticity, surface tension and the underlying hydrodynamics have captured the imaginations of physicists and engineers to study various phenomena of soft condensed matter. For example, one might be interested to understand how slender objects bend, fold, interact[40] and self-assemble with each other on the surface of a soft support (e.g. water). One may also be interested to develop a system to study the elasticity of particle rafts[48], kinetics of self-assembly of particles that form clusters or even jammed phases[49]. There are also several biological phenomena such as tubulation and phagocytosis that one may wish to mimic on the surface of a soft support[50,51]. Another interesting problem is that of soft lubrication[52,53], in which one is interested how frictional resistance to the motion of a particle develops in a system where elastic as well as hydrodynamic stresses act co-operatively. One envisages that many of the above mentioned phenomena would involve mesoscale level objects, which are amenable to detailed studies using an ordinary microscope and analysis using the models of continuum mechanics. Ordinary liquids with which capillary interactions are studied may not permit many of the mesoscale level objects to float on its surface if they are sufficiently denser than water. Furthermore, even if they float, there is very little control over the range, the strength as well as the time scales of such interactions. What we demonstrate in this work is that an ultrasoft hydrogel with a small amount of elasticity affords enough resistance to prevent sinking of a hydrophobic particle significantly denser than the support itself, while not compromising appreciably its (elasticity modified) Laplace length so that the interactions are long range. The abilities to control the elasticity, the elasto-capillary length and the friction of such a support medium are the unique features of this study that vastly extends those of the generic systems used to study the capillary interactions on liquid surfaces.

We demonstrate the main point of this study by performing a basic experiment in which two equal sized hydrophobized (i.e. PDMS, or polydimethylsiloxane grafted) glass spheres are allowed to interact on the surface of an ultrasoft hydrogel. The field energy of the interaction is estimated from the change in the gravitational potential energy of the particles as they approach each other in conjunction with the well-known superposition principle that was used by Nicolson[7,9] to estimate the same. We validate the underlying scaling analysis with measurements performed with glass spheres of three different diameters, gels of two different moduli as well by reducing significantly the interaction between the particle and the gel by a suitable choice of an external medium. We then show how the knowledge of this field energy of attraction, in conjunction with the speed at which the particles approach each other addresses the role of underlying friction, which is a parameter of importance in soft lubrication. We conclude this study with some demonstrations of how one could begin to study such phenomena as tubulation, phagocytosis and self-assembly in many particles systems.

6.2. Results and Discussion

6.2.1. Estimation of Energy of Interaction using Gravity

In this research, we use the change of the gravitational potential energy to estimate the energy of interaction of two spheres while they attract each other on the surface of a gel. We begin with the pioneering idea of Nicolson[7] that the driving force behind the interaction of the particles is derived from the distance dependent excess energy of the surface of the gel that results from the deformation induced by two proximous particles. There is a synergistic interplay between this force that is horizontal to the surface and the forces that give rise to the vertical stability of the particles. As the particles tend to

145

sink inside a gel due to gravity and the adhesion forces, the hydrostatic and the shear deformation fields due to surface tension and elasticity resist them. The balance of the above forces dictates the mechanical stability of a particle in contact with gel. Now, as the particles are attracted towards each other, the mechanical fields surrounding them interact, parts of which are cancelled thus resulting in further penetration of the particles inside the gel. We observed a similar phenomenon previously for the particles plunged in a gel[46]. Even when there may be some compensation of the gravitational potential energy due to the modification of the elastic strain energy, as we have shown in a recent paper[46], the overall change of the energy still scales with the former. i.e. $\Delta U \sim -m^*g\Delta h$. This would also be the case with a gel undergoing an elastic deformation due to the combined actions of the gravity and the adhesion forces. To elaborate this point, we consider the case of the small deformation of the gel that can be described by the theory of Johnson, Kendall and Roberts (JKR)[54], where the total energy of the system is:

$$U = \frac{Ka^5}{15R^2} + \frac{P^2}{3Ka} - \frac{Pa^2}{3R} - \pi Wa^2 \tag{6.1}$$

$$h = \frac{a^2}{3R} + \frac{2}{3}\frac{P}{Ka} \tag{6.2}$$

Here, K is the contact modulus, P ($\equiv m^*g$) is effective weight of the particle of radius R, a is the radius of the contact circle and h is the depth of the penetration of the sphere inside the gel (Figure 6.4a). Now, using the equilibrium condition: $\partial U/\partial a = 0$, and equation (6.2) we have:

$$U = -\frac{3m^*gh}{5} - \frac{3\pi}{5}Wa^2 \tag{6.3}$$

Equation (6.3) shows that the total energy of the system scales with two quantities: the gravitational potential energy Ph (or m^*gh) and the net energy of adhesion $\sim Wa^2$ in the

small deformation limit. For a very soft gel such as our system, there is an additional energy term in this equation due to the stretching of the soft solid[55] underneath the particle deforming it. Furthermore, as the gel undergoes a large deformation, the above JKR equation requires modification[56]. Nevertheless, we expect that the total energy will scale as follows:

$$U \sim -m^* gh - \Delta\gamma A_{contact} \qquad (6.4)$$

Where, $A_{contact}$ is the area of contact between the gel and the sphere, and $\Delta\gamma$ is the net change of the interfacial free energy. Furthermore, in the process of the penetration of the particle in the gel, if the contact line is pinned so that the energy due to the stretching of the gel as well as the energy of adhesion remain more or less constant as the particles approach each other, the overall change of the energy of the system would scale simply with the gravitational potential energy $m^* gh$. A variation of h (i.e. Δh), thus, provides a simple option to gauge how the interaction energy scales with the distance of separation even in the absence of a detailed knowledge of the system. There is also Nicolson's method of expressing the energy of interaction in terms of the separation distance L as $\sim m^* gh_o K_o(L/L_c^*)$, where L_c^* is the elastocapillary decay length that determines the range of interaction and h_0 is the vertical distance of the three phase contact line from the undeformed free surface of the gel (figure 6.4a). The above two forms of estimating interactions energies are equivalent. Thus, to a good order approximation, we may write:

$$m^* g\Delta h \approx m^* gh_o K_o(L/L_c^*) \quad \text{or,} \quad \frac{\Delta h}{h_o} \approx K_o(L/L_c^*) \qquad (6.5)$$

There are certain details about non-linear elasticity that are ignored in the above discussion. We anticipate that an equation of the type described as above would also be

valid in a neo-Hookean gel even though the prefactor may be different. Derivation of equation (6.5) is based upon several approximations and conjectures. We are thus obligated to test its validity experimentally by studying the interaction of two millimeter sized spheres on the surface of low modulus gels where the elastocapillary decay length can be estimated independently. As the particles attract each other, we measure how much they sink (Δh) inside the gel as a function of L. By carrying out experiments with particles of different diameters, using gels of different moduli and virtually switching off the adhesion term by appropriate choice of the surrounding medium, we examine if the data obtained from various experiments would exhibit an universal behavior, i.e. if $\Delta h/h_o$ varies with L/L_c^* following a modified Bessel function of the second kind. In order to achieve the above stated goal, our first objective, however, is to examine how the elastocapillary decay length L_c^* depends on the elasticity of the gel from which to select the appropriate gels for the above stated measurements and analysis.

6.2.2. Capillary Length L_c for water and Elastocapillary Decay Lengths L_c^* for Gels.

Capillary length describes the extent of deformation of a liquid surface due to the competition between the gravity and the surface tension forces. For a liquid surface of surface tension (γ) and density (ρ), this parameter is defined as $L_c = \sqrt{\gamma/\rho g}$, g being the acceleration due to gravity. For pure water, L_c is about 2.7 mm. However, with a hydrogel, this length is expected to be lower than the above value as the elastic modulus of the gel provides additional resistance to surface deformation. We refer this length L_c^* to as 'elasto-capillary decay length' for gels where both elasticity and capillarity contribute. A formal approach to estimate the deformed profile of the surface of the gel

would be via a functional minimization of the Lagrangian of the system consisting of the gravitational, surface and the elastic energies with respect to the surface elevation [$\xi(L)$] (see figure 6.1a for definition of $\xi(L)$), which is postponed for a future publication. We expect that the gravitational and the normal component of the elastic stress would tend to increase the curvature of the gel surface, whereas surface tension and the elastic shear stress would flatten it. The final shape of the surface of the gel is determined by the balance of the above components of stresses, which we examine experimentally and provide a scaling level description of the surface profile as discussed below.

We estimated the elastocapillary decay length by performing experiments with water and gels of different elastic moduli (35Pa to 845Pa), in which a pre-adhered hydrophobic sphere (diameter 2.4mm) was pulled from the surface of either water or a gel and its deformation profile was measured with a microscope. The deformed profile of each of the surface could be fitted with a modified Bessel function of second order of the form $K_0(L/L_c^*)$ from which the characteristic length scale of the deformation L_c^* was obtained (figure 6.1a). In our hand, the value (2.4 mm) of L_c for pure water is found to be slightly smaller than its theoretical value (2.7 mm). As the surface tension of water used for these measurements is close to the literature value, we ascribe this discrepancy to putative experimental shortcomings. Fortunately, the discrepancy is not significant. It is reasonable to expect that the value of L_c^* of the elastic gels would be reduced from that (L_c) of pure water ($\mu=0$: $\sqrt{\gamma/\rho g}$ ~ 2.4 mm) by a function of the elastocapillary number $\mu\xi_0/\gamma$, i.e. $L_c^* = L_c f(\mu\xi_o/\gamma)$, ξ_0 being the maximum elevation of surface (figure 6.1a). The function should have the following properties: $\mu = 0 : f(\mu\xi_o/\gamma) = 1$,

and $\mu \rightarrow \infty : f(\mu\xi_o/\gamma) \rightarrow 0$. Among various possibilities, a functional form of the type $f(\mu\xi_o/\gamma) \sim \exp[-(\mu\xi_0/\gamma)^n]$, with $n \geq 1$, satisfies the above limits and partially justifies the observation that L_c^* decreases exponentially with modulus, i.e. $L_c^* = L_c \exp(-B\mu)$ (Figure 6.1b). Figure 6.1c, however, shows that L_c^* decreases fairly linearly with $\mu\xi_0/\gamma$, i.e.

$$L_c^* \cong L_c \left(1 - \frac{\mu\xi_0}{4\gamma} \right) \qquad (6.7)$$

Equation 6.7 does not satisfy the upper limit, i.e. when the shear modulus of the gel becomes extremely large. This equation is likely a low modulus limit of a hitherto undetermined function (figure 6.1c) relating L_c^* and $\mu\xi_0/\gamma$ over a larger range of moduli.

6.2.3. Attraction of spheres on the surface of gel.

Based on the estimation of the elastic moduli and the elastocapillary decay lengths of gels of different amounts of acrylamide compositions, we found that the gels of modulus ranging from ~ 10 Pa to ~20 Pa are most suitable for studying the elasto-capillary mediated interactions of particles on the surface of a gel. Elastic moduli in this range are significant enough to resist sinking (Figure 6.3b-d) of the glass spheres of radii ranging from 2 to 4 mm in the gel provided that the glass is made suitably hydrophobic, with which water exhibits a contact angle of ~ 113°. These glass particles, be they hydrophobic or hydrophilic, however, immediately sink in water as their Bond numbers are not significantly lower than unity. The relationship between floatability of a particle and its wettability on a liquid surface has already been discussed previously by Marmur et al.[57], albeit for low Bond number systems. The current observations
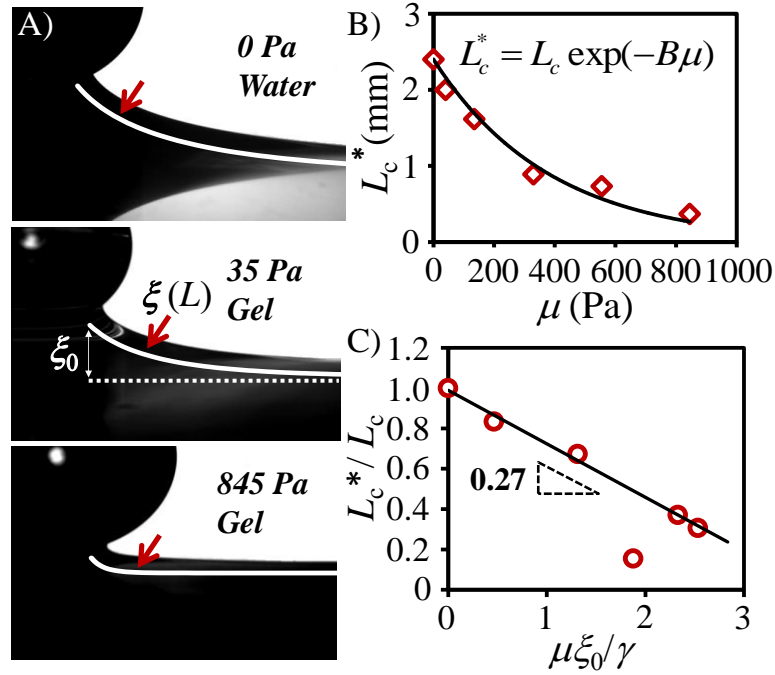
Figure 6.1: (A) Deformed surface profiles of water, and two representative gels are shown. In each case, a 2.4mm diameter PDMS grafted glass sphere was used to deform the surface. The white curves show the fitted Bessel function [$\xi(L) = \xi_0 K_0 (L/L_c^*)$] to match the deformed surface profiles. For clarity the fitted curves have been shifted from the deformed surface profiles along the direction of the red arrows. (B) The plot shows how the elastocapillary decay length decreases with the shear modulus (μ) of the gel. The red open diamonds denote the experimental data and the solid black line is fitted according to $L_c^* = L_c \exp(-B\mu)$ with a value of B as 2.6x10^{-3} m^2/N. (C) This plot shows that the elasto-capillary decay length decreases with the elasto-capillary number ($\mu\xi_0/\gamma$) for gels of shear modules $\leq$555 Pa. The datum for a gel of even a higher modulus (845Pa) deviates from the plot.

suggest a worthwhile new direction for these studies when an ultra-low modulus gel is concerned. However, as the focus of our current study is on how the hydrophobic particles interact with each other on the surface of a low modulus gel, the detailed subject of particle floatation by the combined actions of gravity, elasticity and wettability is deferred for a future in-depth study.

151

Figure 6.2: (A) Figure illustrating fine balances of the elastic, wetting and gravitational forces giving rise to different types of stabilities of glass spheres (3.2 mm diameter) released on the surface of a polyacrylamide hydrogel of modulus 10 Pa. An untreated (hydrophilic) glass sphere (right) immediately plunges into the gel and becomes neutrally buoyant afterwards. A hydrophobic glass (left) floats on the surface of the same gel. (B) This is an extension of the experiment in A, that shows when another hydrophobic particle is released in between the two, (C) it gets strongly attracted toward the hydrophilic particle, but moves on the gel's surface to minimize its distance of separation from the latter.

The value of L_c^* of a gel of $\mu \sim$ 10 Pa to 20 Pa is large (~2.34mm to 2.28mm) enough that capillary interactions are expected to prevail at a distance comparable to that (2.4mm) of pure water. This hypothesis is tested with a basic experiment, in which we place two glass spheres of equal radii on the surface of a gel at a suitable distance of separation then examine how they attract each other. As stated earlier, a hydrophobic glass particle of any size ranging from 2.4 mm to 4 mm diameter floats on the surface of a PAM gel of modulus ~ 10 Pa to 20 Pa after penetrating the gel partially. When the second sphere is released at a distance of about 1 cm from the first sphere, we studied their mutual attraction on the surface of the gel till they finally come into contact, while penetrating a little further down into the gel yet floating on the surface. Some representative sequences of events of the elastocapillary mediated attraction of particles of three different sizes are shown in figure 6.3, where the curvature of surface of the gel intervening two spheres are clearly perceptible. Incomplete wrappings of the gel around the PDMS grafted spheres are also evident in these images, a schematic of which is illustrated in figure 6.4a defining the various parameters that are measured for quantitative analysis of the experimental data. In particular, we measured the average

152

depth of penetration h of both the spheres in the gel with respect to the distance of separation L. The depth (h_0) of the three phase contact line from the flat surface of the gel was also measured for each experiment and the average value for a set of similar experiments was used for the analysis to follow.
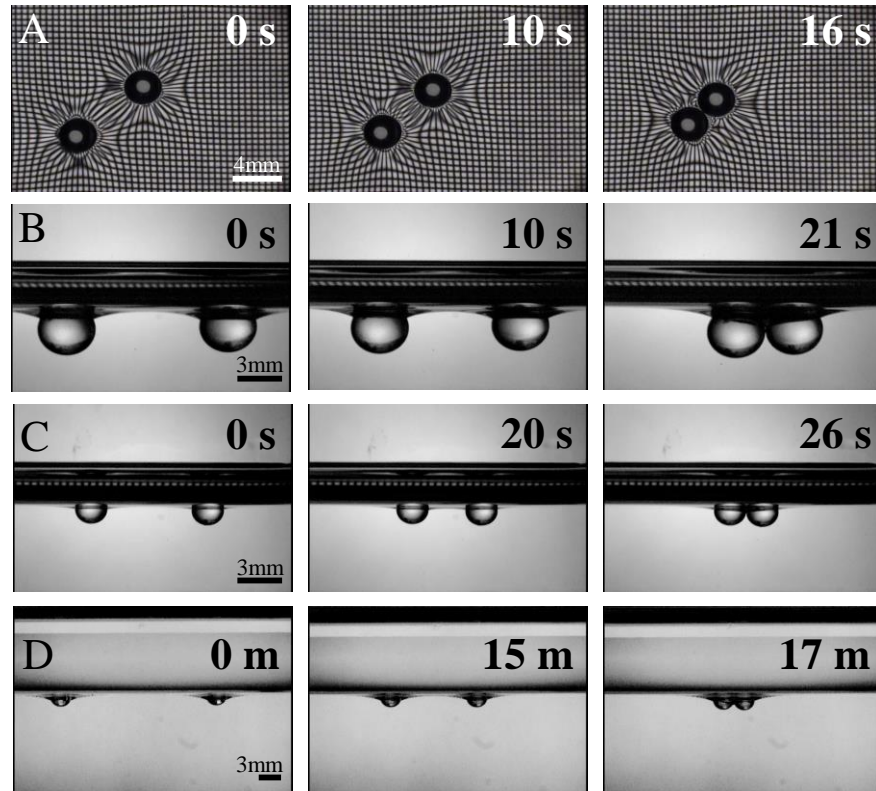
Figure 6.3: (A) A plan view of the interaction of two 3.2 mm hydrophobic glass spheres on the surface of a 10 Pa gel. A wire mesh lined with the base of the glass cell shows the field of deformation of the surface of the gel around the particles. (B) Attraction of the two 4 mm diameter hydrophobic glass spheres on the surface of a 10Pa gel in air (C) Attraction of the two 2.4 mm diameter hydrophobic glass spheres on the surface of a 10Pa gel in air (D) Attraction of the two 2.4 mm diameter hydrophobic glass spheres on the surface of a 10Pa gel in contact with heptane.

For each case, the experiment was repeated at least three times or more to ensure reproducibility. While it is possible to carry out these experiments with a gel of modulus ~140Pa with a significant enough L_c^* (1.62 mm), it was inconvenient to measure Δh and h_o accurately as both these parameters strongly decrease with the elastic modulus. We thus restricted our experiments to two gels of moduli 10 Pa ($L_c^* = 2.34$mm) and 19 Pa

153

($L_c{}^* = 2.28$mm), the L_c values having been estimated from the empirical relationship obtained in figure 6.1(b).
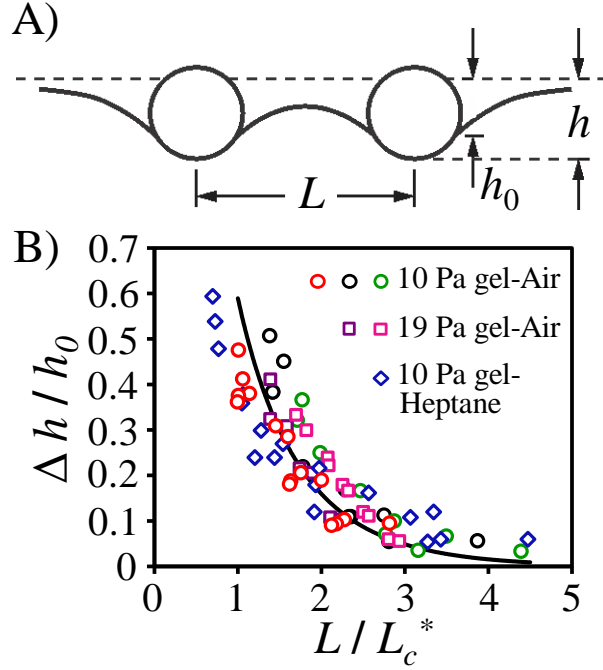
Figure 6.4: (A) Schematic showing elastocapillary attraction of two spheres of identical sizes at a distance L. h denotes the depth of submersion of the ball with respect to the initial undeformed level of the gel. The change of h as the spheres approach each other is denoted by Δh (see text and figure 6.4b) h_0 is the vertical distance of the three phase contact line from the undeformed free surface of the gel when the spheres are far apart. (B) The change in the depth of separation Δh scaled with h_0 is plotted as a function of the non-dimensional distance of separation ($L/L_c{}^*$). Data from all the experiments cluster around the mean curve $\Delta h / h_0 = 1.5 K_o(L/L_c^*)$. The open circles [diameters: 2.4mm (red), 3.2mm (black) and 4mm (green)] denote the 10 Pa gel-Air data. The open squares [diameters: 3.2mm (purple) and 4mm (pink)] denote the 19 Pa gel-Air data. The blue open diamonds (diameter 2.4mm) denote the 10 Pa gel-Heptane data.

In order to compare the results obtained from various experiments, we plotted the normalized average descent of the spheres in the gel, $\Delta h/h_o$, against the normalized separation distance $L/L_c{}^*$ (figure 6.4b). It is gratifying that all the data plotted this way cluster around a mean curve $\Delta h / h_0 \propto K_o(L/L_c^*)$ with a proportionality factor of 1.5 that is close to unity expected from a simple model (equation 6.5) discussed as above.

Note: h_o (figure 6.4a) has the same physical meaning as ξ_0 (figure 6.1a) in that both describe the vertical distance of the three phase contact line from the undeformed free surface of the gel. While ξ_0 depends on the vertical displacement of the sphere that is controlled externally, h_o is determined by the internal balance of different forces.

6.2.4. Attraction of spheres at the interface of n-heptane and gel.

In all the experiments described in section 2.3, adhesion plays a significant role in the sense that the gel wraps around the particle so much that the effective h_o is rather small. One can surmise that if the interfacial adhesion is decreased, the gel would undergo mainly a Hertzian deformation meaning that the sphere mildly deforms the gel so that the value of h_o would increase. The adhesion energy in this system could indeed be reduced considerably by replacing the upper air-layer over gel with n-heptane. The free energy of adhesion between a PDMS grafted glass particle with the gel is[58]:

$$\Delta G_{132} = -2(\sqrt{\gamma_1} - \sqrt{\gamma_3})(\sqrt{\gamma_2^d} - \sqrt{\gamma_3}) \tag{6.8}$$

Where, γ_1 is the surface energy (totally dispersive) of PDMS ($\sim$ 22 mN/m) , γ_2 is the dispersion component of the surface energy ($\sim$ 21.8 mN/m) of the gel, and γ_3 (20.1 mN/m) is the surface tension (totally dispersive) of n-heptane. The adhesion energy of the hydrophobic glass particle with the gel is thus estimated to be -0.08 mJ/m^2 which is negligible compared to the expected value of -44mJ/m^2 in air. h_0 (0.87 mm) of a small particle released on the surface of the gel of modulus 10 Pa through heptane is indeed found to be larger than that (0.32 mm) in air. L_c^* of the gel-heptane interface was measured by releasing a 4 mm diameter hydrophobic glass sphere at the interface and measuring the deformed profile of the same as it bent towards the gel. This contrasts

the method used in air, where a pre-adhered sphere was pulled away from the gel-air interface (Figure 6.1a). The deformed profile at the gel-heptane interface could also be fitted with a modified Bessel function thus yielding an elastocapillary decay length of 3.5 mm, which is found to be larger than the value (2.34mm) of the same gel in contact with air. It is reassuring that the above value of L_c^* is close to that (3.9 mm) estimated using the empirical relationship $L_c^* = L_c \exp(-B\mu)$ (figure 6.1b), in which $L_c = \sqrt{\gamma_{int}/\Delta\rho g}$ is calculated using an interfacial energy (γ_{int}) of the gel-heptane interface as 51mN/m (~ the value at heptane-water interface) and $\Delta\rho$ (the difference in the densities of water and heptane) as 316 kg/m^3. These measurements exemplify that the elastocapillary decay length of an interface can indeed be modified by its surface tension. As a consequence of both larger values of h_o and L_c^*, the spheres recognize each other at a distance much larger than they do on the gel in contact with air. The strength of the interaction is also larger as evidenced from the fact that the net change of the gravitational potential energy for the spheres in going from an infinite separation distance to contact at heptane-gel interface is three times larger than that at air-gel interface. However, the normalized descent of the spheres in the gel, $\Delta h/h_o$, when plotted against L/L_c^* (figure 6.4b) still cluster around the same mean curve obtained from the experiments at air-gel interface.

6.2.5. Role of friction in elasto-capillary attraction: Difference at Gel-Air and the Gel- heptane interfaces

Apart from quantifying how the surface tension and the elastic forces play joint roles in determining the energy of interaction of two spheres on the surface of a soft gel, these experiments also have fascinating prospects in studying how the coupled elastic and

156

hydrodynamics forces play their roles in determining the friction of the spheres with gel. This subject is of interest in the field of so called[52] "soft lubrication", in which both elasticity and hydrodynamics play their respective roles. We begin with the asymptotic logarithmic form of the energy of interaction of the spheres as given in equation (6.5), the derivative of which gives the force of interaction as: $m^* g h_0 / L$. If we assume that this force is balanced by a kinematic resistance that is linearly proportional to velocity, we have:

$$\zeta(-dL/dt) \sim m^* g h_0 / L \qquad (6.9)$$

$$\text{Or,} \quad -L^2/t \sim m^* g h_0 / \zeta \qquad (6.10)$$

Where, ζ is the kinematic friction coefficient. Equation 6.10, in which the negative effective diffusivity (L^2/t) is inversely proportional to friction coefficient, pleasantly is the deterministic analog of the well-known Einstein-Sutherland's equation[59] connecting diffusivity and friction. Here, $m^* g h_0$ is equivalent to an "effective gravitational temperature" introduced earlier by Segre et al[60] in the context of sedimentation of particles. According to equation 6.10, a plot of L^2 versus t should be linear, the slope of which is inversely proportional to the kinematic friction coefficient. The dynamics of the attraction of spheres at the gel-heptane interface is quite different from that at the air-gel interface in that the time taken for the two spheres to come into contact in the former case is much larger than that at the gel-air interface. L^2 is fairly linear with t in both cases (figure 6.5), which further ascertains that the friction is fairly linear with velocity and that the form of the attractive field energy is asymptotically logarithmic at a short separation distance. The slope of the L^2-t for the heptane-gel interface (0.25 mm²/s) is, however, an order of magnitude smaller than that at the air-gel interface (2.3 mm²/s) thus ascertaining the large differences in the friction in both cases. With the

157

appropriate values of h_o and the fair estimations of the buoyancy corrected weights of the spheres in the two cases, we estimate that the kinematic friction coefficient at the heptane-gel interface is about 20 times larger than that at the gel-air interface. The absolute value of ζ for the 2.4 mm diameter spheres attracting at the heptane-gel interface (equation 6.10) is estimated as 0.7 $Nm^{-1}s^{-1}$ whereas that from Stokes drag force ($\sim 6\pi\eta R$) is estimated as 8.7x10^{-6} $Nm^{-1}s^{-1}$ in Heptane. This large discrepancy of the values of ζ suggest a complex origin of friction, part of which could be arising from the deformation of the gel and part due to the wedge flow of the liquid heptane near the sphere-gel interface. The friction coefficient for the spheres undergoing attraction at the gel-air interface is estimated to be 0.03 $Nm^{-1}s^{-1}$. In our previous study involving the attraction of particles that were completely submerged inside the gel, the friction coefficient was estimated to be 1.7 $Nm^{-1}s^{-1}$,[46] which is much higher than the friction coefficient value observed for the spheres in the present study where they are only partially wrapped with the gel surface.
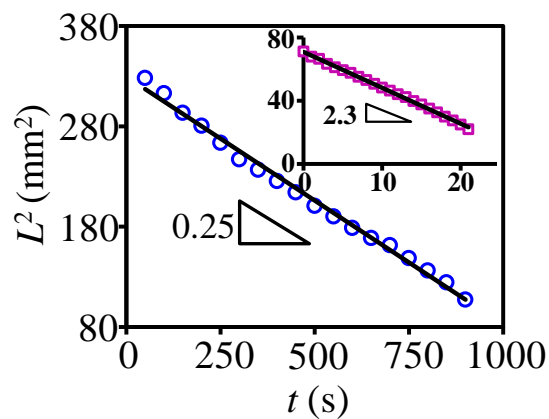
Figure 6.5: This plot shows that the squared distance of separation between two interacting particles decreases linearly with time. The blue open circles correspond to the 2.4mm diameter spheres at the gel- heptane interface. (Inset) The pink open squares correspond to the 2.4mm diameter spheres at the gel- air interface. The shear modulus of the gel in each case is 10 Pa.

6.2.6. Tubulation and Self-Assembly of spheres at the n-Heptane and Gel interface

The long range interaction of the particles in a gel coupled with the fine balance of forces that give rise to their stability perpendicular to the surface of the gel, can give rise to several interesting scenarios mimicking phenomena in biological and other settings[50] that are worth studying in detail. Here we provide two examples: tubulation and self-assembly of the particles at the heptane-gel interface. In our experiments, tubulation has frequently been observed with a very soft gel (10Pa) when covered with a layer of n-heptane that reduces the adhesion energy and thus the propensity for the gel to completely wrap around the particles.
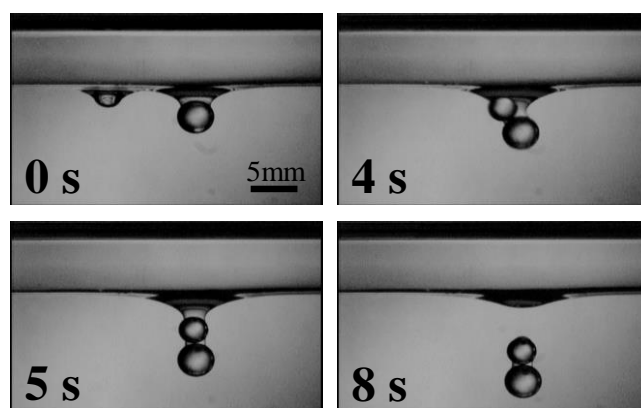
Figure 6.6: A 3.2mm diameter hydrophobic glass sphere is attracted towards a 4mm size hydrophobic glass sphere. As the two spheres contact each other, the pair re-orients inside the tube adjoining the two (tubulation). Finally, the pair penetrates inside the gel and becomes stagnant to a point where it becomes elasto-buoyant.

When a large particle (4 mm) is first introduced on the surface of such a gel, it attains its stability after penetrating the gel to a significant distance, whilst still remaining on its surface (Figure 6.6). However, when a smaller particle (3.2 mm) is released at a distance of about 9 mm from this particle, it traverses on the surface to reach the larger particle due to elastocapillary attraction. As the two particles touch each other, the pair

re-orients and inserts itself in the gel till the accumulated strain induced elastic force

balances the combined weight
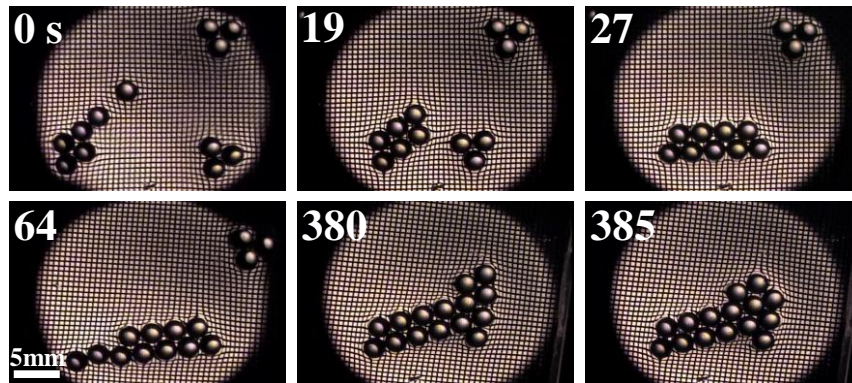
Figure 6.7: A plan view of elastocapillary surface force mediated self-assembly of 2.4mm silanized glass spheres at the interface of a gel (10Pa) and n-heptane. As the spheres are randomly dispersed on the surface of the gel through heptane, they form random clusters, which then move towards each other forming one large cluster. A wire mesh lined with the base of the glass cell shows the field of deformation of the gel surface.

of the particles. The sequence of events mimics what is known as tubulation in

biomembrane system, which underlies the interactions and penetrations of

nanoparticles through a biological membrane[49]. However, it is important to emphasize

that the range, the strength and the origins of interactions here are quite different from

what is observed in typical biomembrane sytems. What is presented here is only a

mimicry of the biological phenomena in a mesoscale level system.

Another observation is the self-assembly in a many particle system that is observed

when several small particles are dispersed on the surface of the gel under heptane

(figure 6.7). The experiments shown in the pictures were performed using silanized

glass spheres, although same kind of interfacial self-assembly was also observed with

PDMS grafted glass spheres. The particles attract and form various structures

resembling chains and triangles. These clusters eventually are attracted towards each

other thus forming larger aggregates. These types of phenomena are generic with

particles dispersed on the surface of liquid, such as water. However, here, the ability to control the range and the strength of the interaction through the modulation of elasticity, the interaction forces, as well as the friction, the parameter space of investigation can be vastly enhanced. Thereby, these systems could potentially be used to study nucleation and clustering phenomena in a 2d system more rigorously than what might be possible with a liquid surface alone.

6.3. Reiterating the Main Points

The elastocapillary force mediated attraction of particles on the surface of an ultra-soft gel follows a modified Bessel function of second kind (zeroth order) much like the generic capillary attractions of particles on the surfaces of liquids. For an elastic hydrogel, however, the range of interaction is reduced by its elasticity, which has implications in designing systems where the range of attraction can be tuned in by the elasticity of the support. A simple relationship between the descents of the particles in the gel with their distance of separation was developed by equating the change of the gravitational potential energy of the attracting spheres with a well-known form of interaction obtained from the superposition principle of Nicolson. Though shrouded by some uncertainties of the implicit assumptions and approximations, the proposed relationship stood firmly against the experimental tests involving spheres of different sizes suspended on gels of different moduli, even when the adhesion of a gel/particle interface is almost non-existent. This experimental assertion gives us confidence to consider that the main physics underlying the interactions of particles on the surface of an elastic gel has been essentially captured. There are, nevertheless, some differences in the data obtained from one set of experiment to another. While, part of this

discrepancy is due to experimental uncertainties, a more precise analysis of the data by taking into consideration the second order effects resulting from the stretching of the gel, its large deformation neo-Hookean behavior and some change of the interfacial energy in those cases where the contact lines are not entirely pinned on the descending spheres may also be required.

In all cases, the particles approach each other with a negative effective diffusivity that is a deterministic analog of the Einstein-Sutherland's relationship. This is a consequence of an attractive force varying inversely linearly with the separation distance and the dynamics of motion being governed by a linear kinematic friction. A surprising observation of this study is that the kinematic friction of the sphere on the gel in contact with heptane is substantially larger than that in air. This, we believe, presents itself as an important problem of soft lubrication that deserves detailed in-depth investigation. While in a thermal system, the particles would move away from each other, here they come closer, i.e. they diffuse negatively with an effective gravitational temperature. An effective gravitational temperature was introduced earlier[60] in the context of the sedimentation of the particles. However, as the "effective gravitational temperature" as introduced here does not possess the feature of fluctuation that allows particles to explore the entire phase space, no major issue is to be made of out of it other than treating this quantity as an "intensive property" of the system that gives rise to an effective diffusion like kinetics. We expect that the putative analogy may be more useful for an ensemble of a large numbers of particles, where they could form random clusters and could even move against a concentration gradient. This particular feature could be interesting in setting up experiments to study clustering phenomena and phase separation kinetics in mixed particle systems.

Elucidation of the nature of friction in such systems is an important challenge, a satisfactory resolution of which would require full knowledge of whether the spheres rotate or slip, and if the wedge flow of the surrounding liquid through the gap formed by the sphere on the gel (that has a diverging stress) plays any role. Preliminary studies with the attracting spheres do not show any clear evidence of rotation as they approach each other, even though, surprisingly, some azimuthal motion of the spheres was noticeable. The subject promises rich underlying physics of soft lubrication, which is a coupled problem of hydrodynamic flow and elastic deformation. Nevertheless, the fact that friction can be modified in such systems provides another avenue to manipulate the dynamics of the motion of the particles as much as the range and the strength of interaction can be modulated by appropriate choices of the surface tension and the elasticity of the gel itself.

We end this section by commenting that what we learned here involving the interaction of particles on the surface of a gel can be combined with what we reported earlier[46], namely the interaction of particles deeply plunged inside a gel in order to enhance the overall scope of the elasto-capillary mediated interactions of particles in a gel. This philosophy can be illustrated with a simple example described in figure 6.2, in which a hydrophilic glass particle plunges inside a gel and a hydrophobic particle released far away from this one floats on the gel's surface. If however, a second hydrophobic particle is released in between the two, it gets attracted more strongly towards the hydrophilic particle, but moves on the gel's surface in order to minimize its distance from it. This observation, in which a floating particle interacts with the strain field produced by a submerged particle, may give rise to new twists to particle interactions that have not been exploited thus far. Thus, artificially created elasto-capillary field

inside a gel may be a novel way to assemble particles on its surface that may even be extended to those of colloidal dimensions.

6.4.   Summary and Conclusion.

This study shows that elastic forces coupled with surface tension are advantageous in studying the attraction mediated 2d organization of particles on a soft support. Dense particles can be easily dispersed on such a support that would otherwise sink in normal liquids. Further control of the particle interaction, i.e. its range, strength and dynamics, can be easily achieved. It should also be possible to support a relatively thin (~ few millimeter) layer of hydrogel on an elastomeric support, e.g. a crosslinked polydimethyl siloxane, that can be stretched or compressed uniaxially or biaxially to induce surface folding, or in which patterns can be formed via an external field, in order to add additional degrees freedom to manipulate interactions and self-assembly of particles suspended on the surface of the gel. This configuration could be particularly useful in studying the elasticity and the buckling transitions of particle rafts formed by self-assembly. These studies are poised for further explorations in many particle systems to gain deeper understanding of such phenomena as clustering, jamming, tubulation and possibly phase separation kinetics in mixed systems.

6.5. Experimental Details.

6.5.1. Materials.

The soft elastic hydrogel was prepared using the following materials: N-(hydroxymethyl)-acrylamide (48% solution in water, Sigma Aldrich), deionized (DI) water (Thermo Scientific Barnstead E-pure unit), potassium persulfate (99.99% trace

metals basis, Sigma Aldrich), and N,N,N',N'- tetramethylethylenediamine (TEMED, ≥ 99.5%, purified by re-distillation, Sigma Aldrich). Heat resistant borosilicate glass spheres (density 2.2 g/cc; their diameters ranging from 2.4mm to 4mm) purchased from Winsted Precision Ball Company through McMaster Carr were used for this study followed by surface using as received trimethylsiloxy-terminated polydimethylsiloxane (DMS T-22, M.W. 9430; Gelest Inc.). 1H,1H,2H,2H-perfluorodecyltrichlorosilane (FC-10, 96%; Alfa Aesar) was used as received for the silanization of particles. For most of the experiments involving the study of interaction between the spheres on the surface of the gel, home built glass cells (each being approximately 70mm x 40mm, 50mm high) were used. The glass cells were built from glass slides (75mm x 50mm x 1mm, Fisher Scientific) by using Permatex 80050 Clear RTV Silicone Adhesive Sealant. These cells were thoroughly cleaned with DI water and blow-dried with nitrogen gas before use. For the measurement of the capillary length and elastocapillary decay length (L_c^*), the gels were cured in a polystyrene petri dish (VWR, 100mm diameter, 15mm high) that were purchased from Fisherbrand. All experiments for the measurement of the elastocapillary decay length L_c^* were performed after placing the test petri dishes on a 3d manipulated stage that was situated on the top of a vibration isolation table (Micro-g, TMC). In some experiments, n-heptane (HPLC grade, Fisher Chemical) was used as received. A steel washer with cadmium coating (1" diameter, Aspen Fasteners) was used for the magnetic material in shear modulus measurement experiments.

6.5.2. Preparation of Gel.

Gels of different concentrations ranging from 3.2% to 5.5% of acrylamide monomer [N-(hydroxymethyl)-acrylamide] were prepared by adding the appropriate amount of monomer to DI (distilled deionized) water in a clean jar. The dilute solution of acrylamide monomer in DI water was stirred for 30 minutes with pure nitrogen gas bubble purging through it. After this step, 0.25% of potassium persulfate was added to the solution and further stirred for 10 minutes. The final step was completed by adding 0.3% of TEMED to the solution following which the gelation begins. For the determination of L_c^*, the freshly prepared gel solution was immediately poured into a polystyrene petri dish till its brim. The entire dish was then placed in a larger glass petri dish containing stacks of DI water-soaked papers to maintain a water vapor-rich environment inside. The estimation of L_c^* was performed on the next day. To study the attraction of the spheres, the gels were cured in the home built glass cells that were covered by glass lids wrapped with parafilm to seal the cell moderately well that effectively prevents the drying of the upper surface of the gel. For the measurement of the shear moduli, the gel was cured in a parallel plate geometry sandwiched between a lower clean glass plate (75mm x 50mm x 1mm, Fisher Scientific) and either a clean cover slip (60mm x 24mm x .18mm, Corning) for softer gels or a clean glass plate (75mm x 25mm x 1mm, Fisher Scientific) for comparatively higher modulus gels. The two glass plates were separated by 1mm thick Teflon coated glass spacers, one each on either side, for their easy removal after the gel cured. The whole setup was placed inside a large polystyrene petri dish with stacks of filter papers soaked with DI water to minimize the evaporation of water from the gel slab. The glass plates in the cure geometry for the shear modulus experiments were pre-marked with a permanent marker to determine the dimensions of the gel slab.

6.5.3. Surface Modification of the Glass spheres.

The glass spheres (2.4 mm to 4 mm diameter) were coated[61] with thin grafted layers (5nm) of polydimethylsiloxane, PDMS (DMS T-22). The glass balls were cleaned with piranha solution (70% Sulfuric acid + 30% Hydrogen Peroxide) for half an hour following which they were rinsed with copious amounts of DI water and dried in the oven. In the experiments that required hydrophilic glass spheres, they were used right after the piranha cleaning and drying step. For making hydrophobic spheres, the following reaction was carried out. The dried glass spheres were placed in a clean glass vial and PDMS (DMS T-22) liquid was poured over the spheres to cover them completely. These were kept in the oven at 80 $^{\circ}$ C for 24hrs, after which they were cooled to room temperature. The glass spheres were then rinsed with chloroform (ACS grade, EMD) and dried at room temperature. Some glass spheres were silanized by soaking them in chloroform with 3-4 drops of the perfluorodecyltrichlorosilane. The silanized spheres were used in the experiment for observing self-assembly at the gel-heptane interface.

6.5.4. Measurement of Shear Moduli of the Polyacrylamide Gel.

The shear moduli of the gels were estimated with a slight modification of a previously reported method[45]. The gel was cured in a thin slab, sandwiched between two glass slides, the preparation of which is described above. We previously observed that the elastic modulus of a gel cured after 2 to 24 hrs exhibit similar elastic properties. However, in order to prevent any possible complications due to the drying of the gel from its exposed edges, we performed all the shear modulus measurements after 2 hrs of curing the gel. After removing the Teflon coated spacers that separated the two parallel glass plates with a thin slab of gel sandwiched between them, the lower larger

glass plate was fixed by means of double sided tape (Scotch) to a stage that firmly rested on a vibration isolation table (figure 6.8a). A steel piece was then glued at the center of the top glass plate/cover slip using Superglue (Scotch) that was used to vibrate the upper plate parallel to the bottom plate. A magnet was attached to the end of an aluminum stage that was connected to a mechanical oscillator (Pasco Scientific, Model No: SF-9324) and driven by a Gaussian white noise of strength 0.12 m^2/s^3 generated by a waveform generator (Agilent, model 33120A), via an amplifier (Sherwood, Model No: RX-4105). As the magnet underwent a random vibration, it excited a random oscillation of the magnetic steel disk, and thus the upper glass plate above the gel. This fluctuation of the plate was captured by a high speed camera (Redlake Motion-Pro, Model no: 2000) operating at 1000 frames/s and later tracked by a motion tracking software MIDAS (Midas2.0, Xcitex Inc., USA). OriginLab software was used to Fourier Transform the displacement fluctuations that yielded the power spectrum of the random motion of the plate, and thus the shear deformation of the gel that allowed estimation of the dominant shear resonant frequency of the gel. Addition of ten such power spectra for each sample eliminated the background noise and resulted in a clear identification of the dominant resonance frequency ω for each gel that was used to estimate the shear modulus of the gel (μ) by means of the expression of a simple harmonic oscillator: $2\pi\omega = \sqrt{\mu A / mH}$, where A the surface area of contact of the gel slab (thickness H) with the glass plate, m is the total mass of the upper glass plate and the iron piece attached to it. In all the five experiments whose data shown in figure 6.8b, same area of contact A, same mass on top m and same thickness of gel slab H allow us to observe the shift of peaks to the right as the modulus increases. Some of the measurements of the shear moduli (3.2% and 3.4% gels) were carried out with a

different technique in which the lower glass plate of the gel slab-glass plate sandwich assembly was attached to the stage in a vertical fashion. A small block of weight w was suspended with the help of a fine wire that was stuck to the upper cover slip. As the gel slab underwent shear deformation due to the suspended weight, the shear modulus of the gel was estimated using $\mu = wH / \Delta x A$, Δx is the net shear displacement of the upper glass plate. The shear moduli of gels with acrylamide monomer concentrations of 3.5%, 4%, 4.5%, 5% and 5.5% resulted in the shear moduli ranging from 35 Pa to 845 Pa that could be fitted nicely with a stretched exponential function (figure 6.8c).
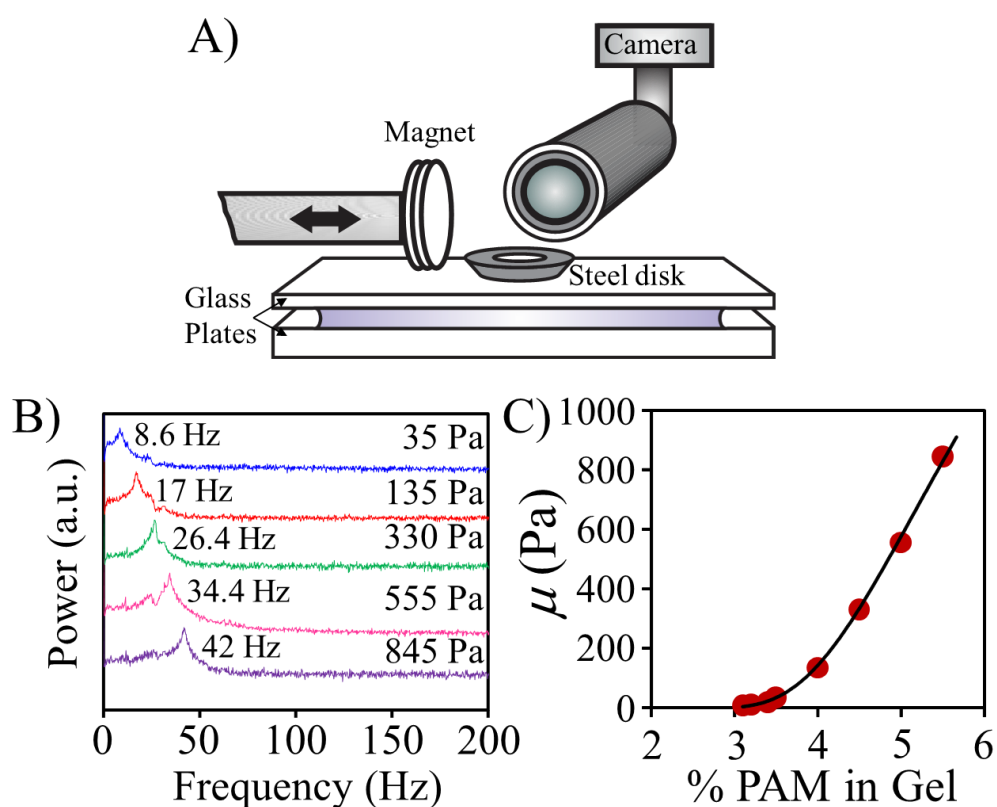
Figure 6.8: (A) Schematic of the method used to measure the shear modulus of a gel. The method involves the creation of a random magnetic field that interacts with the steel disk and vibrates the upper glass plate randomly with respect to the lower plate thus creating a random shear deformation of the gel. (B)The resonance peak of the shear vibration of the gel was obtained from the power spectra of its random vibration with which the shear moduli were calculated using $2\pi\omega = \sqrt{\mu A / mH}$. (C) The shear moduli (μ) of different gels plotted as a function of the percentage of polyacrylamide (x) in them follows an empirical relationship $\mu = 2500\exp(-178/ x^{2.98})$.

6.5.5. Measurements of L_c (Laplace Length) for water and L_c^* (Elasticity modified Laplace Length) for Gels.

The elastocapillary decay length L_c^* of water or a gel was estimated as follows. For water, a clean polystyrene petri dish (100mm ϕ) was placed on a stage in front of a CCD (charged-coupled device) camera (RU, Model: XC-75) atop a vibration isolation table and was filled with DI water till the brim. A hydrophobic glass sphere (2.4mm ϕ) was attached on the bottom of a stage that could be moved up and down using a micromanipulator. The sphere was brought down very close to the surface of the water until its reflection was visible on the surface of the water. By knowing the distance between the object and the image, we could ascertain rather precisely the reference level of the water from the midpoint of the object and its image. The camera was focused in such a way that the sphere was on one side of the frame such that a large area of the deformed surface could be captured. The glass sphere was then brought downward till it touched the surface of the water resulting in a concave meniscus. The sphere was then slowly moved upward while the whole process was captured in the form of a video by using the CCD camera and recorded with WinTV on the computer. The video was decomposed into image sequence in VirtualDub. All the image analysis were performed using ImageJ. The deformed profile was plotted as $\xi(L)$ versus L, where L is the distance measured from the vertical line passing through the center of the glass sphere in the image and $\xi(L)$ is the vertical distance of the deformed profile measured from the undeformed reference level (figure 6.1a). The profile of the deformed surface of water could be fitted with a modified Bessel function $K_0(L/L_c)$ of the second kind where L_c is the capillary or Laplace length of water (figure 6.1a). The same process of measuring the L_c^* was repeated with physically cross-linked polyacrylamide gels of

170

concentrations 3.5%, 4%, 4.5%, 5% and 5.5% of the acrylamide monomer having the shear moduli ranging from 35 Pa to 845 Pa. The gels were cured in clean polystyrene petri dishes and kept inside a large glass petri dish with stacks of DI water-soaked filter papers for 24 hours. The round gel slab was overturned into the lid of the petri dish so that we could measure the L_c^* of the gel's reverse flattened side (Figure 6.1b,c). We repeated the measurements of L_c^* on the top surface of the cured gel slab in the petri dish that also gave almost similar values with the experiments done with the reverse side that is well within the experimental error.

6.5.6. Attraction of spheres on surfaces of gels.

In order to study the attraction of hydrophobic glass spheres on the surface of gel, we placed the home built glass cell containing the cured gel on a stage in front of a CCD camera (MTI, CCD-72). All the experiments were performed followed by 24hrs of the curing the gel, which ensured evaporation of extraneous water from its surface, although we suspect that a very thin layer of water still remains on the surface of the gel. All the experiments were performed on the flattest parts of the gels to eliminate any putative artefacts arising from the curvature of the gel meniscus close to the walls of the test cell. A hydrophobic glass sphere was first released on the gel surface followed by the release of a similar sized sphere within ~10mm away from the first one. Their attraction was recorded using a CCD camera that was attached to a variable focal length microscope (Infinity). Similar experiments were also performed at the interface of gel and n-heptane. When the spheres were released on the surface of n-heptane, they sunk through heptane and rested at the interface formed between n-heptane and the gel. The attractions were recorded in the CCD camera and analyzed using ImageJ. All the experiments were repeated at least three or more times. A stainless steel (SS316) wire

cloth (opening size 0.015", wire diameter 0.010") was lined with the base of the glass cell to observe the deformations in the gel as the particles interacted. At this point, we have not analyzed the optical distortions of the wire mesh; however they can be analyzed with a ray tracing software to quantify the deformations of the surface of the gel (figures 6.3a and 6.7).

References

(1) Krasovitski, B.; Marmur, A. Particle adhesion to drops. *J. Adhes.* **2005**, *81*(7-8), 869-880.

(2) Marmur, A. Tip-surface capillary interactions. *Langmuir* **1993**, *9*, 1922-1926.

(3) Malotky, D. L.; Chaudhury, M. K. Investigation of capillary forces using atomic force microscopy. *Langmuir* **2001**, *17*, 7823-7829.

(4) Shanahan, M. E. R.; de Gennes, P. G. Equilibrium of the triple line solid/liquid/fluid of a sessile drop. *Adhesion* **1987** (ed. Allen, K. W.), Elsevier Appl. Sci., London, *11*, 71–81.

(5) Majumder, A.; Tiwari, A. K.; Korada, K.; Ghatak, A. Microchannel induced surface bulging of soft elastomeric layer. *J. Adhes. Sci. Technol.* **2010**, *24*, 2681– 2692.

(6) Jagota, A.; Paretkar, D.; Ghatak, A. Surface-tension-induced flattening of a nearly plane elastic solid. *Phys. Rev. E* **2012**, *85*, 051602.

(7) Nicolson, M. M. The interaction between floating particles. *Proc. Cambridge Philos. Soc.* **1949**, *45*, 288−295.

(8) Gifford, W. A.; Scriven, L. E. On the attraction of floating particles. *Chem. Engg. Sci.* **1971**, *26*, 287-297.

(9)   Chan, D. Y. C.; Henry, J. D., Jr.; White, L. R. The interaction of colloidal particles collected at fluid interfaces. *J. Colloid Interface Sci.* **1981**, *79*, 410−418.

(10) Denkov, N.; Velev, O.; Kralchevsky, P.; Ivanov, I.; Yoshimura, H.; Nagayama, K. Mechanism of formation of two-dimensional crystals from latex particles on substrates. *Langmuir* **1992**, *8*, 3183-3190.

(11) Bowden, N.; Terfort, A.; Carbeck, J.; Whitesides, G. M. Self-assembly of mesoscale objects into ordered two-dimensional arrays. *Science* **1997**, *276*, 233−235.

(12) Stamou, D.; Duschl, C.; Johannsmann, D. Long-range attraction between colloidal spheres at the air-water interface: The consequence of an irregular meniscus. *Phys. Rev. E* **2000**, *62*, 5263-5272.

(13) Kralchevsky, P. A.; Nagayama, K. Capillary interactions between particles bound to interfaces, liquid films and biomembranes. *Adv. Colloid Int. Sci.* **2000**, *85*, 145-192.

(14) Whitesides, G. M.; Grzybowski, B. Self-Assembly at All Scales. *Science* **2005**, *295*, 2418-2421.

(15) Vassileva, N. D.; van den Ende, D.; Mugele, F.; Mellema, J. Capillary Forces between Spherical Particles Floating at a Liquid-Liquid Interface. *Langmuir* **2005**, *21*, 11190-11200.

(16) Singh, P.; Joseph, D. D. Fluid dynamics of floating particles. *J. Fluid. Mech.* , **2005**, *530*, 31-80.

(17) Vella, D.; Mahadevan, L. The "Cheerios effect". *Am. J. Phys*. **2005**, *73*, 817−825.

(18) Loudet, J. C.; Alsayed, A. M.; Zhang, J.; Yodh, A. G. Capillary interactions between anisotropic colloidal particles. *Phys. Rev. Lett.* **2005**, *94*, 018301.

(19) Botto, L.; Lewandowski, E. P.; Cavallaro, M.; Stebe, K. J. Capillary interactions between anisotropic particles. *Soft Matter* **2012**, *8*, 9957−9971.

(20) Pieranski, P. Two-dimensional interfacial colloidal crystals. *Phys.Rev. Lett.* **1980**, *45*, 569-572.

(21) Furst, E. M. Directing colloidal assembly at fluid interfaces. *Proc. Nat. Acad. Sci.* **2011**, *108*, 20853-20854.

(22) Horozov, T. S.;Aveyard, R.;Clint, J. H.; Binks, B. P. Order-disorder transition in monolayers of modified monodisperse silica particles at the octane-water interface. *Langmuir* **2003**, *19*, 2822-2829.

(23) Luo, M.; Olivier, G. K.; Frechette, J. Electrostatic interactions to modulate the reflective assembly of nanoparticles at the oil–water interface. *Soft Matter* **2012**, *8*, 11923-11932.

(24) Colosqui, C. E.; Morris, J. F.; Stone, H. A. Hydrodynamically Driven Colloidal Assembly in Dip Coating. *Phys. Rev. Lett.* **2013**, *110*, 188302.

(25) Oettel, M.; Dietrich, S. Colloidal interactions at fluid interfaces. *Langmuir* **2008**, *24*, 1425–1441.

(26) Ershov, D.; Sprakel, J.; Appel, J.; Stuart, M. A. C.; van der Gucht, J. Capillarity-induced ordering of spherical colloids on an interface with anisotropic curvature. *Proc. Nat. Acad. Sci.* **2013**, *110*, 9220-9224.

(27) Böker, A.; He, J.; Emrick, T.; Russell, T. P. Self-assembly of nanoparticles at interfaces. *Soft Matter* **2007**, *3*, 1231-1248.

(28) Müller, M. M.; Deserno, M.; Guven, J. Interface-mediated interactions between particles: a geometrical approach. *Phys. Rev. E* **2005**, *72*, 061407.

(29) Bruinsma, R.; Pincus, P. Protein aggregation in membranes. *Curr. Opin. Solid State Mater. Sci.* **1996**, *1*, 401-406.

(30) Dan, N.; Pincus, P.; Safran, S. A. Membrane-induced interactions between inclusions. *Langmuir* 1993, *9*, 2768-2771.

(31) Weikl, T. R. Indirect interactions of membrane-adsorbed cylinders. *Eur. Phys. J. E* **2003**, *12*, 265-273.

(32) Rudnick, J.; Bruinsma, R. DNA-protein cooperative binding through variable-range elastic coupling. *Biophys. J.* 1999, *76*, 1725-1733.

(33) Dean, D. S.; Hammant, T. C.; Horgan, R. R.; Naji, A.; Podgornik, R. Wrapping transition and wrapping-mediated interactions for discrete binding along an elastic filament: An exact solution. *J. Chem. Phys.* **2012**, *137*, 144904.

(34) Poulin, P.; Stark, H.; Lubensky, T. C.; Weitz, D. A. Novel colloidal interactions in anisotropic fluids. *Science* **1997**, *275*, 1770-1773.

(35) Pishnyak, O. P.; Tang, S., Kelly, J. R.; Shiyanovskii, S. V.; Lavrentovich, O. D. Levitation, lift, and bidirectional motion of colloidal particles in an electrically driven nematic liquid crystal. *Phys. Rev. Lett.* **2007**, *99*, 127802.

(36) Lapointe, C.; Hultgren, A.; Silevitch, D. M.; Felton, E. J.; Reich, D. H.; Leheny, R. L. Elastic torque and the levitation of metal wires by a nematic liquid crystal. *Science* 2004, *303*(5658), 652-655.

(37) Cavallaro, M.; Gharbi, M. A.; Beller, D. A.; Čopar, S.; Shi, Z.; Baumgart, T.; Yang, S.; Kamien, R. D.; Stebe, K. J. Exploiting imperfections in the bulk to direct assembly of surface colloids. *Proc. Nat. Acad. Sci.* **2013**, *110*, 18804-18808.

(38) Ardell, A. J.; Nicholson, R. B. On the modulated structure of aged Ni-Al alloys: with an Appendix On the elastic interaction between inclusions by J. D Eshelby. *Acta Metall.* **1966**, *14*, 1295-1309.

(39) Py, C.; Bastien, R.; Bico, J.; Roman, B.; and Boudaoud, A. 3D aggregation of wet fibers. *Europhys. Lett.* **2007**, *77*, 44005.

(40) Evans, A. A.; Spagnolie, S. E.; Bartolo, D.; Lauga, E. Elastocapillary self-folding: buckling, wrinkling, and collapse of floating filaments. *Soft Matter* **2013**, *9*, 1711-1720.

(41) Mora, S.; Phou, T.; Fromental, J. M.; Pismen, L. M.; Pomeau, Y. Capillarity Driven Instability of a Soft Solid. *Phys. Rev. Lett.* **2010**, *105*, 214301.

(42) Extrand, C. W.; Kumagai, Y. Contact Angles and Hysteresis on Soft Surfaces *J. Colloid Interface Sci.* **1996**, *184*, 191-200.

(43) Roman, B.; Bico, J. Elasto-capillarity: deforming an elastic structure with a liquid droplet. *J. Phys.: Condens. Matter* **2010**, *22*, 493101.

(44) Zimberlin, J. A.; Sanabria-DeLong, N.; Tew, G. N.; Crosby, A. J. Cavitation Rheology for Soft Materials. *Soft Matter* **2007**, *3*, 763-767.

(45) Chakrabarti, A.; Chaudhury, M. K. Direct measurement of the surface tension of a soft elastic hydrogel: Exploration of elastocapillary instability in adhesion. *Langmuir* **2013**, *29*, 6926−6935.

(46) Chakrabarti, A.; Chaudhury, M. K. Surface Folding-Induced Attraction and Motion of Particles in a Soft Elastic Gel: Cooperative Effects of Surface Tension, Elasticity, and Gravity. *Langmuir* **2013**, *29*, 15543−15550.

(47) The term 'Emergence' is used here somewhat in loosely, which is sometimes difficult to distinguish from "complexity". For an interesting discussion on this subject, see (Balazs, A. C.; Epstein, I. R. Emergent or just complex? *Science* **2009**, *325*, 1632-1634.)

(48) Vella, D.; Aussillous, P.; Mahadevan, L. Elasticity of an interfacial particle raft. *Europhys. Lett.* **2004**, *68*, 212-218.

(49) Bandi, M. M.; Tallinen, T.; Mahadevan, L. Shock-driven jamming and periodic fracture of particulate rafts. *Europhys. Lett.* **2011**, *96*, 36008.

(50) Nel, A. E.; Mädler, L.; Velegol, D.; Xia, T.; Hoek, E. M.; Somasundaran, P.; Klaessig, F.; Castranova, V; Thompson, M. Understanding biophysicochemical interactions at the nano–bio interface. *Nature mater.* **2009**, *8*(7), 543-557.

(51) Bahrami, A. H.; Lipowsky, R.; Weikl, T. R. Tubulation and Aggregation of Spherical Nanoparticles Adsorbed on Vesicles. *Phys. Rev. Lett.* **2012**, *109*, 188102.

(52) Skotheim, J. M.; Mahadevan, L. Soft lubrication: the elastohydrodynamics of nonconforming and conforming contacts. *Phys. Fluids* **2005**, *17*, 092101.

(53) Sekimoto, K.; Leibler, L. A mechanism for shear thickening of polymer-bearing surfaces: elasto-hydrodynamic coupling. *Europhys. Lett.* **1993**, *23*(2), 113.

(54) Johnson, K. L.; Kendall, K.; Roberts, A. D. Surface energy and the contact of elastic solids. *Proc. Royal Soc. Lond. A.* **1971**, *324*(1558), 301-313.

(55) Style, R. W.; Hyland, C.; Boltyanskiy, R.; Wettlaufer, J. S.; Dufresne, E. R. Surface tension and contact with soft elastic solids. *Nat. commun.* **2013**, *4*, 2728.

(56) Salez, T.; Benzaquen, M.; Raphael, E. From adhesion to wetting of a soft particle. *Soft Matter* **2013**, *45*, 10699-10704.

(57) Marmur, A.; Chen, W.; Zografi, G. Characterization of particle wettability by the measurement of floatability. *J. Colloid Int. Sci.* **1986**, *113*, 114-120.

(58) Van Oss, C. J.; Chaudhury, M. K.; Good, R. J. Interfacial Lifshitz-van der Waals and polar interactions in macroscopic systems. *Chem.Rev.* **1988**, *88*(6), 927-941.

(59) Miguel, M. C.; Rubi, M. *Jamming, Yielding, and Irreversible Deformation in Condensed Matter.* Springer, 2006.

(60) Segre, P. N.; Liu, F.; Umbanhowar, P.; Weitz, D. A. An effective gravitational temperature for sedimentation. *Nature* **2001**, *409*(6820), 594-597.

(61) Krumpfer, J. W.; McCarthy, T. J. Contact Angle Hysteresis: A Different View and a Trivial Recipe for Low Hysteresis Hydrophobic Surfaces. *Faraday Discuss.* **2010**, *146*, 103−111.

Chapter 7

Elastic Cheerios effect: self-assembly of cylinders on a soft solid[a]

7.1. Introduction.

It is well-known that a small particle can float at an air-liquid interface due to the capillary force acting along its contact line[1-3]. The combination of the gravitational and the surface energies can lead to an attractive or a repulsive interaction between particles depending upon their specific gravity relative to the liquid[4-6]. This observation, dubbed the Cheerios effect[7-8] is the basis for capillarity driven self-assembly[9-12]. Similar phenomena are also observed on microscales in such instances as proteins embedded in a lipid membrane[13], in which the interactions are mediated by elasticity and capillarity. These observations lead to a natural question- what if the fluid interface is replaced by its elastic analog, such as the surface of a soft solid, or a thin elastic membrane? Recent experiments[14-16] have shown that this elastic analog of the Cheerios effect, wherein heavy spheres settling on a soft solid deform the interface and create a topography that serves as an energy landscape on which they move. These observations are consistent with a scaling theory[14-16] that captures the essential features for the forces and dynamics between two spheres. Here, we complement these

---

studies by studying the statics and dynamics of heavy parallel cylinders sitting atop a soft substrate using a combination of experiments, theory and numerical simulations.

7.2. Experiment.

Our experiments followed a protocol similar to that in earlier studies[14-16] and used a physically cross-linked gel as the soft substrate, starting with a solution of N-(hydroxymethyl)-acrylamide (48% solution in water, Sigma Aldrich) in water that was then polymerized by adding 0.25wt% of the catalyst potassium persulfate (99.99%, Sigma Aldrich) and initiating the reaction with 0.3wt% N,N,N',N'-tetramethylethylenediamine (TEMED, $\geq$ 99.5%, Sigma Aldrich). After crosslinking was complete, we measured the shear modulus of this gel using an oscillatory rheology test [12] and found that the modulus μ = 18 Pa. For the cylinders, we used highly polished ¾" long aluminum rods (2024 Aluminum, 3/16 "diameter, density 2.8 g/cc, McMaster Carr) which were cleaned and sonicated in acetone and dried with ultrapure nitrogen gas. They were then plasma-oxidized and soaked in trimethylsiloxy-terminated polydimethylsiloxane (DMS T-22, M.W. 9430; Gelest Inc.), and baked at 80ºC for a day to allow the polydimethylsiloxane chains to graft with the surface, and then rinsed with chloroform (ACS grade, EMD) in order to remove the unreacted siloxanes and dried.

When a single cylinder is placed on the gel surface, it deforms the interface locally. When another cylinder is placed within 5-8mm from the first one, they attract towards each other until they coalesce (Appendix, Movie 1) as shown in Figure 7.1A. The interface was filmed with a CCD (charge coupled device) camera (MTI-72) that was equipped with a variable focal length microscope (Infinity), and the images analyzed

using ImageJ to yield the surface of the gel (h) as a function of the edge to edge separation distance (ℓ) between them, as shown in Figure 7.2C (inset). In Figure 7.1B-C, we see that when there are more number of cylinders, they may undergo either complete or arrested coalescence (Appendix, Movies 2 and 3). In the experiments involving two or more cylinders, care was taken to keep them as parallel as possible.
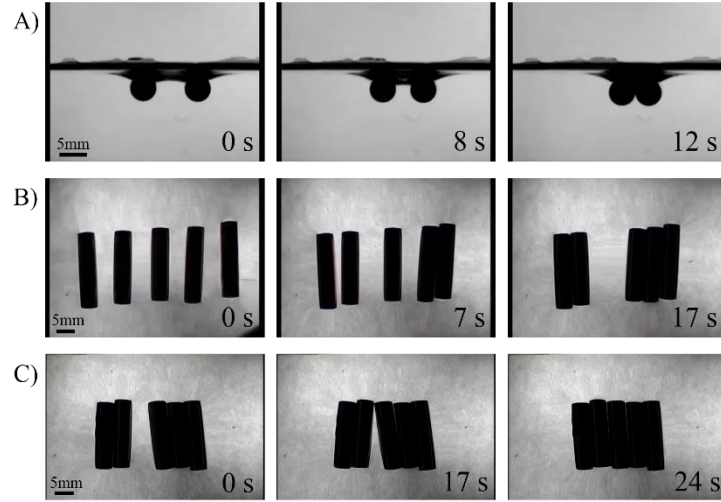
Figure 7.1: (A) Two cylinders placed parallel to each other on a soft gel (μ=18 Pa) move towards each other and eventually coalesce. (B) If the distance between the cylinders is large enough, we also see elastically arrested configurations as well. (C) A similar self-organized pattern to (A) arises for this initial configuration after sufficient time. The time stamps in the second and third images in the panel in C) are relative to the panel's first image.

To understand these results, we first consider the interaction of a slightly heavy cylinder of radius R with a soft gel of shear modulus μ. Assuming that the deformations of the relatively incompressible gel are small and of order h in the vertical direction, the elastic energy of deformation of the medium per unit depth scales as $\mu\varepsilon^2\ell^2$ where the strain $\varepsilon \sim h/R$, and ℓ is a characteristic horizontal scale over which the deformations decay. The gravitational energy of the deformed gel per unit depth scales as $\Delta\rho g h\ell^2$, where $\Delta\rho$ is the density difference between the cylinder and the gel.

Balancing these energies yields the characteristic scale $h \sim \Delta \rho g R^2 / \mu$ over which deformations decay in the horizontal scale[17,18].

7.3. Theory.

A more formal analysis may be carried out by considering the total energy per unit width of the system, composed of the sum of the gravitational potential and elastic energy:

$$U = \left[\frac{\Delta \rho g}{2} \int_{-\infty}^{+\infty} \xi^2 dx + \frac{T}{2} \int_{-\infty}^{+\infty} \xi_x^2 dx \right]$$
$$+ \left[\frac{\mu}{4} \int_{-\infty}^{+\infty} \int_{-\infty}^{0} \left(w_x + u_z \right)^2 dxdz + 2\mu \int_{-\infty}^{+\infty} \int_{-\infty}^{0} w_z^2 dxdz \right] \qquad (7.1)$$

Where the free surface displacement is $\xi(x)$, the surface tension is T, and the vector of displacement fields in the incompressible solid of modulus μ is given by $(u(x,z), w(x,z))$, with $w(x,0) = \xi(x)$. Using a separable potential of the form $\chi(x,z) = \phi(x)\psi(z)$ to characterize the deformations with $u = \chi_z$ and $w = -\chi_x$, we see that the incompressibility condition $u_x + w_z = 0$ is automatically satisfied. Then, (7.1) may be rewritten as:

$$U = \left[\frac{\Delta \rho g}{2} \psi(0)^2 \int_{-\infty}^{+\infty} \phi_x^2 dx + \frac{T}{2} \psi(0)^2 \int_{-\infty}^{+\infty} \phi_{xx}^2 dx \right]$$
$$+ \left[\frac{\mu}{4} \int_{-\infty}^{+\infty} \int_{-\infty}^{0} \left(\phi \psi_{zz} - \phi_{xx} \psi \right)^2 dxdz + 2\mu \int_{-\infty}^{+\infty} \int_{-\infty}^{0} \phi_x^2 \psi_z^2 dxdz \right] \qquad (7.2)$$

Functional minimization of U with respect to ϕ along with the zero shear stress condition on the free surface ($\psi_{zz}(0)\phi(x) - \phi_{xx}(x)\psi(0) = 0$) leads to the following Euler-Lagrange equation:

$$\left(\frac{\mu}{2}\left(\int_{-\infty}^{0}\psi^2 dz\right)+T\psi(0)^2\right)\phi_{xxxx}$$

$$-\left[\Delta\rho\, g\psi(0)^2 + \mu\int_{-\infty}^{0}\psi_{zz}\psi dz + 4\mu\int_{-\infty}^{0}\psi_z^2 dz - \frac{\mu}{2}\int_{-\infty}^{0}\psi_{zz}^2 dz(\frac{\psi(0)}{\psi_{zz}(0)})\right]\phi_{xx} = 0 \tag{7.3}$$

For the case when the shear modulus vanishes, so that $\mu = 0$, the surface profile is controlled by the balance between tension and gravity, and we find that $\phi = \phi_0 e^{-\alpha x}$,
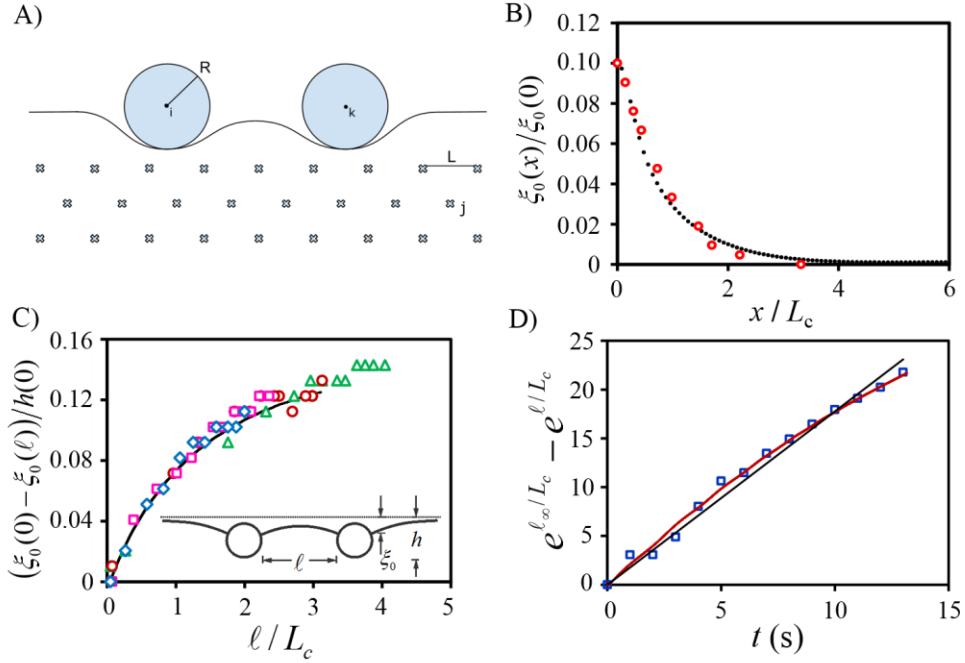
Figure 7.2: (A) A schematic illustrating the numerical model. (B) The deformed profile of the surface of a gel for a single cylinder. The red open circles show the experimental points and the black line are obtained from simulation. Both fit an exponential function $\xi_0(x) = \xi_0(0)\exp(-x/L_c)$, with $L_c = 7.23$ (simulation) and 2.25 mm (experiment). (C) The settling depth of the cylinders $\xi_0(0) - \xi_o(\ell)$ scaled with their initial depth $h(0)$ is plotted as a function of the non-dimensional distance of separation ℓ/L_c where L_c is the effective decay length of elastic deformations. The open symbols represent the data obtained from three different experiments. The black line shows the results of the numerical simulations of the equations of motion (7.4-7.6) with parameter values $R = 3$, $K = 2000$, $\rho = 0.35$ with $\tau = 14.59$. (Inset: Schematic of two cylinders approaching each other on the surface of a gel with appropriate notation used in the text) (D) The dynamics of attraction of two cylinders showing an exponential collapse (see text for details). The open symbols represent the experimental data. The red line is obtained from simulations. The black line corresponds to a linear fit of the experimental data.

and thus $\xi = \xi(0)e^{-\alpha x}$ with a decay length: $\alpha^{-1} = \sqrt{T/\Delta\rho g}$. In the case when the tension vanishes so that $T=0$, the surface profile is controlled simply by the balance between gravity and elasticity, and the surface profile is of the form $\xi = \xi(0)e^{-\beta x}$, where

$$\beta = \left[2\Delta\rho g \psi(0)^2 / \left(\mu \int_{-\infty}^{0} \psi^2 dz \right) \right]^{1/2}$$ with $\beta^{-1} \sim \mu/\Delta\rho g$ being the decay length (we note that in this case the integrals of ψ and its derivatives are all bounded). This implies that the descent of the cylinder can be expressed as $\xi_o \approx \Delta\rho g R^2 / \mu$, which agrees with the scaling ansatz discussed previously. We emphasize that the functional minimization of U has been carried out in the absence of the constraint: $\int_{-\infty}^{+\infty} \xi \, dx = 0$. Consideration of this condition in the constrained functional minimization only requires that all the measurements of ξ_0 need to be performed relative to the plateauing surface of the gel in the deformed state. The energetics remain unaltered; thus the final result of equation 7.3 remains the same.

7.4. Simulation.

To verify our scaling and analytic estimates, we now simulate numerically the interaction of the cylinders on a soft gel. Small particles are used to model the gel and large particles are used to model the cylinders that interact with the gel[19-20], as shown in the Figure 7.2A. The equations of motion for the discretized gel are given by,

$$\ddot{x}_j + b\,\dot{x}_j = -\frac{\partial U}{\partial x_j}, \tag{7.4}$$

$$U = \sum_{\tilde{j} \in \text{Gel}} -\frac{1}{2} K \left(\left\| x_j - x_{\tilde{j}} \right\| - L \right)^2$$

$$-\left(\frac{L}{\left\| x_j - x_{\tilde{j}} \right\|} \right)^6 + \sum_{k \in \text{Cylinders}} \left(\frac{2R}{\left\| x_j - x_k \right\|} \right)^{12} \tag{7.5}$$

Where we use a modified Lennard -Jones potential, that uses springs for short range repulsion, and the viscosity $b = 10$ to eliminate any oscillations. The large particles representing the cylinders had the same equations of motion with the inclusion of a gravity term,

$$\ddot{x}_i + b\dot{x}_i = -\frac{\partial U}{\partial x_i} - \rho g R^2 \hat{y},$$

$$U = \sum_{j \in \text{Gels}} \left(\frac{2R}{\left\| x_i - x_j \right\|} \right)^{12} + \sum_{k \in \text{Cylinders}} \left(\frac{2R}{\left\| x_i - x_k \right\|} \right)^{12} \tag{7.6}$$

With $R = 3$, $g = 9.81$, $\rho = .35$. The equations (7.4-7.6) were numerically integrated using a leap-frog- integration scheme with a time step of $\Delta t = 0.01$, with the gel domain [0, 100] × [0, 40].

The results of our simulations confirmed the experimental observation that the profile of the deformed surface of the gel is indeed exponential with respect to ℓ, i.e $\xi_0(\ell) = \xi_o(0)\exp(-\ell/L_c)$, as shown in Figure 7.2B, upto a simple rescaling of L_c, and show that the omission of a logarithmic correction $\xi_0(\ell) \sim \ln(\ell/L_c)$ due to the classical Boussinesq stress field due to a line force exerted by the cylinder is justified. Simulations reproduced the general features of the attraction of two cylinders on a gel (Appendix, Movie 4) in that the experimental and theoretical results of the energy of

185

two cylinders plotted as $[\xi_o(0) - \xi_o(\ell)]/h(0)$ versus ℓ/L_c exhibit excellent agreement with each other (Figure 7.2C). Since the attractive energy of two parallel cylinders is exponential in ℓ, the resulting force is also exponential. Assuming the friction between the cylinder and gel to be a linear function of their relative velocities, we can write: $-\partial U/\partial \ell \sim \zeta\, d\ell/dt$, ζ being the coefficient of kinematic friction. Integration of the preceding equation leads to $e^{\ell_\infty/L_c} - e^{\ell/L_c} \sim \left(\Delta\rho g R^2 L \xi_0(0)/\zeta L_c^2 \right) t$, where ℓ_∞ is the initial distance of separation between the two cylinders. Plots of $e^{\ell_\infty/L_c} - e^{\ell/L_c}$ versus t shown in Figure 7.2D confirms the agreement between experiment and theory once the differences in kinematic friction are taken into account.
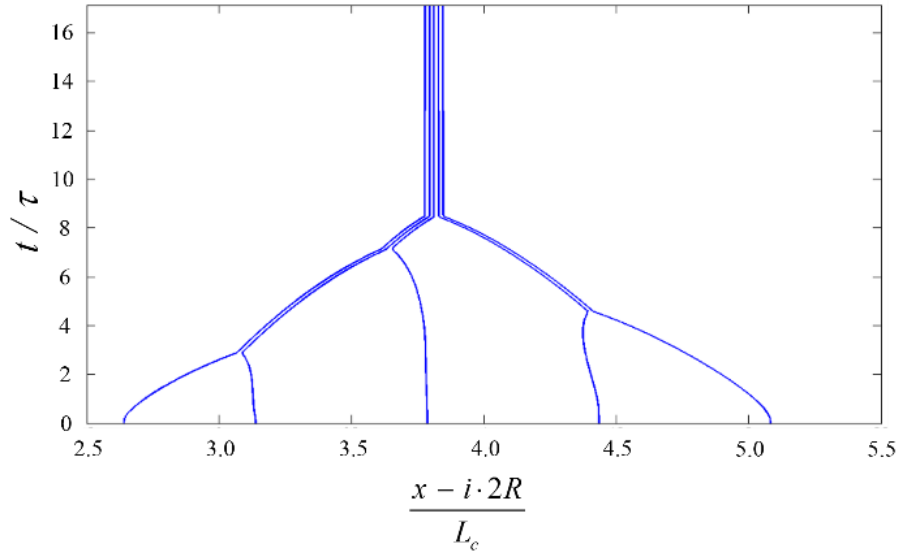
Figure 7.3: The space time dynamics of coalescence of five cylinders. The variable i represents the index of the cylinder and is used to eliminate the space between cylinders in contact. These simulations solve the equations of motion given in (7.4-7.6), with the parameter values $R = 3$, $K = 500$, $\rho = 0.25$, yielding $L_c = 10.03$. The dynamics qualitatively capture the experimental scenario shown in Figure 7.1, wherein the cylinders aggregate in pairs before slowing down and coalescing together.

Finally, in Figure 7.3, we show the space-time plot of the coalescence of five cylinders as obtained from a numerical simulation, where we see that the rate of coalescence changes as the cylinders form pairs and then triplets, qualitatively consistent with our experimental observations (Figure 7.1B-C).

7.5. Conclusion.

Our study has uncovered the profile of the deformed gel around a single cylinder as a simple exponential that is consistent with a simple theory and corroborated by simulations, in which the gel was modelled as a network of beads connected and strings. When multiple cylinders are placed on the surface, they assemble to form smaller clusters that eventually aggregate to form one large cluster (Appendix, Movies 5 and 6), but also may be arrested elastically at times. Our elastic analog of the classical capillary attraction of particles at fluid interfaces opens a plethora of possibilities to be explored that are equally rich and perhaps more interesting, as elasticity provides an additional controllable degree of freedom.

A. Six movies. Available on http://iopscience.iop.org/0295-5075/112/5/54001/media.

Movie 1: Coalescence of two rigid cylinders on gel ($\mu = 18$ Pa) (experiment).

Movie 2: Arrested coalescence of multiple cylinders (experiment).

Movie 3: Complete coalescence of multiple cylinders (experiment).

Movie 4: Coalescence of two cylinders on gel (simulation).

Movie 5: Arrested coalescence of multiple cylinders (simulation).

Movie 6: Complete coalescence of multiple cylinders (simulation).

References

(1)   Allain, C. and Cloitre, M. Interaction between Particles Trapped at Fluid Interfaces: I. Exact and Asymptotic Solutions for the Force between Two Horizontal Cylinders. *J. Colloid Interface Sci.* **1993**, *157*, 261-268.

(2)   Kralchevsky, P. A. and Nagayama, K. Capillary interactions between particles bound to interfaces, liquid films and biomembranes. *Adv. Colloid Interface Sci.* **2000**, *85,* 145-192.

(3)   Chan, D. Y. C.; Henry, J. D. and White, L. R. The interaction of colloidal particles collected at fluid interfaces. *J. Colloid Interface Sci.* **1981**, *79,* 410-418.

(4)   Chaudhury, M. K.; Weaver, T.; Hui, C. Y. and Kramer E. Adhesive contact of cylindrical lens and a flat sheet. *J. Appl. Phys*. **1996**, *80*, 30-37.

(5)   Nicolson, M. M. The interaction between floating particles. *Proc. Cambridge Philos. Soc.* **1949**, *45*, 288-295.

(6)   Botto, L.; Lewandowski, E. P.; Cavallaro, M. and Stebe, K. J. Capillary interactions between anisotropic particles. *Soft Matter* **2012***, 8*, 9957-9971.

(7)   Vella, D. and Mahadevan, L. The "cheerios effect". *Am. J. Phys.* **2005**, *73,* 817-825.

(8)   Larmour, I. A.; Saunders, G. C. and Bell, S. E. Sheets of large superhydrophobic metal particles self assembled on water by the cheerios effect. *Angew. Chem. Int. Ed*. **2008**, *47*, 5043-5045.

(9)   Whitesides G. M. and Grzybowski B. Self-assembly at all scales. *Science* **2002**, *295*, 2418-2421.

(10)   Grzybowski, B. A.; Wilmer, C. E.; Kim, J.; Browne, K. P. and Bishop, K. J. Self-assembly: from crystals to cells. *Soft Matter* **2009**, *5*, 1110-1128.

(11) Cavallaro, M.; Botto, L.; Lewandowski, E. P.; Wang, M. and Stebe, K. J. Curvature-driven capillary migration and assembly of rod-like particles. *Proc. Nat. Acad. Sci*. **2011**, *108,* 20923-20928.

(12) Srinivasan, U.; Liepmann, D. and Howe, R. T. Microstructure to substrate self-assembly using capillary forces. *J. Microelectromech. Sys.* **2001**, *10*, 17-24.

(13) Kim, K.; Neu, J. and Oster, G. Curvature-mediated interactions between membrane proteins. *Biophys. J.* **1998**, *75*, 2274-2291.

(14) Chakrabarti, A. and Chaudhury, M. K. Surface folding-induced attraction and motion of particles in a soft elastic gel: Cooperative effects of surface tension, elasticity, and gravity. *Langmuir* **2013**, *29*, 15543-15550.

(15) Chakrabarti A. and Chaudhury M. K. Elastocapillary interaction of particles on the surfaces of ultrasoft gels: A novel route to study self-assembly and soft lubrication. *Langmuir* **2014**, *30*, 4684- 4693.

(16) Chakrabarti A. and Chaudhury M. K. Attraction of mesoscale objects on the surface of a thin elastic film supported on a liquid. *Langmuir* **2015**, *31,* 1911-1920.

(17) Mora S. and Pomeau Y. Soft granular matter. *arXiv preprint* **2014***, arXiv:1405.0315*.

(18) Chakrabarti, A.; Chaudhury, M.K.; Mora, S. and Pomeau, Y., Elastobuoyant Heavy Spheres: A Unique Way to Study Nonlinear Elasticity. *Phys. Rev. X* **2016**, *6*, 041066.

(19) Haile, J. M., *Molecular Dynamics Simulation: Elementary Methods* (John Wiley & Sons, Inc., New York) **1992**.

(20) Rapaport, D. C., *The Art of Molecular Dynamics Simulation* (Cambridge University Press) **2004**.

Chapter 8

Attraction of Meso-Scale Objects on the Surface of a Thin Elastic Film Supported on a Liquid[a]

8.1. Introduction

Interaction of particles on the surface of a liquid mediated by the joint effects of capillarity and gravity is a well-studied problem[1-6]. Elasticity mediated interactions of molecules and particles on a thin film or a solid surface has also been discussed extensively in the literature[7-11]. The ability to manipulate the properties of soft materials has opened up new experimental and theoretical studies in this subject in recent years involving liquid crystals[12-15] and gels[16-17]. We recently reported[16,17] interactions of different types of solid beads in an ultra-soft gel as a function of latter's elasticity (shear modulus μ). If the density of the bead (ρ_b) is much larger than that of the gel (ρ_g) and if its size (radius R) is significant, it plunges inside the gel and becomes neutrally buoyant due to elastic deformation forces in the gel. While still submerged, the beads, however, attract each other due to the combined effects of elastic and the surface forces of the gel[16]. On the other hand, if its density is not significantly larger than the gel, the beads float on its surface again mainly by the force due to elastic deformation of the gel but attract[17] each other somewhat like the hydrophobic particles

do on the surface of an ordinary liquid[1-6]. Whether the bead will sink in the gel or float on it can be discerned on the basis of a dimensionless number $[EBo = (\rho_b - \rho_g)Rg/\mu$, g being the acceleration due to gravity] – an elastic *Bond* number -- in analogy to the classical *Bond* number, a large value of which indicates sinking, while a low value implies floatation. While studying the interactions of particles in a gel is both interesting and useful, analyses of these interactions are somewhat complicated because of various non-linear effects intrinsic to the gel and the phenomena involved, the full understanding of which requires a 3d analysis of the non-linear field equations describing the deformation of the gel. A model system that simplifies the role of elasticity in particle interactions is a two dimensional elastic membrane that undergoes large deformation under stretching. The situation can be simplified further by studying interactions of two parallel cylinders, which, is ideally a 2d problem. These studies are also valuable in the context of understanding the elasticity mediated interaction of particles that is generic to various phenomena involving biomolecules on a cell membrane.[8-9] Here we report interactions of particles on a thin elastomeric film that is supported on the surface of an incompressible liquid. The advantage of this system is that the role of the thin film can be studied explicitly while the hydrostatic pressure in the liquid tempers the length scale over which interaction prevails. Superficially, the elastic Bond number $[EBo = (\rho_b - \rho_l)R^2g/T$, ρ_l being the density of the supporting liquid], in this case, resembles the classical Bond number, except that the film tension (T) here is composed of the surface free energies (γ) of the air-film and film-liquid interfaces as well as an elastic tension T_E. Furthermore, as there is no pre-existing tension in the film, the elastic tension here is encumbered by the strain in the film induced by its stretching imposed by the weights

191

of the cylinders. Nevertheless, by varying the value of T_E, the magnitude of the vertical penetration of the cylinder in the liquid while still floating the membrane and the range of interaction can be easily controlled.

The main experiment involves the interactions of two parallel cylinders on the surface of a thin elastomeric (polydimethyl siloxane) film supported on the surface of a mixture of glycerol and water. As mentioned above, we chose cylinders as opposed to spheres mainly because of the simplicity of data analysis, in that energy minimization in 2d suffices to capture the main physics of such interactions. Because of the excess elasto-capillary field energy on the surface of the film, the cylinders roll towards each other and come into close contact. At this juncture, we point out that these types of experiments are not easy to perform on a liquid surface as such a parallel configuration is intrinsically unstable; thereby the cylinders approach each other displaying various metastable configurations with a non-parallel geometry[2]. In the case with solid cylinders on an elastic film, the sliding friction at the interface stabilizes their parallel configuration from a modest distance all the way to contact. These interactions are the combined effects of elasticity and gravity. As the elastic strain energy of the deformed film is released, the cylinders descend further in the liquid while still supported by the elastic film. Estimation of the change in the gravitational potential energy, therefore, provides a first order estimate of the energy of interaction of the cylinders as we have also shown recently with various particles interacting in a gel. During the course of the analysis of the data, we noted that the experimentally observed energy of interaction is somewhat smaller than that predicted theoretically. We argue that the discrepancy is related to the hysteresis of adhesion[18,19] between the cylinder and the elastic film. As a cylinder rolls, its leading edge makes new contact with the film, whereas the contact is broken at its rear edge. Due to the difference of these two adhesion energies, some of

192

the elastic field energy released from the intervening region of the cylinders is used up in further stretching the film behind the cylinders. A simple experiment in which a cylinder was forced to roll on the surface of the elastic film provided ample evidence that the role of adhesion hysteresis cannot be ignored. If this frictional resistance is reduced by supporting a layer of an ultra-soft hydrogel on the surface of the elastic film, cylinders as well as spherical beads attract each other from a much larger distance than what is observed with an elastic film alone.

8.2. Results and Discussion.

8.2.1. Estimation of Energy of Attraction Using Gravity. Both the stability of the cylinders in the vertical direction as well as their mutual attraction are the results of the balance of the elastic stretching energy of the film, and the gravitational potential energies of the deformed liquid as well as that of the cylinder itself. For the case of a single cylinder, the profile of the deformed surface can be obtained from the usual minimization of a functional comprising of the gravitational potential energy of the liquid and the stretching energy of the film (see the appendix for a detailed discussion of equation 8.1):

$$U_1 = \frac{L}{2} \int \rho g \xi^2 dx + \frac{L}{2} T \int \xi_x^2 dx \tag{8.1}$$

Where, $\xi (= \xi(x))$ is the deformation of the surface measured from the far field undisturbed surface of the film, ρ is the density of the liquid, g is the acceleration due to gravity and T is the tension in the film. A clarification of equation 8.1 is waranted here. Equation 8.1 is what one would expect for a deformed liquid surface as the surface of the liquid has a surface free energy that increases with the curvature of the surface.

193

However, for the elastic film considered here, it has no excess free energy in the unstretched state in the absence of a pre-stress. We confirmed that the pre-stress in the film is negligible from a simple obervation in which a small hole is created at the center of the film with a sharp needle. If there is a substantial pre-tension, one would expect the hole to grow. We, however, observed that the punctured hole either does not grow or grows by such a small amount that it is inconceivable that any substantial pre-tension exists in the films. The justification of using a linear model for elastic modulus is based on the experimental observation that the profile of the membrane on both sides of the cylinders decay exponentially and that in between them it decays following a cosine hyperbolic function (see below).

A minimization of the energy functional [*i.e.* $\delta U_1/\delta\xi=0$] leads to the familiar[3] differential equation of capillarity, [*i.e* $\xi_{xx}=\alpha^2\xi$], the solution of which leads to an exponential variation of surface deformation $\xi=\xi_0 e^{-\alpha x}$ with a decay length $\alpha^{-1}=\sqrt{T/\rho g}$. The exponential solution ensures that ξ vanishes far field with its maximum value ξ_o at $x=0$. The experimental measurement of the deformed surface profile in conjunction with the preceding expression for ξ can be used to estimate the decay length α^{-1}. The differential equation needed to estimate the surface profile[20,21] of the film that undergoes both bending and stretching would be: $D\xi_{xxxx}-T\xi_{xx}+pg\xi=0$ (*D* being the bending constant), which has a periodic solution with an exponential decay when bending dominates. A scaling analysis leads to the ratio of the bending and the stretching terms in the above equation as $(1/\varepsilon)(H\alpha)^2$, where *H* is the thickness of the film (<10 μm), α^{-1} (~1 cm) is the relevant lateral length scale (the decay length: see below) and ε (~10^{-1}) is the strain in the membrane due to the stretching induced by the

194

weight of the cylinder. Using the above parameters, the ratio of the bending to stretching terms is on the order of 10^{-5} ; thus, the bending term is negligible as compared to the stretching of the elastomeric membrane. Its neglect is also justified on the basis of the observation that the interface profile is only exponential in x within an observation window of about 5 cm; no oscillatory profile was visible in the region where membrane undergoes out of plane stretching.

In order to estimate the energy of interaction of the parallel cylinders, we need to consider their potential energies in addition to the stretching energy of the film as well as the gravitational free energy of the liquid in the region intervening the cylinders and beyond. The total excess energy U_T then becomes:

$$U_T = -2m^* gh + L \left[\int_0^\infty \rho g \xi^2 dx + T \int_0^\infty \xi_x^2 dx \right] + \frac{L}{2} \left[\int_{-\ell/2}^{+\ell/2} \rho g \xi'^2 \, dx' + T \int_{-\ell/2}^{+\ell/2} \xi'^2_x \, dx' \right] \quad (8.2)$$

Where, ℓ represents the separation distance between the lines where the film meet the cylinders and h represents the depth of immersion of the base of the cylinder measured from the far away undeformed surface of the film (Figure 8.5 a). The minimizations of the above energy functional with respect to ξ and ξ' lead to two differential equations, the subsequent solutions of which lead to exponential profiles of the film beyond the intervening space, but has a solution of the type shown in equation (8.3) in the space intervening the cylinders:

$$\xi' = \xi'_0 \frac{\cosh(\alpha x)}{\cosh(\alpha \ell / 2)} \quad (8.3)$$

Using these surface profiles and taking the depth h to be nearly equal to the ξ_o (based on experimental observations) , equation (8.2) can be integrated to obtain the following result:

$$U_T = -2m^* g \xi_0 + \frac{\rho g \xi_0^2 L}{\alpha} \left(1 + \frac{\sinh(\alpha \ell)}{2 \cosh^2(\alpha \ell / 2)} \right) \qquad (8.4)$$

The stability condition $\partial U / \partial \xi_0 = 0$, furthermore, leads to:

$$m^* g = \frac{\xi_o \rho g L}{\alpha} \left(1 + \frac{\sinh(\alpha \ell)}{2 \cosh^2(\alpha \ell / 2)} \right) \qquad (8.5)$$

Substitution of the above expression in U_T, and appropriate algebraic manipulations

yield the following result:

$$U_T = -m^* g \xi_0 \qquad (8.6)$$

Equation 8.6 is a form of U_T that can be estimated from the change in the gravitational

potential energy of a single cylinder in which ξ_o depends implicitly on the distance

of separation ℓ, which can also be expressed explicitly as a function of ℓ using

equation 8.5. Combining these two forms of the energy, we obtain the following

equation:

$$\frac{h_\infty - h(\ell)}{h_\infty} = \frac{\sinh(\alpha \ell)}{2 \cosh^2(\alpha \ell / 2) + \sinh(\alpha \ell)} \qquad (8.7)$$

Since there is not much of a difference in the experimentally measured values of ξ_0

and h, we express the net change in energy with respect to the final energy in terms of

h as it is more convenient to measure the depth of submersion of the cylinder from the

images. h_∞ is the final depth of submersion when the cylinders make contact. Thus,

from the vertical descents of the cylinders alone, it is possible to estimate the form of

the attractive energy of the cylinders as a function of their distance of separation.

8.2.2. Thin Elastic Films Supported on a Pool of Liquid. Thin elastomeric films were prepared by depositing drops of a (1:1) mixture of Sylgard 184 and Sylgard 186 (Dow Corning®) on the surface of a (1:1) Glycerol-Water solution that pre-filled part of a petri dish. Such a composite elastomer possesses high tear strength with an elastic modulus ~ 1MPa. Thus, it is quite durable and withstands the weights (1.2 gm) of the steel cylinders placed above it. The choice of liquid was made on the basis of certain complementary properties it affords. For example, its dispersion component (29 mN/m) of the surface tension being higher than that of PDMS (22 mN/m) allows uniform spreading of the drops of PDMS on its surface without undergoing dewetting that could happen on the surface of pure water. Furthermore, its moderate viscosity (6 cP, 20°C)[22] ensures that the film remains reasonably undisturbed while handling and transporting the samples from one location to another. The uniform interference colors observed on the surfaces of the cured elastic films are indicative of the fact that uniform films of PDMS can be successfully prepared using the mixture of sylgard 184 and sylgard 186 on the water-glycerol solution.

8.2.3. Estimation of the Decay Length (α^{-1}).

Our main experiment was to study the distance dependent attraction of two solid cylinders on the surfaces of the thin elastic films with their long axes parallel to each other and to analyze the data in view of the equation (8.7) proposed as above. These experiments were performed with steel cylinders on the surface of PDMS films of different thicknesses, hence with different tensions. In order to study the universal behavior of these attraction, the non-dimensional descents of the cylinder (LHS of equation 8.7) were plotted in terms of a non-dimensional distance of separation ($\alpha\ell$).

Our first task, therefore, was to estimate α^{-1} as a function of film thickness, which we accomplished in two different ways and selected the more reliable method of estimating the same based on the criteria discussed below.

A. Estimation of the Decay Length from the Side-View.

A cylinder was placed on the elastic film parallel to the edge of a square petri dish containing the solution of water and glycerol that supported the film. Image of the side view of the deformed profile was captured by placing the axis of microscope (equipped with a CCD camera) parallel to that of the cylinder, which were then analysed in ImageJ and fitted with an exponential equation of the form:

$$(\xi_0 - \xi) = \xi_0(1 - e^{-\alpha x}) \tag{8.8}$$

All the analyses were performed with an Originlab software, by setting the point where the film meets the cylinder as a reference. The decay length α^{-1} for each film could thus be obtained from the fitted profile directly. The decay length α^{-1} could also be estimated from the deformed profile of the elastomeric film in between the parallel cylinders floating on an elastic film in view of equation 8.3. While both these methods yielded similar values of α^{-1}, there are concerns that these values could be somewhat obscured by the folding and wrinkling instabilities (Figure 8.1) that ensue near the edges of the cylinders (somewhat similar to what happens with a drop liquid on a floating elastic film[23]), which is the region that is captured by the optical method used here. We thus opted for another direct method of estimating α^{-1} from the deformed profile of the film near the mid-section of the cylinder as discussed below.

B. Estimation of the Decay Length from the Mid-Section of the Surface Profile.

In order to visualize the profile of the surface near the mid-section of the cylinder, we deposited a thin line of ink on the film spanning across a square petri dish prior to placing a cylinder upon
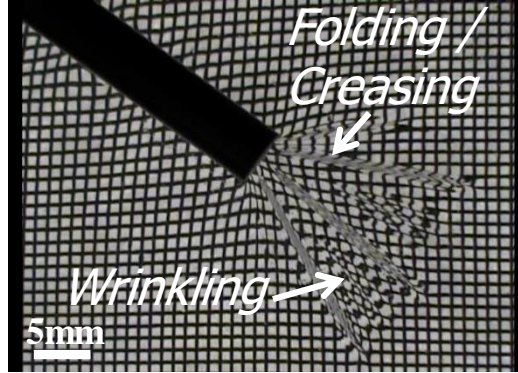
Figure 8.1: Plan view of the folding and wrinkling instabilities at the end of a cylinder placed on an elastic film (3.3 μm thick) supported on a pool of a water-glycerol solution. The wire mesh lined with the base of the petri dish containing the sample shows the deformations in the film surface.
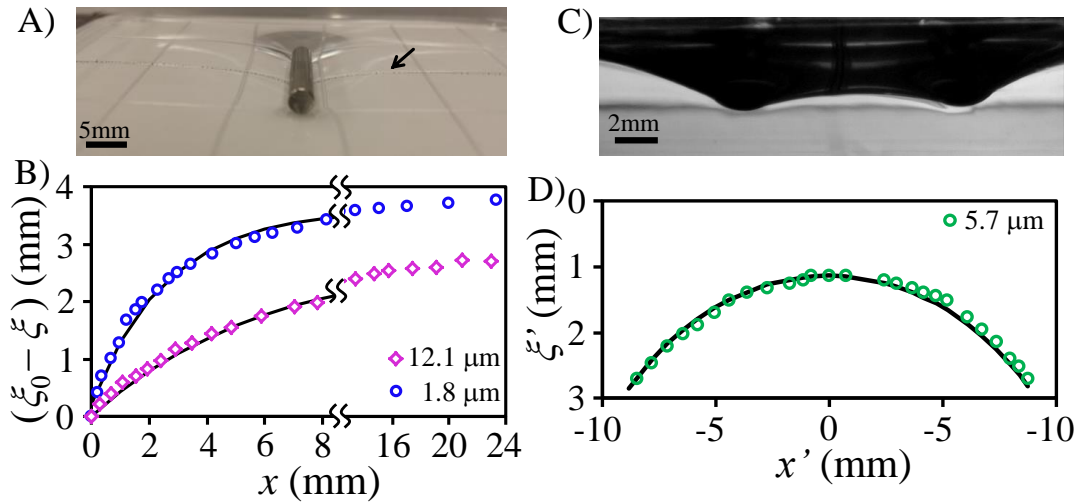
Figure 8.2. (A) The ink line (as shown by the arrow) follows the deformation of the surface of a 7.2 micron thick elastic film supported on the glycerol-water solution when a steel cylinder (diameter 1/8") is placed upon it. (B) The deformed profiles analysed from images of two different elastic films (1.8 μm and 12.1 μm) and the values of α^{-1} obtained from the analysis of the data using equation 8.8 are 2.7 mm and 5.9 mm respectively. (C) A typical snapshot of the intermediate profile between two steel cylinders on a 6.2 micron thick film. (D) Intermediate profile between two steel cylinders resting on a 5.7 micron film (having an initial separation distance of 17 mm) fitted with equation 8.3 to obtain the decay length (5.6 mm).

199

it. (Figure 8.2 a) After gently placing a cylinder on the surface of the film perpendicular to the ink line, its deformation was captured with a camera. The deformed profile from the image was then analysed using ImageJ and fitted with equation 8.8 to obtain the decay length α^{-1} of the film. (Figure 8.2 b).

C. Analysis of Data by Contrasting the Two Approaches:

The values of α^{-1} as a function of the thicknesses of the PDMS films obtained from the above two methods fortunately do not differ in a significant way although a slight difference was observed as noted below. If the surface tension of the solid contributes to the total tension of the film, T should be expressed as $T = T_E + \gamma$, where elastic tension $T_E \sim f(E, H, \varepsilon)$, E being its elastic Young's modulus, ε is the strain in the film and H is its thickness (see appendix). As the decay length is given by $\alpha^{-1} = \sqrt{(T_E + \gamma)/\rho g}$, we plot the experimental values of α^{-2} as a function of H and found an empirical systematic linear relationship (figure 8.3). Thus the extrapolated value for *H=0* should provide an approximate estimate of the surface tension of the solid film, which is contributed by the free surface of the film and that of the film-solution interface. While the decay lengths were measured for a range of elastic film thicknesses, the data were well-behaved (i.e. α^{-2} is fairly linear with H) for films of thickness less than 15 μm. For films thicker than 15 μm, some wrinkling was observed underneath the cylinder along its length of contact that was not evident in the thinner films. Since these wrinklings use up some of the available energy, the decay length is somewhat underestimated that introduces uncertainity in quantitative analysis of the attractions of the cylinders on such thicker films. We thus avoided using such thick

films for additional measurements and analysis in the current study. At a 95% Confidence Limit, the surface tension γ is found to be about -7 ± 29 mN/m from the data obtained from the side view of the profiles and about 56 ± 27 mN/m with the profile obtained from the mid section of the cylinder. Although both the methods yield large uncertainity of estimating γ, the latter method, at least, yields a positive mean value of the surface tension of the solid. Based on the above observations and due to the possibility of α^{-1} measured from the side view being somewhat obscured by the folding and wrinking of the film around the edges, we relied on its value obtained from the profile near the mid-section of the cylinder.
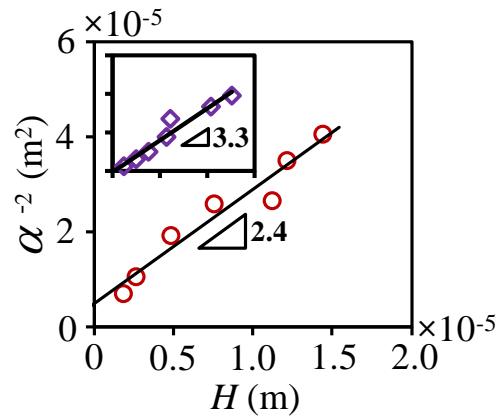
Figure 8.3: Squared values of the decay length α^{-1} are plotted as a function of the film thickness H. The red open circles represent the data obtained from the profile of the deformed line of ink as discussed in section 8.2.3 B. (Inset) The purple open diamonds represent the decay lengths measured from the side view of the deformed profile as discussed in section 8.2.3 A. The scales of the X and Y axes in the inset graph are same as those of the main plot.

8.2.4. Estimation of Elastic Modulus of the Film.

In order to ascertain that the thin films have been adequately crosslinked on the surface of the water-glycerol solution, we estimated its elastic modulus. For a quick estimation of the elastic modulus, we induced buckling by compressing a section of the film by bringing in closely the edges of two glass slides gently touching a section of the film

resting on the pool of a liquid. The Young's modulus E of the film was estimated from its bending modulus $[D = Eh^3/12(1-v^2)]$, which is related to the buckling wavelength (λ) as[20,21] $D = \rho g (\lambda/2\pi)^4$. While the Young's modulus of the PDMS films was in the range of 1-2 MPa, the method was suitable only for thinner films (4-10 μm). It was rather difficult to generate uniform buckles perperndicular to the edges of the glass that made it difficult to measure the wavelength accurately and hence the method was unsuitable for the thicker films. Since our main purpose was to determine if all the films had the same elastic modulus, we opted for a different technique to test the same by deforming the films by a thin plate as described below.

In this method, a thin plate (Cover Glass Slide, 0.18mm, 24 mm x 50mm) was pushed into the film vertically and the force of penetration was measured as a function of the displacement of the edge of the plate (figure 8.4 a). Modification of equation (8.1) by considering the energy due to the profiles on either side of the plate yields the total gravitational and elastic energies of the liquid and the elastic film as $U_2 = 2U_1$. The force per unit width of the glass cover slip (F/L) can be obtained as $F = -\partial U_2/\partial \xi_0$. Using the method described in the appendix, we obtain two expressions (under two different assumptions) for the pushing force F as a function of the depth of penetration ξ_0 as:

$$F/L = 1.3(\rho g)^{3/4}(EH)^{1/4}\xi_0^{3/2} \qquad (8.9A)$$

$$F/L = 1.1(\rho g)^{2/3}(EH)^{1/3}\xi_0^{4/3} \qquad (8.9B)$$

The results summarized in figure 8.4 b show that F/L is slightly super-linear with respect to ξ_o with a power law exponent close to 1.3, which is closer to the prediction of equation 8.9B. Using a value of E=1.2 MPa, which is the modulus expected[24] of a

composite film of sylgard 184 and 186, a plot of F/L against $(\rho g)^{3/4}(EH)^{1/4}\xi_0^{3/2}$ for seven different elastic films (1.8 μm to 14.4 μm) yields a slope of 1.58 ± 0.02, which is close to the theoretically predicted value 1.3 (equation 8.9a).
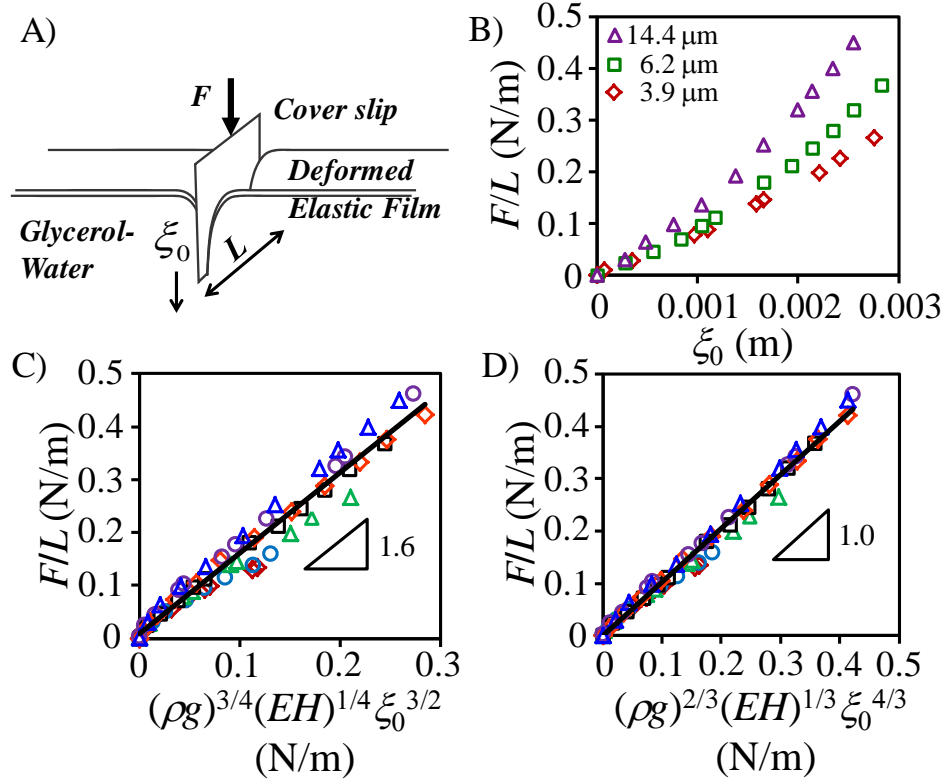
Figure 8.4: (A) Schematic of a thin cover glass (width L= 50mm) indenting the surface of the composite elastic film of Sylgard 184 and 186 due to a vertically applied force F. The indentation depth ξ_0 increases slightly super-linearly with F (not shown here) (B) The force per unit width of the glass plate F/L increases super- linearly with ξ_0 with an exponent close to 1.3. Here data are shown for three representative film (1.8, 6.2, 14.4μm). (C) F/L is plotted against $(\rho g)^{3/4}(EH)^{1/4}\xi_0^{3/2}$ (equation 8.9a) for seven different elastic films (1.8 μm to 14.4 μm) (D) F/L is plotted against $(\rho g)^{2/3}(EH)^{1/3}\xi_0^{4/3}$ (equation 8.9b) for the same films as above.

On the other hand, a plot of F/L against $(\rho g)^{2/3}(EH)^{1/3}\xi_0^{4/3}$ for the same films yields a slope of 1.03 ± 0.01, which, in fact is in much better agreement with the theoretically predicted value of 1.1 (equation 8.9b) than that of the previous plot. The excellent collapse of the load-displacement data, nevertheless, suggests that all the elastic films have very similar Young's modulus.

8.2.5. Attraction of Cylinders on Thin Elastic Films. We studied the attraction of two identical cylinders on three PDMS films of thickness ranging from 5.7 μm to 12.6 μm while they rolled and made final contact in perfect alignment on the film (Figures 8.5 a-b). The force of attraction between the cylinders increases as their separation distance decreases with concomittant descent of the cylinders in the liquid while still floating atop the film. The results obtained from three different sets of experiments were compared by plotting the normalized descent of the cylinder $\Delta h/h_\infty$ against the normalized separation distance $\alpha\ell$. The α^{-1} values (4.3 mm, 5.5 mm and 6 mm respectively) used for these analyses were obtained from the experiments described in section 2.3 C. Although an excellent collapse of the data was obtained for three different films with each experiment repeated 5 times, the magnitude of the attraction energy is lower than that predicted by equation 8.7. We discuss the possible origin of this discrepancy in the following section.

At this juncture, we point out that we estimated the gravitational potential energy of the cylinders with the depth *h* estimated from its base from the undeformed surface of the elastic film (figure 8.5a), whereas ξ_0 is the distance of the contact line where the film meets the cylinder from the undeformed surface. The separation distance between the contact lines of the two cylinders is only slightly greater than that of the contact edges. Fortunately, the errors associated with these approximations are rather small and thus shifting (Figure 8.5 c) all the minimum values of $\alpha\ell$ to zero introduces negligible error in the estimation of the net attraction energy.
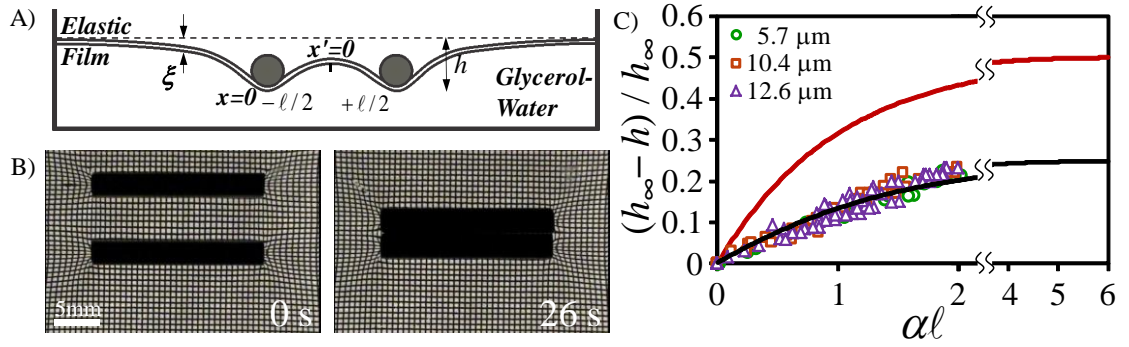
Figure 8.5: (A) Schematic of the side view for the attraction of two PDMS coated steel cylinders on the surface of an elastic film (PDMS 1:1 Sylgard 184 and 186) supported on glycerol-water solution in a polystyrene petri dish. (B) Plan view of the attraction of two steel cylinders from an intermediate separation distance (5 mm) to final contact preserving parallel alignment. The wire mesh lined with the base of the petri dish shows the deformation field of the film. (C) This graph summarizes the non-dimensional descents of the cylinders $\Delta h/h_\infty$ as a function of the non-dimensional distance of separation $\alpha\ell$. The red curve shows the theoretically predicted (Equation 8.7) energy of attraction in an ideal situation without adhesion hysteresis. The experimental data for the attraction of two cylinders on three different films (5.7, 10.4 and 12.6 μm) show a good collapse but being much lower in magnitude than that predicted from theory. The theoretical black curve accounts for the role of adhesion hysteresis (Equation 8.12).

8.2.6. Role of Adhesion Hysteresis

Equation 8.7 is applicable when the cylinders roll freely from a pre-determined distance on the elastic film till the final contact is established. However, rolling hardly occurs freely on any surface. Rolling of a cylinder on a surface can be viewed as the propagation of two cracks, one in the front and the other at its rear edge[18, 19]. The energy to break contact is usually somewhat higher than the energy gained in making contact. Thus, not all of the available energy of attraction is converted to the gravitational potential energy of the cylinders -- some of the energy is stored in stretching the film behind the cylinders. In the absence of a detailed model, we assume that this additional energy is proportional to the square of the descents of the cylinders from the starting position (third term on the RHS in equation 8.10):

$$U^* = -2m^* g \xi_0 + \frac{\rho g \xi_0^2 L}{\alpha}\left(1 + \frac{\sinh(\alpha \ell)}{2\cosh^2(\alpha \ell/2)}\right) + C(\xi_0 - \xi_{01})^2 \qquad (8.10)$$

Using the stability condition $\partial U^* / \partial \xi_0 = 0$, we obtain an expression for ξ_o as a function of ℓ:

$$\xi_0 = \frac{m^* g + C \xi_{01}}{\dfrac{\rho g L}{\alpha}\left(1 + \dfrac{\sinh(\alpha \ell)}{2\cosh^2(\alpha \ell/2)}\right) + C} \qquad (8.11)$$

At this point, we again replace ξ_o with $h(\ell)$ and ξ_{o1} with h_0 as the depth of submersion (h) of the cylinders into the film for the reasons already discussed above. Evaluation of C from equation 8.11 yields a modified form of equation 8.7 that takes into account the role of adhesion hysteresis, where all the parameters can be estimated experimentally as shown below:

$$\frac{h_\infty - h(\ell)}{h_\infty} = \frac{\sinh(\alpha \ell)}{\left\{\dfrac{m^* \alpha}{\rho L (h_\infty - h_0)}\right\}\cosh^2(\alpha \ell/2) + \sinh(\alpha \ell)} \qquad (8.12)$$

8.2.7. Analysis of the Energetics of Attraction

It is evident in figure 8.5 c that equation 8.7 over-predicts the descents of the cylinders as a function of the separation distance than what is observed experimentally. When the denominator of equation 8.12 is calculated with the corresponding value of $m^* \alpha / [\rho L (h_\infty - h_0)]$, the corrected values of the descents of the cylinders are in excellent agreement with those observed experimentally.

Based on the above discrepancy between the experimental results and theoretical predictions of the descends of the cylinders, it is possible to make an approximate estimate of the magnitude of adhesion hysteresis as follows. The main difference comes

from the theoretical value of $(h_\infty - h_0)/h_\infty = 0.5$ without adhesion hysteresis and that [$(h_\infty' - h_0)/h_\infty' = 0.25$] with adhesion hysteresis. The adhesion hysteresis ΔW (energy/area) is the difference in the energies of adhesion in opening a crack at the trailing edge and closing a crack at the advancing edge of the rolling cylinder. For a cylinder of length L (19 mm) rolling over a distance ℓ (8 mm), the energy due to adhesion hysteresis can be represented as: $(\Delta W)\ell L = m^* g(h_\infty - h_\infty')$. From the experimentally estimated value of $(h_\infty - h_\infty')$, the adhesion hysteresis ΔW is estimated to be about 135 mJ/m^2, which we now compare with that obtained from the forced rolling of a cylinder on the surface of a PDMS film.

8.2.8. Adhesion Hysteresis From Forced Rolling

We confirmed the presence of adhesion hysteresis at the interface of the steel cylinder and a PDMS film as follows. After placing a PDMS coated cylinder on the elastic film it was pushed by one end of a tungsten wire spring. As the stage containing the cylinder translated quasi-statically, the cylinder deflected the spring as it rolled on the PDMS film (Figure 8.6). Three different elastic films (7, 11, 16 μm) were used to perform these experiments. By knowing the spring constant of the wire, the adhesion hysteresis ($\Delta W = F/L$) was estimated[18,19] from the deflection of the spring at the onset of rolling that yielded a value close to 100 mJ/m^2 for all the films, which agrees well with the value (135 mJ/m^2) reported in section 2.7 above.

8.2.9. Attraction of Cylinders on a Hydrogel Coated Elastic Film. In view of the previous observations, it is transparent that rolling friction impedes the attraction of cylinders beyond only about 3-4 times its diameter. We hypothesized that the cylinders

could attract from a much larger separation distance taking lesser amount of time than what is observed with a bare
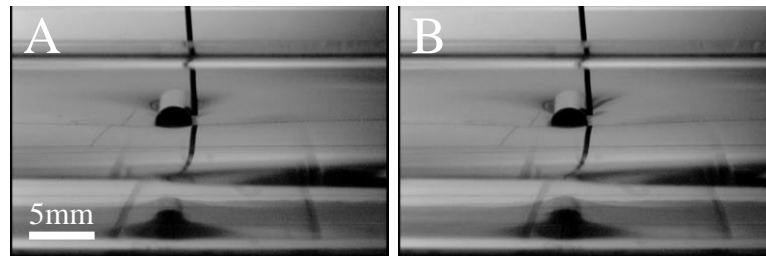
Figure 8.6: Displacement of the end of a tungsten spring wire caused by the rolling of a cylinder on the surface of a 11.2 μm elastic film supported on glycerol water solution. Image (A) shows when the wire just touches the cylinder and image (B) shows the maximum deflection the wire spring as the cylinder continues to roll on the surface.

PDMS film if the impeding friction is reduced or eliminated. In order to test this hypothesis, we designed an experiment in which a thin uniform layer of a low modulus (~ 10 Pa) hydrogel (1.5mm thick) was cross-linked above the thin PDMS film so that the deformation of the PDMS/Gel composite layer provides the energy of attraction, whereas the low friction hydrogel affords this attraction to commence from a large distance (Figure 8.7 a). What we observe on the surfaces of these supported gel films is the steel cylinders (as well as steel spheres) attract from an initial separation distance of about 6 times the diameter of the particles (Figure 8.7 b-c), that is almost more than double of what is observed with the cylinders on the bare elastic films. Because of the low friction of the hydrogel film, the cylinders occasionally attain intermediate non-parallel configurations that is similar to that observed with the cylinders on the surface of a liquid[2]. When several particles are released on such a surface, they formed clusters (figure 8.8).

In order to prove that the long range attraction observed with the hydrogel-PDMS film composite is indeed due to their complementary properties, we performed a control experiment in which the cylinders were placed in close proximity on the surface of a

208

thin hydrogel film cured against a rigid substrate (glass plate or flat base petri dish). Here, either no visible interaction, or sometimes a very weak attraction, was observed between the cylinders or particles, thus suggesting that the long range attraction observed on the composite of the hydrogel and PDMS film is unique. A more detailed study of the interaction of particles on thin hydrogel film on a rigid substrate is reserved for a future in-depth study as the shear deformation in such thin films could give rise to new length scales of attraction and repulsion of particles on its surface.

8.2.10. Role of Instability on the Hydrogel Coated Elastic Film. Soon after the hydrogel films are deposited on the PDMS film, it remained smooth. However, with time, morphological instabilities develop on the surface of the hydrogel (Figure 8.9 a) that leads to a rough energy terrain with intermittent barriers. When particles are deposited on such a surface they do not necessarily move in straight path; instead they follow corrugated (minimum energy) paths guided by the folds on the surface. Occasionally, the particles get pinned on such a surface at local energy minima, which prevents them from attracting from even a very small separation distance. When many particles are released on such a surface, they formed clusters (Figure 8.9b) around the edges of the folded structures, which are reminiscent (in a microscopic sense) of the assembly of particles along the defects of liquid crystals.[15]
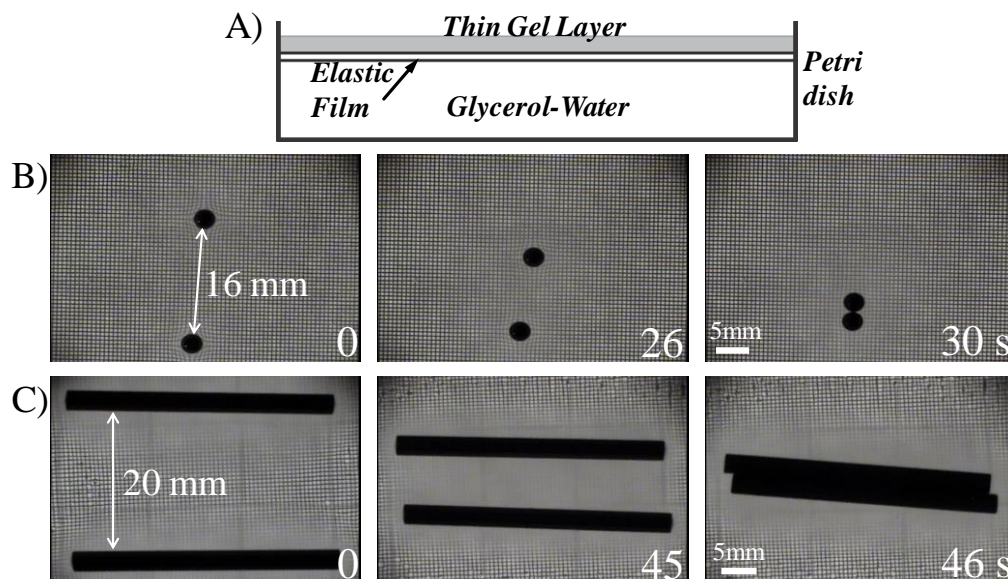
Figure 8.7: (A) Schematic of the thin gel layer (1.5 mm thick, 10 Pa shear modulus) supported on the elastic film (14.4 μm thick) on the pool of liquid. A super-wetting silicone surfactant was added to the gel to promote its spreading on the PDMS film (B) Long range attraction of two steel spheres (diameter 3mm) making final contact on the surface of the gel layer. (C) Long range attraction of two cylinders (length 1.5") approaching each other in a parallel fashion on the similar gel supported on 19.7 μm thick elastic film.
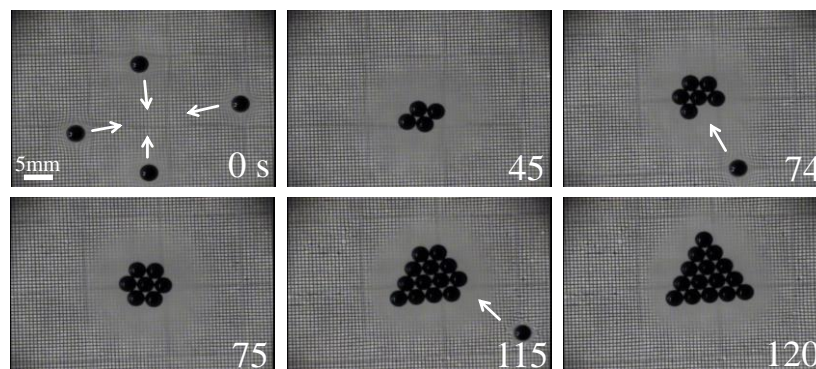
Figure 8.8: Assembly of particles via long range attraction on the surface of a thin hydrogel layer supported on a 19.7 μm elastic film. The steel spheres (diameter 3mm) seek the minimum energy state and move towards the gaps crated by the neighboring spheres. The white arrows indicate the direction of the movement of the spheres.
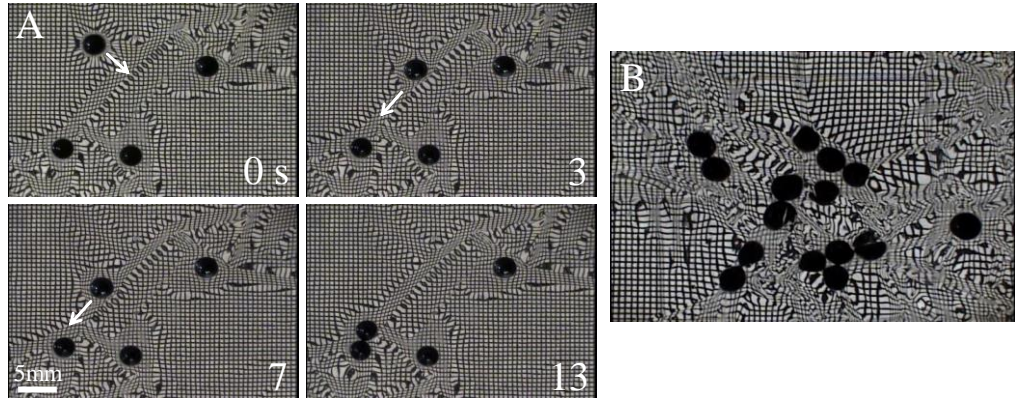
Figure 8.9: (A) Surface instabilities on the hydrogel layer (1.5mm) supported on a 12.6 μm elastic film guide the corrugated paths of particles (steel sphere, diameter 3mm) as indicated by the white arrows, following a minimum energy path. The wire mesh lined with the base of the petri dish helps in the visualization of the instabilities. (B) Several metastable states as created on a hydrogel layer (1mm) supported on the surface of a 7.4 μm elastic film prevent a global clustering of the steel spheres even when the separation distance is small, even though local aggregation of particles are evident near the defects.

8.3. Summarizing Main Points

As far as we know, this is the first systematic study of the attraction of two cylinders on a surface that preserves its parallel configuration from a modest separation distance all the way to contact. This contrasts with what is observed[2] with the attraction of cylinders on liquid surface, where they attain several intermediate unstable configurations before coming into final contact without necessarily preserving a parallel configuration. The difference in these two types of behaviors lies in the sliding friction between the cylinder and the substrate, a finite value of which stabilizes the parallel configuration on the surface of a thin elastomeric film. The results presented here demonstrate that a thin PDMS film prepared from the mixtures of Sylgard 184 and 186 supported on a pool of glycerol-water solution is a viable way to study interaction of particles mediated by elastic tension and gravity. The energy analysis demonstrates that the energetics of attraction can be adequately quantified by the change in the gravitational potential energy resulting from the descents of the cylinders into the liquid

211

while still floating on the surface. Examination of the profile of the deformed surface in the vicinity of the mid-section of the cylinder provides a slightly more reliable estimate of the characteristic material length scale $\alpha^{-1} = \sqrt{T/\rho g}$ than that estimated from the side view due to the obscurities resulting from folding and wrinkling instabilities of the film. However, the value of the solid surface tension of the film (56 ± 27 mN/m) obtained from the extrapolation of α^{-1} to zero film thickness is unreliable due to large standard deviation. This result, however, contrasts a recent report[25] where significantly higher values (100 – 200 mN/m) of solid surface tension for PDMS was obtained from the deformations of thin films caused by liquid drops. The observations of the exponential profile of the thin film PDMS when deformed by a cylinder as well the results of the indentation experiments are all consistent with a linear elasticity model. Hence, no attempt was made to invoke a non-linear elasticity model in all the subsequent analysis of the data presented in this study.

Although the change of the gravitational potential energy of the cylinder provides an easy option to estimate the energy of attraction of the cylinders, it is found that not all of the available energy is converted to the gravitational potential energy. This discrepancy can be ascribed reasonably to the hysteresis of adhesion due to rolling of the cylinders on the elastic film, which in turn converts some of the energy to stretching the film behind the cylinders as they approach each other. This conjecture has been supported by both an energy analysis accounting for hysteresis and an experiment that provided direct evidence of its presence at the cylinder-film interface. While performing the experiments involving the attraction of the cylinders on the elastic film, we frequently noticed that when the initial separation distance is much larger than the decay length α^{-1}, they approach towards each other initially by a slight amount, but then

no perceptible movement is observed. This is an evidence of the adhesion hysteresis providing a threshold force that prevents the rolling of the cylinders on a thin elastic film. Then again, we made some infrequent observations in which the cylinders approach towards each other very slowly over a long time (> 30 min) and come into contact starting from a rather large separation distance (~ 1.5 cm) , thus suggesting that hysteresis may relax with time. However, a further in-depth study is needed to characterize the origin of the hysteresis, as it is not entirely clear, at present, if this hysteresis only provides a threshold force or it relaxes with time. In particular, the roles of the weak bonds between the cylinder[19] and the elastic film or formation of the wetting ridges[26] at the trailing edge of the cylinders rolling on the film need to be investigated. The role of rolling resistance due to adhesion hysteresis, motivated us to carry out a new experiment with which to observe what happens when such a frictional resistance is eliminated. Indeed, with the deposition of a low friction hydrogel layer atop the thin elastomeric film led to a much longer range attraction of the cylinders (as well as solid spheres) than what was observed with the PDMS film alone. We reserve further analysis of the distance dependent attraction energy in such a system for future. Such a composite film, however, became the ground for more fascinating experiments involving the assembly of multiple particles on its surface. A potentially important observation is that morphological instabilities on the hydrogel layer may induce creation of metastable states leading to a mechanically tunable rough energy terrain. We may expect that more interesting studies could be performed with such a surface exhibiting rugged energy landscapes with which to perform mechanical computation of the paths that the particles would follow to reach a global energy minimum state.

The model system in this study and a 2d analysis used to describe the phenomena reported in this work are deceptively simple. The real situation is somewhat more

complex. For example, surrounding the out-of-plane stretched region brought about by the weight of the cylinder lie a region where compressive stress develops in the film. In this compressed region, bending of the film also plays a role, which induces wrinkling and the folding instabilities that are evident near the two poles of the cylinders (Figure 8.1). Even beyond the out-of-plane stretched region that we subscribe as the "active zone" lie a region extending all the way to the wall of the container, where the film undergoes an in-plane stretching that accommodates the liquid displaced from the out-of plane stretched zone. While the resulting gravitational head of the liquid near the walls may be ignored while accounting for the profile in the out-of-plane stretched region, it should play a role in defining the state of the film in the in-plane stressed region. Full understanding of the problem, therefore, would require a rigorous analysis of the mechanics of thin film (e.g. extending the type of analysis reported in reference 27) while sacrificing the simplicity used here. Nevertheless, the success of the approximate analysis to account for the main observations reported here may be motivational in terms of the reasonableness of the approximations that need to be made in developing a more rigorous 3d analysis of the problem.

8.4. Conclusion

Our system comprising of a thin elastic film supported on a pool of liquid allows the study of interaction of particles on its surface, in which a two dimensional energy minimization captures the main underlying physics of the problem. An advantage of studying interactions on thin elastic film is that both the strength and the range of interactions can be easily controlled by the thickness and the elasticity of the film. The work points out the eminent role of adhesion hysteresis between the particle and the film that impedes long range attraction to an appreciable degree. This problem can,

however, be alleviated by supporting a thin layer hydrogel on the elastic film, where the low friction of the hydrogel and the deformability of the membrane provide complementary properties with which a long range attraction can be studied. Modification of the property of the hydrogel (including its morphological instability) and that of the elastic membrane could vastly extend the range of studies involving elasto-capillarity thus enriching the scope of new physics to be discovered.

8.5. Experimental Details

8.5.1. Materials. Stainless steel cylinders (Length ¾", Diameter 1/8", Density 7.8g/cm^3) were used for all the experiments in this study that were treated with trimethylsiloxy-terminated polydimethylsiloxane (DMS T-22, M.W. 9430; Gelest Inc.) for 24 h in the oven followed by an oxygen plasma cleaning for an hour. This is a modified method of the treatment explained by Krumpfer et al.[28] The contact angle of water on such a treated cylinder was found to be around 90°. Steel balls (E52100 alloy steel or SS316, density 7.8g/cm^3, McMaster Carr) were used as is. A stainless steel (SS316) wire cloth (opening size 0.015 in., wire diameter 0.010 in., McMaster Carr), was lined with the base of the glass cell to observe the deformations in the gel as the particles interacted for the plan view images of the experiments.

8.5.2. Preparation of the Elastic Film on a Pool of Liquid. A 1:1 solution (density ρ 1.13 g/cc, 20°C) of glycerol (Fisher Chemical) and deionized (DI) water was degassed for 30 min using a vacuum pump (Welch Duo-Seal, Model no. 1402). Sylgard 184 and Sylgard 186 (Dow Corning®) were mixed in 1:1 ratio (the amount of crosslinker added to the mixture was 10% of the weight of the base polymer) that was degassed for 10 min under high vacuum. Such a combination of the polymers was chosen to ensure that

the film has a high tear strength as well as a moderately high elastic modulus[24]. All the samples were prepared in square polystyrene petri dishes (VWR, 100mm ×100mm ×10mm). The petri dishes were filled with the glycerol-water solution to about half of their height. Different quantities of the PDMS mixture were gently released on the surface of the liquid with the help of micropipettes and the added amount was weighted using a sensitive balance. The samples were allowed to stand for 15 min that allowed the spreading of the PDMS mixture on the liquid surface following which they were carefully placed inside an oven and cured for 90 min at 75° C. Using the known cross sectional area of the dish and the weight of the polymer added, the thicknesses of the elastic films (2 - 17 μm) were estimated. The cured samples were cooled before using them for further experiments. The time duration from the preparation of the samples to further experiments was >2 hrs. For the purpose of plan viewing of the samples, some round petri dishes (VWR, 100mm diameter, 10 mm high) containing the samples were used occasionally.

8.5.3. Estimation of the Decay Length (α^1). The decay lengths of the different thickness elastic films were estimated using two different techniques. In the first technique (discussed in Section 2.3 A), a cylinder was placed on the surface of the film and the deformed profile was imaged using a microscope (Infinity) equipped with a Charge Coupled Device camera (MTI, CCD-72) from the side through the transparent wall of the polystyrene petri dish. The calibration factor was obtained from the image itself from the known diameter of the cylinder.

In the second technique (discussed in Section 2.3 B), a linear trace of ink was made by a glass slide whose edge was inked with a black water-based marker (Crayola). A

cylinder was placed at the centre of the petri dish such that the ink trace was at its mid section. The deformed profile of the ink was then imaged using a regular camera (Samsung, angle of lens at 75 ^{0} from the horizontal surface of the film) (figure 8.2 a). Prior to performing the final experiments with the elastic films, we verified the appropriateness of this method and estimating the appropriate calibration factors by taking an image of a graph having an pre-designed exponential profile. On each image, a horizontal line was drawn parallel to the undeformed portions of the ink line at the two sides of the cylinder. The composite image with the line was then analysed using ImageJ where the vertical distance of the deformed ink trace was calculated from this horizontal line as a reference. In all experiments, it was ensured that vibration has no significant effects in the measurements.

8.5.4. Attraction of Cylinders on the Elastic Film. Experiments involving the attraction of cylinders were carried out on three different PDMS films of thicknesses 5.7 μm, 10.4 μm and 12.6 μm. Two identical PDMS coated stainless steel cylinders (Length ¾", Diameter 1/8") were placed on the surface of the film such that they were in perfect alignment. With the help of two pairs of tweezers, they were then separated to a considerable distance (several times the diameter of the cylinders) and then brought back slowly to about 1 cm separation till they started to attract each other. We recorded the attraction as the cylinders rolled towards each other and descended in the liquid with a CCD camera, MTI CCD-72. The separation distance between the cylinders and their descents (h, the vertical distance of the base of the cylinder from the undeformed surface of the gel) were noted using the ImageJ software.

217

8.5.5. Adhesion Hysteresis: Rolling of Cylinder on Elastic Film. A cylinder was placed on the sample containing the elastic film that was placed on the X-Y manipulator stage. A tungsten wire (diameter 0.02", SPI) of a known spring constant was fixed above the cylinder so that it just touched one edge of the cylinder (figure 8.6 a). The stage was moved quasistatically so that the cylinder rolled on the elastic film while displacing the spring wire laterally. From the maximum deflection of the wire, the adhesion hysteresis was estimated using the equation[19] $\Delta W = F / L$ as shown in section 2.8. The spring constant of the wire was determined from the deflection of its one end by hanging a known weight from it. The image analysis was performed in ImageJ.

8.5.6. Hydrogel Coated Elastic Film. In a clean glass jar, N-(hydroxymethyl)-acrylamide (48% solution in water, Sigma Aldrich) and Deionized water were mixed to prepare a 3.2% (w/w) of the monomer in the solution that was followed by purging it with ultrapure nitrogen gas for 30 minutes while stirring it constantly. This was followed by stirring in 0.25 wt% Potassium Persulphate (99.99% trace metals basis, Sigma Aldrich) for 10 min. Few drops of a surfactant (Q2-5211 Superwetting agent , Dow Corning ®) was stirred in following the addition of 0.3 wt% N,N,N′,N′-tetramethylethylenediamine (TEMED, ≥99.5%, purified by redistillation, Sigma Aldrich). The surfactant ensured that the gel solution spreaded completely on the surface of the PDMS thin film, which afforded preparation of a thin gel layer. The shear modulus of such a gel is about 10 Pa[16]. The experiments involving the long-range attraction of particles on the Gel/PDMS composite were performed after 1 h of curing the gel. Morphological instabilities developed on some of the gels that were allowed to stay in the ambient condition for a much longer time (>2 h).

A. Appendix Justification of Equation 8.1

The constancy of the tension of the film is related to the fact that there is no interfacial shear stress to balance the gradient of stress along the deformed arc length of the film. If a rectangular strip anchored on both ends is depressed in its middle by the weight of a cylinder, then the entire film will have uniform tension of magnitude, EHu_o/L, where u_o is the total deformation and L is the total length of the film. In our case, however, because of lateral constraints, the film cannot deform all the way to the length scale of the container. There will be a cut-off length (L^*), up to which the tension will be more or less uniform and beyond which the tension should be vanishingly small. Since, $u_o \sim (1/2)\int_0^\infty \xi_x^2 dx$; the elastic tension is: $T_E \sim (EH/2L^*)\int_0^\infty \xi_x^2 dx \sim EH\xi_o^2\alpha/4L^*$.

The total energy functional comprising of the gravitational potential energy of the liquid and the stretching and the surface energies of the film on both sides of a cylinder resting on its surface is thus given as follows:

$$U_f = L\int \rho g \xi^2 dx + T_E L\int \xi_x^2 dx + \gamma L\int \xi_x^2 dx \tag{A.1}$$

A functional derivative of U_f yields:

$$\frac{\delta U_f}{\delta \xi} = 2L\int \left(\rho g \xi - \left(\gamma + T_E\right)\xi_{xx}\right) dx \tag{A.2}$$

Setting $\delta U_f/\delta \xi = 0$ and denoting the $\gamma + T_E$ as T, we obtain the desired differential equation the solution of which yields the exponential profile of the film.

Discussion of Equations 8.9:

Substituting $\xi = \xi_0 e^{-\alpha x}$ in equation A.1 (ignoring the role of surface tension γ) yields:

$$U_f / L = \rho g \xi_o^2 / 2\alpha + 3\mu H \xi_o^4 \alpha^2 / (16 L^*) \tag{A.3}$$

At this point, we make two bold (ad hoc) assumptions and test their validities experimentally. The first one is to assume that L^* is on the order of $1/\alpha$, but somewhat larger than the latter. With this assumption, the minimization of U_f/L with respect to α yields $\alpha \sim (8\rho g / 3EH\xi_o^2)^{1/4}$. Eliminating α in equation A.3 and taking the derivative of the energy with respect to ξ_0, we obtain equation (8.9A) in the text. The experimental data are, however, more consistent with the strain scaling as $\xi_0 \alpha$, which yields equation (8.9B) of the text. The change of the power index could be the result of the finite contact area between the cylinder and the film due to adhesion that we have neglected so far.

References

(1)   Nicolson, M. M. The interaction between floating particles. *Proc. Cambridge Philos. Soc.* **1949**, *45*, 288−295.

(2)   Gifford, W. A.; Scriven, L. E. On the attraction of floating particles. *Chem. Engg. Sci.* **1971**, *26*, 287-297.

(3)   Chan, D. Y. C.; Henry, J. D., Jr.; White, L. R. The interaction of colloidal particles collected at fluid interfaces. *J. Colloid Interface Sci.* **1981**, *79*, 410−418.

(4)   Bowden, N.; Terfort, A.; Carbeck, J.; Whitesides, G. M. Self-assembly of mesoscale objects into ordered two-dimensional arrays. *Science* **1997**, *276*, 233−235.

(5)   Kralchevsky, P. A.; Nagayama, K. Capillary interactions between particles bound to interfaces, liquid films and biomembranes. *Adv. Colloid Int. Sci.* **2000**, *85*, 145-192.

(6)   Loudet, J. C.; Alsayed, A. M.; Zhang, J.; Yodh, A. G. Capillary interactions between anisotropic colloidal particles. *Phys. Rev. Lett.* **2005**, *94*, 018301.

(7)   Lau, K. H.; Kohn, W. Elastic interaction of two atoms adsorbed on a solid surface. *Surf. Sci.* **1977**, *65*, 607-618.

(8)   Bruinsma, R.; Pincus, P. Protein aggregation in membranes. *Curr. Opin. Solid State Mater. Sci.* **1996**, *1*, 401-406.

(9)   Dan, N.; Pincus, P.; Safran, S. A. Membrane-induced interactions between inclusions. *Langmuir* **1993**, *9*, 2768-2771.

(10)   Rudnick, J.; Bruinsma, R. DNA-protein cooperative binding through variable-range elastic coupling. *Biophys. J.* **1999**, *76*, 1725-1733.

(11)   Weikl, T. R. Indirect interactions of membrane-adsorbed cylinders. *Eur. Phys. J. E* **2003**, *12*, 265-273.

(12)   Poulin, P.; Stark, H.; Lubensky, T. C.; Weitz, D. A. Novel colloidal interactions in anisotropic fluids. *Science* **1997**, *275*, 1770-1773.

(13)   Pishnyak, O. P.; Tang, S., Kelly, J. R.; Shiyanovskii, S. V.; Lavrentovich, O. D. Levitation, lift, and bidirectional motion of colloidal particles in an electrically driven nematic liquid crystal. *Phys. Rev. Lett.* **2007**, *99*, 127802.

(14) Lapointe, C.; Hultgren, A.; Silevitch, D. M.; Felton, E. J.; Reich, D. H.; Leheny, R. L. Elastic torque and the levitation of metal wires by a nematic liquid crystal. *Science* **2004**, *303*(5658), 652-655.

(15) Cavallaro, M.; Gharbi, M. A.; Beller, D. A.; Čopar, S.; Shi, Z.; Baumgart, T.; Yang, S.; Kamien, R. D.; Stebe, K. J. Exploiting imperfections in the bulk to direct assembly of surface colloids. *Proc. Nat. Acad. Sci.* **2013**, *110*, 18804-18808.

(16) Chakrabarti, A.; Chaudhury, M. K. Surface Folding-Induced Attraction and Motion of Particles in a Soft Elastic Gel: Cooperative Effects of Surface Tension, Elasticity, and Gravity. *Langmuir* **2013**, *29*, 15543−15550.

(17) Chakrabarti, A.; Chaudhury, M. K. Elastocapillary Interaction of Particles on the Surfaces of Ultrasoft Gels: A Novel Route to Study Self-Assembly and Soft Lubrication *Langmuir* **2014**, *30*, 4684-4693.

(18) Kendall, K. Rolling friction and adhesion between smooth solids. *Wear* **1975**, *33*, 351-358.

(19) She, H.; Chaudhury, M. K. Estimation of adhesion hysteresis using rolling contact mechanics. *Langmuir* **2000**, *16*, 622-625.

(20) Milner, S. T.; Joanny, J. F.; Pincus, P. Buckling of Langmuir monolayers. *Europhys. Lett.* **1989**, *9*, 495.

(21) Cerda, E.; Mahadevan, L. Geometry and physics of wrinkling. *Phys. Rev. Lett.*, **2003,** *90*, 074302.

(22) Segur, J. B.; Oberstar, H. E. Viscosity of glycerol and its aqueous solutions. *Ind. & Engg. Chem.* **1951**, *43*, 2117-2120.

(23) Huang, J.; Juszkiewicz, M.; De Jeu, W. H.; Cerda, E.; Emrick, T.; Menon, N.; Russell, T. P. Capillary wrinkling of floating thin polymer films. *Science* **2007**, *317*, 650-653.

(24) McClain, M. A.; Clements, I. P.; Shafer, R. H.; Bellamkonda, R. V.; LaPlaca, M. C.; Allen, M. G. Highly-compliant, microcable neuroelectrodes fabricated from thin-film gold and PDMS. *Biomed. Microdev.* **2011**, *13*, 361-373.

(25) Nadermann, N.; Hui, C. Y.; Jagota, A. Solid surface tension measured by a liquid drop under a solid film. *Proc. Natl. Acad. Sci.* **2013**, *110*, 10541-10545.

(26) Shanahan, M. E. R.; Carre, A. Viscoelastic dissipation in wetting and adhesion phenomena. *Langmuir* **1995**, *11*, 1396-1402.

(27) Davidovitch, B.; Schroll, R.D.; Vella, D.; Adda-Bedia, M.; and Cerda, E.A. Prototypical model for tensional wrinkling in thin sheets. *Proc. Natl. Acad. Sci.* **2011***, 108*, 18227-18232.

(28) Krumpfer, J. W.; McCarthy, T. J. Contact Angle Hysteresis: A Different View and a Trivial Recipe for Low Hysteresis Hydrophobic Surfaces. *Faraday Discuss.* **2010**, *146*, 103−111.

Chapter 9

Wetting of Soft Elastic Gel Spheres on Flat Rigid Substrates

9.1. Introduction

Contact Mechanics is an important field that constitutes the study of how a solid surface deforms when it touches another substrate or when a force is applied to it. While the Hertz model[1] forms the basis to characterize infinitesimal deformations for relatively hard spheres, the Johnson-Kendall-Roberts (JKR) theory[2,3] has been found to be more appropriate for situations in which adhesion becomes important in for soft surfaces such as rubbers in contact. There is yet another regime where the elasticity of the sphere is even lower such that its surface tension also contributes to its mechanics in a non-trivial manner. This regime, where the elastocapillary length much greater than micron scale, can be important to understand cell adhesion and migration on substrates[4–7], nanoparticle adhesion[8] for various industrial applications and for designing new approaches for atomic level characterizations[9–11]. In such cases, it has been found that the JKR theory is no more applicable[11,12]. One has to then invoke the contribution of the surface tension forces acting on the solid and modify the laws of contact mechanics appropriately. While previous attempts to include this correction in order to explain the softer limit of the JKR theory has been mainly theoretical[8,13], not many experimental studies have been performed to shed light upon the same. Our objective in this work is to firstly show that when soft gel spheres are placed on rigid hydrophilic substrates,

they deform by forming a "foot"-like regime close to the contact while retaining its global spherical shape due to its elasticity. This is quite different from the picture that is generally considered[8,13] for all theoretical explications where the entire free surface of the sphere is assumed to shift laterally maintaining its volume conservation. In such a consideration, one misses the point that for such a shape, the sphere needs to pay a huge elastic energy cost, however, in reality, as we observed in the current experiments, it bypasses such a scenario by deforming to a greater extent closer to the contact thereby forming a lip while still retaining its spherical bulk shape away from it. Secondly, we point out that the contact angles of the gel spheres increase as their elastic moduli increases[15] and they decrease as the adhesion energy of the substrates increases. Additionally, we show qualitatively that when these sphere/substrate systems are immersed in another liquid (*e.g.* heptane) such that the gel's interfacial tension is lowered, the general scenario observed for these systems in air is maintained where we can still capture the essence of the "foot"-forming regime in the most wetting case.

To the best of our knowledge, these studies are the first of its kind to describe wetting of soft spheres in the macroscopic regime, nevertheless, we would like to briefly discuss the previous theoretical and simulation analyses in this subject. Joanny *et. al.*[16] considered a problem of adsorption of a cylindrical polymer gel on a rigid substrate where they envisioned an equilibrium shape with a *lip* due to a positive spreading coefficient *S* such that its dimension at the scaling level obeys the ratio S/μ , μ being the elastic shear modulus of the polymer. They, however, ignored the effect of surface tension of the polymer in their analyses. This scenario is more applicable to cases of polymeric materials spreading at interfaces[17,18]. Lau *et. al.*[19] studied the spreading of latex particles on rigid substrates using atomic force microscopy (AFM)

technique very carefully where they observed the extended foot like regime. However, there are a few limitations of their studies that we would like to point out. Firstly, due to very small sample size (~0.1 μm), it was only possible to image them from the top. Therefore, instead of directly measuring the contact angle at the triple line, they used the equilibrium height of the latex particles measured by AFM to estimate them based on their global shape. We know that in the large spreading limit for such soft particles, the contact angle measured at the triple line deviates from the global shape due to the presence of a "foot". Secondly, latex is a glassy material that can flow if the contact stresses exceed its yield point thus limiting its applicability in studying the elastic properties in the soft wetting problem. The conjugate problem of a rigid sphere deforming a soft elastic half-space[12,20–22] has also been studied and complemented with experiments to understand the regime where the solid surface tension becomes important. As pointed out by Style *et. al.*[12], the approximation of using a linear Hookean law to describe the elastic deformations does not affect the JKR or capillary-dominated limits however it may lead to inaccuracies in the transition region where strains are large[23].

In our study, we have not limited ourselves to a Hookean description for the strains of the soft spheres undergoing large deformation during spreading. We derived an expression for the excess elastic force in the gel spheres at the crack tip by using an approach that is similar to estimating the viscous dissipation at the contact line during spreading of liquids. By using a general constitutive law where the elastic energy is not limited to the square of the strains, the singularity at the crack tip vanishes thereby forcing the gel to assume an artificial liquid-like behavior. Our experimental results agreed reasonably well with the model. Furthermore, we measured the length of the

foot and found that it follows the relationship $\left(W\,R^2 / \mu \tan \theta^* \right)^{1/3}$ linearly, a scaling that comes out of a dimensional analysis by balancing the adhesion and the elastic shear energies. Our study involved hydrogel spheres of shear moduli in the range of ~ 61 Pa – 789 Pa with their surface tension close to water[24] such that we could use millimetric sized spheres for the same to afford a large elastocapillary number ($\gamma / \mu R$) thereby providing a direct way to image from the side via usual microscopy techniques.

9.2. Experimental Details.

9.2.1. Preparation of Hydrogel Spheres.

We used physically crosslinked polyacrylamide gel[24] prepared from the monomer N-(hydroxymethyl)-acrylamide (48% solution in water, Sigma Aldrich®) and deionized water. Its polymerization was initiated by the catalyst and promoter system of potassium persulphate (99.99% trace metals basis, Sigma Aldrich®) and N,N,N',N'-Tetramethylethylenediamine (TEMED, ≥99.5%, purified by re-distillation, Sigma Aldrich®). We varied the monomer concentrations to control the elasticity of the cured gels. In order to synthesize highly spherical gel spheres[15], we used a method of suspending drops of gel solution in a beaker containing a liquid density gradient. The density gradient was formed in small beakers with two sparingly miscible liquids: a heavier Silicone oil (Poly[dimethylsiloxane-co-methylphenylsiloxane], Sigma Aldrich, $\rho = 1.05$ g/cc) at the bottom and lighter n-Octane (99+% pure, Acros organics, $\rho = 0.71$ g/cc) at the top that was gently added using a pipette. The ratio of the volumes of silicone oil to octane used in these experiments were around 2:1 to prolong the time of suspended state of the spheres as the diffusing front continues to move down gradually. The interface between these two liquids was allowed to be well diffused to attain a

uniform composition. When the gel drops of different volumes were released slightly into the octane layer, they sank to the level where their density was matched with the surrounding medium. Even though the two liquids used to create the density gradient have slightly different surface tension values, by having a greater diffused zone at the interface, we ensured uniform curvature of the cured gel spheres. All experiments involving the gel spheres were performed after allowing them to completely cure for two hours in the liquid density gradient such that they were elastic. The elastic modulus of these gels (μ ranging from 61 Pa – 789 Pa) were measured using an oscillatory shear rheology experiment that has been reported previously[15].

9.2.2. Diffusion Controlled Silanization of Silicon Wafers.

Silicon wafers were cut into small pieces of about 2 cm^2 each. They were burnt with the flame of a propane torch to remove all the organic contaminants and render them hydrophilic. After cooling each of these silicon wafer pieces, they were placed in a chamber underneath a horizontal silane source at a separation distance of about 13 mm. The silane source was prepared by attaching a flat sheet of filter paper to a glass slide with double-sided tape. A few drops of silane (Dodecyltrichlorosilane, Gelest Inc.) were spread uniformly on the filter paper backed with the rigid glass slide and any excess silane was removed with Kim-wipes. The samples were treated by the diffusing silane vapors in the chamber at a room temperature and relative humidity of 20°C and 35% respectively. In our experimental configuration, an exposure time of about 2 minutes led to surfaces with contact angle (CA) of water ~60° and that of about 12 minutes led to complete grafting of the surfaces giving CA_{water} ~106°, the untreated one

being most hydrophilic. Other variations of this diffusion controlled silanization process can be found in a recent review by Chaudhury *et. al.*[25]

9.2.3.   Measurement and Estimation of the Contact Angles of Hydrogel Spheres.

Each elastic gel sphere was gently taken out from the surrounding oil medium with a plastic pipette (whose tip was cut to remove rough edges) and rinsed in pure n-heptane (Fisher Chemicals) repeatedly followed by moderate drying in air to evaporate traces of heptane. The inner walls of the containers, which were used to house the heptane for cleaning, were also hydrophobized with dodecyltrichlorosilane to prevent the gel spheres from sticking to the walls thereby avoiding any possible damage to their soft surfaces. A treated silicon wafer was placed on a weighing balance and a cleaned elastic gel sphere was placed upon it. The radius of the original perfectly spherical gel drop was estimated from its weight and its value ranged from 1.2 mm – 3.8 mm for the ones we used for our experiments. The gel-sphere-on-substrate-system was immediately photographed with a CCD camera (Sony Model XC-75). The images of the shape and thus the contact angle of the gel spheres in their equilibrium wetting configuration were analyzed using a DropSnake[26] plugin on ImageJ software. This software gives away the contact angle of the sphere at both left and right edges from a spline fitting tool. Each measurement was completed in a few minutes within which there was no observable loss in volume of the gel sphere due to evaporation. For the measurements of the contact angle of gel spheres in the liquid environment, we placed a treated silicon wafer at the base of a quartz cuvette (45 mm $\times$ 30 mm, 45 mm high, Rame Hart) that was filled with n-heptane. An elastic gel sphere was placed through the liquid environment onto the silicon substrate. The analysis of the CA and the shape was performed in the same way as mentioned above. These experiments are very

sensitive and each gel sphere was used for the measurement only once since after its contact with a rigid substrate, it is not possible to remove it without damaging the surfaces of the sphere.

9.2.4. Measuring the length of "Foot" of the Hydrogel Spheres placed on the Substrates.

As explained before, when the elastic gel spheres are placed on the rigid substrates, they spread to their equilibrium shape by extending a "foot" close to the contact regime between the sphere and the substrate. We measured its length in the following way: a circle of the known diameter of the sphere (estimated from its weight) was fitted such that its top coincided with the upper periphery of the deformed gel sphere on the substrate. A line was drawn to highlight the rigid substrate by joining the two triple contact points of the sphere along the reflection plane. The distance between a triple contact point of the gel sphere and the point of intersection of the fitted circle with the horizontal was noted as the length of the "foot" for every measurement (Figure 9.6, inset). While for the softer gel spheres the deformation was much larger than the stiffer gels, we used the mentioned technique to measure the foot lengths to be consistent with the analysis of the data.

9.3.   Observations and Results.

9.3.1   Contact angle of Gel Spheres different than that of Liquid on Same Substrates.

The measured contact angles of the gel spheres was found to increase as a function of elasticity of spheres (shear modulus μ) and decrease with increase of work

of adhesion, they don't change much as a function of size (and radius R) although it was not possible to vary the radii of spheres much as well as it was important to stay below the elastocapillary length (to neglect gravity). Figures 9.1 and 9.2 summarize the observations of the contact angle and shape of the soft gel spheres.

Increasing Hydrophobicity of Surface
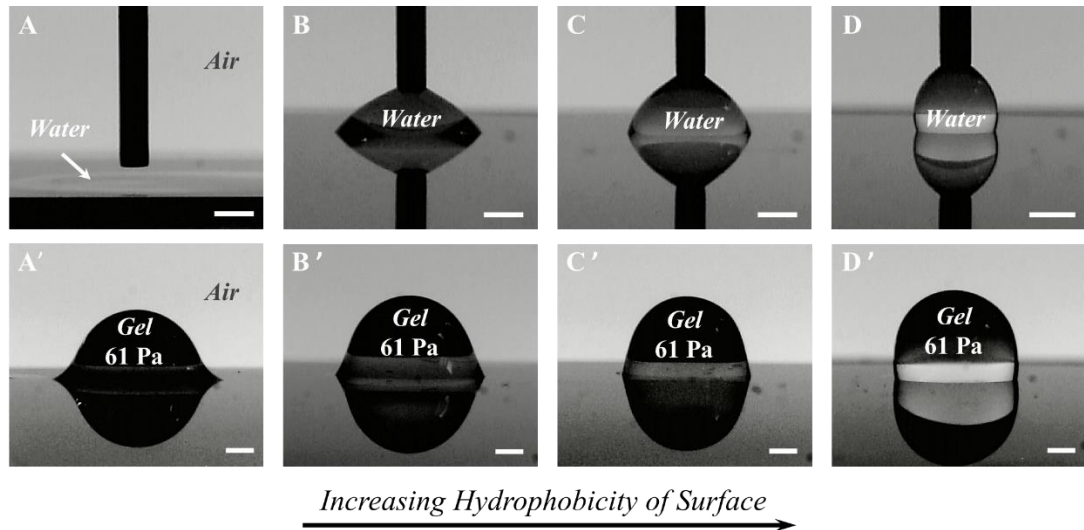
Figure 9.1: Comparison of contact angles of water (top panel, A-D) and those of gel spheres (shear modulus = 61 Pa) (bottom panel, A'-D') on silicon wafers of varying work of adhesion. Each column (*e.g.* A-A') corresponds to silicon wafers of same surface energy, with (A-A') being completely hydrophilic. (B-D') are hydrophobized by exposure to vapors of dodecyltrichlorosilane. Scale bars indicate 1 mm.
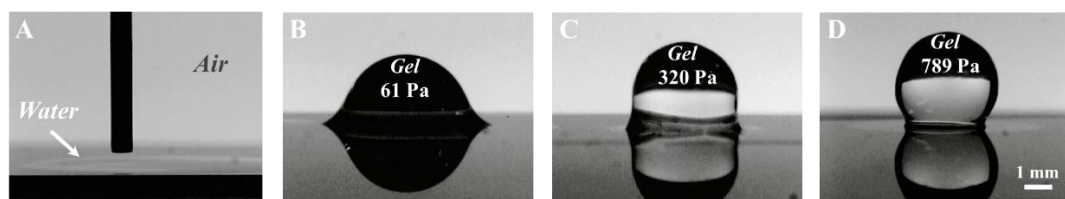
Figure 9.2: The panel shows four different cases of wetting on completely hydrophilic silicon wafers. Water spreads completely as a thin film in (A). (B-D) As the shear modulus of the gel sphere increases, its contact angle increases with lesser deformation. The foot size also progressively decreases with increase in shear modulus.

The observed contact angles (θ^*) of the gel spheres are plotted as a function of their size (R) and work of adhesion (W) in Figure 9.3.
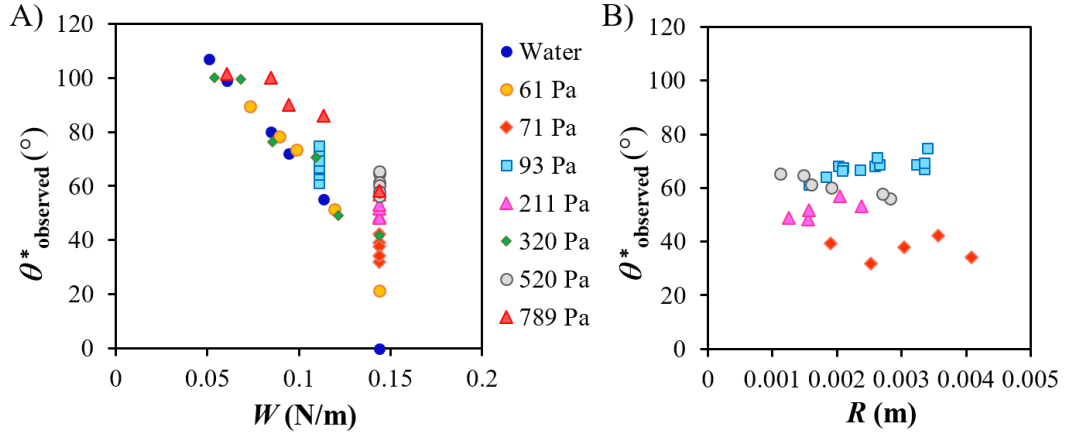
Figure 9.3: (A) Observed contact angles $\theta*$ of gel spheres of different shear moduli as a function of work of adhesion W between the gel and the silanized silicon wafers. The data sets for ($\mu=$ 61 Pa, 320 Pa and 789 Pa) indicate contact angles for gel spheres with similar radii ($R\sim$ 0.0019 mm) on surfaces with varying W. The data sets for ($\mu=$ 71 Pa, 93 Pa, 211 Pa and 520 Pa) indicate contact angles for constant W and varying as a function of the sphere radius R. The latter group is plotted separately in (B) to indicate the trend of the contact angle $\theta*$ as a function of sphere radius R.

9.3.2 Theory to explain the difference in contact angle of gel and that of water.

In order to explain the observed contact angles of the gels, we present a theory based on a general constitutive law that is chosen to remove the singularities at the crack tip of the gel sphere. From the incompressibility condition, at a scaling level, we can write: $\partial u/\partial x \sim \partial w/\partial z$. The displacement in the x-direction, $u \sim l$, where l is the characteristic length of the lip formed by the gel sphere. The displacement in the z-direction, $w \sim \delta$, where δ is the normal deflection of the gel from its original spherical shape. The characteristic lengths in the x- and z- directions are contact length, a and the maximum height in the lip region, $h \sim l\tan(\theta*)$, where $\theta*$ is the contact angle of gel. By using these, we have a relationship for the lip l from the incompressibility condition,

$$l \sim \sqrt{\delta a/\tan(\theta*)} \; . \tag{9.1}$$

From JKR, we have the relationship between the tensile load ($\sim WR$) and the contact length a, i.e,

$$WR \sim \mu\left(a^3/R\right). \tag{9.2}$$

In order to derive the excess tensile force, T_E (this is an average value of elastic force) at the contact line due to elasticity, we approach that is similar to estimating the viscous dissipation at the contact line during spreading of liquids. Here, instead of considering a quadratic form of the strain for the elastic energy, we used a shear thinning model that helps to remove the singularity at the crack tip (i.e. the elastic material is forced to behave like a liquid at the crack tip as elastic stress vanishes). Thus, we write the tensile force as follows:

$$T_E \sim \frac{\mu}{l} \iint \left(\frac{\partial u}{\partial z}\right)^n dxdz \tag{9.3}$$

By solving the above differential equation assuming that at the contact line ($\tan\theta^* \sim z/x$),

$$\therefore T_E \sim \frac{\mu\,l}{\left(\tan\theta *\right)^{n-1}} \tag{9.4}$$

Combining equation (9.4) for the expression for T_E, the scaling for lip l derived from the incompressibility condition [equation (9.1)] and using the relationship between the contact length a and vertical deformation δ from geometry ($\delta = R - \sqrt{R^2 - a^2}$), we have:

$$\therefore T_E \sim \frac{\sqrt{\mu R W}}{\left(\tan\theta *\right)^{n-1/2}}. \tag{9.5}$$

Now, let us consider that the gel sphere has an effective tension T_{eff} comprising the elastic component T and surface tension γ. The work of adhesion for a gel sphere and a liquid drop, $T_{eff}(1+\cos\theta^*) \sim W$ and $\gamma(1+\cos\theta) \sim W$ where $\theta*$ is the contact

angle of gel and θ is the contact angle of pure liquid. The excess tensile force in the horizontal direction will be given by,

$$T_E \sim \left(T_{eff} - \gamma\right)\cos\theta^*. \tag{9.6}$$

Thus, by equating the expressions of T_E from the two equations (9.5) and (9.6), we have:

$$\therefore \left[\frac{1}{(1+\cos\theta^*)} - \frac{1}{(1+\cos\theta)}\right]\cos\theta^*\left(\tan\theta^*\right)^{n-1/2} \sim \sqrt{\frac{\mu R}{W}} \tag{9.7}$$

We consider a value for $n = 1.5$, that is in the shear thinning regime for the spreading of the gels, which artificially removes the singularity at the crack tip. The left-hand side of equation (9.7) then simplifies to $\left(1/1+\cos\theta^* - 1/1+\cos\theta\right)\sin\theta^*$ and is plotted as a function of $\sqrt{\mu R/W}$ for our experimental data in Figure 9.4. Although this model is approximate, it can capture the physics well with a reasonable collapse of the data but with a slight deviation from the origin. We need to delve deeper into the problem to understand the discrepancies that lead to such a result.
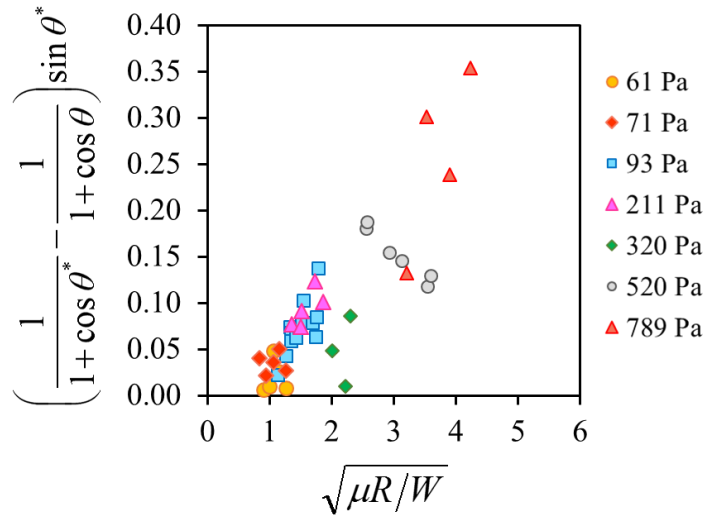
Figure 9.4: Plot of experimental data by using the model expressed in equation 9.7. The excess elastic tension $\left(1/1+\cos\theta^* - 1/1+\cos\theta\right)\sin\theta^*$ is plotted as a function of a dimensionless elasto-adhesive number, $\sqrt{\mu R/W}$. Here, θ^* indicates contact angle of gel and θ indicates contact angle of pure liquid formed on the same surface. In the X-axis, μ represents shear modulus of the gel, R is the radius of the gel sphere and W is the work of adhesion of the liquid/substrate.

9.3.3. Scaling Analysis for "Foot" during Spreading of Gel Spheres on Hydrophilic Substrates.

In the last section, we discussed a general constitutive model to express the excess elastic tension in the gel spheres that reasonably agree with our experimental data. Here, we describe a scaling analysis by comparing the adhesion energy (WlR) in the "foot" region with the elastic energy in the peripheral deformed region $\mu(l/R)^2 V$, where V is the volume of the deformed region. Thus, we get by balancing the adhesion and the elastic energies,

$$WlR \sim \mu \left(\frac{l}{R} \right)^2 l^2 R \tan \theta *$$

(9.8)

Simplifying the above expression in equation 9.8, we get the scaling for the lip l,

$$l \sim \left(\frac{WR^2}{\mu \tan \theta *} \right)^{1/3}$$

(9.9)

We plot the experimental data by using the expression derived in equation 9.9 in Figure 9.5.

9.4. Summary

We presented some new results on how soft elastic gel spheres spread on rigid substrates. Our observations indicate that the contact angles of gel spheres are slightly greater than those of equivalent liquid drops on similar substrates. The contact angles of these gel spheres increase as a function of elasticity and decrease when work of adhesion increases. We derived an expression for the excess elastic force in the gel spheres at the crack tip by using an approach that is similar to estimating the viscous
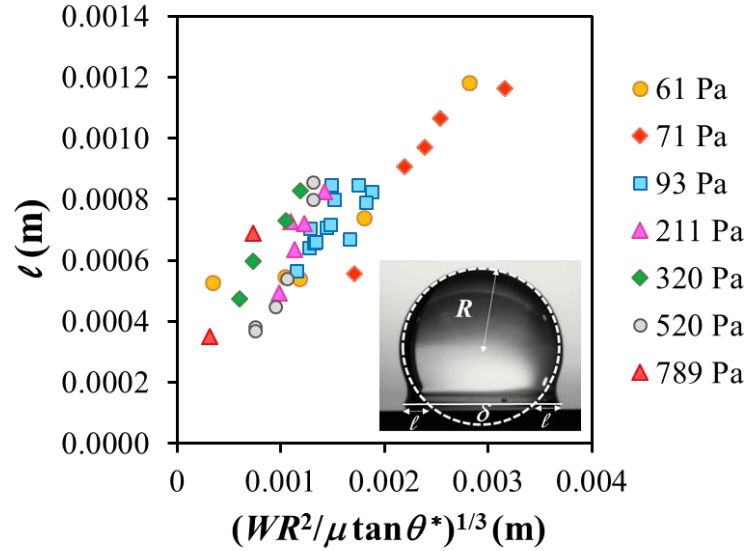
Figure 9.5: Plot of experimental data for lip lengths (ℓ) as a function of the scaling obtained from the balance of surface and elastic shear energies in equation (9.9). **Inset**. An experimental snapshot to show how the lengths of lips were measured. The dotted circle is of diameter of the undeformed gel sphere (estimated from its weight). The horizontal line represents the reflection plane, *i.e,* at the substrate. The distance between a triple contact point of the gel sphere and the point of intersection of the dotted circle with the white horizontal line was noted as the lip.

dissipation at the contact line during spreading of liquids. By using a general constitutive law where the elastic energy is not limited to the square of the strains, the singularity at the crack tip vanishes thereby forcing the gel to assume an artificial liquid-like behavior. This model agrees with the experiments reasonably well. We also measured the contact angle of gels on surfaces of different hydrophobicity through another liquid medium (heptane) as shown in Figure 9.6. Since, our theoretical model is applicable to gel contact angles of less than 90°, we did not include the results from the wetting of gels through a liquid medium in the current analysis. However, the interesting thing to note from these is that we see the formation of the "foot" in the gel sphere in the completely hydrophilic case even through heptane (Figure 9.6 A').
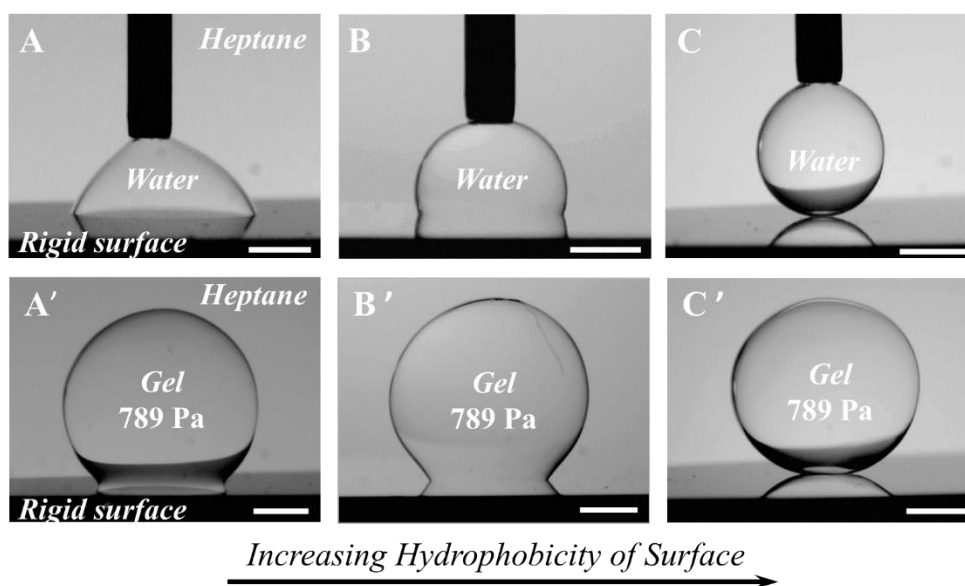
Figure 9.6: Comparison of water (top panel, A-C) and the shape of the gel spheres (shear modulus 789 Pa) (bottom panel, A'-C') on silicon wafers with varying work of adhesion while completely immersed in a surrounding medium of heptane. Each column (*e.g.* A-A') corresponds to silicon wafers of same surface energy, with (A-A') being completely hydrophilic. (B-C') are hydrophobized by exposure to vapors of dodecyltrichlorosilane. A 'foot' has formed in the gel sphere in (A'). Scale bars represent 1 mm.

In such soft gels, there is always a possibility of phase separation due to osmocapillarity[27,28], however, even if the liquid is squeezed out from the network it will be limited to very small scales close to the triple point and it will not affect the contact angle of the gel sphere.

References

(1)   Hertz, H. Ueber Die Beruhrung Fester Elastischer Korper. *J. fur die Reine und Angew. Math.* **1882**, *1882* (92), 156–171.

(2)   Johnson, K. L.; Kendall, K.; Roberts, A. D. Surface Energy and the Contact of Elastic Solids. *Proc. R. Soc. A Math. Phys. Eng. Sci.* **1971**, *324* (1558), 301–313.

(3)   Johnson, K. L. Contact Mechanics. *Journal of the American Chemical Society*. 1985, pp 1–17.

(4)   Joanny, J.-F.; Jülicher, F.; Prost, J. Motion of an Adhesive Gel in a Swelling Gradient: A Mechanism for Cell Locomotion. *Phys. Rev. Lett.* **2003**, *90* (16), 168102.

(5)   Engler, A. J.; Sen, S.; Sweeney, H. L.; Discher, D. E. Matrix Elasticity Directs Stem Cell Lineage Specification. *Cell* **2006**, *126* (4), 677–689.

(6)   Schwarz, U. S.; Safran, S. A. Physics of Adherent Cells. *Rev. Mod. Phys.* **2013**, *85* (3), 1327–1381.

(7)   Fischer-Friedrich, E.; Hyman, A. a; Jülicher, F.; Müller, D. J.; Helenius, J. Quantification of Surface Tension and Internal Pressure Generated by Single Mitotic Cells. *Sci. Rep.* **2014**, *4*, 6213.

(8)   Carrillo, J. M. Y.; Raphael, E.; Dobrynin, A. V. Adhesion of Nanoparticles. *Langmuir* **2010**, *26* (15), 12973–12979.

(9)   Evans, E.; Ritchie, K.; Merkel, R. Sensitive Force Technique to Probe Molecular Adhesion and Structural Linkages at Biological Interfaces. *Biophys. J.* **1995**, *68* (6), 2580–2587.

(10)   Erath, J.; Schmidt, S.; Fery, A. Characterization of Adhesion Phenomena and Contact of Surfaces by Soft Colloidal Probe AFM. *Soft Matter* **2010**, *6* (7), 1432.

(11)   Luan, B.; Robbins, M. O. The Breakdown of Continuum Models for Mechanical Contacts. *Nature* **2005**, *435* (7044), 929–932.

(12)   Style, R. W.; Hyland, C.; Boltyanskiy, R.; Wettlaufer, J. S.; Dufresne, E. R. Surface Tension and Contact with Soft Elastic Solids. *Nat. Commun.* **2013**, *4*, 2728.

(13)   Salez, T.; Benzaquen, M.; Raphaël, É. From Adhesion to Wetting of a Soft Particle. *Soft Matter* **2013**, *9* (45), 10699.

(14)   Maugis, D. Extension of the Johnson-Kendall-Roberts Theory of the Elastic

Contact of Spheres to Large Contact Radii. *Langmuir* **1995**, *11* (2), 679–682.

(15) Chakrabarti, A.; Chaudhury, M. K. Vibrations of Sessile Drops of Soft Hydrogels. *Extrem. Mech. Lett.* **2014**, *1*, 47–53.

(16) Joanny, J. F.; Johner, A.; Vilgis, T. A. Gels at Interfaces. *Eur. Phys. J. E* **2001**, *209* (6), 201–209.

(17) Daillant, J.; Benattar, J. J.; Bosio, L.; Leger, L. Final Stages of Spreading of Polymer Droplets on Smooth Solid Surfaces. *Europhys. Lett.* **1988**, *6* (5), 431–436.

(18) Martin, A.; Clain, J.; Buguin, A.; Brochard-Wyart, F. Wetting Transitions at Soft, Sliding Interfaces. *Phys. Rev. E - Stat. Nonlinear, Soft Matter Phys.* **2002**, *65* (3), 5–8.

(19) Lau, A. W. C.; Portigliatti, M.; Raphael, E.; Leger, L. Spreading of Latex Particles on a Substrate. *Europhys. Letts* **2002**, *60* (5), 717–723.

(20) Rimai, D. S.; Quesnel, D. J.; Bowen, R. C. Particle Adhesion to Highly Compliant Substrates: Anomalous Power-Law Dependence of the Contact Radius on Particle Radius. *Langmuir* **2001**, *17* (22), 6946–6952.

(21) Hui, C.-Y.; Liu, T.; Salez, T.; Raphael, E.; Jagota, A. Indentation of a Rigid Sphere into an Elastic Substrate with Surface Tension and Adhesion. *Proc. R. Soc. A Math. Phys. Eng. Sci.* **2015**, *471*, 20140727.

(22) Butt, H.-J.; Pham, J. T.; Kappl, M. Forces between a Stiff and a Soft Surface. *Curr. Opin. Colloid Interface Sci.* **2016**, *27*, 82–90.

(23) Chakrabarti, A.; Chaudhury, M. K.; Mora, S.; Pomeau, Y. Elastobuoyant Heavy Spheres: A Unique Way to Study Nonlinear Elasticity. *Phys. Rev. X* **2016**, *6* (4), 41066.

(24) Chakrabarti, A.; Chaudhury, M. K. Direct Measurement of the Surface Tension

of a Soft Elastic Hydrogel: Exploration of Elastocapillary Instability in Adhesion. *Langmuir* **2013**, *29* (23), 6926–6935.

(25) Chaudhury, M. K.; Chakrabarti, A.; Daniel, S. Generation of Motion of Drops with Interfacial Contact. *Langmuir* **2015**, *31* (34), 9266–9281.

(26) Stalder, A. F.; Kulik, G.; Sage, D.; Barbieri, L.; Hoffmann, P. A Snake-Based Approach to Accurate Determination of Both Contact Points and Contact Angles. *Colloids Surfaces A Physicochem. Eng. Asp.* **2006**, *286* (1–3), 92–103.

(27) Jensen, K. E.; Sarfati, R.; Style, R. W.; Boltyanskiy, R.; Chakrabarti, A.; Chaudhury, M. K.; Dufresne, E. R. Wetting and Phase Separation in Soft Adhesion. *Proc. Natl. Acad. Sci.* **2015**, *112* (47), 14490–14494.

(28) Liu, Q.; Suo, Z. Osmocapillary Phase Separation. *Extrem. Mech. Lett.* **2016**, *7*, 27–33.

Chapter 10

Summary and Future Directions

In this dissertation, we studied the joint roles of surface tension (γ), elasticity (μ) and gravity ($\Delta\rho g$) in various phenomena in soft elastic solids. The interplay of each of these forces in soft solids leads to important material lengthscales such as *elastocapillary* length (γ/μ) or *elastobuoyant* length ($\mu/\Delta\rho g$), which interact with the geometric lengthscales of the system giving rise to diverse interesting scenarios. Although each chapter in this thesis has its standalone summary and conclusions, we will reiterate some of the key results and findings here. It will then be followed by a discussion highlighting some additional lines of investigations that are inspired from my doctoral work.

10.1. Summary of Doctoral Research

In chapter 2 of this thesis, we discussed how elastocapillarity affects the adhesion-induced pattern formation in thin films during debonding from rigid substrates. While such instabilities have been well studied for the purely elastic case, our experiments and theory uncovered the role of surface tension in amplifying the wavelength of interfacial pattern formation in very soft and thin films. We also found that the critical stress to fracture the film/substrate interface is very high for these soft films. A part of the reason for such high values is the enhancement of the Griffith's stress by the elastocapillary number that can be quite high. Another reason may be due

to the extension of long fibrils of gel from the film about a few anchor points on the substrate when it is being removed, which can store a lot of elastic energy that is ultimately dissipated when the film detaches completely. During the course of this research, we designed a new oscillatory rheology test to measure the shear modulus of such soft gels with the help of only a high-speed camera and an oscillator. This home-built rheometer is very convenient to use and gives accurate results of the modulus as was verified with another independent zero-frequency modulus measurement.

Another highlight of our work was to directly estimate the surface tension of the soft hydrogels since it was essential to establish the role of elastocapillarity in these solids. In chapter 3, we studied the vibration modes of sessile spherical gels as a function of their volume and elastic moduli. We found that the spheroidal resonance mode (ω) varies with volume as is the case with a liquid drop governed by capillarity and its effective surface tension is weakly dependent on the modulus as expected of a pseudo-capillary mode. All the resonance frequencies could be collapsed about a line obtained from a plot of ω versus $\omega^* \sqrt{1 + \mu h / 2\gamma}$ using γ to be the surface tension of water (72 mN/m) and the measured elastic moduli of the gels. Therefore, we concluded that the surface tension of the gels is similar to that of water.

In chapter 4, we introduced the phenomenon of '*elastobuoyancy*', where a particle when placed on a soft elastic gel is engulfed by it, such that its weight is balanced at a depth δ, by the strain energy of the surrounding medium. In the elastobuoyant regime, where the spheres are completely engulfed, the depth of the spheres varies as the radius as $\delta \sim R^{3/2}$. For slightly stiffer gels, where the spheres only partially deform the interface remaining largely on the surface, their depths scale as $\delta \sim R^2$. An asymptotic analysis explained the experimentally observed scaling law in

the large deformation limit. That the elastic energy scales over a large volume ($\varepsilon_{elastic} \sim \delta^3$) is confirmed by a different experiment of indenting the gel with a sharp slender needle. Comparing the variation of the gravitational energy ($\varepsilon_{gravity} \sim \Delta\rho g R^3 \delta$) with that of the elastic energy at equilibrium, we find that the penetration depth of an elastobuoyant sphere scales as its radius raised to the exponent 3/2 in the limit of large deformations. This study defines a new paradigm in the field of contact mechanics, for the softest limit of a sphere indenting an elastic half-space.

In Chapters 5-8, we showed how self-assembly of particles can be brought about by using elastic forces in conjunction with capillarity and gravity. While motions of particles due to the gradient of elastic strain energy is well-known in various settings, the fact that particles can interact with the help of long range forces in elastic mediums in the macroscopic realm is the main finding of this group of studies. We studied particle assembly inside a soft gel, on the surface of a soft gel and on a thin elastic film supported on a pool of liquid. Dense particles can be easily dispersed on such elastic supports that would otherwise sink in normal liquids and thus ensure better control in designing self-organizing systems. One could then extend this philosophy to microscopic size objects with even softer gels and by replacing gravity with an electrical or a magnetic force, or, perhaps, even subjecting the gel to a pre-determined mechanical deformation.

The penultimate Chapter 9 discusses how hydrogel spheres spread on substrates with different surface energies. While the work is still ongoing, we summarize the main observations of this study. For the completely hydrophilic case, the gels spread by forming a "foot"-like regime closer to the substrate, while maintaining its spherical global shape is maintained away from the contact region due to elasticity. The measured

contact angles at the triple line of these soft spheres show that they systematically increase with their elasticity and decrease as the work of adhesion is increased. Additionally, we learned that the dimension of the "foot" follows a simple scaling law derived from the balance of the adhesion and elastic strain energies in that region. A constitutive model to describe the elastic tension similar to that of the viscous dissipation for the spreading of liquids but with an arbitrary exponent for the strain to remove the singularity at the crack tip, reveals that it may be a good assumption for the elastic wetting since the deformations are large and highly nonlinear.

Therefore, through this dissertation, we learned how elastocapillarity and elastobuoyancy can play profound roles in diverse phenomena in soft solids. The surface tension of these soft solids plays a significant role in the mechanics of deformation of the soft solids along with their elasticity that manifests in surface instabilities, adhesion, wetting and substrate induced particle aggregation. In the following section, we will present some new ideas and directions that we plan to pursue in the future.

10.2. Suggestions for Future Work

10.2.1. Elastic Vibration of Soft Spheres by Suppressing Surface Tension.

In chapter 3, we found a scaling for the resonant modes of vibration of the soft hydrogel spheres, subjected to random noise, which is weakly dependent on elasticity and mainly governed by capillarity. It will be interesting to check the robustness of the scaling by varying the interfacial tension of the gel spheres. This can be done by submerging the spheres in another liquid of known surface tension and subjecting the whole system to random Gaussian noise. The asymptotic limit would be to nullify the

surface tension completely by making the interfacial tension zero. In this case, one could expect only the role of elastic spring constant to govern the resonant modes of the hydrogel spheres. One has to be careful about the optical contrast between the gel spheres and the surrounding liquid as well as make sure that there is an effective gravity in the system to allow for the surface fluctuation of the spheres.

10.2.2. Effect of Surface Energy of Particles in Elastobuoyancy Phenomenon.

In Chapter 4, we talked about the effect of elastobuoyancy and how a sphere is engulfed by a gel in the large deformation limit and on the other hand remains largely on the surface of stiffer gels. An experiment depicted in Figure 10.1 shows that a hydrophobic glass sphere remains on the surface whereas a hydrophilic one of the same size is engulfed to reach the elastobuoyant state. While our analyses in the asymptotic regimes of large and small deformations stand, it will be interesting to see how the surface energy of the sphere may play a role in the intermediate regime where the ratio of the radius to the elastobuoyant length ($\Delta \rho g R / \mu$) is of the order of one. This analysis
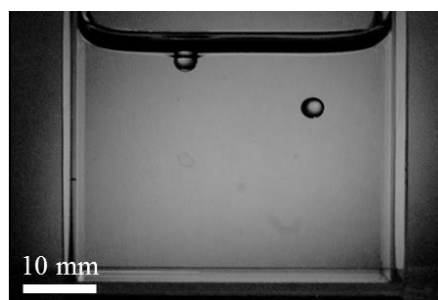
Figure 10.1. Figure illustrating fine balances of the elastic, wetting and gravitational forces giving rise to two different scenarios for same sized glass spheres (3.2 mm diameter) but with different surface energy in a polyacrylamide hydrogel of shear modulus 10 Pa. An untreated (hydrophilic) glass sphere (right) immediately plunges into the gel and becomes neutrally buoyant afterward. A hydrophobic glass (left) floats on the surface of the same gel. [1]

of including the role of surface tension in the intermediate regime will be very useful in designing systems to guide the self-assembly of particles or under-substrate soft-fluidic devices.

10.2.3. Elastocapillary Assembly followed by Dis-Assembly: Design Protocol.

While we stressed upon new protocols to design self-assembly in elastic systems, one could also ask the question: how one could bring about disassembly of particles to make it a reversible process. We know that when a polymer gel is heated, it becomes stiffer while its elastic modulus is lowered when it is cooled. Beginning with a container of homogeneously elastic gel, we can release particles such that they will undergo elastocapillary aggregation to form a cluster floating at the central region in the container. Now, if we heat the region that has the group of particles, such that it becomes stiffer while the outer periphery is cooled, there will be a radial gradient of elasticity and the particles will migrate away from the stiff part into the softer parts. Daniel *et. al.*[2] used the idea of creating radial gradients for surface energy for asymmetric wetting and outward migration of the liquid drops condensing on them. Here, we propose to do the same but with spheres on a gradient elasticity substrate (Refer to Appendix IV for more details on thermally induced motion of particles along a strain energy gradient). In this way, one can essentially design at her/his own will a system to control particle assembly or disassembly and even have a sorting device. A soft fluidic device could also be generated *in situ* by cooling selective channels to create "soft pathways" without actually designing a fluidic device *a priori*. One could then also think of creating an *Elasto-thermal* trap whereby a particle could be manipulated on a soft substrate by modulating the elasticity with a moving cooling source.

References

(1)   Chakrabarti, A.; Chaudhury, M. K. Elastocapillary Interaction of Particles on the

Surfaces of Ultrasoft Gels: A Novel Route To Study Self-Assembly and Soft

Lubrication. *Langmuir* **2014**, *30* (16), 4684–4693.

(2)   Daniel, S.; Chaudhury, M. K.; Chen, J. C. Fast Drop Movements Resulting from

the Phase Change on a Gradient Surface. *Source Sci. New Ser.* **2001**, *291* (5504),

633–636.

Appendix I

Rayleigh Taylor Instability in Soft Elastic Solids[a]

I.1 Introduction

When elastic solids are subjected to a stress, they undergo morphological transitions forming different kinds of instability patterns.[1,2] Several experiments and theoretical studies have been performed to show how relatively stiffer elastic materials undergo wrinkling, folding or creasing.[3–9] Similarly, elastic solids also undergo instabilities by the influence of destabilizing adhesive forces,[10–12] by electric field[13] or when elastic properties are partially altered due to either stiffening[14] or swelling.[15] Very compliant softer solids where surface forces are of the order of the strain energy deform somewhat differently from their stiffer counterparts and an entire class of such instabilities have been recently discovered.[16–18] We explore one such instability in a layer of soft solid attached to a rigid substrate, whose free surface develops periodic hexagonal undulations due to downward gravitational volume force.[18] The other scenario where such an instability will be observed is when a heavier phase (a liquid layer that has a higher density than the soft solid) is placed above the soft solid.

Formation of hexagonal patterns in elastic systems undergoing instability have been experimentally observed before, however the nature of the bifurcation, the control parameter that drives the instability or stability of the patterns differ from one situation to another. Extensive theoretical work has also been done to study all possible patterns that may form during bifurcation from the base state.[4–8,19–21] These studies compare the relative energies as well as the stability of the various possible patterns and match their predictions with experimental studies in some cases. In our system of a soft elastic layer that is subjected to the downward gravitational volume force, only hexagonal patterns were observed experimentally. The origin of this elastic instability bears stark similarities with its analogous hydrodynamic version: the Rayleigh Taylor instability (RTI) that arises due to the mismatch of densities in the two adjacent fluid layers where the upper heavier fluid (liquid) tries to displace a lower lighter fluid (air). However, the fluctuations that develop on the free surface of liquid in RTI grow with time that eventually drains the liquid by pinching off into droplets from the surface.[22–24] In this regard, the elastic version of the RTI is different in that once the patterns form on the surface, they remain stationary until the downward gravitational acceleration is switched off by reversing the boundary conditions of the top and bottom surfaces of the soft layer.

Before going into the detailed bifurcation analysis of such a system, we recall that occurrence of hexagons in fluid instabilities has been reported by Beńard[25] around a century ago. When a liquid layer is heated from the bottom and the upper surface is free, flow patterns are observed due to surface tension gradients induced by temperature, which is commonly known as the Beńard-Marangoni instability.[26] However, when the upper layer of the fluid is bounded by a cooler plate, flow patterns are due to gradients in buoyancy, termed as the Rayleigh-Bénard instability.[27] Palm[28] was the first to explain a perceived tendency towards formation of hexagonal cells in Rayleigh-Bénard convection by an argument of the

resonance of three linear modes superimposed in a way such that the phase of each one is separated from the adjacent ones by $2\pi/3$ and the sum of their wave-vectors in the three direction resulted to zero. Similarly, one would expect for an elastic system that the resonance of the modes will lead to the formation of hexagonal patterns, failing which may result in dis-ordered patterns.[14] Experiments reveal that such patterns appear subcritically. This enforces us to compare our system again with that of liquids undergoing Bénard convection where Segel and Stuart,[29] Busse[30] and Joseph and Sattinger[31] showed that it was theoretically possible to obtain hexagonal patterns through a subcritical bifurcation.[32] Extensive reviews discuss this subject in detail.[33–36]

In this study, we also considered a more formal approach based on the Lyapunov-Schimdt decomposition along with an asymptotic expansion about the bifurcation point. This is particularly applicable to elastic systems that have a well defined potential energy function. Koiter developed this theory to analyze the stability of loaded elastic systems with or without the presence of imperfections.[37–39] This has been widely used to analyze the problems of shell-buckling,[2,40,41] casting light upon the highly nonlinear postbuckling behavior that had great practical implications on the design and engineering of almost perfect shells. The advantage of this method is that it provides a reduced nonlinear system of equations that gives better insight into the nature of postbuckling behavior of an elastic system as well as help in deducing the stability of the same.[42,43] The scenario of buckling arises in various other elastic systems, *e.g,* a thin stiff film on compliant elastic substrate subjected to compressive bi-axial stresses.[4–6,8,9,44] Another scenario of these buckling instabilities arise when there is a rigid shell on a soft cylindrical or a spherical core.[19,45,46] While these studies have considered other approaches, we show how to study the bifurcation of an elastic system undergoing instability by using the LSK approach on the model system of a soft elastic layer that is supported by experimental observations.

This paper is organized as follows. In Section 2, we report our experimental observations. In Section 3 we present the general framework of the energy formulation of the elastic system and we reiterate the linear stability analysis that yields the threshold for the parameter α. In Section 4, we discuss the hexagonal pattern formation in the regime of the small amplitudes, and discuss its stability. Section 5 is devoted to patterns of finite amplitude obtained by numerical simulations or from an heuristic functional energy. Section 6 discusses other possible patterns, which are shown to be less stable than hexagonal patterns. In the final Section 7, we summarize our results and we extend our analysis to the wide range of patterns formation cases in elastic systems.

I.2 Experiments

A square container of sides equal to $\ell \times \ell \times h = (40 \text{ cm})^2 \times 2.5 \text{ cm}$ is filled with the reagents generating a crosslinked polyacrylamide gel, dissolved in ultra-pure water. The resulting gel behaves as an incompressible, isotropic and purely elastic solid for strains up to several hundred percent. The shear modulus (μ) can be finely tuned by varying the concentrations in monomers and cross-linkers or the temperature. The density (ρ) is almost equal to the density of water. After the gel has cured, the container is turned upside down so that its free surface undergoes the normal outgoing gravitational acceleration g. Several experiments have been performed with different concentrations and temperatures, by gradually decreasing the shear modulus. We observe that the surface remains perfectly flat (see Fig. I.1-a) in all the experiments made with shear moduli larger than 40.5 Pascals, whereas many hollows spontaneously appear, and remains permanently for all the tested gels having a shear modulus lower than 40.5 Pascals (see Fig. I.1-b). These hollows, which are separated by vertical walls, are organized following a quasi-hexagonal patterns.
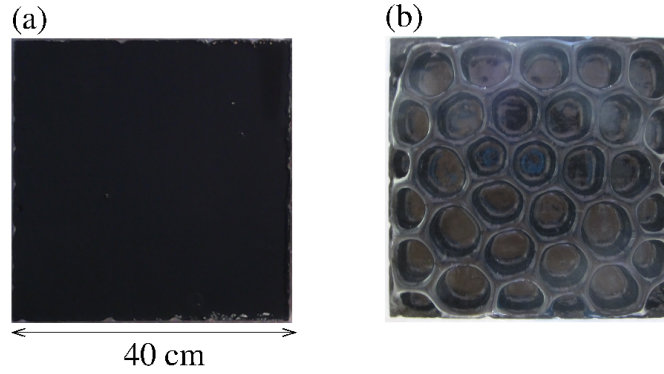
Figure I.1: Downward-facing initially flat surfaces of two gel slabs fixed in a square container of lateral size 40 cm and height 2.5 cm. The free surfaces are pictured from below. (a) Specimen with a shear modulus equal to 45 Pa: the inverted surface remains flat. (b) Specimen with a shear modulus equal to 37 Pa: a quasi-hexagonal pattern spontaneously appears as soon as the sample is turned upside down.

The average depth of the hollows has been measured as a function of the shear modulus of the specimen. To avoid bias due to the proximity of the borders of the container, we have selected for averaging the hollows whose boundaries are not in direct contact with the borders. In figure I.2, the mean depth is plotted as a function of the dimensionless control parameter $\rho g h/\mu$. Strikingly, the depth of the hollows is directly finite and we do not observe a regime of smaller amplitudes, in contrast with previous observations made in containers with a far smaller lateral size compared to the height.[18] The absence of small amplitude near the threshold appears here as a specific feature to systems with lateral sizes far larger than the thickness ($\ell \gg h$). Moreover, the value for the instability threshold is found at $\rho g h/\mu = 5.67 \pm 0.1$ for the experiments made in the large cells ($\ell = 40$ cm, $h = 2.5$ cm), a value significantly smaller than the value of instability threshold found with the cells having a smaller aspect ratio (diameter $= 18$ cm ; h=2.75 cm).[18]

Below we explain why either flat surfaces or hexagonal patterns with finite amplitudes are observed, we show that the value of the threshold defining the boundary between the two regimes is well captured by the corresponding non-
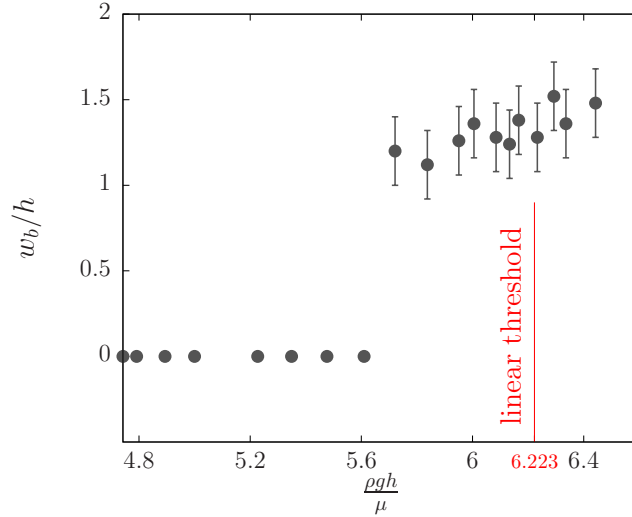
Figure I.2: Mean amplitude (downward displacement) of the deformed gel surface as a function of the control parameter $\rho g h / \mu$.

linear analysis, as well as the geometry of the patterns.

I.3 Linear Stability Analysis

I.3.1 Energy

In order to define the total potential energy of the incompressible and isotropic elastic material subjected to the downward volume force ρg, we begin with the most general form for its strain energy density. Let $\underline{x} = (x, y, z)$ denote the deformed coordinates in terms of $\underline{X} = (X, Y, Z)$, the Lagrangian coordinates (the axis for Z in the Cartesian coordinate system is vertical and upward, see Fig. I.3). We consider a block of elastic material initially contained in the domain $0 \leq Z \leq h$, with free lateral boundaries, and a total potential energy:

$$
\begin{aligned}
\mathcal{E} = & \iiint W(I_1, I_2) \, \mathrm{d}X \, \mathrm{d}Y \, \mathrm{d}Z - \iint p(X, Y, Z) \left(\det \underline{\underline{F}} - 1 \right) \mathrm{d}X \, \mathrm{d}Y \, \mathrm{d}Z \\
& + \iint \rho \, g \, x(X, Y, Z) \, \mathrm{d}X \, \mathrm{d}Y \, \mathrm{d}Z
\end{aligned}
\tag{I.1}
$$

where $W(I_1, I_2)$ is the strain energy, $\underline{\underline{F}} = \underline{\nabla}\, \underline{x}(\underline{X})$ is the deformation gradient and $p(X, Y, Z)$ is a Lagrange multiplier connected to the pressure. The three terms in (I.1) are the potential elastic energy, the Lagrange multiplier term associated with the incompressibility condition and the potential energy due to gravity, respectively.
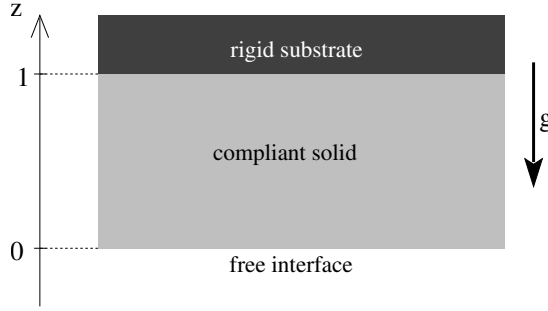
Figure I.3: A compliant layer of thickness $h = 1$ and shear modulus $\mu = 1$ is rigidly attached at its upper surface to a undeformable horizontal flat substrate. The lower surface is free to deform. The system undergoes the downward volume force $\alpha = \rho g$ with ρ the mass density of the elastic material and g the gravity acceleration.

For an isotropic material, the strain energy is a function of the strain invariants,

$$\left(I_1, I_2\right) = \left(\operatorname{tr}\underline{\underline{C}} - 3,\ \frac{\operatorname{tr}^2\underline{\underline{C}} - \underline{\underline{C}} : \underline{\underline{C}}}{2} - 3\right) \tag{I.2}$$

where $\underline{\underline{C}} = \underline{\underline{F}}^T \cdot \underline{\underline{F}}$ is the Green's deformation tensor. Different constitutive laws correspond to different choices of the strain energy function $W(I_1, I_2)$; the particular case of a neo-Hookean material corresponds to

$$W_{\mathrm{NH}}(I_1, I_2) = \frac{\mu}{2}\, I_1. \tag{I.3}$$

In the following, we work with units such that $h = 1$, and the tangent shear modulus is $\mu = 1$. We denote by α the dimensionless gravity, *i.e.* we substitute $\rho\, g \to \alpha$ in the above equations.

In terms of W, one can express the tangent shear modulus as

$$\mu = 2 \left(\frac{\partial W}{\partial I_1}(0,0) + \frac{\partial W}{\partial I_2}(0,0) \right). \tag{I.4}$$

Therefore, for our particular choice of units such that $\mu = 1$, we have

$$\frac{\partial W}{\partial I_1}(0,0) = \frac{1}{2} - \tau_0, \tag{I.5}$$

where we denote by τ_0 the strain second energy gradient near the undeformed configuration:

$$\tau_0 = \frac{\partial W}{\partial I_2}(0,0). \tag{I.6}$$

By (I.3), we have $\tau_0 = 0$ in the neo-Hookean case.

We denote by $\underline{t} = (x, y, z, p)$ the extended set of unknowns including the pressure.

I.3.2   Base solution

The undeformed solution is given by

$$\underline{t}_0(\alpha) = \left(x_0 = X, y_0 = Y, z_0 = Z, p_0 = \alpha Z + 1 \right). \tag{I.7}$$

It is a solution of the nonlinear equations of equilibrium,

$$\forall \hat{t}(X, Y, Z) \text{ k.a}, \quad D\mathcal{E}(\alpha, \underline{t}_0(\alpha)) \cdot [\hat{\underline{t}}] = 0 \tag{I.8a}$$

and of the kinematical boundary conditions

$$\left(x_0, y_0, z_0 \right)_{(X,Y,1)} = 0. \tag{I.8b}$$

Virtual displacements $\hat{\underline{t}}$ in (I.8a) must be kinematically admissible (k.a), *i.e.* must satisfy the incremental kinematical boundary conditions $\left(\hat{x}, \hat{y}, \hat{z}\right)_{(X,Y,1)} = 0$. In (I.8a), $D\mathcal{E}(\underline{t}) \cdot [\underline{t}_1]$ denotes the first variation of the energy evaluated in the configuration $\underline{t}$ with an increment $\underline{t}_1$ of the unknowns.

I.3.3 Linear stability

For the linear stability,[18] one seeks a perturbation about the base solution in the form $\underline{t}_1(X, Y, Z) = \underline{T}_1(Z)\, e^{\imath \underline{k} \cdot (X,Y)}$, where $T_1(Z)$ is a set of four complex amplitudes, and $\underline{k}$ is a 2D wavevector in the plane (OXY). Since we consider a pure harmonic wave for the moment, one can temporarily align the X axis with the wavenumber $\underline{k}$. In this frame, the perturbation reads

$$\underline{t}_1^X(X, Y, Z) = \underline{T}_1^X(Z)\, e^{\imath k X} \tag{I.9}$$

where now $\underline{k} = (k, 0)$. The equations of equilibrium linearized about the base solution $\underline{t}_0(\alpha)$ read, in weak form,

$$\forall \hat{t}(X, Y, Z) \text{ k.a}, \quad D^2\mathcal{E}(\alpha, \underline{t}_0(\alpha)) \cdot [\underline{t}_1^X, \hat{t}] = 0 \tag{I.10a}$$

where $D^2\mathcal{E}$ is the second variation, which is a bilinear form on the real increment $\underline{t}_1^X$ and on the virtual increment $\hat{\underline{t}}$. The increment is subjected to the incremental boundary conditions

$$\left(x_1^X, y_1^Y, z_1^Z\right)_{(X,Y,1)} = 0. \tag{I.10b}$$

Inserting the special form (I.9) of the perturbation and integrating by parts, the problem (I.10) is transformed into a set of 12 homogeneous linear differential equations with 12 boundary conditions. There exists non-trivial solutions only

when the critical condition is met,[18]

$$\alpha^*(k) = 2\,k\,\frac{1 + 2\,k^2 + \cosh(2\,k)}{\sinh(2\,k) - 2\,k}.$$

<div align="right">(I.11)</div>

Neither the linear mode $\underline{t}_1^X$ nor the critical load $\alpha^*(k)$ depend on the strain energy function W and on its derivatives as long as $\mu = 1$ in equation (I.5). As a result, the results of the linear stability analysis presented here are universal, *i.e.* they apply to any constitutive law. The value of k that minimizes α^* is denoted by k_c and satisfies

$$\frac{\mathrm{d}\alpha^*}{\mathrm{d}k}(k_{\mathrm{c}}) = 0.$$

<div align="right">(I.12)</div>

The corresponding value of α^* is the critical load,

$$\alpha_{\mathrm{c}} = \alpha^*(k_{\mathrm{c}}).$$

<div align="right">(I.13)</div>

The numerical values are found by root-finding as

$$\alpha_{\mathrm{c}} \simeq 6.223, \quad k_{\mathrm{c}} \simeq 2.120.$$

<div align="right">(I.14)</div>

These values were previously derived for analyses on adhesion induced instability patterns in thin elastic films.[10] The explicit expression of the marginal mode, in the frame such that $\underline{k} = (k_{\mathrm{c}}, 0)$ reads

$$x_1^X(X, Y, Z) = \Re\!\left(-\imath\,\xi\,e^{\imath\,k_{\mathrm{c}}\,X}\right) f_x(Z) \tag{I.15a}$$

$$y_1^X(X, Y, Z) = 0 \tag{I.15b}$$

$$z_1^X(X, Y, Z) = \Re\!\left(\xi\,e^{\imath\,k_{\mathrm{c}}\,X}\right) f_z(Z) \tag{I.15c}$$

$$p_1^X(X, Y, Z) = \Re\!\left(\xi\,e^{\imath\,k_{\mathrm{c}}\,X}\right) f_p(Z) \tag{I.15d}$$

where $\Re$ stands for the real part, ξ is a complex amplitude and f_x, f_z and f_p are known functions of Z:

$$f_x(Z) = \frac{1}{2k_c - \sinh(2k_c)} \left[Z\sinh(k_c Z)\left(\alpha_c \sinh k_c \cosh k_c - k_c\left(\alpha_c + 2k_c^2\right)\right) \right.$$
$$\left. + k_c(2k_c(Z-1) - Z\sinh(2k_c))\cosh(k_c Z) \right] \tag{I.16}$$

$$f_z(Z) = \frac{1}{4k_c(k_c - \sinh k_c \cosh k_c)} \left[(\sinh(2k_c) - 2k_c)\left(\alpha_c + 2k_c^2 Z\right)\sinh(k_c Z) \right.$$
$$bigg. + k_c\cosh(k_c Z)\left(2k_c\left(2k_c^2 Z + \alpha_c Z + 2\right) - \sinh(2k_c)(\alpha_c Z + 2)\right) \Bigg] \tag{I.17}$$

$$f_p(Z) = -\frac{1}{4k_c(k_c - \sinh k_c \cosh k_c)} \left[k_c\cosh(k_c Z)\left(4k_c^3(\alpha_c Z - 2) + 2\alpha_c^2 k_c Z - \alpha_c^2 Z\sinh(2k_c)\right) \right.$$
$$\left. + (\sinh(2k_c) - 2k_c)\left(\alpha_c^2 + 2k_c^2(\alpha_c Z - 2)\right)\sinh(k_c Z) \right] \tag{I.18}$$

Note that the normalization of this mode is such that $f_z(0) = 1$. As a result, the complex amplitude of the mode ξ can be interpreted as the complex amplitude of the deflection of the free surface,

$$z_1^X(X, Y, 0) = \Re(\xi\, e^{i\,k_c\,X}). \tag{I.19}$$

The mode in (I.15a–I.18) having a wavevector along the X axis is written in compact form as

$$\underline{t}_1^X = \Re\left(\xi\, \underline{\tilde{T}}_1^X(Z)\, e^{i\,k_c\,X}\right) \tag{I.20}$$

where $\underline{\tilde{T}}_1^X(Z) = \left(-i\,f_x(Z), 0, f_z(Z), f_p(Z)\right)$ collects the complex amplitudes of the

unknowns.

Relaxing the assumption that $\underline{k}$ is aligned with the X axis, and denoting by ϕ the polar angle of $\underline{k}$ in the (OXY) plane, $\underline{k} = k_c\,(\cos\phi, \sin\phi)$. The corresponding linear mode is easily obtained by applying a rotation with angle ϕ about the the Z axis onto the special solution $\underline{t}_1^X$ corresponding to $\phi = 0$. The result reads

$$\underline{t}_{1,\phi}(X, Y, Z) = \Re\left(\xi_\phi\,\underline{\tilde{T}}_{1,\phi}(Z)\,e^{\imath\,k_c\,(X\cos\phi + Y\cos\phi)}\right), \tag{I.21}$$

where ξ_ϕ is the complex amplitude of this harmonic solution, and $\underline{\tilde{T}}_{1,\phi}(Z)$ is a vector containing the complex amplitudes of the 4 unknowns,
$\underline{\tilde{T}}_{1,\phi}(Z) = \left(-\imath\,f_x(Z)\,\cos\phi, \imath\,f_x(Z)\,\sin\phi, f_z(Z), f_p(Z)\right)$.

I.4   Hexagonal Patterns with infinitesimal amplitudes

Different instability patterns, e.g: hexagons, stripes or even rhombics, may be theoretically possible in a confined layer of elastic solid undergoing Rayleigh Taylor Instability. We discussed in Section I.2 that the experimental patterns in such an instability are always hexagons. Thus, firstly we dedicate this section to the discussion of the hexagonal patterns. To begin with, we study the weakly nonlinear regime of the formation of these patterns by using the framework of General Lyapunov Schmidt Koiter (LSK) Expansion which is a nonlinear perturbation method, used to study asymptotic postbuckling theory.[37] Using the LSK approach, one can gain valuable insights about the bifurcated states of a particular system from its equilibrium solution by the expansion of the reduced equilibrium equations about any reference point. In our problem, we have considered the expansion of the reduced equilibrium condition about the critical threshold point that is obtained from the linear stability analysis. One could also, by employing the LSK method, look at the decomposition of the displacements into various admissible planes, however for our particular problem of the Elastic Rayleigh Taylor Instability, we

did not need such decomposition of the displacements.

In what follows, we systematically discuss the asymmetric bifurcation case that is a precursor to derive the hexagonal solutions for Elastic Rayleigh Taylor Instability. After obtaining the various branches from the weakly nonlinear perturbation analysis, we discuss stability of these branches.

I.4.1 Asymmetric Bifurcation: Introduction to LSK

The nonlinear equilibrium condition is given by Eq. I.8a. The force parameter α and the deformed coordinates $\underline{t}(X, Y, Z)$ are weakly perturbed in terms of a small parameter η as follows:

$$\alpha = \alpha_{\mathrm{c}} + \eta\,\alpha_1 \tag{I.22a}$$

$$\underline{t}(\alpha) = \underline{t}_0(\alpha) + \eta\,\underline{t}_1 + \eta^2\,\underline{t}_2 + \cdots \tag{I.22b}$$

The expansion of the nonlinear equilibrium condition (Eq. I.8a) for the weakly perturbed parameters α and $\underline{t}$ (Eq. I.22) about the bifurcation point (given by the base solution, Eq. I.7) gives rise to the reduced equilibrium conditions at different orders of the small parameter η, which are given below. At order η, we have linear stability criterion as already discussed before (Eq. I.10):

$$\forall \hat{t}(X, Y, Z) \text{ k.a,} \quad D^2\mathcal{E}(\alpha_{\mathrm{c}}, \underline{t}_0(\alpha_{\mathrm{c}})) \cdot [\underline{t}_1, \hat{t}] = 0. \tag{I.23}$$

At order η^2, we have:

$$\forall \hat{t}(X, Y, Z) \text{ k.a,} \qquad D^2\mathcal{E}(\alpha_{\mathrm{c}}, \underline{t}_0(\alpha_{\mathrm{c}})) \cdot [\underline{t}_2, \hat{t}] + \quad \frac{1}{2}D^3\mathcal{E}(\alpha_{\mathrm{c}}, \underline{t}_0(\alpha_{\mathrm{c}})) \cdot [\underline{t}_1, \underline{t}_1, \hat{t}]$$
$$+ \quad \alpha_1 \left.\frac{\mathrm{d}D^2\mathcal{E}(\alpha, \underline{t}_0(\alpha))}{\mathrm{d}\alpha}\right|_{\alpha=\alpha_{\mathrm{c}}} \cdot [\underline{t}_1, \hat{t}] = 0, \tag{I.24}$$

where $\hat{\underline{t}}(X, Y, Z)$ is the set of virtual functions $\left(\hat{x}, \hat{y}, \hat{z}, \hat{p}\right)$ that represent infinites-

imal increments of the displacements and the Lagrange multiplier. The solvability conditions are obtained by setting the arbitrary incremental displacements $\hat{\underline{t}}(X, Y, Z)$ to the linear order solution for the displacement $\underline{t}_1(X, Y, Z)$ that leads to the simplification of of the above equation as a consequence of Eq. I.23. As a result, Eq.I.24 now writes:

$$\frac{1}{2} D^3 \mathcal{E}(\alpha_c, \underline{t}_0(\alpha_c)) \cdot [\underline{t}_1, \underline{t}_1, \underline{t}_1] + \alpha_1 \left. \frac{\mathrm{d} D^2 \mathcal{E}(\alpha, \underline{t}_0(\alpha))}{\mathrm{d}\alpha} \right|_{\alpha=\alpha_c} \cdot [\underline{t}_1, \underline{t}_1] = 0. \qquad \text{(I.25)}$$

I.4.2 Solution of the Hexagons

In this section we show that the possibility of a resonance between three wave-vectors $\underline{k}_i$ with the same modulus and at $2\pi/3$ angle of each other explains the hexagonal patterns.[28] We first combine three linear modes (Eq. I.21) with independent complex amplitudes ξ_1, ξ_2 and ξ_3 and polar directions $\phi_1 = 0$, $\phi_2 = 2\pi/3$ and $\phi_3 = 4\pi/3$, respectively. The expression of the linear mode $\underline{t}_1(X, Y, Z)$ obtained by superposition of these three modes with arbitrary complex amplitudes reads, in compact form,

$$\underline{t}_1(X, Y, Z) = \Re \left(\sum_{j=1} \xi_i \, \underline{\tilde{T}}_{1,\phi_j}(Z) \, e^{\imath \, k_c \, (X \cos \phi_j + Y \cos \phi_j)} \right). \qquad \text{(I.26)}$$

The resulting deflection of the free surface, for instance, writes

$$z_1(X, Y, 0) = \Re \left(\sum_{j=1}^{3} \xi_j \, e^{\imath \, k_c \, (X \cos \phi_j + Y \sin \phi_j)} \right)$$

thanks to the normalization convention used in Eq. I.17. We use the solvability condition obtained from the LSK expansion at order 2. From Eq. I.24, by taking $\hat{t} = \hat{t}_1$, we get:

$$\forall (\hat{\xi}_1, \hat{\xi}_2, \hat{\xi}_3) \in \mathbb{C}^3 \quad D^3 \mathcal{E}(\alpha_c, \underline{t}_0(\alpha_c)) \cdot [\underline{t}_1, \underline{t}_1, \hat{\underline{t}}_1] + \alpha_1 \left. \frac{\mathrm{d} D^2 \mathcal{E}(\alpha, \underline{t}_0(\alpha))}{\mathrm{d}\alpha} \right|_{\alpha = \alpha_c} \cdot [\underline{t}_1, \hat{\underline{t}}_1] = 0,$$
(I.27)

where (i) $\hat{\underline{t}}_1(X, Y, Z)$ is the set of virtual functions $(\hat{x}, \hat{y}, \hat{z}, \hat{p})$ obtained by replacing the true complex amplitudes (ξ_1, ξ_2, ξ_3) with virtual complex amplitudes $(\hat{\xi}_1, \hat{\xi}_2, \hat{\xi}_3)$, (ii) the first term involves the third variation of the energy $D^3 \mathcal{E}$ evaluated in the marginally stable state with 2 increments equal to the marginal mode (I.26) and the last increment equal to the virtual increment $\hat{\underline{t}}_1$, and (iii) the last term involves the second variation $D^2 \mathcal{E}$ of the energy, which is sequentially evaluated in a base state $\underline{t}_0(\alpha)$, then differentiated with respect to α, then evaluated in the marginally stable state $\alpha = \alpha_c$ and finally evaluated with the real and virtual increments.

Equation (I.27) is polynomial with respect to the true complex amplitudes (ξ_1, ξ_2, ξ_3), and linear with respect to the virtual complex amplitudes $(\hat{\xi}_1, \hat{\xi}_2, \hat{\xi}_3)$. With the help of a symbolic calculation language, it has been rewritten in a more explicit form as

$$\forall (\hat{\xi}_1, \hat{\xi}_2, \hat{\xi}_3) \in \mathbb{C}^3 \quad -\gamma \, \Re\left(\xi_1 \, \xi_2 \, \hat{\xi}_3 + \xi_2 \, \xi_3 \, \hat{\xi}_1 + \xi_1 \, \xi_3 \, \hat{\xi}_2 \right) - \frac{\alpha_1}{2} \, \Re\left(\overline{\xi}_1 \, \hat{\xi}_1 + \overline{\xi}_2 \, \hat{\xi}_2 + \overline{\xi}_3 \, \hat{\xi}_3 \right) = 0,$$
(I.28)

where $\bar{\xi}$ denotes the complex conjugate of ξ and γ is the numerical constant,

$$\gamma = -\frac{k_{\rm c}^2}{16(\sinh(2k_{\rm c}) - 2k_{\rm c})^3} \left(96(4\tau_0 - 1)k_{\rm c}^3 \cosh(k_{\rm c}) + 32(4\tau_0 - 1)k_{\rm c}^3 \cosh(3k_{\rm c}) \cdots \right.$$

$$+12\left(-8\tau_0 + (8\tau_0 - 1)k_{\rm c}^2 + 2\right)\sinh(4k_{\rm c}) - 48k_{\rm c}\left(-8\tau_0 + (8\tau_0 - 1)k_{\rm c}^2 + 2\right)\cosh(2k_{\rm c}) \cdots$$

$$+ 4k_{\rm c}\left(39(4\tau_0 - 1) + 6(7 - 24\tau_0)k_{\rm c}^4 + (68 - 320\tau_0)k_{\rm c}^2\right)\cdots$$

$$+ 3\left(-68\tau_0 + 4(24\tau_0 - 7)k_{\rm c}^4 + 8(64\tau_0 - 15)k_{\rm c}^2 + 17\right)\sinh(2k_{\rm c})\cdots$$

$$\left. + (4\tau_0 - 1)\sinh(6k_{\rm c}) + 60(1 - 4\tau_0)k_{\rm c}\cosh(4k_{\rm c}) \right) \quad \text{(I.29)}$$

With $k_{\rm c}$ given by Eq. I.14, this evaluates to

$$\gamma = 1.191594 - 9.139691\,\tau_0. \quad \text{(I.30)}$$

The nonlinear elastic modulus $\tau_0 = \frac{\partial W}{\partial I_2}(0,0)$, as defined in Eq. I.6, fully captures the dependence on the constitutive law. It is in fact remarkable that only a single modulus enters into the final result: the *second* derivatives $\frac{\partial^2 W}{\partial I_1{}^2}(0,0)$, $\frac{\partial^2 W}{\partial I_1\,\partial I_2}(0,0)$ and $\frac{\partial^2 W}{\partial I_2{}^2}(0,0)$ do enter into the intermediate expressions of γ but they ultimately cancel out when simplifications are carried out. As mentioned above, the case of an incompressible neo-Hookean material corresponds to $\tau_0 = 0$.

Note that the dependence on the complex amplitudes in Eq. I.28 could have been anticipated easily by analyzing the average of the products of the various harmonic components. To calculate the coefficients, however, one needs to evaluate integrals involving the functions (f_x, f_z, f_p) and their derivatives across the thickness.

I.4.3 Branches of the hexagonal patterns

In this section, we show that a resonance between three wave-vectors $\underline{k}_i$ with the same modulus and at $2\pi/3$ angle of each other (*i.e.* such that $\sum_i \underline{k}_i = 0$) explains the hexagonal patterns.[28]

The amplitudes of the three modes are connected with each other in the following manner as obtained from Eq. I.28 by setting sequentially two of the three virtual increments $\left(\hat{\xi}_3, \hat{\xi}_1, \hat{\xi}_2 \right)$ to 0:

$$2\gamma\, \xi_1\, \xi_2 = -\alpha_1\, \bar{\xi}_3 \tag{I.31a}$$

$$2\gamma\, \xi_2\, \xi_3 = -\alpha_1\, \bar{\xi}_1 \tag{I.31b}$$

$$2\gamma\, \xi_3\, \xi_1 = -\alpha_1\, \bar{\xi}_2 \tag{I.31c}$$

By combining Eqs. I.31-a and I.31-b, we have as follows:

$$-2\gamma\, |\xi_1|^2 \cdot \xi_2 = -2\gamma\, |\xi_3|^2 \cdot \xi_2. \tag{I.32}$$

Equation I.32 implies that either $\xi_2 = 0$ or $|\xi_1| = |\xi_3|$. Similarly, by combining Eqs. I.31-a & c and Eqs. I.31-b & c as above, we find that $\xi_1 = \xi_2 = \xi_3 = 0$ or, $|\xi_1| = |\xi_2| = |\xi_3|$: for the non trivial solution, the moduli of the complex amplitudes are equal. Let us denote this value of the uniform amplitude by β.

We now introduce an unknown phase φ_i such that the complex amplitudes for the three modes write: $\xi_i = \beta e^{\varphi_i}$, where the arbitrary phases φ_i ($i =$1,2,3) can be denoted by a unique phase variable $\psi = (\varphi_1 + \varphi_2 + \varphi_3)$ such that $\xi_1 = |\beta| e^{\psi}$ and $\xi_2, \xi_3 = |\beta|$ due to translation invariance. On multiplying Eq. I.31-a with ξ_3 the

following is obtained:

$$2\gamma \xi_1 \xi_2 \xi_3 = -\alpha_1 \beta^2 \Rightarrow \beta e^{(\varphi_1 + \varphi_2 + \varphi_3)} = -\frac{\alpha_1}{2\gamma}. \tag{I.33}$$

Thus, $\beta = \alpha_1/2\gamma$ and $\psi = \pi$ if $\alpha_1/\gamma > 0$. Otherwise, $\beta = -\alpha_1/2\gamma$ and $\psi = 0$. Note that α_1 varies between negative and positive values depending upon subcritical and supercritical bifurcation. β is plotted as function of α in Fig. I.5.

These equilibrium solutions correspond to a deflection at the interface $w|_{interface}$ as follows:

$$z|_{interface}(X, Y, 0) = 0 + \eta \beta \Re \left(e^{i(k_c X + \psi)} + e^{i k_c \left(-\frac{X}{2} + \frac{Y\sqrt{3}}{2}\right)} + e^{i k_c \left(-\frac{X}{2} - \frac{Y\sqrt{3}}{2}\right)} \right). \tag{I.34}$$

Two kinds of periodic hexagonal patterns emerge, depending on the value of ψ (see Fig. I.4): for $\psi = \pi$ the deflection of the interface is minimum and negative at the center of the hexagons, whereas for $\psi = 0$ the deflection of the interface is maximum and positive. The center of the hexagons can thus be either bumps ($\psi = 0$) of hollows ($\psi = \pi$).

From Eq. I.34 we can evaluate the peak of the maximum deviation of the surface height, $w_b = 3\left|\eta \frac{\alpha_1}{2\gamma}\right|$.

Let us summarize: γ (defined in Eq. I.30) can be positive or negative, depending on the constitutive law of the elastic layer.

- If $\gamma > 0$ then for an applied volume force smaller than the one corresponding to the linear threshold, $\alpha < \alpha_c$, the ratio α_1/γ is negative. In this case, the equilibrium solution emerging from the weakly nonlinear analysis is for $\psi = 0$ and the center of the hexagons are hollows. On the contrary, beyond the linear threshold ($\alpha_1 > 0$), the weakly nonlinear equilibrium solution if for $\psi = \pi$ and the center of the hexagons are bumps (Fig. I.5-left).

- If $\gamma < 0$, $\psi = \pi$ for $\alpha < \alpha_c$ and $\psi = 0$ for $\alpha > \alpha_c$ (Fig. I.5-right).
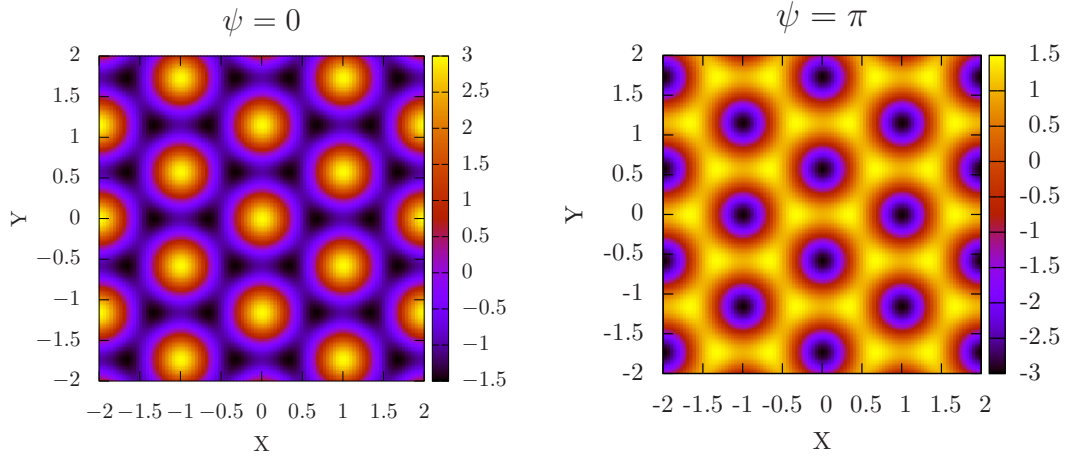
Figure I.4: $z_{interface}(X, Y, 0)$ computed from Eq. I.34 with $\eta\beta = 1$, $k_c = 2\pi$, $\psi = 0$ (left) and $\psi = \pi$ (right). For $\psi = 0$, $z_{interface}(X, Y, 0)$ is maximum at the center of the hexagons, hence hollows at the center of the hexagons. For $\psi = \pi$, $z_{interface}(X, Y, 0)$ is minimum at the center of the hexagons, hence bumps at the center of the hexagons.
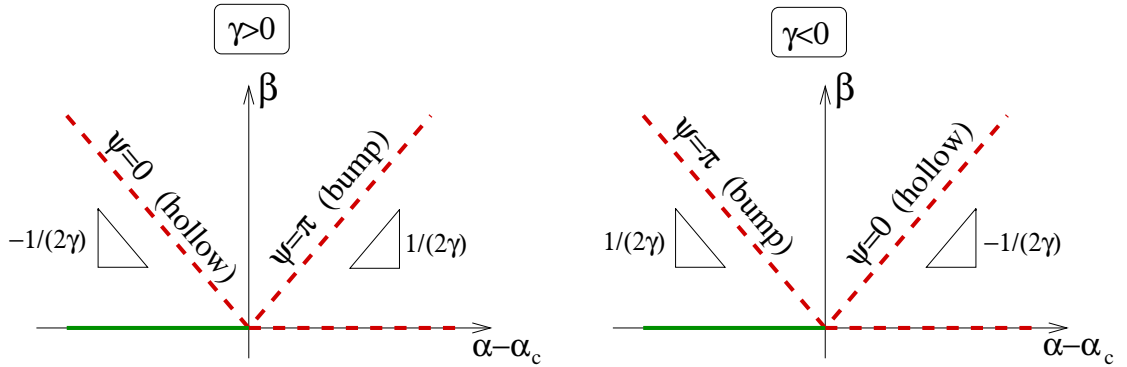
Figure I.5: Amplitude β of the modes constituting the four branches arising from the LSK expansion at order 3, plotted as a function of the distance from the critical value of the control parameter. The unique stable branch is for $\beta = 0$ and $\alpha < \alpha_c$ (green solid line). The other branches are unstable (red dashed lines). Left: for an elastic layer with $\gamma > 0$. Right: for an elastic layer with $\gamma < 0$.

I.4.4 Stability Analysis of the branches found with the LSK expansion

Here we discuss the stability of the hexagonal equilibrium patterns emerging from the weakly nonlinear analysis. The basic principles of determining whether an equilibrium state of a particular system is stable or not depends on the second variation of the free energy of the system. If this quantity is positive definite, the

equilibrium state is energetically stable. On the other hand if the second variation of the free energy is negative, the equilibrium state is unstable.

We derive a generic expression for the energy of the non linear solution intridued in Eq. I.22, $\underline{t}(\alpha) = \underline{t}_0(\alpha) + \eta\underline{t}_1 + \eta^2\underline{t}_2 + \cdots$ where $\underline{t}_1$ is given by Eq. I.26. The equilibrium state(s) are found by minimizing an energy functional denoted as $\mathcal{V}$ which is assumed to depend on the three complex amplitudes ξ_i of $\underline{t}_1$.

The translational symmetry of the system in plane (OXY) imposes that $\mathcal{V}$ expressed as a function of the complex amplitudes is invariant upon any horizontal translation. Therefore, the more general expression of $\mathcal{V}$ is:

$$\mathcal{V}(\xi_i) = A(\xi_1\,\overline{\xi}_1 + \xi_2\,\overline{\xi}_2 + \xi_3\,\overline{\xi}_3) + B(\xi_1\,\xi_2\,\xi_3 + \overline{\xi}_1\,\overline{\xi}_2\,\overline{\xi}_3) + \cdots. \qquad (I.35)$$

The cubic term is invariant through horizontal translations thanks to the condition $\sum_i \underline{k}_i = 0$. Otherwise, the coefficient γ would be zero. The functional Eq. I.35 can be viewed as a series expansion at order 3 in the amplitudes, of a quantity proportional to the total energy of the system. A and B are two real parameters which depend on α. In order to be consistent with the linear stability analysis, A has to be positive for $\alpha < \alpha_c$ and negative for $\alpha > \alpha_c$. As shown in section I.4.3, one can take, for any equilibrium solutions of the system, $\xi_1 = \beta e^{i\psi}$ and $\xi_2 = \xi_3 = \beta$. Eq. I.35 simplifies in:

$$\mathcal{V}(\beta, \psi) = 3A\beta^2 + 2B\beta^3 \cos\psi + \cdots \qquad (I.36)$$

The equilibrium condition $\partial\mathcal{V}/\partial\beta = 0$ yields $A/B = (\alpha - \alpha_c)/(2\gamma)$. One rewrites $\mathcal{V}$ (up to a multiplicative positive constant) as:

$$\mathcal{V}(\beta, \psi) = -\frac{3(\alpha - \alpha_c)}{2}\beta^2 - 2\gamma\beta^3 \cos\psi + \cdots \qquad (I.37)$$

From $\partial^2\mathcal{V}/\partial\beta^2|_{\beta=0} = -3(\alpha - \alpha_c)$, $\partial^2\mathcal{V}/\partial\psi^2|_{\beta=0} = 0$ and $\partial^2\mathcal{V}/\partial\psi\partial\beta|_{\beta=0} = 0$, we

conclude that the branches with $\beta = 0$ are stable for $\alpha < \alpha_c$, and unstable for $\alpha > \alpha_c$.

For the amplitude of the non trivial branches deduced from the LSK method, $\beta = -(\alpha - \alpha_c)/(2\gamma \cos \psi)$, one finds $\frac{\partial^2 \mathcal{V}}{\partial \beta^2} = 3(\alpha - \alpha_c)$. Thus, the non zero equilibrium solution for $\alpha < \alpha_c$ is unstable (with respect to a perturbation of the amplitude of the modes). Furthermore, $\partial^2 \mathcal{V}/\partial \psi^2 = 2\gamma \beta^3 \cos \psi$ is negative if $\gamma > 0$ and $\psi = \pi$ or if $\gamma < 0$ and $\psi = 0$. Thus the non zero equilibrium solution for $\alpha > \alpha_c$ is also unstable (with respect to a perturbation of the relative phase). One concludes that the non trivial branches found with the LSK expansion at order 2 (in Sec. I.4.2) are unstable, expect for the trivial branch $\beta = 0$ for $\alpha < \alpha_c$ (see Fig. I.5).

Above, we have considered arbitrary small amplitudes, hence $|\alpha - \alpha_c| \ll 1$. In the next section we deal with finite amplitudes of the deformations, and we demonstrate that, upon a gradual decrease of α, the subcritical branch (corresponding to $\alpha < \alpha_c$) continuously leads to a new branch which is stable, the structure of the hexagonal patterns being identical (with hollows at the center of the hexagons).

I.5   A tentative functional for the energy

The series expansion at order 3 of $\mathcal{V}$ developed in section I.4.4 (see Eq. I.37) has been deduced from the LSK development at order 2, taking into account the translational symmetry of the system. It is valid in the small amplitudes limit. On the other side, the limit of the energy as the deformation approaches infinity anywhere in the system, has to be infinity (due to the elastic part of the energy). In order to get a series expansion that captures this property, one considers the quartic terms in the energy expansion, and we arbitrarily drop the higher order terms. Here, the goal is not to obtain a quantitative description of the system but to get a qualitative, yet heuristic, description able to give insight on features related to finite deformations. With the requirement of the translational symmetry,

the functional to be minimized reads now:

$$
\begin{aligned}
\mathcal{V}(\xi_i) \;=\; & -\frac{\alpha - \alpha_c}{2}\,(\xi_1\,\overline{\xi}_1 + \xi_2\,\overline{\xi}_2 + \xi_3\,\overline{\xi}_3) - \gamma(\xi_1\,\xi_2\,\xi_3 + \overline{\xi}_1\,\overline{\xi}_2\,\overline{\xi}_3) \\
& + \kappa(\xi_1^2\,\overline{\xi}_1^2 + \xi_2^2\,\overline{\xi}_2^2 + \xi_3^2\,\overline{\xi}_3^2) + \lambda(\xi_1\,\overline{\xi}_1\xi_2\,\overline{\xi}_2 + \xi_3\,\overline{\xi}_3\xi_2\,\overline{\xi}_2 + \xi_3\,\overline{\xi}_3\xi_1\,\overline{\xi}_1)
\end{aligned}
\tag{I.38}
$$

We assume that quartic terms are positive definite ($\kappa + \lambda > 0$). Again, we look for the minimum of $\mathcal{V}$ as a function of β, restricted to cases (see below) where all ξ_i's have the same modulus β but an arbitrary phase ψ. The quantity to be be minimized reads:

$$
\mathcal{V}(\beta, \psi) = -\frac{3(\alpha - \alpha_c)}{2}\beta^2 - 2\gamma\beta^3 \cos(\psi) + 3(\kappa + \lambda)\beta^4.
\tag{I.39}
$$

As previously, the sign of γ is irrelevant because it can always be changed by a change of ψ into $\psi + \pi$. Therefore we shall take γ positive. The equation of equilibrium with respect to the fluctuations of ψ is:

$$
\frac{\partial \mathcal{V}}{\partial \psi} = 0.
\tag{I.40}
$$

This yields $\psi = 0$ or $\psi = \pi$. The equation of equilibrium with respect to the fluctuations of β is:

$$
\frac{\partial \mathcal{V}}{\partial \beta} = 0.
\tag{I.41}
$$

This yields

$$
\beta\left[-3(\alpha - \alpha_c) - 6\gamma\beta \cos(\psi) + 12(\kappa + \lambda)\beta^2\right] = 0.
\tag{I.42}
$$

One finds for the equilibrium values of the amplitude $\beta = 0$, $\beta = \beta_\pi$, $\beta = \beta_{0+}$, or $\beta = \beta_{0-}$. β_π is for a phase $\psi = \pi$. β_{0+} and β_{0-} are for $\psi = 0$. Since β has to be

real and positive, the three last solutions are limited to restricted ranges of α:

$$\beta_\pi = \frac{-\gamma + \sqrt{\gamma^2 + 4(\kappa + \lambda)(\alpha - \alpha_c)}}{4(\kappa + \lambda)} \qquad \forall \alpha > \alpha_c \qquad \text{(I.43)}$$

$$\beta_{0+} = \frac{\gamma + \sqrt{\gamma^2 + 4(\kappa + \lambda)(\alpha - \alpha_c)}}{4(\kappa + \lambda)} \qquad \forall \alpha > \alpha_c - \frac{\gamma^2}{4(\kappa + \lambda)} \qquad \text{(I.44)}$$

$$\beta_{0-} = \frac{\gamma - \sqrt{\gamma^2 + 4(\kappa + \lambda)(\alpha - \alpha_c)}}{4(\kappa + \lambda)} \qquad \forall \alpha \in \left[\alpha_c - \frac{\gamma^2}{4(\kappa + \lambda)} : \alpha_c\right] \quad \text{(I.45)}$$

β is plotted as function of α in Fig. I.6. The branch β_π is unstable with respect
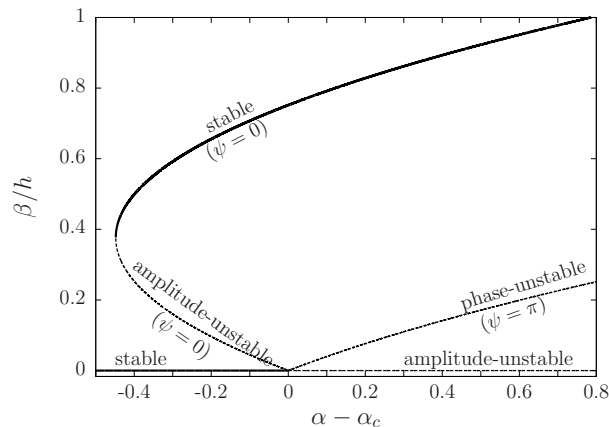
Figure I.6: Bifurcation diagram showing the amplitude of the modes as a function of the control parameter α, for $\gamma = 1.19$ (from Eq. I.30) and $(\kappa + \lambda) = 0.79$ in Eq. I.42. The stability of the branches are indicated in the plot.

to small fluctuations of ψ because the coefficient $-\gamma\beta^3$ of $\cos\psi$ in the expression of $\mathcal{V}$ is negative. This branch is stable with respect to small fluctuations of β because, as it can be checked, the sign of $\partial^2\mathcal{V}/\partial\beta^2(\beta_\pi, \pi)$ is positive. In the same way, the branch β_{0+} is stable with respect to small fluctuations of β or ψ, whereas the branch β_{0-} is stable with respect to small fluctuations of π but unstable with respect to small fluctuations of ψ (see Fig. I.6).

To conclude, one has found a unique stable non trivial branch, β_{0+}. The corresponding patterns are hexagonal, with hollows of finite amplitude at the center of the hexagons. The two other non-trivial branches, whose instability for infinitesimal amplitudes were already demonstrated (see I.4.4), are unstable even for finite

amplitudes.

Beyond this conclusion arising from a heuristic form for the energy functional, one can infer the existence of a branch of stable subcritical solutions by a general argument. The subcritical branch has been rigorously evidenced in the limit of infinitesimal amplitudes, and it is found to correspond to a saddle point of the energy, with a maximum in the β-direction. The existence of a local minimum beyond the linear threshold in the energy landscape is ensured by the infinite limit of the energy as β approaches infinity.

I.6   Conclusions

Above we have considered equilibrium solutions emerging from the superposition of three modes whose wave-vectors fulfill the resonance condition, and we have focused on hexagonal patterns for which, as demonstrated above, the (real) amplitude of the modes are equal. Consider the fourth order series expansion of the energy functional, which is formally given by Eq. I.39. As stated above, the energy is stationary against a variation of the amplitudes and the phase for $|\xi_1| = |\xi_2| = |\xi_3|$ and $\psi = \pm\pi$, yielding the hexagonal patterns.

We have demonstrated, with the help of the LSK Expansion, the existence of two non trivial branches of periodic hexagonal equilibrium patterns. One of them is supercritical, and leads to unstable patterns with bumps at the centers of the hexagons. The subcritical one, for which the centers of the hexagons are hollows, is also unstable for infinitesimal amplitudes. It is connected to another non trivial branch with the same type of hexagons, which are stable. Other patterns are possible but they lead to either unstable states, or patterns with a higher energy compared to the energy of the stable hexagons. This scenario, in which the instability is subcritical, is fully consistent in with experiments. Thes observations and calculations have also been confirmed with the help of Finite Element Simulations

which we mention briefly below.

The non-linear threshold, at which the instability patterns appear, obtained from the simulations ($\alpha = \alpha_{min}(k_c) \simeq 5.75$) is in agreement with the experimentally observed threshold (Fig. I.2). The maximum vertical deviation of the surface calculated from the simulations are slightly smaller than those measured experimentally. This small difference is probably due to the constitutive law of the polyacrylamide gels, which may not be rigorously neo-Hookean for these large deformations. The mean area $\mathcal{A}$ per hexagons has been estimated by dividing the area occupied by the hexagons whose boundaries are not in direct contact with the borders. One finds $\mathcal{A} = 53 \pm 6$ cm^2. The corresponding area calculated from the simulations, *i.e.* for $\ell \simeq 2.96h$,[10] is $\simeq 47.4$ cm^2, in agreement with the experiments.

References

(1) Biot, M. A. Surface instability of Rubber in Compression. *Appl. Sci. Res.* **1963**, *12*, 168–182.

(2) Hutchinson, J. W. Imperfection sensitivity of externally pressurized spherical shells. *Journal of Applied Mechanics* **1967**, *34*, 49–55.

(3) Cerda, E.; Mahadevan, L. Geometry and physics of wrinkling. *Physical review letters* **2003**, *90*, 074302.

(4) Audoly, B.; Boudaoud, A. Buckling of a stiff film bound to a compliant substratePart I:: Formulation, linear stability of cylindrical patterns, secondary bifurcations. *Journal of the Mechanics and Physics of Solids* **2008**, *56*, 2401–2421.

(5) Audoly, B.; Boudaoud, A. Buckling of a stiff film bound to a compliant

substratePart II:: A global scenario for the formation of herringbone pattern. *Journal of the Mechanics and Physics of Solids* **2008**, *56*, 2422–2443.

(6) Audoly, B.; Boudaoud, A. Buckling of a stiff film bound to a compliant substratePart III:: Herringbone solutions at large buckling parameter. *Journal of the Mechanics and Physics of Solids* **2008**, *56*, 2444–2458.

(7) Ben Amar, M.; Ciarletta, P. Swelling instability of surface-attached gels as a model of soft tissue growth under geometric constraints. *Journal of the Mechanics and Physics of Solids* **2010**, *58*, 935–954.

(8) Cai, S.; Breid, D.; Crosby, A. J.; Suo, Z.; Hutchinson, J. W. Periodic patterns and energy states of buckled films on compliant substrates. *Journal of the Mechanics and Physics of Solids* **2011**, *59*, 1094–1114.

(9) Cao, Y.; Hutchinson, J. W. From wrinkles to creases in elastomers: the instability and imperfection-sensitivity of wrinkling. *Proc. R. Soc. A* **2012**, *468*, 94–115.

(10) Ghatak, A.; Chaudhury, M. K.; Shenoy, V.; Sharma, A. Meniscus instability in a thin elastic film. *Physical Review Letters* **2000**, *85*, 4329.

(11) Chaudhury, M. K.; Chakrabarti, A.; Ghatak, A. Adhesion-induced instabilities and pattern formation in thin films of elastomers and gels. *The European Physical Journal E* **2015**, *38*, 1–26.

(12) Mönch, W.; Herminghaus, S. Elastic instability of rubber films between solid bodies. *EPL (Europhysics Letters)* **2001**, *53*, 525.

(13) Arun, N.; Sharma, A.; Shenoy, V. B.; Narayan, K. S. Electric-field-controlled surface instabilities in soft elastic films. *Advanced Materials* **2006**, *18*, 660–663.

(14) Tanaka, T.; Sun, S.-T.; Hirokawa, Y.; Katayama, S.; Kucera, J.; Hirose, Y.; Amiya, T. Mechanical instability of gels at the phase transition. *Nature* **1987**, *325*, 796–798.

(15) Trujillo, V.; Kim, J.; Hayward, R. C. Creasing instability of surface-attached hydrogels. *Soft Matter* **2008**, *4*, 564–569.

(16) Mora, S.; Phou, T.; Fromental, J. M.; Pismen, L. M.; Pomeau, Y. Capillarity Driven Instability of a Soft Solid. *Phys. Rev. Lett.* **2010**, *105*, 214301.

(17) Mora, S.; Abkarian, M.; Tabuteau, H.; Pomeau, Y. Surface Instability of Soft Solids under Strain. *Soft Matter* **2011**, *7*, 10612–10619.

(18) Mora, S.; Phou, T.; Fromental, J. M.; Pomeau, Y. Gravity driven instability in solid elastic layers. *Phys. Rev. Lett.* **2014**, *113*, 178301.

(19) Li, B.; Jia, F.; Cao, Y.-P.; Feng, X.-Q.; Gao, H. Surface wrinkling patterns on a core-shell soft sphere. *Physical Review Letters* **2011**, *106*, 234301.

(20) Jia, F.; Amar, M. B. Theoretical analysis of growth or swelling wrinkles on constrained soft slabs. *Soft Matter* **2013**, *9*, 8216–8226.

(21) Ciarletta, P. Wrinkle-to-fold transition in soft layers under equi-biaxial strain: A weakly nonlinear analysis. *Journal of the Mechanics and Physics of Solids* **2014**, *73*, 118–133.

(22) Strutt, J. W.; Rayleigh, L. Investigation of the character of the equilibrium of an incompressible heavy fluid of variable density. *Proc. London Math. Soc* **1883**, *14*, 8.

(23) Chandrasekhar, S. The character of the equilibrium of an incompressible heavy viscous fluid of variable density. Mathematical Proceedings of the Cambridge Philosophical Society. 1955; pp 162–178.

(24) Fermigier, M.; Limat, L.; Wesfreid, J. E.; Boudinet, P.; Quilliet, C. Two-dimensional patterns in Rayleigh-Taylor instability of a thin layer. *Journal of Fluid Mechanics* **1992**, *236*, 349–383.

(25) Bénard, H. *Les tourbillons cellulaires dans une nappe liquide propageant de la chaleur par convection: en régime permanent*; Gauthier-Villars, 1901.

(26) Scriven, L.; Sternling, C. On cellular convection driven by surface-tension gradients: effects of mean surface tension and surface viscosity. *Journal of Fluid Mechanics* **1964**, *19*, 321–340.

(27) Rayleigh, L. On convection currents in a horizontal layer of fluid, when the higher temperature is on the under side. *The London, Edinburgh, and Dublin Philosophical Magazine and Journal of Science* **1916**, *32*, 529–546.

(28) Palm, E. On the tendency towards hexagonal cells in steady convection. *Journal of Fluid Mechanics* **1960**, *8*, 183–192.

(29) Segel, L. A.; Stuart, J. T. On the question of the preferred mode in cellular thermal convection. *Journal of Fluid Mechanics* **1962**, *13*, 289–306.

(30) Busse, F. H. Stabilitätsverhalten der Zellularkonvektion bei endlicher Amplitude. Ph.D. thesis, U. Munich, 1962.

(31) Joseph, D. D.; Sattinger, D. H. Bifurcating time periodic solutions and their stability. *Archive for Rational Mechanics and Analysis* **1972**, *45*, 79–109.

(32) Pomeau, Y. Front motion, metastability and subcritical bifurcations in hydrodynamics. *Physica D: Nonlinear Phenomena* **1986**, *23*, 3–11.

(33) Palm, E. Nonlinear thermal convection. *Annual Review of Fluid Mechanics* **1975**, *7*, 39–61.

(34) Normand, C.; Pomeau, Y.; Velarde, M. G. Convective instability: a physicist's approach. *Reviews of Modern Physics* **1977**, *49*, 581.

(35) Koschmieder, E. L. *Bénard cells and Taylor vortices*; Cambridge University Press, 1993.

(36) Manneville, P. *Dynamics of Spatio-Temporal Cellular Structures*; Springer, 2006; pp 41–65.

(37) Koiter, W. T. On the Stability of an Elastic Equilibrium. Ph.D. thesis, Delft; H. J. Paris, Amsterdam, The Netherlands, 1945.

(38) van der Heijden, A. *W. T. Koiter's elastic stability of solids and structures*; Cambridge University Press Cambridge, 2009.

(39) Koiter, W. T. Nonlinear buckling problem of a complete spherical shell under uniform external pressure. I. *Proceedings of the Koninklijke Nederlandse Akademie van Wetenschappen Series B-Physical Sciences* **1969**, *72*, 40.

(40) Hutchinson, J. W.; Koiter, W. T. Postbuckling theory. *Appl. Mech. Rev* **1970**, *23*, 1353–1366.

(41) Budiansky, B. Theory of buckling and post-buckling behavior of elastic structures. *Advances in applied mechanics* **1974**, *14*, 1–65.

(42) Peek, R.; Kheyrkhahan, M. Postbuckling behavior and imperfection sensitivity of elastic structures by the Lyapunov-Schmidt-Koiter approach. *Computer methods in applied mechanics and engineering* **1993**, *108*, 261–279.

(43) Peek, R.; Triantafyllidis, N. Worst shapes of imperfections for space trusses with many simultaneously buckling members. *International journal of solids and structures* **1992**, *29*, 2385–2402.

(44) Reissner, E. On Postbuckling Behavior and Imperfection Sensitivity of Thin Elastic Plates on a Non-Linear Elastic Foundation. *Studies in Applied Mathematics* **1970**, *49*, 45–57.

(45) Yao, J. C. Buckling of axially compressed long cylindrical shell with elastic core. *Journal of Applied Mechanics* **1962**, *29*, 329–334.

(46) Karam, G. N.; Gibson, L. J. Elastic buckling of cylindrical shells with elastic coresI. Analysis. *International Journal of Solids and Structures* **1995**, *32*, 1259–1283.

Appendix II

Propagation of Interfacial Waves in a Thin film supported over Liquid

II.1. Introduction

Understanding the friction between solid surfaces is of utmost importance due to its widespread practical implications. The common modes of propagation of a rigid slider over an elastomeric material are either by true sliding or stick-slip. Schallamach[1] made an important observation that there can be a third mode via which a rigid object moves over the elastomer, *i.e*, via forming interfacial surface instabilities that are commonly known as 'Schallamach waves'. Schallamach waves[2,3] can be considered as waves of detachment that induce localized slip and thus help in sliding. When the rigid slider is brought into contact with the elastomer and set into motion in one direction, the elastomeric substrate at the slider's frontal edge is compressed, whereas the rear edge is stretched. When the stored elastic energy in the buckle (formed at the front edge of the contact) exceeds the adhesion energy in the contact region, it relaxes and passes as a wave underneath it. The motion of these interfacial waves is in a direction opposite to the motion of the slider. This is in contrast with the movement of bubbles observed[4] under the contact between a rigid slider and an elastic substrate where they move in the same direction as the slider. In spite of several studies in this field, there are opposing ideas regarding the origin of these interfacial waves: some authors argue that they are

278

purely elastic[5] while others believe that these are viscoelastic[6]. Recent experiments[7–9] to understand these points were performed using semi-infinite elastic media. We propose that studying the statics and dynamics of these waves by sliding a smooth rigid indenter over a thin elastomeric film[10] may give a better understanding of these interfacial instabilities. Not only is such a system more suitable to understand Schallamach waves but the moving wrinkle could also serve as a nice model system to study the motion of an elastic contact line[11] that may be pinned via double or multivalued energy wells.

II.2. Experimental Section

II.2.1. Preparation of the Elastic Film on a Pool of Liquid.

A 1:1 solution (density ρ 1.13 g/cc, 20°C) of glycerol (Fisher Chemical) and deionized (DI) water was degassed for 30 min using a vacuum pump (Welch Duo-Seal, Model no. 1402). Sylgard 184 and Sylgard 186 (Dow Corning®) were mixed in 1:1 ratio (the amount of crosslinker added to the mixture was 10% of the weight of the base polymer) that was degassed for 10 min under high vacuum. Such a combination of the polymers was chosen to ensure that the film has a high tear strength as well as a moderately high elastic modulus. All the samples were prepared in round polystyrene Petri dishes (VWR, 100 mm diameter and 10 mm high). The Petri dishes were filled with the glycerol-water solution to about half of their height. Different quantities of the PDMS mixture were gently released on the surface of the liquid with the help of micropipettes and the added amount was weighted using a sensitive balance. The samples were allowed to stand for ~1h that allowed the spreading of the PDMS mixture on the liquid surface following which they were carefully placed inside an oven and cured for 90 min at 75° C. Using the known cross-sectional area of the dish and the

weight of the polymer added, the thicknesses of the elastic films (2 - 20 μm) were estimated. The elastic modulus of these films is about 1MPa.

II.2.2. Observation of Schallamach Waves in the thin Elastic film.

A glass hemisphere (7.5 or 12.5 mm diameter) was cleaned in piranha solution and grafted with polydimethylsiloxane chains (DMS T-22, Gelest Inc.). It was then thoroughly washed with chloroform and dried with ultrapure nitrogen gas. A micro-load cell (Phidgets Inc.) was attached to the glass indenter such that it could measure the tangential force (Labview) that it experiences. The sample containing the thin elastic film supported over liquid is placed on a motorized stage that is moved at fixed velocities. The whole setup is placed atop a vibration isolation table (Micro-G, TMC). A high-speed camera (Redlake MotionPro) is used to record the interfacial phenomena.

II.3. Observations and Results

Preliminary observations show that when a PDMS grafted glass hemisphere is slid laterally against a thin elastomeric film ($\sim$ 5-20 μm) supported on an incompressible liquid (1:1 aqueous glycerol), interfacial wrinkles form in the contact region that passes through the area of contact as pulses (Figure II.1). Our experiments show that the tangential force experienced by the hemispherical slider increases by almost three times when the film thickness is increased by a factor of three (Figure II.2).
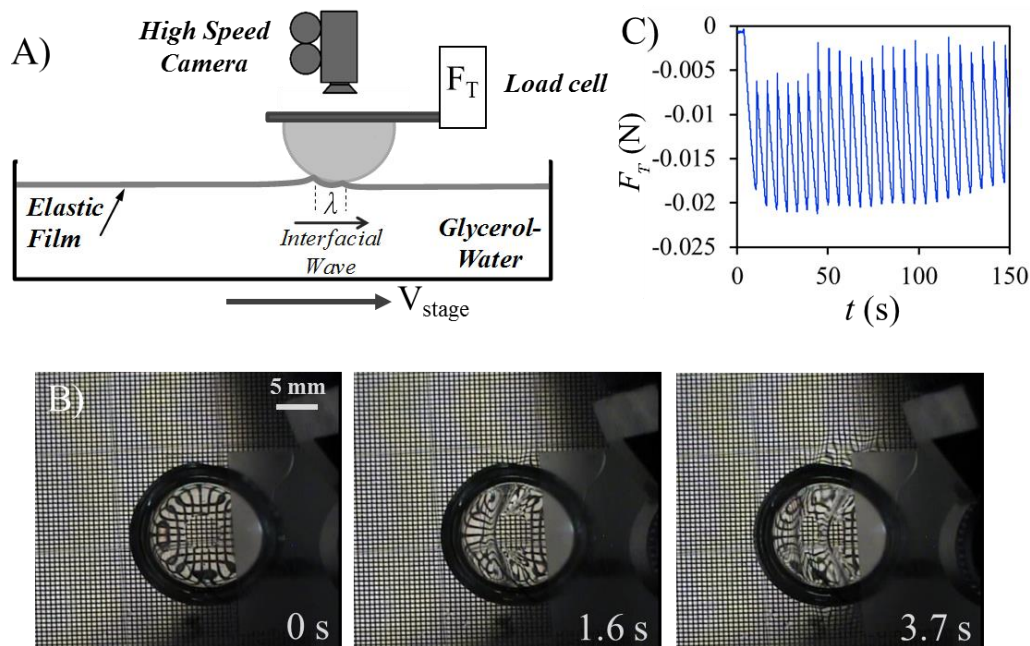
Figure II.1: (A) Formation of interfacial waves at the interface of a PDMS-grafted rigid hemisphere and a thin film of silicone elastomer supported on the surface of an incompressible liquid (1:1 mixture of water and glycerin by volume) due to sliding. When the hemispherical indenter (PDMS) is slid past the elastomeric film of thickness (7.5 µm), a single wrinkle develops, which propagates through the interface when the bending energy stored in it overcomes the adhesive energy. The sequences of the motion of the wrinkle are shown in (B). (C) A typical graph of the tangential force (F_T) experienced by the indenter as a function of time (Film thickness: 16µm and Stage velocity V_{stage}: 0.2 mm/s) that shows the signature of the periodic pulses of the Schallamach waves.[10]

Figure II.2: Graphs of the tangential force (F_T) experienced by the PDMS-grafted hemispherical glass slider (12.5 mm diameter) during each pulse of the interfacial instability as a function of the film thickness (left: 8 µm and right: 22 µm) on a pool of 1:1 aqueous glycerol. The stage velocity is 0.2 mm/s in each case. If a pulse gets pinned somehow, multiple waves may pin additionally thereby increasing the tangential force recorded by the load cell as seen here (left), which collectively depin from the contact region.

Now, when the contact area between the glass slider and the thin elastic film was increased by using a larger slider, the tangential force experienced by the same film was much higher (Figure II.3). We also note that experiments of sliding over a 16 μm thick elastomeric film showed that the maximum tangential force experienced during each wave pulse increased as the stage velocity was increased (Figure II.4). With an order of magnitude increase in the stage velocity (0.2mm/s to 2mm/s), the force increased by 70%.
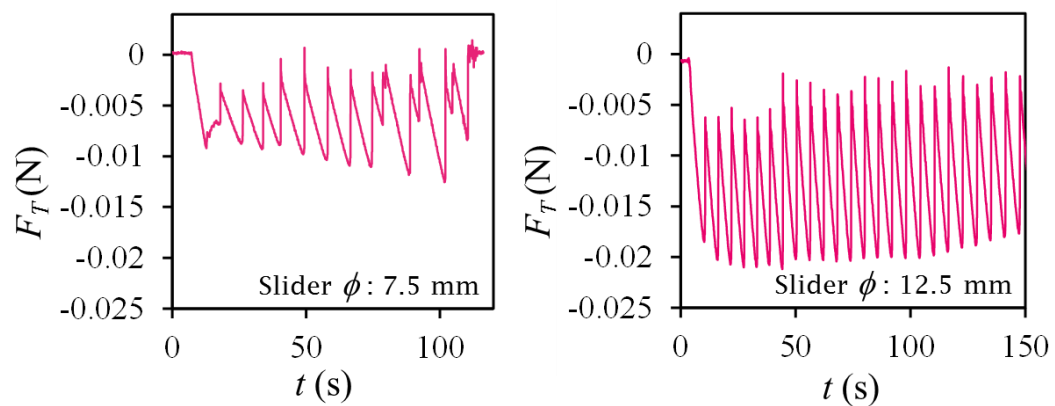
Figure II.3: Graphs of the tangential force (F_T) experienced by PDMS-grafted hemispherical glass sliders of different diameters (7.5 mm and 12.5 mm) during each pulse of the interfacial instability over an elastic film (thickness: 16μm) over a pool of 1:1 aqueous glycerol at stage velocity, V_{stage}=0.2 mm/s.
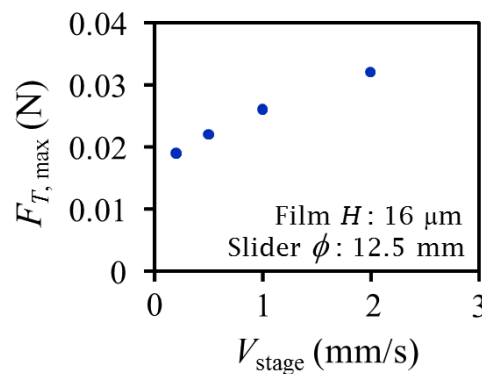
Figure II.4: The maximum tangential force experienced by a PDMS-grafted hemispherical slider (diameter: 12.5 mm) as the stage velocity (V_{stage}) is varied. These experiments were performed with a 16 μm thick PDMS film over a pool of 1:1 aqueous glycerol (by volume).

A possible way to approach understanding the interfacial wave motion in these thin elastic films is given below. Initially, the rigid contactor is brought into contact with the film due to which there is bending in the film against which there is the hydrostatic loading of the liquid. We expect there to be a characteristic lengthscale in the system from the balance of the bending and the gravitational energies, $L_c = (D/\rho g)^{1/4}$, [12] where D is the bending rigidity of the film [$D = EH^3/12(1-v^2)$], ρ is the density of the liquid underneath and g is the acceleration due to gravity. Now, when the contactor (or the stage on which the sample is placed) is moved, a wrinkle forms at the frontal edge of the contact that stretches to a point when the stored energy in the wrinkle becomes equal to that of the adhesion energy in between the contact region of the hemisphere and the elastic film. The viscoelastic dissipation in the wrinkle can be linked to an analysis by Chaudhury and Kim[13] for the case of bubble motion underneath a contact of the rigid object over a thick substrate. Our case is slightly different as we have thin films and the relationship for the dissipation rate will modify as follows,

$$F_T V \sim \mu H \, a \left(V/V_0\right)^n V \qquad \qquad (II.1)$$

Where μ is the shear modulus, a is the contact diameter, V is the stage velocity and V_o is a constant. We can take $n = 1$ for polymeric materials and for these thin films too.[13] In figure II.2, we observed that when the film thickness was increased by three times, the tangential force F_T became twice. In figure II.3, we observed that when the contact diameter was increased by about two times, the tangential force F_T also doubled. Finally, figure II.4 points to the fact the tangential force is linear with the stage velocity. All these observations show that the model used for the viscoelastic dissipation in the bulk may also be applicable to the thin films, however the vertical deformation into the bulk may be limited by the film thickness that reduces the resistive force in sliding over

surfaces. This leads us to the expression of the tangential force experienced in these thin films as $F_T \sim \mu H a(V/V_0)$.

II.4. Summary and Future Work

We observed the formation and sliding of interfacial wrinkles in between a rigid glass hemispherical slider and a thin PDMS elastic film supported over a pool of aqueous glycerol. We showed preliminary results of how the tangential force experienced by the slider during each wave pulse varies with the velocity of the substrate, the thickness of the elastic film and the contact diameter. These results may help in developing a model for the interfacial wave propulsion. The tangential force and the velocity will give us an estimate of the viscoelastic dissipation.[13] At this stage, we have some understanding of the mechanism of the motion of the waves and it can be linked to the viscoelastic dissipation in the bulk. Sliding over thin films is much easier than over bulk as the tangential force is proportional to the film thickness as opposed to the vertical deformation in the bulk. This model study will be useful to understand viscoelastic dissipation at the crack tip and even rate dependent adhesion hysteresis. Measuring the shape of the elastic contact line (pinned wrinkle) will give an estimate of the spring constant. At the end, defects (in the form of tiny bumps of different geometry) can be introduced over the curved surface of the hemisphere to study pinning and depinning of the elastic contact line over them that may give us important insights into the rich field of contact line phenomena.

References

(1)   Schallamach, A. How Does Rubber Slide? *Wear* **1971**, *17* (4), 301–312.

(2)   Barquins, M. Friction and Wear of Rubber-like Materials. *Wear* **1993**, *160* (1), 1–11.

(3)   Barquins, M. Sliding Friction of Rubber and Schallamach Waves — A Review. *Mater. Sci. Eng.* **1985**, *73*, 45–63.

(4)   Chaudhury, M. K.; Kim, K. H. Shear-Induced Adhesive Failure of a Rigid Slab in Contact with a Thin Confined Film. *Eur. Phys. J. E* **2007**, *23*, 175–183.

(5)   Best, B.; Meijers, P.; Savkoor, A. R. The Formation of Schallamach Waves. *Wear* **1981**, *65* (3), 385–396.

(6)   Barquins, M.; Courtel, R. Rubber Friction and the Rheology of Viscoelastic Contact. *Wear* **1975**, *32* (2), 133–150.

(7)   Mowery C. L., Crosby A. J., Ahn D., S. K. R. Adhesion of Thermally Reversible Gels to Solid Surfaces. *Langmuir* **1997**, *13* (23), 6101–6107.

(8)   Viswanathan, K.; Sundaram, N. K.; Chandrasekar, S. Stick-Slip at Soft Adhesive Interfaces Mediated by Slow Frictional Waves. *Soft Matter* **2016**, *12* (24), 5265–5275.

(9)   Viswanathan, K.; Sundaram, N. K.; Chandrasekar, S. Slow Wave Propagation in Soft Adhesive Interfaces. *Soft Matter* **2016**, *12* (45), 9185–9201.

(10)   Chaudhury, M. K.; Chakrabarti, A.; Ghatak, A. Adhesion-Induced Instabilities and Pattern Formation in Thin Films of Elastomers and Gels. *Eur. Phys. J. E* **2015**, *38* (7), 82.

(11)   Joanny, J. F. A Model for Contact Angle Hysteresis. *J. Chem. Phys.* **1984**, *81* (1), 552.

(12)   Reis, P. M.; Hure, J.; Jung, S.; Bush, J. W. M.; Clanet, C. Grabbing Water. *Soft Matter* **2010**, *6* (22), 5705.

(13)   Chaudhury, M. K.; Kim, K. H. Shear-Induced Adhesive Failure of a Rigid Slab in Contact with a Thin Confined Film. *Eur. Phys. J. E* **2007**, *23* (2), 175–183.

Appendix III

Motion of Soft Gel Spheres over Soft Substrate

III.1. Introduction and Observations

Particles[1] or drops[2] on a soft deformable substrate can move if they experience a strain energy gradient underneath it. An elastomeric object can also roll up an inclined flat solid substrate due to the differential swelling on the either edges of its contact that creates a torque.[3] We ventured to see what happens when a highly deformable soft sphere is placed atop a soft thin film so that their strain energy fields can interact cooperatively. When a single such sphere of a very soft gel is placed upon the gel thin film, it appears somewhat like a hemisphere. Close observation at the contact line reveals that the lower substrate deforms significantly too due to the normal upward component of the surface tension of the gel drop[4–6]. When two of these spheres are placed on the gel film close to each other, they attract and soon upon formation of a bridge at the base of the two, their edges heal instantaneously (Figure III.1 A). The scenario here is somewhat similar to that of two coalescing liquid drops[7,8]. However, when the spheres were placed at some distance away from each other, they were found to repel (Figure III.1 B). We made these observations in the summer of 2014 and a recent publication reported how liquid drops repel from each other on a soft thin support[9]. Performing very careful experiments with our system maybe a better way to study such motions on thin substrates as one need not have to make the substrate vertical

to facilitate the motion of liquid drops by gravity[9] as the deformations in the silicone gel films are much smaller than those in our softer polyacrylamide gels.

If many such gel spheres are placed on the soft film, they may all coalesce to form a tightly packed array that could have potential use in optics as an assembly of lenses. One could then vary their curvature by changing the modulus and sizes. The motion of a gel sphere on a substrate may also serve as a model system to understand how cells move on tissue substrates.
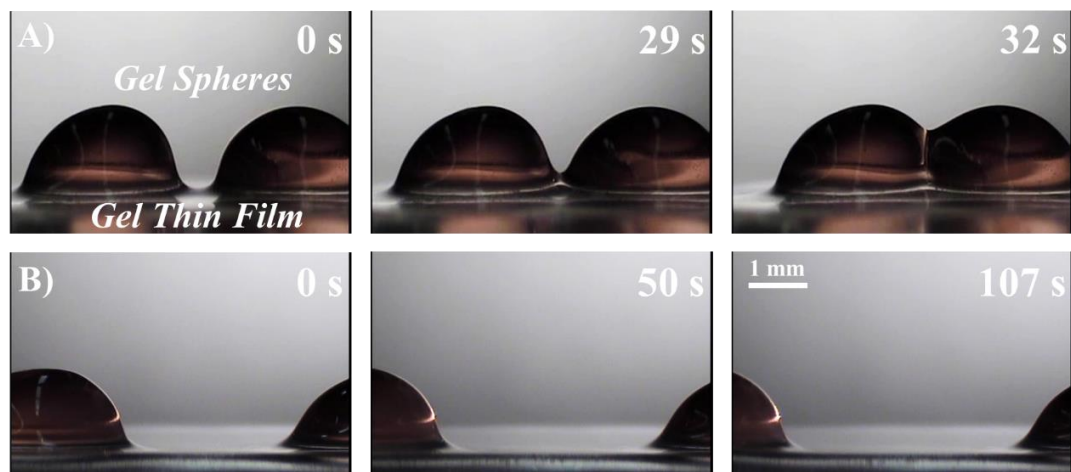
Figure III.1: Attraction or Repulsion of two gel spheres (shear modulus ~ 40 Pa) when placed on a thin gel film (40 Pa, 1 mm thick) (A) When two such gel spheres were placed close enough, they attracted and coalesced forming a curved ridge in between the two spheres. The coalesced gel spheres (A, final snapshot) maintain their original shape partially as opposed to that of liquid drops where they meet to form a single drop finally. (B) When the gel spheres were placed a little further away from each other, they were found to repel, thus moving apart.

The problem of studying the coalescence of two gel spheres is complex and needs a detailed theoretical analysis in conjunction with clean experiments. To begin with, one could write down the total energy of the system due to the different contributions (adhesion energy, surface energy and elastic energies due to the deformation in the sphere as well as the gel film). By performing a functional minimization of the total

energy as a function of the separation distance between the two gel spheres, we will be able to find the energy of attraction in such a system. Thus, a thorough analysis by taking into consideration large deformation theory of the soft solid along with the appropriate adhesion and surface energies will be required.

III.2. Experiments

Highly spherical gel spheres were made by curing polyacrylamide gel solution drops of different volumes by suspending them in a liquid density gradient (Figure III.2) The density gradient was formed in small beakers with a liquid heavier than the gel solution (PDM-7040, Gelest Inc., density 1.07 g/cc) at the bottom and a lighter liquid (n-octane, 97% pure, Acros organics, density 0.7 g/cc) on the top. After all the ingredients of the gel were mixed, different volumes of the gel solution were released gently over the top surface of the octane in the container housing the density gradient. The drops of gel solution become neutrally buoyant at the diffusing interface of the two liquids forming the density gradient. These suspended gel drops cure to form highly spherical gel drops that were subsequently washed in fresh n-heptane (Fisher Chemicals) repeatedly and dried moderately in air. The shear modulus of this gel was measured to be 40Pa. The addition of a red dye in the gel solution to form spheres allows better visualization. The gel film was cured between two parallel glass plates separated by 1mm thick Teflon coated spacers. The upper glass plate being hydrophobic allowed its easy removal from the gel film. The events of attraction or repulsion of the gel spheres on the gel film were recorded using a CCD camera.
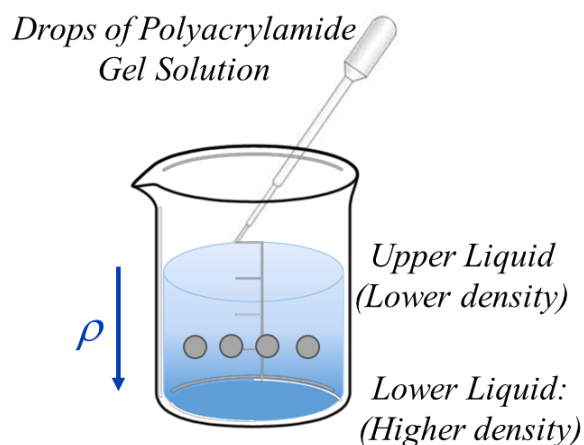
Figure III.2: Schematic of the experimental method to prepare perfectly spherical gel spheres in a density gradient, where the upper lighter liquid was octane (density 0.7 g/cc) and the lower heavier liquid was silicone oil (PDM-7040, density 1.07 g/cc). The gel drops were introduced in the density gradient as soon as the catalyst and initiator were mixed in the precursor solution and the drops were cured to form elastic gel spheres in the density gradient for 2h at room temperature before any experiments were performed.

References

(1)   Chakrabarti, A.; Chaudhury, M. K. Elastocapillary Interaction of Particles on the Surfaces of Ultrasoft Gels: A Novel Route To Study Self-Assembly and Soft Lubrication. *Langmuir* **2014**, *30* (16), 4684–4693.

(2)   Style, R. W.; Che, Y.; Park, S. J.; Weon, B. M.; Je, J. H.; Hyland, C.; German, G. K.; Power, M. P.; Wilen, L. a; Wettlaufer, J. S.; et al. Patterning Droplets with Durotaxis. *Proc. Natl. Acad. Sci. U. S. A.* **2013**, *110* (31), 12541–12544.

(3)   Hore, D.; Majumder, A.; Mondal, S.; Roy, A.; Ghatak, A. How to Make a Cylinder Roll Uphill. *Soft Matter* **2012**, *8* (18), 5038–5042.

(4)   Lester, G. R. Contact Angles of Liquids at Deformable Solid Surfaces. *J. Colloid Sci.* **1961**, *16*, 315–326.

(5)   Rusanov, A. I. Theory of the Wetting of Elastically Deformed Bodies. 1. Deformation with a Finite Contact-Angle. *Colloid J. USSR* **1975**, *37*, 614–622.

(6)   Pericet-Cámara, R.; Best, A.; Butt, H. J.; Bonaccurso, E. Effect of Capillary Pressure and Surface Tension on the Deformation of Elastic Surfaces by Sessile Liquid Microdrops: An Experimental Investigation. *Langmuir* **2008**, *24* (19), 10565–10568.

(7)   Eggers, J.; Lister, J. R.; Stone, H. A. Coalescence of Liquid Drops. *J. Fluid Mech.* **1999**, *401*, 293–310.

(8)   Andrieu, C.; Beysens, D. A.; Nikolayev, V. S.; Pomeau, Y. Coalescence of Sessile Drops. *J. Fluid Mech.* **2002**, *453*, 427–438.

(9)   Karpitschka, S.; Pandey, A.; Lubbers, L. A.; Weijs, J. H.; Botto, L.; Das, S.; Andreotti, B.; Snoeijer, J. H. Liquid Drops Attract or Repel by the Inverted Cheerios Effect. *Proc. Natl. Acad. Sci.* **2016**, *113* (27), 7403–7407.

Appendix IV

Thermally Induced Durotaxis of Rigid Spheres on a Soft Hydrogel: Elastic Marangoni Effect

IV.1. Introduction

Directional transport of particles induced by a gradient of elasticity is well known. Cells[1,2] and droplets of water[3] have been found to move along stiffness gradients, an elastic cylinder can be rolled on a surface by differential swelling[4–6] and this also manifests in the study of crystal dislocations, where solute atoms diffuse from one region to another in an inhomogeneous strain field in a crystal.[7] Our own studies[8,9], reported in the previous chapters, show how rigid particles interact to form dimers and clusters when they are suspended in soft elastic gels that are also induced by the gradient of strain energy density. While most of the studies depend upon the differential strain induced in an elastic system due to stretching, swelling or designing thickness graded substrates, our idea is to find a way to generate a gradient of the elastic modulus itself by controlling a system parameter, *i.e, temperature.* Soft polymers like rubbers and soft gels have unique mechanical properties. According to the theory of rubber elasticity, their elastic modulus is directly proportional to the temperature of the state it is in. Thus, the polymeric gel's modulus increases when it is heated, and it becomes softer upon cooling. Now, if we have a uniformly thick gel slab such that it is cooled on one edge and heated on its opposite edge, we would expect a gradient of elasticity to be generated along the length of the slab. Using this system with a temperature-induced elasticity

gradient and combining our knowledge of how rigid spheres indent soft gels of different elastic moduli from *elastobuoyancy* phenomenon[10], we studied how particles move along these gradients in soft substrates. Our philosophy was to see the possibility of finding an elastic analog of Marangoni flows, the latter being driven by temperature-induced surface tension gradients in liquids[11,12], where we would have a motion of particles along a temperature induced elasticity gradient.

IV.2. Experiments

IV.2.1. Preparation of Gel

Crosslinked polyacrylamide gels were used for our studies that were prepared using the experimental protocol mentioned in Chapter 2. The shear modulus of the 11% gel used for the current experiments was measured using the oscillatory rheology test described in Chapter 6 and it was found to be 294 Pa. The gel solutions were cured in home built-glass containers (75mm x 50mm x 50 mm) whose inner walls were grafted with polydimethylsiloxane chains (DMS T-22, Gelest Inc.) to ensure that the gel solutions contacted the walls at 90° such that the cured gel would be flat. The containers housing the gels were covered with Parafilm to avoid evaporation and after 30 minutes of curing, a layer of PDMS oil (DMS T-22, DMS T-31, DMS V-35, Gelest Inc.) was poured on top of the gel surface. The gels were cured for 2h at room temperature with a layer of oil on top to avoid evaporation and formation of surface corrugations.

IV.2.2. Surface modification of steel spheres via grafting their surfaces with Polydimethylsiloxane chains.

Steel spheres (bearing-quality E52100 alloy steel, density 7.8g/cm^3, McMaster-Carr) of diameters ranging from 2mm to 10mm were sonicated in acetone in a Fisher Scientific Ultrasonic Cleaner (Model no. FS5) for 10 minutes followed by sonication in ethyl alcohol for another 10 minutes after which they were blow dried with ultra-pure nitrogen gas. These spheres were submerged in vials containing PDMS oil (DMS T-22, Gelest Inc.) and heated in the oven at 80 °C for 24h. After the grafting reaction was over, they were cleaned with chloroform thoroughly and dried with compressed nitrogen gas.

IV.2.3. Experiment with a directional gradient of elasticity of gel due to a thermal gradient.

The gel container was fixed on a 3D manipulated stage with two degrees of rotation about the X and Y-axes, which was mounted on a vibration isolation table (Micro-g, TMC) (Figure IV.1). In order to create a temperature gradient across the length (75 mm) of the glass container housing the elastic gel, we adhered two flat conductive copper circulators to its opposite walls with thermal (conductive) resistant double-sided tapes. By convectively circulating liquids at the desired temperature through these copper walls, it would be possible to either heat or cool the gel. PDMS oils (DMS T-22, DMS T-31, DMS V-35, Gelest Inc., with different viscosities depending on the molecular weight) were used over the surface of the gel in different containers during the curing process. Since the surfaces of the steel spheres were grafted with PDMS chains, we used PDMS oils of the same chemical composition, the reason for which is

294

explained in the following. The free energy of adhesion between a steel bead and the gel[13] is given by $\Delta G_{132} = -2(\sqrt{\gamma_1} - \sqrt{\gamma_3})(\sqrt{\gamma_2^d} - \sqrt{\gamma_3})$ where, γ_1 is the surface energy of the steel bead, γ_2^d is the dispersion component of the surface energy of the gel and γ_3 is the surface tension of the surrounding liquid medium. The surface energies of the PDMS grafted bead and surrounding PDMS liquid medium are equal, $\gamma_1 = \gamma_3$ (~ 22 mN/m), which makes the free energy of adhesion between the bead and gel zero allowing a thin lubricating layer of the PDMS oil in between the steel bead and the gel. While using water as the surrounding medium would also give a zero work of adhesion ($\gamma_2 = \gamma_3$), we saw some swelling induced instability patterns on the surfaces of the gel and thus chose PDMS oils and PDMS grafted chains on the beads as our system. Subsequently, the surface of the gel was adjusted for zero tilt before we started the heating/cooling processes. Each of these copper circulators was then connected to temperature baths maintained at 368 K and 268 K respectively. The gel was conductively heated and cooled from the two opposite walls of the container over a period of 1h to generate the temperature gradient across its length before any experiments were performed. We measured the temperature gradient along the length using a thermocouple (Figure IV.2). The sphere was placed on the hotter side of the gel and its motion was recorded using a Video Microscope (Infinity) that was equipped with a CCD camera (Sony, Model no. XC-75).
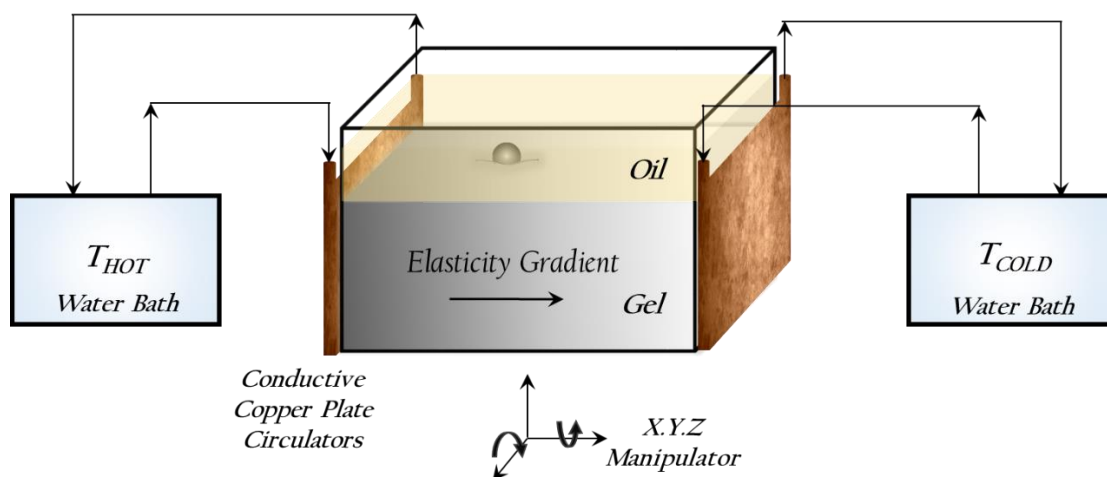
Figure IV.1: Schematic of thermally induced durotaxis of rigid spheres on a soft hydrogel. The two opposite walls of a home-built glass container are attached with copper plate circulators (with temperature resistant double sided tapes). One of the circulators is connected to a hot temperature bath (T_{HOT} ~ 368 K) and the other one to a cold temperature bath (T_{COLD} ~ 268 K). The temperature gradient established in the gel (after 1h) leads to the gradient of elasticity (modulus decreasing in the direction of the arrow). The sphere moves towards the right as will be seen in experimental snapshots later. We used PDMS oil as the upper phase to prevent evaporation of the gel as well as maintain a thin lubricating layer between the PDMS grafted steel spheres and the gel.
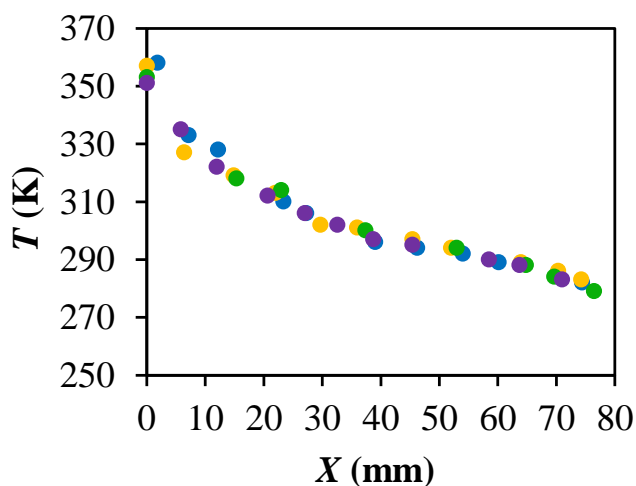
Figure IV.2: A typical temperature profile generated in the gel across its length inside the glass container for four different experiments. The temperatures on the two extreme ends here denote those measured at the walls from the inner side of the glass container with the gel. The temperatures of the two copper plate circulators (attached to the glass with temperature resistant tapes), read (left: T_{HOT} ~ 368 K) and (right: T_{COLD} ~ 268 K) respectively as measured from the outer exposed side.

IV.2.4. Measurement of the Viscosity of the PDMS oils used as the lubricant.

We used Ostwald viscometer to measure the kinematic viscosity of the oils at a room temperature of 21°C. For the PDMS oils that we used, we found the viscosities as 259.9 cSt for DMS T-22; 552.8 cSt for the mixture of DMS T-23 & DMS T-31; 1171.7 cSt for DMS T-31 and 4743.8 cSt for DMS V-35 (Gelest Inc.). The density of these PDMS oils is about 970 kg/m^3.

IV.3. Observations of thermally induced Durotaxis of rigid spheres.

We observed that the spheres moved from the stiffer (hot) side of the gel to the softer (cold) side across a temperature-induced elasticity gradient (Figure IV.3). We also found experimentally that spheres were able to move upward a slope of about 0.6° due to the driving force of the temperature induced elasticity gradient (Figure IV.3 C). These experiments show that stiffness gradient gives a driving force to the spheres that generates the motion in these gels. We studied the motion of the thermally induced Durotaxis of rigid steel spheres by varying their sizes and using PDMS oils of different viscosities as the upper phase. The oils prevented evaporation of the water from the gel network as well as maintained a thin lubricating layer between the sphere and the gel as explained in the previous section. While the spheres moved along the gradient well till about ~ 5 – 15 mm depending on the size of the sphere. It was not possible to see motions for larger distances probably because the driving force was not enough. At times, when the sphere sizes were large, we also saw some tiny droplets of water appearing on the gel surface[14,15] after a prolonged contact of the sphere with the soft gel. These tiny drops of water might also prevent the motion of the sphere by forming

liquid water bridges between sphere and gel, leading to breakage of the oil film thus

thwarting its motion.
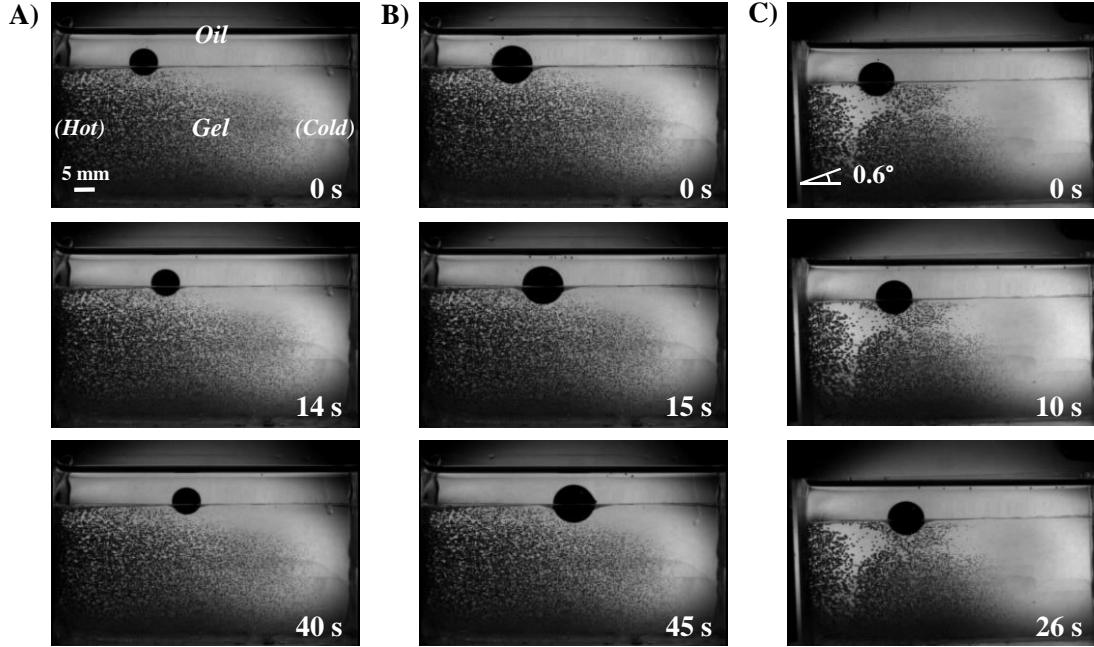
Figure IV.3: Experimental snapshots of motion of steel spheres (PDMS grafted) along a temperature-induced elasticity gradient in the gel (shear modulus 294 Pa) with an upper layer of PDMS oil (DMS T-22, kinematic viscosity: 259.9 cSt). The temperature of the gel at the left wall was about 348 K and that at the right wall was about 278 K. (A) The motion of a 7mm diameter steel sphere on a horizontal surface along the gradient. (B) The motion of a 10mm diameter steel sphere on a horizontal surface along the gradient. (C) The motion of a 9mm diameter steel sphere uphill (0.6°). We observe the formation of some bubbles in the gel after it has been heated that is not present when the gel is at room temperature or has been cooled.

IV.4. Mechanism of thermally induced Durotaxis of rigid spheres.

We describe in the following a possible mechanism of the Elastic Marangoni effect. When a rigid sphere is placed on a soft solid, its depth (δ) into the solid is determined by the balance of its weight and the elastic forces of deformation. Our previous work[9,10] shows that as the modulus increases, the depth decreases. The typical material length scale in such a system is defined by δ_0 ($\sim \mu / \Delta \rho g$). We chose to work with sphere-gel systems in which the deformations were not very large and the depth

of the sphere into the substrate scaled[10] as $\delta \sim \Delta \rho g\, R^2 / \mu$. When we place a rigid sphere on the stiffer (hot) part of the substrate, we observe that it migrates towards the colder and softer region. During this process of the sphere traversing on the gel, the latter undergoes continuous cycles of deformation followed by subsequent relaxation. While part of the potential energy is converted into the elastic energy cost to deform the softer substrate further as the sphere moves, another part is dissipated due to the continuous deformation-relaxation of the elastic substrate. We can express the driving force experienced due to the gradient of elasticity as follows,

$$F_{driving} \sim m^{*} g (d\delta / dx) . \tag{IV.1}$$

Substituting for $\delta \sim \Delta \rho g\, R^2 / \mu$ from the elastobuoyancy theory in the above equation ($F_{driving} \sim \Delta \rho\, g\, R^3\, (d\delta / dx)$), and after some manipulations, we get:

$$F_{driving} \sim \left(\Delta \rho\, g / \mu \right)^2 R^5\, (d\mu / dx) \tag{IV.2}$$

Now, using a scaling for the elastic shear modulus, $\mu \sim kT / a^3$, where k is the Boltzmann constant, T is the temperature and a is a molecular dimension, we get the following expression: $F_{driving} \sim \left(\Delta \rho\, g / T \right)^2 R^5 \left(a^3 / k \right) (dT / dx)$. The temperature gradient is considered to be more or less linear and therefore a constant at the central part of the container as seen from Figure IV.2. If we assume that the thin viscous film is draining out gradually from the lubricating layer in between the sphere and the gel, the scaling for the thickness of the film, h, as a function of time, t, is:

$$\frac{1}{h} \sim \sqrt{\frac{\Delta \rho\, gt}{\eta R}} \tag{IV.3}$$

where η is the viscosity and R is the lateral size of the contact. The viscous stress in the thin lubricating film scales as $\eta \dfrac{V}{h}$ and the viscous force $\eta \dfrac{V}{h} R^2$. Comparing the

299

viscous force with the driving force and solving the differential equation (and taking $V \sim dX/dt$), we find an expression as follows:

$$XT^2 \sim \frac{(\Delta \rho g)^{3/2} R^{7/2}}{\sqrt{\eta}} \left(\frac{a^3}{k} \right) \sqrt{t} \qquad (IV.4)$$

Plotting the experimental data from spheres of different radii and oils of different viscosities as XT^2 as a function of $\sqrt{t}$, we get slopes of each that we plot in Figure IV.4 A as a function of the size of the spheres. The black dotted line shows arbitrarily the slope of this plot if it followed as $R^{7/2}$ as suggested by the scaling in equation IV.4. In any case, we show in Figure IV.4 B the rescaled values of the slope of $(XT^2/\sqrt{t})$ with the square root of the dynamic viscosity as suggested by the equation IV.4. These scaling results are very preliminary and may not be the correct description of the thermal induced Durotaxis of these rigid spheres.
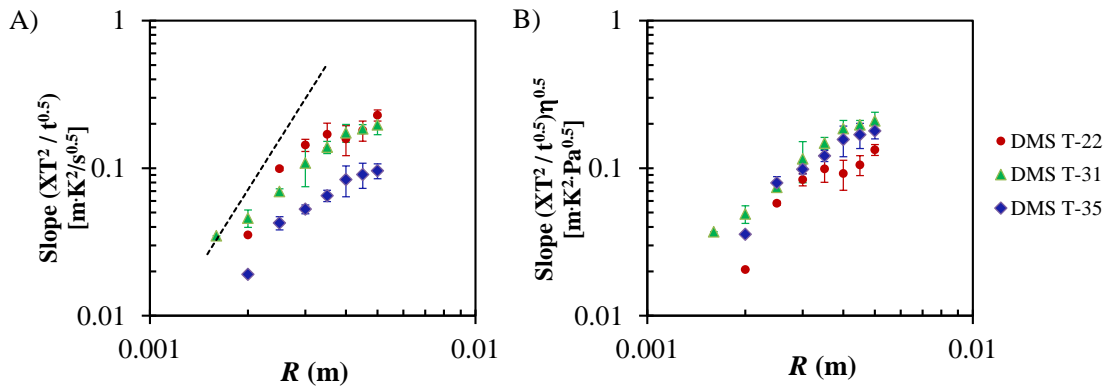
Figure IV.4: (A) Experimental data showing the slopes of $(XT^2/\sqrt{t})$ for steel spheres of different radii and moving on a gel (shear modulus 294 Pa) through different PDMS oils DMS T-22 ($\eta = 0.259$ Pa s), DMS T-31 ($\eta = 1.172$ Pa s) and DMS V-35 ($\eta = 4.744$ Pa s). The dotted line shows a slope of $R^{7/2}$, which shows the experimental data does not follow the scaling for R as predicted by equation IV.4. (B) Rescaled slopes of $(XT^2/\sqrt{t})$ by multiplying with $\sqrt{\eta}$ (equation IV.4) show somewhat collapse of the experimental data.

Another mechanism for the thermally induced Durotaxis would be to consider the viscous dissipation in the gel underneath the sphere because as it moves over the surface, the gel undergoes constant cycles of deformation and relaxation. Since these elastomeric processes are rate dependent and includes viscoelastic dissipative contributions, we consider a power law for the fraction of energy dissipated[16,17] during the motion of the sphere on the gel, $\zeta \sim (V/V_0)^n$, where V is the velocity of the sphere and V_o and n are constants. The rate of energy dissipated is then,

$$\frac{d\varepsilon_{dissipation}}{dt} \sim \mu R \delta (V/V_0)^n V \tag{IV.5}$$

Here, δ is given by the elastobuoyant equation in the small deformation limit ($\sim$ $\delta \sim \Delta\rho g R^2 / \mu$), and the force is then given by,

$$F_{driving} \sim \Delta\rho g R^3 (V/V_0)^n \tag{IV.6}$$

Comparing the expressions from equations (IV.2) and (IV.6), we get a relationship for the velocity of the motion of the spheres in along the temperature gradient as follows:

$$(V/V_0)^n \sim \frac{\Delta\rho g}{\mu^2} R^2 \frac{d\mu}{dx} \tag{IV.7}$$

For a linear viscoelastic rubber, Chaudhury and Kim[17] considered $n=1$ in the equation (IV.5) for their analyses in bubble motion underneath a shear induced motion of the rigid contactor that gave reasonable explanations for their observations. Thus, we have for the velocity of the motion of sphere under a thermal gradient, by replacing $\mu \sim kT/a^3$,

$$XT^2 \sim V_0 \Delta\rho g \ R^2 \left(\frac{a^3}{k}\right) t \tag{IV.8}$$

While these analyses are preliminary, we hope that it will inspire to develop better models of the thermally driven elastic motion of the spheres on a soft gel.

IV.5. Summary and Future Work.

In the above, we have reported some preliminary observations of the motion of rigid spheres along a temperature induced gradient of elasticity. While our results are promising, we have to study this effect more carefully by taking into consideration possible volume changes due to the heating or cooling of the polymer that may lead to local curvatures in the gel surface. We have observed that in some cases when the spheres are large, few microdroplets of water squeezes out from the gel network[14,15] that leads to the formation of liquid bridges in between the sphere and the gel, thus thwarting its motion. Effects of electrostatics between the sphere surfaces and the gel may also be the reason why the spheres often abruptly stopped their motion along the gradient. The oil phase on top of the gel surface prevented evaporation from the polymer network, however, if the experiments were performed over a long time (8 or more hours), we observed rigidifying of the gel especially close to the hot wall thus forming undulatory grooves. We also saw the formation of bubbles in the hotter region of the gel that may induce slight curvature of the gel due to volume expansion. A possibility to overcome these would be to use a polymeric gel made in a solvent different than water that would not evaporate in the temperature conditions needed for this study. This would also allow us to increase the temperature gradient thus allowing higher variations of elasticity. Another point is that steel is thermally very conductive and it may quickly equilibrate the surrounding temperature of the gel thus its elasticity. Using a non-conductive yet heavy particle may be better to get unambiguous results of

the thermal Durotaxis. The elastohydrodynamics of a rigid particle moving over a thin elastic film through a viscous liquid has been studied via theory[18–21] and experiments[22] recently that could shed light upon our experiments. Performing these experiments using hydrocarbon oils like heptane or octane, which are much less viscous than PDMS oils, provided more friction to the motion of spheres. We currently don't understand the origins of some of these issues that remain subjects for rigorous investigations in the future.

References

(1) Lo, C.-M.; Wang, H.-B.; Dembo, M.; Wang, Y. Cell Movement Is Guided by the Rigidity of the Substrate. *Biophys. J.* **2000**, *79* (1), 144–152.

(2) Engler, A. J.; Sen, S.; Sweeney, H. L.; Discher, D. E. Matrix Elasticity Directs Stem Cell Lineage Specification. *Cell* **2006**, *126* (4), 677–689.

(3) Style, R. W.; Che, Y.; Park, S. J.; Weon, B. M.; Je, J. H.; Hyland, C.; German, G. K.; Power, M. P.; Wilen, L. a; Wettlaufer, J. S.; et al. Patterning Droplets with Durotaxis. *Proc. Natl. Acad. Sci. U. S. A.* **2013**, *110* (31), 12541–12544.

(4) Joanny, J.-F.; Jülicher, F.; Prost, J. Motion of an Adhesive Gel in a Swelling Gradient: A Mechanism for Cell Locomotion. *Phys. Rev. Lett.* **2003**, *90* (16), 168102.

(5) Hore, D.; Majumder, A.; Mondal, S.; Roy, A.; Ghatak, A. How to Make a Cylinder Roll Uphill. *Soft Matter* **2012**, *8* (18), 5038–5042.

(6) Mondal, S.; Ghatak, A. Rolling of an Elastomeric Cylinder: A Marangoni like Effect in Solid. *Extrem. Mech. Lett.* **2015**, *3*, 24–35.

(7) Nabarro, F. R. N. *Theory of Crystal Dislocations*; Oxford University Press, 1967.

(8)   Chakrabarti, A.; Chaudhury, M. K. Surface Folding-Induced Attraction and Motion of Particles in a Soft Elastic Gel: Cooperative Effects of Surface Tension, Elasticity, and Gravity. *Langmuir* **2013**, *29* (50), 15543–15550.

(9)   Chakrabarti, A.; Chaudhury, M. K. Attraction of Mesoscale Objects on the Surface of a Thin Elastic Film Supported on a Liquid. *Langmuir* **2015**, *31* (6), 1911–1920.

(10)   Chakrabarti, A.; Chaudhury, M. K.; Mora, S.; Pomeau, Y. Elastobuoyant Heavy Spheres: A Unique Way to Study Nonlinear Elasticity. *Phys. Rev. X* **2016**, *6* (4), 41066.

(11)   Brochard, F. Motions of Droplets on Solid Surfaces Induced by Chemical or Thermal Gradients. *Langmuir* **1989**, *5* (2), 432–438.

(12)   Brzoska, J. B. .; Brochard-Wyart, F.; Rondelez, F. Motions of Droplets on Hydrophobic Model Surfaces Induced by Thermal Gradients. *Langmuir* **1993**, *9*, 2220–2224.

(13)   Van Oss, C. J.; Chaudhury, M. K.; Good, R. J. Interfacial Lifshitz-van Der Waals and Polar Interactions in Macroscopic Systems. *Chem. Rev.* **1988**, *88* (6), 927–941.

(14)   Liu, Q.; Suo, Z. Osmocapillary Phase Separation. *Extrem. Mech. Lett.* **2016**, *7*, 27–33.

(15)   Jensen, K. E.; Sarfati, R.; Style, R. W.; Boltyanskiy, R.; Chakrabarti, A.; Chaudhury, M. K.; Dufresne, E. R. Wetting and Phase Separation in Soft Adhesion. *Proc. Natl. Acad. Sci.* **2015**, *112* (47), 14490–14494.

(16)   Shanahan, M. E. R.; Carré, A. Viscoelastic Dissipation in Wetting and Adhesion Phenomena. *Langmuir* **1995**, *11*, 1396–1402.

(17)   Chaudhury, M. K.; Kim, K. H. Shear-Induced Adhesive Failure of a Rigid Slab

in Contact with a Thin Confined Film. *Eur. Phys. J. E* **2007**, *23* (2), 175–183.

(18) Sekimoto, K.; Leibler, L. A Mechanism for Shear Thickening of Polymer-Bearing Surfaces Elasto-Hydrodynamic Coupling. *Europhys. Lett.* **1993**, *23* (2), 113–117.

(19) Skotheim, J. M.; Mahadevan, L. Soft Lubrication. *Phys. Rev. Lett.* **2004**, *92* (24), 245509–1.

(20) Skotheim, J. M.; Mahadevan, L. Soft Lubrication: The Elastohydrodynamics of Nonconforming and Conforming Contacts. *Phys. Fluids* **2005**, *17* (9), 1–23.

(21) Salez, T.; Mahadevan, L. Elastohydrodynamics of a Sliding, Spinning, Sedimenting Particle near a Soft Wall. *J. Fluid Mech.* **2015**, *779*, 181–196.

(22) Saintyves, B.; Jules, T.; Salez, T.; Mahadevan, L. Self-Sustained Lift and Low Friction via Soft Lubrication. *Proc. Natl. Acad. Sci. U. S. A.* **2016**, *113* (21), 5847–5849.

Appendix V

Elastobuoyant Liquid Inclusion inside a Soft Elastic Hydrogel

V.1. Introduction and Observations

A heavy sphere is engulfed by a soft elastic gel due to Elastobuoyancy phenomenon[1], where its depth inside the gel is determined by the balance of its weight with the accumulated strain energy in the surrounding elastic medium. This phenomenon is discussed in details in chapter 4. Now, we observed that instead of a rigid particle, when a denser liquid was poured over the surface of the soft gel (density: 1000 kg/m^3, like water) the weight of the liquid deformed the gel forming a deep cavity at its central region. When we used chloroform (density: 1450 kg/m^3) as the liquid phase over the gel (μ = 14 Pa), we saw the complete closure of the stretched gel surface around the liquid forming a pendant shape (Figure V.1).

However, with silicone oil (density: 1050 kg/m^3) that it is moderately higher than the gel, we see the formation of the long finger-like well (Figure V.2). Now, when the gel is slightly stiffer, and the density of the liquid phase is slightly higher than the gel, we see formation of undulations of the gel surface that are similar to the lobe-formation due to gravity acting on the free surface when a flat container of soft gel is turned upside down[2] (Figure V.3).
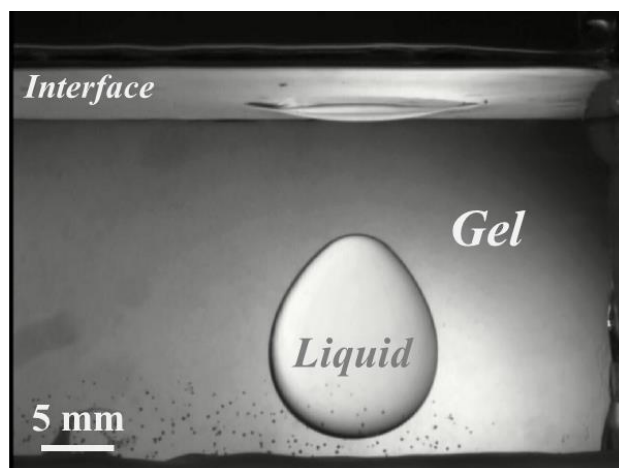
Figure V.1: An elastobuoyant liquid inclusion inside a soft gel (μ = 14 Pa, density: 1000 kg/m³). We used chloroform (density: 1450 kg/m³) as the heavy liquid for this experiment. As soon as the chloroform was poured on the gel surface, due to its weight, a cavity was formed inside the gel substrate that was filled by the liquid. The stretched gel surfaces folded over the liquid forming a pendant shaped liquid inclusion. The entire experiment took about a few seconds and the picture was captured immediately. Even after several days, we didn't see any noticeable evaporation from the stored chloroform inside the gel pointing to the fact that the gel surfaces adhesively seal quite well above the liquid.

Figure V.2: An elastobuoyant liquid filled cavity inside a soft gel (μ = 14 Pa, density: 1000 kg/m³). We used silicone oil (density: 1050 kg/m³) as the liquid phase for this experiment. As soon as the oil was poured on the gel surface, due to its weight, a cavity was formed inside the substrate storing the liquid inside it. However, we do not see the closure of the gel above. A layer of the oil is still maintained over the gel surface as shown in the figure.

In these studies, apart from the density difference between the liquid and the gel ($\Delta\rho$) and the elastic modulus of the gel, the interfacial tension between the gel and the liquid will also play a very important role. For instance, if the interfacial tension is very low or close to zero, the surfaces will not prefer to fold over each other. Also, the shape of the liquid pendant drop inside will be determined by the interfacial energy of the gel/liquid surface. A higher interfacial energy would mean more circular drops of liquid inclusions as the surfaces would prefer to seal as much as possible, whereas, its lower values would imply the formation of elongated drops as the surfaces may not close that much. One could perhaps even find a phase diagram for the shape of the liquid inclusions inside the gel by varying the interfacial energy of the gel/liquid, the elastic modulus of the gel and the effective density ($\Delta\rho$). For slightly stiffer gels, the liquid phase due to its weight deforms the gel surface forming undulatory wavy patterns just like the elastic Rayleigh-Taylor instabilities observed in inverted gel slabs.[2] All our experiments were performed with a crosslinked polyacrylamide gel, the preparation method for which is described in Chapter 2 and its elastic modulus was measured using a protocol mentioned in Chapter 6.

AV.2. Discussion and Future Work

In the following, to understand the elastobuoyant liquid inclusion, we draw an analogy with the experimental configuration used by Mora *et. al.*[2] in their study of Rayleigh-Taylor instability in soft elastic solids. A large gel slab in a rectangular container, when turned upside down undergoes surface instabilities due to its own weight and stabilizing elastic energy. When the systems are unconfined (depth of container proportional to its width) and elastic modulus of the gel is low, they see
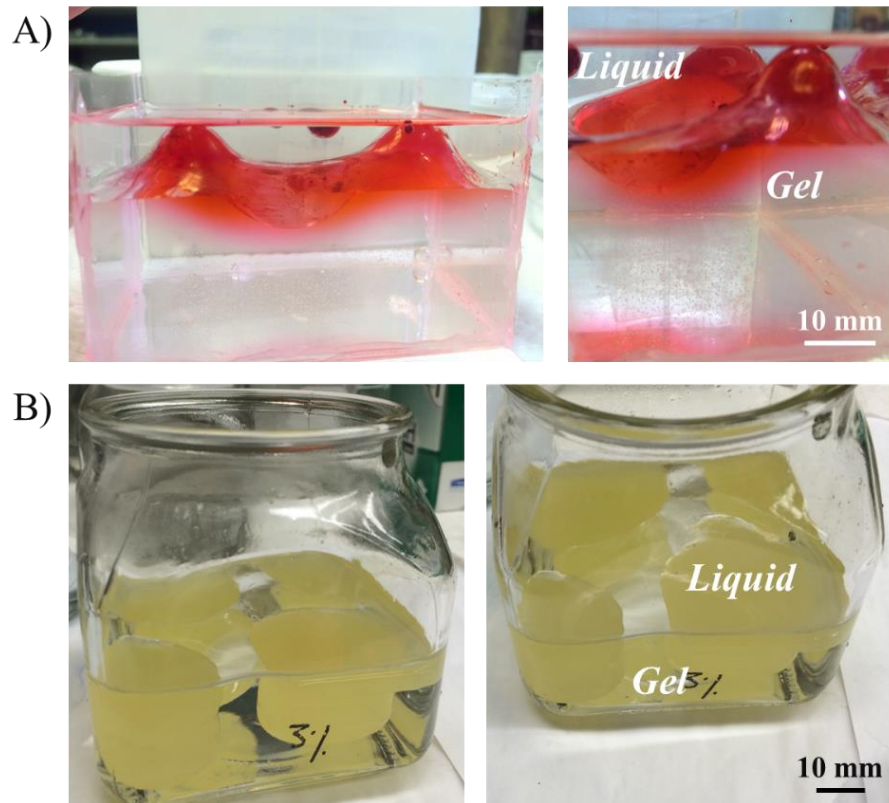
Figure V.3: Rayleigh-Taylor instability in soft gels[2] due to a heavier liquid phase at the top of the elastic gel (density: 1000 kg/m³). (A) The liquid used here is a silicone oil (density: 1050 kg/m³) and the shear modulus of the gel is 24 Pa. The gel interface was marked with a water-soluble red dye to help in visualizing the deformation of its surface. The snapshot on the right gives a side view of the same experiment. (B) The liquid used here is diiodomethane (density: 3320 kg/m³) and the shear modulus of the gel is 52 Pa. Diiodomethane has been filled completely in the four lobes formed due to the gravity induced instability.

formation of one large finger at the center of the downward facing gel slab. In our current experiments, the formation of a large cavity at the center of the soft gel due to the heavier liquid phase on top resembles the former case. However, an important distinction in these two cases is that when the upper heavier phase is the solid, as in the experiments of Mora *et. al.,* the largest finger formed will be limited by the critical stress developed in the system that would ultimately lead to fracture of the solid blob. On the other hand, when the upper heavier phase is a liquid, large deformations will only lead to the pinching off the liquid from the top forming an enclosed drop. The fact

that the entire surface does not undergo Rayleigh-Taylor like instability in Figures V.1 and V.2 is reminiscent of a situation as pointed out by Pomeau for the case of subcritical instability limited to the growth of a narrow band like regime in Taylor-Couette flow because by growing it lowered the Reynolds outside and brought it to a linearly stable situation.[3] This can be thought analogously to our situation as "once the drop begins to sink down, all the rest of the silicon layer becomes stable against Rayleigh-Taylor."

Before we come to a more definite conclusion about our observations on the elastobuoyant liquid inclusions, we must conduct more detailed experiments to study the effect as a function of important parameters such as elastic modulus, the density difference between the two phases and interfacial tensions as well as the geometry of the containers. We can also vary the quantity of the liquid added to know if the pinch-off is only for a small amount of liquid. Also, when the liquid is poured progressively, it will be interesting to observe the evolution of the shape from a long liquid cavity to an engulfed drop where the dynamics would be important. Performing the experiments with larger containers might lead to multiple liquid inclusions and in turn, the upper free surface of the gel would be covered with topological defects that may serve useful for various applications, *e.g.* self-assembly.

References

(1)   Chakrabarti, A.; Chaudhury, M. K.; Mora, S.; Pomeau, Y. Elastobuoyant Heavy Spheres: A Unique Way to Study Nonlinear Elasticity. *Phys. Rev. X* **2016**, *6* (4), 41066.

(2)   Mora, S.; Phou, T.; Fromental, J.-M.; Pomeau, Y. Gravity Driven Instability in Elastic Solid Layers. *Phys. Rev. Lett.* **2014**, *113*, 178301.

(3)   Hayot, F.; Pomeau, Y. Turbulent Domain Stabilization in Annular Flows. *Phys. Rev. E* **1994**, *50* (3), 2019–2021.

Appendix VI

Elastocapillary Attraction of Spherical Beads on a Soft Solid through a Liquid Medium

1. Introduction and Objective

The objective of these experiments was to study the effect of viscosity of the surrounding medium in the elastocapillary attraction of rigid particles on a soft solid. Coupled effects of hydrodynamics with elastic effects has been a subject of detailed studies in the past.[1–4] Our observations[5] from previous experiments indicate that the friction experienced by the particles moving on the surface of gel through a layer of heptane housed on top of the gel was much higher than that experienced by the particles when they moved on the air-gel interface. We had suggested previously[5] that the higher friction may be due to the effect of viscous dissipation in the thin lubricating liquid film in between the particle and the solid. Inspired by a suggestion from Professor Stone upon presenting our initial results to him, we carried out the following investigations to study the effect of viscosity of the surrounding liquid medium on particle attraction in such an elastohydrodynamic setting.

2. Experiment

A physically crosslinked polyacrylamide gel[6] (shear modulus ~ 14.3 Pa) was used for these studies and cured in different containers such that each oil was poured in a fresh container of cured gel with which to study the elastohydrodynamics of the particle attraction. We used two identical hydrophobic glass beads[5] (3.2 mm diameter, density 2.4 g/cc, its surface grafted with PDMS T-22) for our studies. We used six different oils of different viscosities, three of which were PDMS oils and the other three were alkanes. The physical properties of all the oils used for these experiments are tabulated below:

Oil (Upper phase, Medium 3)	Dynamic Viscosity, η ($\times 10^{-3}$ Pa s)	Density, ρ (kg/m^3)	Surface Tension (γ_3) (mN/m)	Free energy of Adhesion (ΔG_{132}) (mJ/m^2)
n-Heptane	0.376	684	20.14	-0.149096159
n-Dodecane	1.49	749	25.35	-0.099432127
n-Hexadecane	3	773	27.47	-0.391574024
PDMS T-05	5	918	22	0.008913491
PDMS T-15	50	960	22	0.008913491
PDMS T-31	1000	971	22	0.008913491

Our choice of liquids was based on a calculation of the free energy of adhesion (ΔG_{132}) between the particle and the soft substrate through a liquid medium, such that the values were close to zero or positive that would imply that the particles would not stick to the surface of the gel. This is only a first order approximate calculation that may not imply that the spheres will never adhere to the gels and it was only to help us select

which liquids to work with from a wide range. The free energy of adhesion between a rigid particle (Medium 1) and the gel[7] (Medium 2) through a liquid phase (Medium 3) is given by $\Delta G_{132} = -2(\sqrt{\gamma_1} - \sqrt{\gamma_3})(\sqrt{\gamma_2^d} - \sqrt{\gamma_3})$, where, γ_1 is the surface energy of the glass bead, γ_2^d is the dispersion component of the surface energy of the gel and γ_3 is the surface tension of the surrounding liquid medium. The hydrogel is polar since it is largely composed of water but as the oils used for our experiments exhibit only dispersive interactions, only the dispersion component of the surface tension of gel ($\gamma_2^d \sim 21.8$ mN/m) will account for the interactions between itself and the particles. The surface energy of the PDMS grafted glass bead (γ_1) is 24 mN/m (for a disordered packing of the grafted polymers that is usually the case when the grafting is not done in a highly precise manner). While using water as the surrounding medium would also give a zero work of adhesion ($\gamma_2 = \gamma_3$), we often observed swelling induced instability patterns on the surfaces of the gel that made water an unsuitable surrounding medium for these studies. The computed values of the free energy ΔG_{132} are also tabulated in the table above.

In our experiments, the two identical hydrophobic glass beads were released on the surface of the gel through the oil medium with an initial separation distance of about three times the diameters of the bead. A video of their elastocapillary attraction through the liquid was recorded. Using image analysis, we measured how the separation distance (between the centers of the two particles) decreased as a function of time until they made contact and plotted the data for approach through each liquid in Figure VI.1.
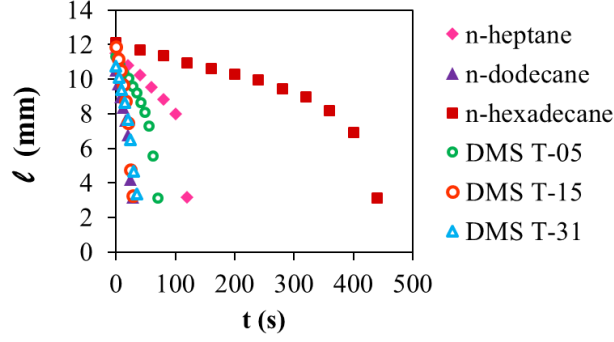
Figure VI.1: The center-to-center separation distance (ℓ) between two PDMS grafted glass beads (3.2 mm diameter) decreasing as a function of time as they attract on the surface of gel (shear modulus ~ 14.3 Pa) through a liquid medium and come into final contact. Each data set represents experiments with a different oil as the upper liquid medium on the gel as indicated in the legend.

3. Observations and Conclusions

From the experimental data (Figure VI.1) of the distance of separation changing as a function of time for the two hydrophobic glass beads, a first general idea can be obtained the frictional resistance experienced by them. The trend we observed was not monotonous in the increasing or decreasing direction of the viscosities of the surrounding medium. Yet, we describe below a scaling analysis that predicts the effect of viscous dissipation on the friction coefficient. Based on the well-established elastohydrodynamic scaling laws, we calculated the friction coefficient (ζ) by balancing the driving force with the viscous dissipative forces ($F_{vis} \sim \eta V \ell^2 / h$) exerted by the thin lubricating film in between the particle and the gel, where ℓ is the contact length, V is the steady state velocity of the particle and h is the thickness of the lubricating thin film of the liquid in between the particle and the gel. The vertical lift force ($F_l \sim \eta^2 R^2 V^2 / \mu h^3$)[8] is balanced by the weight of the particle (m^*g). Here, R is the radius of the particle and μ is the shear modulus of the soft elastic substrate. This leads us to a relationship that predicts the friction coefficient should increase weakly with the

viscosity, $\zeta \sim \eta^{1/3}$. Since this effect is not that pronounced in our experiments (Figure VI.1), we feel there may be an additional effect due to the hysteresis of adhesion that is briefly described below.

When the PDMS-grafted glass beads move over the gel, despite the free energy of adhesion being zero or positive necessitating a thin liquid film in between the particle and the gel, local microscopic contacts may still be made between the polymer chains of the gel with the particle surface during its motion. The hysteresis of the formation and breakage of these local bonds give rise to additional dissipation and thus combining with the effect of the viscosity, the dependence of friction may not be a monotonic function of either of the sources but a complex function of all the contributing factors.

These experiments point us to an interesting problem of friction between soft and hard surfaces through a liquid that may be important in ball bearings with soft coatings or even designing *soft fluidic* devices in the future. Further studies will reveal the intricate complexities of the coupled effects of adhesion and viscosity mediated dissipative effects on particle motion in elastohydrodynamics.

References

(1)   Sekimoto, K.; Leibler, L. A Mechanism for Shear Thickening of Polymer-Bearing Surfaces Elasto-Hydrodynamic Coupling. *Europhys. Lett.* **1993**, *23* (2), 113–117.

(2)   Skotheim, J. M.; Mahadevan, L. Soft Lubrication. *Phys. Rev. Lett.* **2004**, *92* (24), 245509–1.

(3)   Salez, T.; Mahadevan, L. Elastohydrodynamics of a Sliding, Spinning, Sedimenting Particle near a Soft Wall. *J. Fluid Mech.* **2015**, *779*, 181–196.

(4)   Saintyves, B.; Jules, T.; Salez, T.; Mahadevan, L. Self-Sustained Lift and Low Friction via Soft Lubrication. *Proc. Natl. Acad. Sci. U. S. A.* **2016**, *113* (21),

5847–5849.

(5)   Chakrabarti, A.; Chaudhury, M. K. Elastocapillary Interaction of Particles on the Surfaces of Ultrasoft Gels: A Novel Route To Study Self-Assembly and Soft Lubrication. *Langmuir* **2014**, *30* (16), 4684–4693.

(6)   Chakrabarti, A.; Chaudhury, M. K. Direct Measurement of the Surface Tension of a Soft Elastic Hydrogel: Exploration of Elastocapillary Instability in Adhesion. *Langmuir* **2013**, *29* (23), 6926–6935.

(7)   Van Oss, C. J.; Chaudhury, M. K.; Good, R. J. Interfacial Lifshitz-van Der Waals and Polar Interactions in Macroscopic Systems. *Chem. Rev.* **1988**, *88* (6), 927–941.

(8)   Skotheim, J. M.; Mahadevan, L. Soft Lubrication: The Elastohydrodynamics of Nonconforming and Conforming Contacts. *Phys. Fluids* **2005**, *17* (9), 1–23.

Vita

Aditi Chakrabarti was born to Chandana Chakrabarti and Parthapratim Chakrabarti on November 14, 1989, in Jabalpur, Madhya Pradesh in India. She has a younger sister, Suriti. Aditi grew up in Kolkata, India where she attended Auxilium Convent School, Dum Dum until her tenth grade graduating in March 2006. She completed her eleventh and twelfth grades in Our Lady Queen of the Missions School in Salt Lake from where she graduated in March 2008. Her parents were always keen on a well-rounded development of their daughters and encouraged them to pursue many extra-curricular activities. Aditi trained in Vocal Hindustani Classical Music as well as learned songs of Rabindranath Tagore throughout her years in Kolkata. She also learned Bharatnatyam, an Indian classical dance form that originated in Tamil Nadu, India. After finishing high school, Aditi completed her Bachelor of Technology in Chemical Engineering in May 2012 at Heritage Institute of Technology, Kolkata that is affiliated to the West Bengal University of Technology.

From August 2012, she began her doctoral research in the department of Chemical and Biomolecular Engineering at Lehigh University under the guidance of Professor Manoj K. Chaudhury on elastocapillary phenomena in soft elastic solids. From November 2015 to May 2016, she had the opportunity to spend seven months at University of Montpellier, working with Professors Serge Mora, Basile Audoly and Yves Pomeau on nonlinear analyses of elastic Rayleigh-Taylor Instability in soft solids. After the completion of her Ph.D. degree at Lehigh in May 2017, she will join Professor L. Mahadevan's group at Harvard University as a postdoctoral fellow.

EDUCATION

Ph.D. Chemical Engineering (August, 2012-May, 2017) Lehigh University,
Bethlehem, PA.

  Topic of Research: Adhesion on thin elastic films, Elasticity mediated
     interaction of particles on thin elastic films and soft gels,
     Role of elastocapillarity in adhesion induced instabilities.
  Adviser: Prof. Manoj K. Chaudhury

Research Experience (Nov, 2015- May, 2016) LMGC (Équipe: Physique et
     Mécanique des Milieux Divisés),
     University of Montpellier, France.

  Topic of Research: Non-linear analysis of elastic Rayleigh Taylor
     instabilities in soft solids; Theoretical studies
     on large deformation behavior of ultra-soft gels.
  Advisers: Prof.(s) Yves Pomeau, Serge Mora and Basile Audoly.

B.Tech Chemical Engineering (2008-2012) Heritage Institute of Technology,
     Kolkata, West Bengal University of
     Technology, India, GPA: 9.28/10.

  Undergraduate Thesis Topic: Ultrafiltration using High Shear Devices
  Adviser: Dr. Sangita Bhattacharjee

AWARDS AND HONORS

- **Leonard A. Wenzel Award (2013),** Lehigh University
  For best performance in Qualifying Examination in the Department of Chemical Engineering in 2013.

- Selected as one of the 10 candidates to contribute an oral presentation in the AIChE MESD-**Polymers Excellence in Graduate Polymer Research** honorary session (08A18) during the **2014** AIChE Annual Meeting (Atlanta, GA).

- Awarded for **Excellence in Polymer Science and Engineering Research** from Society of Plastics Engineers SPE Lehigh Valley, November 17, **2015**.

PUBLICATIONS (Peer Reviewed)

14. **Chakrabarti, A.**; Porat, A; Salez, T.; Raphäel, E.; Chaudhury, M. K. Wetting of Soft Elastic Hydrogels. (Under Preparation, **2017**).

13. **Chakrabarti, A.**; Mora, S.; Audoly, B.; Phou, T.; Fromental, J. M.; Richard, F.; Pomeau, Y. Weakly nonlinear regime of rayleigh taylor instability in soft solids. (Under Preparation, **2017**).

12. **Chakrabarti, A.**; Chaudhury, M. K.; Mora, S.; Pomeau, Y. Elasto-buoyant heavy spheres: a unique way to study non-linear elasticity. *Physical Review X*, **2016**, *6*(4), 041066.

11. Biswas, S.; **Chakrabarti, A.**; Chateauminois, A.; Wandersman, E.; Prevost, A. M.; Chaudhury, M. K. Soft Lithography using Nectar Droplets. *Langmuir* **2015**, *31*, 13155-13164.

10. Jensen, K. E.; Sarfati, R.; Style, R. W.; Boltyanskiy, R.; **Chakrabarti, A.**; Chaudhury, M. K.; Dufresne, E. R. Wetting and Phase Separation in Soft Adhesion. *Proc. Natl. Acad. Sci.* **2015**, *112*, 14490-14494.

9. **Chakrabarti, A.**; Ryan, L.; Chaudhury, M. K.; Mahadevan, L. Elastic Cheerios effect: Self-Assembly of Cylinders on a Soft Solid. *Europhys. Lett.* **2015**, *112*, 54001.

8. Chaudhury, M. K.; **Chakrabarti, A.**; Ghatak, A. Adhesion Induced Instabilities and Pattern Formation in Thin Films of Elastomers and Gels. *Eur. Phys. J. E* **2015**, *38*, 82. (Invited Colloquium Paper)

7. Chaudhury, M. K.; **Chakrabarti, A.**; Daniel, S. Generation of Motion of Drops with Interfacial Contact. *Langmuir* **2015**, *31*, 9266–9281. (Invited Feature Article) (*Cover Page Illustration*).

6. **Chakrabarti, A.**; Chaudhury, M. K. Attraction of Meso-Scale Objects on the Surface of a Thin Elastic Film Supported on a Liquid. *Langmuir* **2015**, *31*, 1911-1920. (*Cover Page Illustration*)

5. Chaudhury, M. K.; **Chakrabarti, A.**; Tibrewal, T. Coalescence of drops near a hydrophilic boundary leads to long range directed motion. *Extreme Mechanics Letters* **2014**, 1, 104-113.

4. **Chakrabarti, A.**; Chaudhury, M. K. Vibrations of Sessile Drops of Soft Hydrogels. *Extreme Mechanics Letters* **2014**, 1, 47-53.

3. **Chakrabarti, A.**; Chaudhury, M. K. Elasto-capillary interaction of particles on the surfaces of ultra-soft gels: A novel route to study self-assembly and soft lubrication *Langmuir* **2014**, *30*, 4684-4693.

2. **Chakrabarti, A.**; Chaudhury, M. K. Surface Folding-Induced Attraction and Motion of Particles in a Soft Elastic Gel: Cooperative Effects of Surface Tension, Elasticity, and Gravity. *Langmuir* **2013**, *29*, 15543−15550. (*Cover Page Illustration*)

1. **Chakrabarti, A.**; Chaudhury, M. K. Direct measurement of the surface tension of a soft elastic hydrogel: Exploration of elastocapillary instability in adhesion. *Langmuir* **2013**, *29*, 6926−6935.

INVITED TALKS

6. **Chakrabarti, A.**; Chaudhury, M. K. Elasto-capillary Phenomena in Soft Solids. February, **2017**, Prof. L. Mahadevan's Group, Harvard University, Cambridge, MA, USA.

5. **Chakrabarti, A.**; Mora, S.; Audoly, B.; Fromental, J.-M.; Phou, T.; Richard, F.; Pomeau, Y. Rayleigh Taylor instability in soft elastic solids. February, **2017**, ChBE Graduate Symposium, Lehigh University, Bethlehem, PA, USA.

4. **Chakrabarti, A.**; Chaudhury, M. K.; Mora, S.; Pomeau, Y. Elastobuoyant Heavy Spheres in a Soft Gel: Understanding large deformations in soft materials. March, **2016**, Department of Agrotechnology and Food Sciences, Subdivision: Physical Chemistry and Soft Matter, Wageningen University, Netherlands.

3. **Chakrabarti, A.**; Chaudhury, M. K. Oscillations of Sessile Drops of Soft Hydrogels. April, **2016**, Equipe: Matière Molle, Laboratoire Charles Coulomb, CNRS, University of Montpellier II, Montpellier, France.

2. **Chakrabarti, A.**; Chaudhury, M. K. Role of Elastocapillarity in Pattern Formation and Adhesion. November, **2014**, Department of Chemical and Biomolecular Engineering, Lehigh University, Bethlehem, PA, USA.

1. **Chakrabarti, A.**; Chaudhury, M. K. Elasticity Mediated Long Range Attraction of Particles. October, **2014**, Department of Chemical Engineering, Indian Institute of Technology, Kanpur, India.

CONFERENCE TALKS

9. **Chakrabarti, A.**; Chaudhury, M. K.; Mora, S.; Pomeau, Y. Elastobuoyant Heavy Spheres in a Soft Gel: Understanding Large Deformations in Soft Elastic Polymeric Gels. (November, **2016**, AIChE Annual Meeting, San Francisco, CA).

8. **Chakrabarti, A.**; Audoly, B.; Mora, S.; Pomeau, Y. Weakly nonlinear regime of Rayleigh Taylor instability in soft solids. (October, **2016**, Society of Engineering Science (SES) Technical Meeting, University of Maryland College Park, MD).

7. **Chakrabarti, A.**; Chaudhury, M. K. Role of Elasto-capillarity in Pattern Formation and Adhesion. (**Award Talk**, Society of Plastics Engineers, Lehigh Valley Section Regional Meeting, November, **2015**, Bethlehem, PA).

6. **Chakrabarti, A.**; Chaudhury, M. K. Role of Elasto-capillarity in Pattern Formation and Adhesion. (November, **2014**, Session: Excellence in Graduate Polymer Research, AIChE Annual Meeting, Atlanta, GA).

5. **Chakrabarti, A.**; Chaudhury, M. K. Elasticity Mediated Long Range attraction of Particles. (September, **2014**, Workshop on Adhesion/Friction of Soft Materials, GDR MePhy, ESPCI, Paris, France).

4. **Chakrabarti, A.**; Chaudhury, M. K. Interaction of Rigid Cylinders on a Thin Elastic Film Supported on Liquid. (**Soundbite**, August, **2014**, 13th Mid-Atlantic Soft Matter Workshop, Johns Hopkins University, Baltimore, MD).

3. **Chakrabarti, A.**; Chaudhury, M. K. Elasticity modified capillary attraction of particles on the surface of an ultra-soft gel. (May, **2014**, ACS Colloid & Surface Science Symposium, Philadelphia, PA).

2. **Chakrabarti, A.**; Chaudhury, M. K. Roles of the Elasto-Capillary Instability in the Adhesion of Soft Gels. (May, **2014**, ACS Colloid & Surface Science Symposium, Philadelphia, PA).

1. **Chakrabarti, A.**; Chaudhury, M. K. Direct measurement of the surface tension of a soft elastic hydrogel: Exploration of elastocapillary instability in adhesion. (November, **2013**, AIChE Annual Meeting, San Francisco, CA).